

ABSTRACT

Title of Dissertation: ULTRA-SMALL METAL NANOPARTICLES:
AEROSOL- AND LASER-ASSISTED
NANOMANUFACTURING,
CHARACTERIZATION, AND
APPLICATIONS

Yong Yang, Doctor of Philosophy, 2019

Dissertation directed by: Prof. Michael R. Zachariah
Department of Chemical and Biomolecular
Engineering

Ultrasmall metal nanoparticles (1-10 nm) are certain to be the building blocks of the next generation of electronic, catalytic, and energy storage devices. Despite their importance, synthesizing these extremely small nanoparticles, at least in sufficient quantities to enable their industrial utility however, is challenging due to their low stability and tendency to agglomerate.

Numerous techniques developed thus far typically generate metal nanoparticles in small quantities with a main difficulty in industrial scale-up being poor thermal control. This shortcoming often leads to wide size distributions, inhomogeneous dispersion, and aggregation. Thus, there is a pressing need for developing new strategies for scalable manufacturing of ultrasmall metal nanoparticles towards industrial applications.

This dissertation identifies two techniques for scalable manufacturing of ultrasmall metal nanoparticles with tunable size, constituency, microstructure, and other properties: an aerosol droplet mediated approach and an ultrafast laser shock approach.

The aerosol droplet mediated approach employs the fast heating and quenching nature of aerosol droplet nanoreactors containing precursor species to produce ultrasmall metal nanoparticles uniformly dispersed in polymer or graphene matrices. The fast heating and quenching nature intrinsic to the aerosol droplets is also employed to fabricate a new type of engineering material, notably high entropy alloy nanoparticles, defined as five or more well-mixed metal elements in near equimolar ratios. As an example of application, I further employ the aerosol droplets to create antimony nanoparticles incorporated carbon nanosphere network and the resulting architecture offered one of the best potassium ion battery anode performances in terms of both capacity and cycling stability.

This dissertation also introduces an ultrafast laser shock technique to decorate metal nanoparticles onto carbon nanofibers (CNFs) in-situ with kinetically tunable size and surface density. A shorter laser shock enables the formation of metal nanoclusters with higher number densities and smaller sizes while longer laser shock leads to the further growth of metal nanoclusters and the achievement of their equilibrium shape. The catalytic performance towards electrocatalytic hydrogen evolution was greatly enhanced for CNF supported metal nanoclusters with a smaller size and higher number density.

ULTRA-SMALL METAL NANOPARTICLES:
AEROSOL- AND LASER-ASSISTED NANOMANUFACTURING,
CHARACTERIZATION, AND APPLICATIONS

by

Yong Yang

Dissertation submitted to the Faculty of the Graduate School of the
University of Maryland, College Park, in partial fulfillment
of the requirements for the degree of
Doctor of Philosophy
2019

Advisory Committee:

Professor Michael R. Zachariah, Chair
Professor Akua Asa-Awuku
Professor Dongxia Liu
Dr. George W. Mulholland
Professor Taylor J. Woehl
Professor Liangbing Hu, Dean's Representative

© Copyright by
Yong Yang
2019

Dedication

To my parents, whose love and support made everything in my life possible. To my sister and niece, for being such kind and lovely people.

谨以此文献给我所亲爱的爸爸妈妈，感恩你们一如既往的疼爱与支持，愿平安喜乐常与你们同在！也以此文献给我美丽的姐姐和外甥女，你们总是那么的温柔可爱！

Acknowledgements

I am incredibly gratefully for all the people who helped make this dissertation a possibility.

First and foremost, I would like to thank my advisor, Dr. Michael Zachariah for his guidance, support, and patience throughout my studies. I feel very fortunate to be his student, and his great example has taught me so much about how to be a successful researcher and person.

I would also like to thank all my current and former lab mates, particularly Dr. Rohit Jacob, Pankaj Ghildiyal, Dylan Kline, Xiang Ke, Dr. Haiyang Wang, Dr. Guangjie Feng, Miles Rehwoldt, Feiyu Xu, Dr. Xizheng Wang, Dr. Scott Holden, Dr. Tao Wu, , Dr. Jiaojie Tan, Dr. Jeffery Delisio, Dr. Phillip Guerieri, Dr. Yichen Zong, Dr. James Corson, Dr. Lu Liu, Dr. Garth Egan, Dr. Mingdong Li, Dr. Wenbo Zhou, Dr. Rian You for the discussions and assistance. Without their support and help, this journey of my PhD studies would have been less enjoyable. In addition, thanks to my many collaborators, in particular, Dr. Chunsheng Wang, Dr. Liangbing Hu. Dr. Reza Shahbazian-Yassar, Dr. Dongxia Liu, Dr. Yonggang Yao, Dr. Jing Zheng, Boao Song, Tangyuan Li for all their time, efforts, and expertise. Also thanks to Dr. Sz-Chian Liou (UMD) and Dr. Krassimir N. Bozhilov (UC Riverside) for training me on operating SEM/TEM/STEM/EDS instruments.

Finally, I would like to acknowledge my advisory committee, Dr. Michael Zachariah, Dr. Akua Asa-Awuku, Dr. Liangbing Hu, Dr. Dongxia Liu, Dr. George W. Mulholland, Dr. Taylor J. Woehl for their valuable input. I would also like to thank the Office of Naval Research's Multidisciplinary University Research Initiatives (ONR-MURI), National Science Foundation (NSF), the University of Maryland (UMD) and its

Nanocenter, and the University of California, Riverside (UCR) for financial support of my projects.

Table of Contents

Dedication.....	ii
Acknowledgements.....	iii
Table of Contents.....	v
List of Tables.....	vii
List of Figures.....	viii
List of Abbreviations.....	xv
Chapter 1: Introduction.....	1
1.1. Metal Nanoparticles.....	1
1.2. Synthesis techniques.....	1
1.2.1. Top-down approach.....	2
1.2.2. Bottom-up approach.....	4
1.3. Nanoparticle growth mechanism.....	6
1.4. Potential Applications.....	11
1.5. Current Challenges.....	13
1.5.1. Scalable manufacturing of ultra-small metal nanoparticles.....	13
1.5.2. Scalable manufacturing of multi-component metal nanoparticles.....	14
1.6. Research Plan.....	16
1.7. Scope of the Dissertation.....	18
Chapter 2: Experimental Design and Characterizations.....	22
2.1. Aerosol assisted nanomanufacturing.....	22
2.2. Aerosol droplets as building blocks for functional nanostructured design.....	25
2.3. Laser-assisted nanomanufacturing.....	26
2.4. High speed color pyrometry.....	28
2.5. Catalytic performance tests.....	29
2.6. Battery performance tests.....	30
2.7. Characterization.....	31
Chapter 3: Growth of Sub- 5nm Metal Nanoclusters in Polymer Melt Aerosol Droplets	
3.1. Introduction.....	36
3.2. Experimental section.....	40
3.3. Results and Discussion.....	42

3.4. Conclusions	59
3.5. Supporting Information	60
Chapter 4: Thermal Shock Synthesis of Metal Nanoclusters within On-the-fly Graphene Particles	66
4.1. Introduction	67
4.2. Experimental Section	70
4.3. Results and Discussion.....	73
4.4. Conclusions	88
4.5. Supporting Information	89
Chapter 5: Extremely Stable Antimony-Carbon Composite Anodes for Potassium-ion Batteries 97	
5.1. Introduction	98
5.2. Experimental section	101
5.3. Results and discussion.....	104
5.4. Conclusions	120
5.5. Supporting Information	121
Chapter 6: Aerosol synthesis of high entropy alloy nanoparticles	129
6.1. Introduction	130
6.2. Experimental section	134
6.3. Results and discussion.....	137
6.4. Conclusions.....	149
6.5. Supporting information	150
Chapter 7: Laser Shock-Assisted Ultrafast Synthesis of Supported Metal Nanoclusters with Kinetically Tunable Size and Surface Density	158
7.1. Introduction	159
7.2. Experimental section	161
7.3. Results and Discussion.....	164
7.4. Conclusions	180
7.5. Supporting Information	181
Chapter 8: Summary and Future Work.....	190
8.1. Summary	190
8.2. Future Work	193
Bibliography	196
Publications and Presentations.....	215

List of Tables

Table 3.1. Synthetic conditions for spray pyrolysis	43
Table 3.2. Geometric Standard deviations σ , for Ni nanoparticles generated at different conditions.....	57
Table 3.3. Volume fraction of metal, areal concentration and average diameter of metal in polymer.....	61
Table 4.1. Comparison of catalytic activity of the catalysts for the reduction of 4-NP with NaBH ₄	84
Table 4.2. Property data used to calculate saturation ratio.....	91
Table 4.3. Property data used for the characteristic time analysis.....	93
Table 4.4. Geometric standard deviations σg for Ni nanoclusters generated at different conditions.....	94
Table 5.1. A comparison summary of potassium storage performances for the most common anodes materials in the previous reports.....	126
Table 5.2. Atomic percentage concentrations of different elements with increasing etching time for the SEI layers on Sb@CSN electrode formed in 1M KTFSI and 4M KTFSI electrolytes.....	127
Table 6.1. Physical properties of different metal investigated in this study	156
Table 6.2. Standard reduction potentials for different metals	157
Table 7.1. Property data used to calculate saturation ratio.....	183
Table 7.2. Release time, release temperature for different species detected by time of flight mass spectrometry.....	184
Table 7.3. Overpotentials for CNF supported Pt nanoclusters at various current densities applied.....	186
Table 7.4. Property data used for the characteristic time analysis.....	189

List of Figures

Figure 1.1. Gibbs free energy change as a function of particle radius.....	7
Figure 2.1. Schematic of aerosol assisted scalable manufacturing of ultrasmall metal nanoparticles.	23
Figure 2.2. Schematic illustration of electrospray-assisted strategy for fabricating Sb@CSN material.....	26
Figure 2.3. Schematic of laser shock synthesis of high-density ultrasmall metal nanoparticles uniformly decorated on carbon nanofiber thin film.....	28
Figure 3.1. Schematic of formation of nanoclusters in aerosol polymer droplet.....	41
Figure 3.2. SEM images of metal polymer nanocomposites. (a)Ni PVP8k, (b)Co PVP58k, (c)Cu PVP8k. The length of the scale bar in the inset images is 1 μm	43
Figure 3.3. TEM images and metal nanocluster size distribution in metal polymer nanocomposites. (a)(d)(g) Ni PVP8k; (b)(e)(h) CoPVP58k; (c)(f)(i) CuPVP8k.	46
Figure 3.4. XRD of metal polymer nanocomposite synthesis under various reaction temperatures.....	47
Figure 3.5. SEM and TEM images of Ni/NiO polymer nanocomposites synthesized at different reaction temperatures. (a)(f)(k) 400 $^{\circ}\text{C}$, (b)(g)(l) 500 $^{\circ}\text{C}$, (c)(h)(m) 600 $^{\circ}\text{C}$, (d)(i)(n) 700 $^{\circ}\text{C}$, (e)(j)(o) 800 $^{\circ}\text{C}$	49
Figure 3.6. Size and number concentration evolution of Ni/NiO nanoparticles with reaction temperature	49
Figure 3.7. SEM and TEM images of metal polymer nanocomposites with different metal salt to PVP ratio. (a)(e)(i) 0.1 (b)(f)(j) 0.3, (c)(g)(k) 0.5, (d)(h)(l) 1.0	51
Figure 3.8. Average diameter and areal concentration of Ni nanoparticles as a function of metal salt to polymer ratio	51
Figure 3.9. Characteristic sintering and coagulation time as a function of Ni nanoparticle diameter at 600 $^{\circ}\text{C}$. The green dash line represents the transition of the melting point of Ni nanoparticles.	55
Figure 3.10. Scaled nanoparticle size distribution measured for three different reaction temperatures with a fixed metal salt to PVP ratio of 0.3 (a) and for four different metal salt to PVP ratios with a fixed reaction temperature of 600 $^{\circ}\text{C}$ (b). The dashed light blue line is the size distribution obtained for log-normally self-preserving size, and the dashed black line is the LSW size distribution.....	57
Figure 3.11. Schematic of the nucleation and growth of metal nanoparticles in polymer melt at 600 $^{\circ}\text{C}$	58

Figure 3.12. TGA of PVP polymer (MW. 8000g/mol) with a heating rate of 10C/min in Ar gas	60
Figure 3.13. FTIR spectra of PVP polymers with different molecular weights before and after spray pyrolysis at 600 °C with 5% H ₂ and 95%N ₂ as carrier gas	60
Figure 3.14. SEM images of PVP polymers with different molecular weights after spray pyrolysis: (a) 8000g/mol; (b)58000g/mol;(c)1300000g/mol	61
Figure 3.15. XRD Patterns of metal (Ni, Co, Cu) polymer nanocomposites.....	61
Figure 3.16. (a-c) STEM images of Ni PVP8k nanocomposite prepared at 600 °C from a precursor with a 1 to 1 metal salt to polymer ratio; (d) Line scanning profile of two nickel nanoparticles labeled with two red arrows in image (c); (e-f) EDS mapping of Ni, C, O and N elements, respectively.	62
Figure 3.17. Viscosity of PVP polymer (MW. 8000g/mol) as a function of temperature. (Values of empirical constant A and B are 6.7 and 7.6 respectively in order to achieve a good fit.).....	63
Figure 3.18. Diffusion coefficient of Ni nanoclusters as a function of diameter in polymer melt at 600 °C.....	63
Figure 3.19. Variation of melting point as a function of Ni nanoparticle diameter.....	64
Figure 4.1. Gibbs free energy change as a function of particle radius.....	67
Figure 4.2. a) Nucleus critical radius as a function of metal atom saturation ratio; b) time resolved saturation ratio with different initial concentrations of metal ion loadings (10 ¹⁹ , 10 ²⁰ , and 10 ²¹ #/m ³).....	74
Figure 4.3. Synthesis of metal nanoclusters via aerosol-based thermal shock technique: a) a schematic representation of the in-situ growth of metal nanoclusters in the one-the-fly graphene aerosol nanoreactors; b) SEM image of a nickel nanoclusters incorporated graphene aerosol particle (reaction temperature: 600 °C; residence time: ~1 s); c) TEM image of Ni nanoclusters incorporated graphene aerosol particles; the structure with the red dash circle depicts one single aerosol particle.	77
Figure 4.4. Microstructure of the Ni nanoclusters graphene aerosol particles: a) TEM image of Ni nanocluster dispersed graphene aerosol, b) High-resolution TEM of one single Ni nanocluster, c) SAD pattern of the Ni nanocluster dispersed graphene particle. d-g) TEM, Scanning TEM images of one single Ni graphene particle and the corresponding EDS mappings for nickel and carbon.	79
Figure 4.5. Effect of the reaction temperature on the formation of Ni nanoclusters: a-f) TEM images of Ni graphene aerosols and g-i) histograms of the size distributions of the Ni nanoclusters synthesized at different temperatures (600, 800, 1000 °C); the red curves represent gaussian fits to the size distributions. j) effect of the reaction temperature on the average size of Ni nanoclusters: the data points labeled as “measured” are the size of Ni nanoclusters determined by statistical analysis of the TEM images; the data points labeled	

as “predicted” are the size predicted using Scherrer equation based on the XRD; k) XRD patterns for Ni-rGO nanocomposites generated at different temperatures. 80

Figure 4.6. Effect of the metal salt loading on the size of Ni nanoclusters: a-f) TEM images of Ni graphene aerosols and g-i) histograms of the size distributions of the Ni nanoclusters synthesized at different mass loadings (1.0, 2.0, 4.0); j) effect of the mass ratio between Ni salt and GO on the size of Ni nanoclusters; k) XRD patterns of Ni-rGO nanocomposites generated at different mass ratios. 81

Figure 4.7. Co and Sn nanoclusters generated with the aerosol based thermal shock technique: a) SEM, b-c) TEM, d) histogram of the size distribution of Co nanoclusters decorated in graphene particles; e) SEM, f-g) TEM, h) histogram of the size distribution of Sn nanoclusters generated in graphene particles. 83

Figure 4.8. Characteristic coagulation and coalescence times of monodispersed Ni nanoclusters at 600 °C without the presence of the graphene matrix. 87

Figure 4.9. XRD and Raman characterizations of Ni nanoclusters decorated graphene nanocomposite: XRD profiles of (a) Ni nanocluster incorporated graphene aerosol particles (4:1 mass ratio of nickel nitrate salt to GO), b) NiO incorporated graphene aerosol particles. c) Raman spectra of the Ni nanocluster incorporated graphene aerosol particles (1:1 mass ratio of nickel nitrate salt to GO), reduced graphene oxide sheets (graphene oxide sheets heated at 600 °C for 30 min in the argon gas); as-prepared graphene oxide sheets prepared using the modified Hummer’s method. (a 632 nm He-Ne laser was used for the Raman spectrum measurement) 91

Figure 4.10. a) XRD profile of Co-rGO nanocomposite generated using aerosol spray pyrolysis approach at 1000 °C; b) XRD profile of Sn powder generated using aerosol spray pyrolysis approach at 600 °C. Please note that the XRD profile of Sn powder confirms the formation of the complete reduction of tin chloride to metallic tin at a temperature of 600 °C. 92

Figure 4.11. TGA profile of Ni-rGO 1.0 nanocomposite generated at 1000 °C. (TGA was operated under air atmosphere with a heating rate of 5°C/min.) The mass ratio between nickel and rGO matrix calculated based the TGA profile is ~1.0. Note that the final product in the TGA test is nickel oxide (*Ni2O3*). 92

Figure 4.12. Catalytic properties of metal nanoclusters in graphene particles: a) Absorbance spectra of 4-nitrophenol and 4-nitrophenolate; b) time-resolved absorbance spectra of 4-nitrophenolate and c) peak absorbance verse the reaction time with Ni nanoclusters (6.7 nm, generated at 600 °C) as the catalyst; d)time-resolved absorbance spectra of 4-nitrophenolate and e) peak absorbance verse the reaction time with Co nanoclusters (10 nm, generated at 1000 °C) as the catalyst; f)the post-reaction solutions containing the catalysts with and without the presence of a magnet. 95

Figure 5.1. Schematic illustration of electrospray-assisted strategy for fabricating Sb@CSN material. 104

Figure 5.2. a) XRD pattern, b) Raman spectra, and c) TG-DSC curves for Sb@CSN material; SEM images of the d-f) as-prepared SbCl ₃ /PAN precursor and g-i) Sb@CSN composite.....	105
Figure 5.3. a) Schematic illustration of uniform Sb nanoparticles confined in a carbon sphere (Sb@CSN); b) TEM image of an individual Sb@CSN sphere and c) corresponding size distribution curve of Sb nanoparticles from image b); d) HRTEM image, e) selected-area electron diffraction pattern, and f-h) EDS images for one individual Sb@CSN sphere, g) for C and h) for Sb element.	107
Figure 5.4. a) Crystal structure of K and stage structure evolutions from Sb to K ₃ Sb during potassiation process; b) DFT calculated equilibrium voltages (vs. K/K ⁺) for the potassiation process; c) CV curves for Sb@CSN electrode at scan rate of 0.05 mV/s; d) Relative atom% of K and Sb from EDS with different discharge cut-off voltage; e) EDS element analysis for K ₃ Sb with discharge cut-off voltage of 0.01 V. (Cells from d-f are all in 4M KTFSI electrolyte)	108
Figure 5.5. Electrochemical K storage properties for Sb@CSN in the 4M KTFSI electrolyte. a) Typical 2 nd charge/discharge profile at 50 mA/g; b) quasi-equilibrium voltage profile from galvanostatic intermittent titration technique (GITT) at 100 mA/g.	111
Figure 5.6. Electrochemical performance for Sb@CSN anode: a) cycling performance at 100 mA/g in 1M KTFSI and 4M KTFSI electrolyte (Inset: Lighting electronic candle with a coin cell in 4M KTFSI electrolyte after 100 cycles); b) charge/discharge curves and c) its corresponding cycling performance at 200 mA/g in 4M KTFSI electrolyte; d) The 50 th charge/discharge curves under various current densities from 50 to 200 mA/g; e) Capacity comparison of Sb@CSN anode with previous reported anodes in PIBs, the numbers in brackets is the cycle numbers, the color code represents the cycling number range: red is < 50 cycles, olive is 50 cycles, orange is 50 to 200 cycles, magenta is > 200 cycles... ..	115
Figure 5.7. a, b) Atomic percentage concentrations of different elements with increasing etching time and c, d) corresponding high-resolution F1s XPS spectra for the Sb@CSN electrode in a, c) 1M KTFSI and b, d) 4M KTFSI electrolyte; e) Illustration of the influence of dilute and concentrated electrolytes on the formation of SEI layer.	117
Figure 5.8. a) Oxygen-antimony binary phase diagram ²⁰¹ ; b-c) TEM images of Sb nanoparticles in associated carbon sphere network.	121
Figure 5.9. a) Potassium-antimony binary phase diagram; b) SEM image and c-f) the corresponding EDS elemental mapping of Sb@CSN electrode at discharge cut-off voltage of 0.01 V in 4M KTFSI electrolyte.....	122
Figure 5.10. Charge/discharge curves for CSN material a) in 4M KTFSI electrolyte with different current densities, b) in different electrolytes.....	122
Figure 5.11. 1 st charge/discharge voltage profile for Sb@CSN electrode at 50 mA/g in 4M KTFSI electrolyte.....	123

Figure 5.12. a) four successive GITT curves after 10 activation cycles; b) the potential difference curves for the successive GITT curves in 4M KTFSI electrolyte (Potential difference= rest end potential - rest initial potential).....	123
Figure 5.13. Electrochemical performance in 1M KPF ₆ electrolyte: a) charge/discharge curves for CSN material; charge/discharge curves for Sb@CSN anode at b) 2nd and c) 50th cycling; d) its corresponding cycling performance.....	124
Figure 5.14. a, b) Crystal structures of a) Sb (space group: R3m[166]) and b) K ₃ Sb (space group: P63/mmc[194]); c, d) SEM images of c) fresh prepared Sb@CSN and d) cycled Sb@CSN; e, f) TEM images of cycled Sb@CSN.	125
Figure 5.15. EIS curves before and after 100 cycling at 100 mA/g in a) 1M KTFSI and b) 4M KTFSI electrolyte.....	125
Figure 5.16. Ignition and combustion experiments for different electrolytes used in PIBs.	128
Figure 6.1. Aerosol droplet-mediated technique for scalable synthesis of high entropy alloy nanoparticles: a) schematic of the evolution of aerosol droplets during the high temperature treatment; b) EDS mappings for a single high entropy alloy nanoparticle.....	140
Figure 6.2. Morphology and microstructure of HEA nanoparticles: a) SEM image of high entropy alloy nanoparticles; b) low-magnification HAADF-STEM image of high entropy alloy nanoparticles; c) size distribution of high entropy alloy nanoparticles measured by DMA-CPC on-line size analysis system; d-e) HAADF and annular bright field (ABF) STEM for a single high entropy alloy nanoparticle; f, h, and i) atomic STEM of the high entropy alloy nanoparticle; g) FFT analysis on high entropy alloy nanoparticle.	143
Figure 6.3. Composition analysis of HEA nanoparticles: a) HAADF EDS image of high entropy alloy nanoparticle; b) atomic percentages for five elements at different regions of the HEA nanoparticle in a; c) statistical distributions for atomic percentages of each elements for nanoparticles with different diameters.....	145
Figure 6.4. Aerosol processing: a generic approach for high entropy alloy nanoparticle synthesis. a) miscibility between binary elemental combinations with a 1:1 ratio, data obtained from ASM Alloy Phase Diagram Database (1 represents the formation of an alloy or intermetallic, 0 represents two metals are immiscible.); several types of high entropy alloy nanoparticles synthesized: b) NiCoFeCuPt, c)NiCoFePdPt, and d)NiCoCuFePd.	148
Figure 6.5. Schematic of the aerosol reactor with detailed geometry and operation parameters.....	151
Figure 6.6. a) XRD patterns of NiCoCuFePt high entropy alloy nanoparticles (data collected from the samples containing the polycarbonate membrane filter), polycarbonate membrane filter, and zero-diffraction Si plate substrate, respectively; b) zoom-in XRD pattern of NiCoCuFePt high entropy alloy nanoparticles.....	152
Figure 6.7. EDS spectrum for NiCoCuFePt high entropy alloy nanoparticle.....	152

Figure 6.8. Vapor pressures of metallic elements in solid state.....	153
Figure 6.9. Size distribution of dried aerosol particles containing metal salt mixtures measured by DMA-CPC system. (mobility size: 92.0 nm, total concentration: 2.51848e+006#/cc)	154
Figure 6.10. Temperature profiles of the gas flow in the aerosol reactor simulated with COMSOL: a) overall temperature profile of the aerosol reactor, b)temperature profile of the gas flow in the sample collector, c) temperature profile of the gas flow in the sample collector in the radial direction; d) temperature profile along the centerline of the gas flow.	155
Figure 6.11. HAADF and ABF images of NiCoFeCuPt HEA nanoparticles showing the hollow sphere shape.....	155
Figure 6.12. HAADF image and EDS maps containing multiple NiCoFeCuPt HEA nanoparticles with different sizes.....	156
Figure 7.1. Laser induced thermal shock technique for nanocluster synthesis. a-c) relationship between the critical nucleus radius and the saturation ratio of metal atoms. d) schematic of apparatus; e) effect of laser shock duration on nanocluster size and number density; f) SEM image of H ₂ PtCl ₆ coated CNF film; g-h) CNF supported Pt nanoclusters synthesized by 50 ms and 1 s laser shocks, respectively.	166
Figure 7.2. Spatiotemporal temperature mapping; a) principle of recording a color image with a Bayer filter; b-c) time-resolved color images of the sample during the laser shock process and the corresponding time-resolved temperature maps of the sample during the laser shock process; d) temperature profile of the thin film sample;	171
Figure 7.3. Microstructure analysis of CNF supported Pt nanoclusters synthesized by 50 ms laser induced thermal shock. a-c) TEM images of supported Pt nanoclusters; d) Selected-area electron diffraction pattern of Supported Pt nanoclusters; e-h) Scanning TEM of supported Pt nanoclusters and their corresponding EDS mappings.	173
Figure 7.4. Effect of the duration of laser induced thermal shock on the nanocluster size and number density supported on the carbon nanofibers. a-d) SEM images of metal nanoclusters with different laser shock pulses (50ms, 0.2s, 1s, 60s) and e-h) their corresponding histograms of size distribution; i) variations of particle diameter and number density with laser pulse; j) polarization curve of CNF supported Pt nanoclusters; k) characteristic times for coagulation, sintering, Ostwald Ripening of monodispersed Pt nanoclusters on the carbon nanofiber surface at 1550 K.	175
Figure 7.5. Temperature Jump/Time of Flight Mass Spectrometry (T-Jump/TOFMS) Apparatus Schematic ⁵⁴	183
Figure 7.6. Mass spectrum results for metal salt during ultrafast heating detected by time of flight mass spectrometry.....	184
Figure 7.7. EDS spectra of CNF supported Pt nanoclusters before (a) and after (b) 50ms laser shock treatment.....	185

Figure 7.8. SEM image of a single particle generated with a 60 s laser pulse..... 185
Figure 7.9. Metal point of Pt nanoparticle versus particle diameter. 186

List of Abbreviations

TEM	Transmission Electron Microscopy
SEM	Scanning Electron Microscopy
STEM	Scanning Transmission Electron Microscopy
EDS	Energy Dispersive X-Ray Spectroscopy
FTIR	Fourier Transmission Infrared Spectroscopy
UV vis	Ultraviolet-visible Spectroscopy
XRD	X-Ray Powder Diffraction
XPS	X-Ray Photoelectron Spectroscopy
TGA	Thermogravimetric Analysis
DSC	Differential Scanning Calorimetry
TOFMS	Time of flight Mass Spectroscopy
DMA	Dynamic Mobility Analyzer
CPC	Condensation Particle Concentration Analyzer
PVP	Polyvinylpyrrolidone
NP	Nanoparticle
ASP	Aerosol spray pyrolysis
CNF	Carbon nanofiber
rGO	Reduced graphene oxide
PIBs	Potassium ion batteries

Chapter 1: Introduction

1.1. Metal Nanoparticles

Metal nanoparticles have been of great interest due to their unique size- and shape-dependent properties, enabling potential applications in the fields of plasmonics, electronics, catalysis, nanomedicine, magnetic storage, energy and fuels, among others.¹⁻⁶ For instance, cobalt nanoparticles have been applied to construct two dimensional ferromagnetic thin films as high-density magnetic storage devices.⁷ Due to their biocompatibility and stability, Au nanoparticles can be used as potential nanocarriers for drug delivery and gene therapy.⁸⁻⁹ Silver nanoparticles have been demonstrated as promising coating materials of solar cells to enhance solar harvesting because of their localized surface plasma resonance property under light exposure.¹⁰ The extremely high surface aspect ratio of small platinum nanoparticles enhances their performance as electrocatalysts used in fuel cells.¹¹

Although important progresses and critical breakthroughs in the field of nanoscience and nanotechnology have been made in the last several decades¹², the transfer from fundamental research to practically industrial applications is greatly hindered because synthesizing these extremely small NPs, at least in sufficient quantities to enable its utility, is still challenging due to their high mobility and meta-stable nature either resulting in aggregates or particle growth.

1.2. Synthesis techniques

Various kinds of methods have been developed to synthesize metal nanoparticles. In general, these methods can be divided into two categories: top-down approach and

bottom-up approach. The top-down approach starts with bulk metals, and breaks them into nanosized particles with physical techniques such as ball milling, laser ablation, magnetron sputtering.¹³ The bottom-up approach however starts with atomic or molecular species, and uses these species as building blocks to build up metal nanoparticles through nucleation and growth via either chemical or physical process conducted in either liquid or gas phase.¹⁴

1.2.1. Top-down approach

Ball milling. Ball milling method has been developed and adopted as an industrial process for particle processing since 1970.¹⁵ One advantage of this method is that it has the ability to overcome the quantity limitations and produce nanosized powders with multiple components, phases and nanostructures in large quantity. In a typical process, the micro-sized powders or flakes are placed in a sealed container with spherical beads like ZrO₂. By shaking or violent agitation of the container, the beads collide with each other so that the micro-size powders are milled and mechanically break into nanosized powders during this process.¹⁶ However, the disadvantage of the method is that this method might not be suitable to generate nanoparticles with an extreme small size because nanoparticles with such a small size might go through cold welding and sintering even through the surrounding temperature is relatively low.¹⁵

Laser ablation. Another top-down approach which is commonly used for nanoparticle synthesis is laser ablation.¹⁷ For a typical laser ablation process, a focused laser beam locally heats up and vaporize the surface of a metal target to create a plume, which expands into the space above the target to condense and form metal nanoparticles.

Depending on the component of the target material, the phase of the surrounding medium, and the operation parameters of the laser, nanoparticles with different size and concentration are generated.¹⁸ Generally speaking, particles generated in gas phase often have a wide size distribution with relatively large size, and these particles are often in agglomerated form compared to particles generated in a liquid medium. In order to prevent these nanoparticles from agglomeration, surfactants or ligands might be introduced during the laser ablation process. One advantage of the laser ablation method is that a variety of metal nanoparticles can be produced since this approach is a simple physical process and there is no complex chemistry involved. This technique is practically useful for production of very active metal nanoparticles like aluminum (Al), titanium (Ti), and zirconium (Zr). For instance, Zong et al. adopted a Nd:YAG laser to generate titanium and zirconium nanoparticles with an average diameter of 20 nm under Ar gas and explored the burning behavior of these metal nanoparticles.¹⁹ However, the high cost and low yield of the materials prevents this method from industrial utility.¹⁵

Magnetron sputtering condensation. Magnetron sputtering condensation has been reported to fabricate small metal nanoparticles in gas phase.²⁰ The principle of magnetron sputtering condensation is following: a metal target is sputtered under a pressure of several torrs via magnetron sputtering to produce a dense metal vapor; the dense metal vapor carried by a carrier gas such as argon moves into the low temperature aggregation zone to nucleate and grow to form nanoparticles. The growth of the particles is quenched once they move into a low-pressure deposition chamber attached to the aggregation zone through a critical orifice. Similar to the laser ablation technique, particle size and morphology generated with the magnetron sputtering condensation are controlled by the

power density applied, type of the target material, carrier gas property and its flow rate, and length of the aggregation zone. Metal nanoparticles generated with this technique often have a broad particle size distribution and agglomeration due to their fast diffusion nature in the gas phase. Besides, the low yield of the technique is not suitable for industrial utility.

1.2.2. Bottom-up approach

Wet chemistry: Wet chemistry, also called colloidal chemistry, is arguably the most popular bottom-up technique to produce metal nanoparticles with excellent control of their structural, physical and chemical properties. Several wet chemistry synthesis methods are mentioned here, including citrate reduction method,²¹ Brust method²², and polyol reduction method²³. For a typical citrate reduction method, take synthesis of gold (Au) nanoparticles for instance. Metal precursor, HAuCl_4 is reduced by a reducing agent, sodium citrate, at elevated temperatures to form monodispersed Au nanoparticle colloid.²¹ The size of Au nanoparticles can be tuned by adjusting the concentrations of the metal precursor and the reducing agent, and the reaction temperature applied. Another wet chemistry method which has been extensively studied is Brust method. In this method, a metal salt precursor HAuCl_4 initially dissolved in an aqueous solution is extracted into a non-water-soluble solvent such as toluene by a phase transfer reagent, tetraoctyl ammonium bromide (TOAB). In the presence of a surfactant such as thioalkanes or aminoalkanes, the metal precursor in toluene is mixed and stirred with an aqueous reducing agent, sodium borohydride to produce Au nanoparticle coated with the surfactant. The size of Au nanoparticles is controlled by the concentration ratio between Au salt and surfactant. For the polyol reduction method, ethylene glycol or higher diols can be applied

as both solvent and reducing agent to fabricate noble metal nanoparticles in the presence of poly (vinyl pyrrolidone) (PVP) as a protecting polymer. Although precise control over particle size, component, and morphology can be achieved, there are several disadvantages which are often inherent in the wet chemistry approach for metal nanoparticle synthesis. First, metal nanoparticles synthesized by the chemical process are commonly covered by a protective layer such as surfactants, ligands, capping agents. The existing protective layer could prevent researchers from fully exploring surface properties of these nanoparticles and requires them to do complex surface modification for further applications of the nanoparticles. Besides, wet chemistry synthesis techniques reported typically generate metal nanoparticles in small batch reactors. Increasing the production rate which for a bulk system often involves inhomogeneous and slow heating and cooling rates. This often leads to a wide size distribution, inhomogeneous dispersion and aggregation, which prevents these nanoparticles from practical usage.²⁴⁻²⁵

Aerosol spray pyrolysis: Aerosol spray pyrolysis (ASP) has been used to generate NPs and nanocomposites. In a typical ASP process, the precursor solution is continuously nebulized to produce aerosol droplets from hundred nanometers several micrometers in diameter and these aerosol droplets, acting like small isolated reactors, pass through a heating element (high temperature flame or heating furnace) where the reaction in each aerosol reactor is triggered by a short thermal pulse to generate nanostructured materials upon solvent evaporation. Although the ASP technique has been used to produce and assemble a large range of materials (metals²⁶, alloys²⁷, metal oxide²⁸⁻³⁰, composites³¹⁻³³) with controllable size and morphologies, fabrication of NPs with a diameter of sub- 50 nm, which is much smaller than that of the nebulized aerosol droplets, using this technique

remains challenging. Recently, efforts have been made to produce small and monodisperse NPs by introducing an inert solute into the aerosol droplets to guide the nucleation and growth of NPs.³⁴⁻³⁵ For example, Xia et al. have introduced sodium chloride into the precursor solution to guide formation of sub- 10 nm NiO and ZnS NPs.³⁴ However, generating ultrasmall metal nanoparticles with this approach has never been reported.

Joule heating: Recently, people have used Joule heating induced thermal shock to synthesize well-dispersed nanoparticles decorated on carbon nanofibers.³⁶⁻³⁸ The metal salt is first incorporated into the carbon nanofiber thin film sample, and then an electric current is applied onto the conductive thin film to rapidly heat the thin film sample via Joule heating. Joule heating induced thermal shock triggers the thermal decomposition of the metal salt and formation of nanoparticles, and the subsequent cooling freezes the nanoparticles in the carbon nanofiber matrix. Although ultrasmall metal nanocluster can be generated in a very short time, it is very difficult to convert Joule heating induced thermal shock to an industrially scalable process.

1.3. Nanoparticle growth mechanism

The growth mechanism of nanoparticles in both gas and liquid phases have been extensively studied for the last two decades.³⁹ Since the governing principles of nanoparticle growth should be similar in gas and liquid phases, I choose to discuss possible mechanisms governing nanoparticle formation in the gas phase in this section. The possible mechanisms include nucleation, surface growth, coagulation, sintering, and Ostwald ripening.

Nucleation. The process of homogenous nucleation is interpreted thermodynamically by looking at the total Gibbs free energy change (**Figure 1.1**) of forming a spherical metal NP, which is given in eqn. 1.1¹⁴

$$\Delta G = 4\pi r^2\gamma + \frac{4}{3}\pi r^3\Delta G_v \quad (1.1)$$

Where γ is surface tension, r is the radius of the NP, ΔG_v is the free energy of the crystal in bulk phase. ΔG_v is defined in eqn. 1.2 where V_m is the molar volume of the crystal, S is the supersaturation of the solution

$$\Delta G_v = (-RT\ln S)/V_m \quad (1.2)$$

Since surface tension term is always positive and ΔG_v term is negative as long as the solution is supersaturated, it is possible to find a maximum value on the ΔG curve with respect to r . By setting $\frac{d\Delta G}{dr} = 0$, a critical radius r_c is obtained above which the nucleus can grow spontaneously without being redissolved. The critical radius is defined in Eqn. 1.3

$$r_c = 2\gamma V_m / (RT\ln S) \quad (1.3)$$

The equation indicates that increasing either the temperature of the tube furnace or mass loading of metal salt precursors can reduce the critical radius of the nuclei.

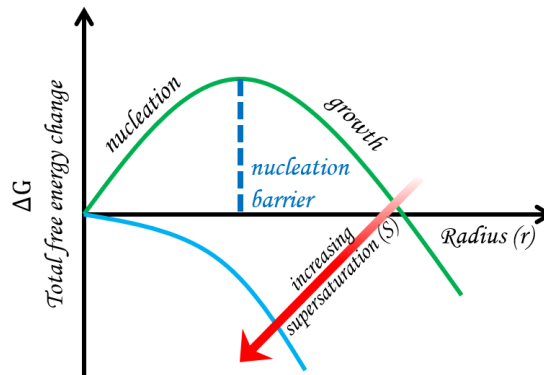


Figure 1.1. Gibbs free energy change as a function of particle radius

Substituting Eqn.1.3 and Eqn. 1.2 into Eqn. 1.1, a critical free energy ΔG_c is obtained. ΔG_c is the minimum free energy required to form a stable nucleus.

The rate of nucleation of N nanoparticles during time t can be written in term of ΔG_c , which has Arrhenius type given in Eqn. 1.4 ³⁹

$$\frac{dN}{dt} = A \exp \left[-\frac{\Delta G_c}{kT} \right] = A \exp \left[-\frac{16\pi\gamma^3 V_m^2}{3k^3 T^3 N_A^2 (\ln S)^2} \right] \quad (1.4)$$

One can conclude that increasing the supersaturation ratio S will not only decrease the critical radius of the nuclei but also greatly enhance the rate of nucleation.

Surface growth. One mechanism that governs particle growth is surface growth where metal vapors diffuse around and attach to the surface of the existing nuclei by vapor condensation and/or surface reactions. Depending on the ratio of the mean free path of the metal vapors (λ) and the size of the particles (Knudsen number, Kn), there are three possible scenarios concerning the surface growth of the particles: free molecular flow regime ($Kn \gg 1$), transition flow regime ($Kn = 0.4$ to 20), and continuum gas flow regimes ($Kn \ll 1$).⁴⁰ For the continuum regime, the vapor near particles is a fluid continuum with a concentration boundary around particle. The net flux of metal vapor to the surface of the particle with a certain size can be evaluated using Fick's first law:

$$J_{surface} = D \left. \frac{\partial n}{\partial r} \right|_{r=r_p} = D \frac{n_1 - n_{eq}}{r_p} \quad (1.5)$$

Where, D is the diffusion coefficient, n_{eq} is the equilibrium vapor concentration or in other words, the vapor concentration at the surface of the particle ($r = r_p$), n_1 is metal vapor concentration when r goes to infinity. For the free molecular flow regime, the net monomers flux can be evaluated as:

$$J_{surface} = \frac{p - p_{eq}}{\sqrt{2\pi m k T}} \quad (1.6)$$

Where p is vapor pressure of the metal over the surface of the nuclei, and p_{eq} is vapor pressure of the metal at the equilibrium condition; m is the mass of the metal monomer; k is Boltzmann constant; T is the reaction temperature.

Coagulation. Coagulation or aggregation of nanoparticles is a process of particle growth, where nanoparticles moving relative to each other collide and stick together. Coagulation is often caused by the relative motion of particles due to the Brownian coagulation. The process of coagulation will lead to decrease of particle number concentration and increase of particle size. The net rate of particle of size k can be described using Smoluchowski population balance equation:⁴⁰

$$\left[\frac{\partial n_k}{\partial t} \right]_{coagulation} = \frac{1}{2} \sum_{j=1}^{k-1} \beta_{k-j,j} n_{k-j}(t) n_j(t) - n_k \sum_{j=1}^{\infty} \beta_{j,k} n_j \quad (1.7)$$

Where β_{ij} is the collision frequency function between particles with a size i and j . In the continuum regime, the collision frequency function is expressed as follows:

$$\beta(d_i, d_j) = \frac{2kT}{3\mu} \left(\frac{1}{d_i} + \frac{1}{d_j} \right) (d_i + d_j) \quad (1.8)$$

Where d_i and d_j represent particle diameters; μ is the viscosity of the medium.

Sintering. Sintering describes the particle growth process where two attached particles merge into one single particles. The coalescence of metal nanoparticles is sensitive to the phase (molten or solid) of the nanoparticles. Research has shown that the melting point of a nanoparticle changes with the particle size. For the nanoparticles in liquid phase, a viscous flow mechanism as shown in Eqn. 1.9 is used to calculate the coalescence time:⁴¹

$$\tau_l = \frac{\mu d_{eff}}{2\sigma_l} \quad (1.9)$$

Where μ is the viscosity of metal nanoparticle, σ_l is the surface tension of metal nanoparticle in liquid state; d_{eff} is the effective diameter of the coalescing particle pair, which is $6V_p/a_p$, V_p and a_p are volume and surface area of the coalescing particle pair, respectively.

For metal nanoparticles in the solid phase, the coalescence time can be described with the following equation:⁴²

$$\tau_s = \frac{3k_B T_p N}{64\pi\sigma_s D_{eff}} \quad (1.10)$$

Where T_p is the temperature of a particle pair undergoing coalescence, N is the number of atoms in the particle pair, σ_s is the surface tension of solid Ni nanoparticle, D_{eff} is the effective atomic diffusion coefficient in the particle pair.

Ostwald ripening. Ostwald ripening involves the dissolution of smaller particles and the redeposition of the dissolved species on the surfaces of the larger particles that are far more thermodynamically favorable. At elevated temperatures, the metal atoms release from small particles and migrate onto large particles in the gas phase due to a vapor pressure difference between two particles with different sizes caused by Kelvin effect, which is described below:⁴³

$$\ln \frac{P_{d_p}}{P_\infty} = \left(\frac{M_{d_p}}{TR\rho} \right) \left(\frac{2\sigma_s}{d_p} \right) \quad (1.11)$$

Where M_{d_p} is the molecular weight, R is the gas constant, ρ is the density of the solid, T is the temperature, P_{d_p} is the vapor pressure above a particle of diameter d_p , P_∞ is the equilibrium vapor pressure of the sublimating species over a flat surface, σ_s is the surface tension of the solid.

1.4. Potential Applications

Energy storage materials. Although lithium-ion batteries (LIB) as an efficient electrical energy storage technology have been widely used ranging from the portable electronics to electric vehicles, the fast expansion of their commercial applications requires further investigation of the electrode materials both anodes and cathode so as to achieve high energy storage density, high power density, and long cycling stability of LIBs.⁴⁴⁻⁴⁶ In particular, one typical anode material used in the current LIBs is graphite. However, graphite anodes can only deliver a maximum theoretical capacity of 372 mAh/g.⁴⁷ Compared to carbonaceous materials like graphite, metal-based electrode materials usually provide much higher gravimetric and volumetric specific capacities. For instance, tin (Sn) anode materials can deliver a theoretical capacity of 993 mAh/g, which is two time higher than that of graphite.⁴⁸ However, lithium insertion/desertion into/from Sn anode causes a large volume change (~300%), leading to pulverization of the Sn anode, fast deterioration of the capacity, and poor cycling performance. In order to solve this problem, researchers have designed an anode material made of ultras-small Sn nanoparticles (10 nm) dispersed in carbon matrix, which greatly improved the electrochemical performance of the Sn anode.⁴⁵ By using nanosized Sn, the absolute strain induced by the large volume change during lithiation/delithiation can be greatly mitigated. Moreover, dispersing Sn nanoparticles into carbon matrix can also accommodate the volume change and keep the composite anode intact mechanically.

Electrocatalysts. Electricity generated from renewable energy such as solar and wind must be stored durably for off-grid applications. Electrochemical water splitting to produce hydrogen and oxygen provides a promising solution to convert the electrical

energy to chemical energy in the form of chemical bonds.⁴⁹ Among various types of catalysts reported, metal nanoparticles have been considered as promising materials for electrochemical water splitting. Because only metal atoms on the surface of the metal nanoparticles can act as active sites for the catalytic process, the catalytic performance of these nanoparticles can be tuned by adjusting the particle size, component, and microstructure.

Nanoenergetic materials. Energetic materials, also referred to explosives, propellants, and pyrotechnics, represent a broad range of systems which process a huge amount of chemical energy that can be released in an extremely short time upon the initiation of the reaction.⁵⁰⁻⁵³ The common type of energetic materials is monomolecular such as trinitrotoluene (TNT) and cyclotrimethylenetrinitramine (RDX) in which both fuel and oxidizer are held within a single molecule. The other type of energetic materials are composites, where the fuel and oxidizers are different materials and are physically mixed together. For such energetic materials, metals can be used as the fuel because they are often stable and store a large amount of chemical energy compared to the traditional monomolecular explosives.⁵⁰ The composite energetic containing a metal fuel and a metal oxide oxidizer is referred to as thermite. The thermite reaction is exothermic reaction and can release a lot of energy. Although the energy density of the thermite materials is high, their application is greatly hindered by slow reaction kinetics and high ignition thresholds. But the development of nanoscience and nanotechnology has made it possible to overcome these limitations. Using nanoscale materials with high specific surface area can decrease the diffusion length between metal fuels and oxidizers, leading to the enhancement of the reaction, rapid energy release rate, and low ignition threshold.⁵³⁻⁵⁴ These highly reactive

nanocomposites have been referred as nanothermites. The unique properties of the nanothermites such as high reaction rate, high energy density have drawn great attention from the energetic community. In addition, the reactivity of the nanothermites can be precisely tuned by varying particle size, oxidizer choice, stoichiometry, microstructure, and morphology, which make them attractive for a wide range of applications including explosive additives, propellant rate modifiers, and microelectromechanical systems.^{52, 55-56}

1.5. Current Challenges

1.5.1. Scalable manufacturing of ultra-small metal nanoparticles

To bridge the gap between scientifically interesting properties and practical technological impact of metal nanoparticles, researchers have explored encapsulating NPs into various matrices such as polymeric or carbon-based materials. There are numerous advantages of encapsulating nanoparticles into proper matrices including: a) these NPs are chemically stabilized via forming covalent bonds with polymer molecules or physically frozen in the matrix (ultimately prevents NP agglomeration and oxidation) and b) embedding metal nanoparticles into a proper matrix enhance their physical and chemical properties for potential applications. Numerous approaches have been successfully developed to incorporate nanoparticles within polymeric and carbon-based materials. These approaches can be classified primarily into two categories: *ex situ* and *in situ* techniques. In *ex situ* methods, the metal nanoparticles are first synthesized by various processes, and subsequently introduced into a support matrix via physical mixing.⁵⁷⁻⁶⁰ This approach affords a precise control of the size and morphology of the nanoparticles. A significant challenge in these techniques, however, is that the high reactivity and

metastable nature of the metal particles often leads to non-uniform dispersion of nanoparticles in the supporting matrix. This inhomogeneity unavoidably causes a gradual deterioration in the performance of the resulting nanohybrid materials.

On the other hand, *in situ* techniques allow direct growth of metal nanoparticles in the host materials.^{36, 61-64} Metal-ion precursors are first incorporated into the host matrix and then metal nanoparticles are generated within the matrix via chemical reduction or thermal decomposition. This approach, thus, eliminates the need for surfactants and capping agents and yields a higher nanoparticle number density with a more uniform nanoparticle distribution throughout the host matrix. However, most *in situ* and *ex situ* techniques reported in the literature typically generate metal polymer nanocomposites in small quantities. The difficulty lies in increasing the production rate which, for a bulk system, typically involves inhomogeneous and slow heating and cooling rates and typically leads to a wide size distribution, inhomogeneous dispersion and aggregation.⁶⁵ Thus, there is a pressing need for developing new strategies for scalable manufacturing of high-quality ultrasmall metal nanoparticles to enable their industrial applications.

1.5.2. Scalable manufacturing of multi-component metal nanoparticles

Combining multiple metals into one single parultraultraticle at nanoscale enables the formation of multicomponent metal nanoparticles with unique physical and chemical properties.⁶⁶ The electronic interactions between different metal components, make them potentially promising materials for a broad range of applications in the fields of catalysis, plasmonics, nanomedicine, and electronics.⁶⁷ Among all the multicomponent metallic nanostructures investigated, the attention on high entropy alloy nanoparticles have been

growing dramatically. High entropy alloys represent such nanostructures, defined as five or more well-mixed metal elements in near equimolar ratios.⁶⁸ The maximized interactions between different metal atoms leads to the formation of the unique architectures with a high configurational entropy of mixing, resulting in advanced properties, including high mechanical strengths at high temperature, high corrosion resistance, and high oxidation resistance, among others.⁶⁹

To date, the primary techniques used to produce multicomponent metal nanoparticles, either in an alloyed or phase-separated state, are wet-chemistry based approaches, including bulk solution synthesis⁷⁰, microfluidic method⁷¹, and microemulsion⁷². However, forming metallic nanostructures containing more than three metal elements using traditional wet-chemistry approaches becomes challenging due to the increasing difficulty arising from balancing diverse reduction kinetics of different metal precursors. This often results in site-selective nucleation of each metal and the formation of nanoparticles with components and structures varying from particle to particle. In order to address this issue, a site-specific lithography-based synthesis technique has been recently reported to fabricate multicomponent metal nanoparticles containing five metal elements by confining the corresponding metal precursors in a small reaction volume on a desired site followed by hydrogen reduction procedures at elevated temperatures.⁷³ Although this technique has greatly expanded the composition and structure diversities of multicomponent metal nanoparticles, phase-separated nanostructures were always generated when incompatible metal elements (like Cu and Co) were used. The reason is that the slow heating and slow quenching applied in the hydrogen reduction procedures in this technique caused multi-component nanoparticles to reach their thermodynamically

favorable phase-separation state. Alternatively, melting processing has been developed to create bulk-size multicomponent alloys with uniformly mixed metal atoms - high entropy alloy, via melting and quenching physically mixed multiple metals.⁷⁴ However, a recent study on atomic distributions of Al_{1.3}CoCrCuFeNi alloy generated via the melting technique reveals that Cu rich precipitates were formed in the final product.⁷⁵ Furthermore, although melt processing has been successful in the synthesis of bulk high entropy alloys as structural materials, generating high entropy alloys at the nanoscale is extremely difficult with this technique.

1.6. Research Plan

One of the most important operation parameters for nanoparticle synthesis is reaction temperature since it has a profound effect on nanoparticle formation pathways. For instance, increasing reaction temperature can accelerate the rates of the precursor reduction, monomer diffusion, and nucleation, coagulation and sintering of nanoparticles. In principle, one can control the rate of the nucleation and growth through precisely controlling the temperature of the reaction. Particularly, in order to synthesize smaller nanoclusters with a higher number concentration, one needs to promote the nucleation rate of nanoclusters and inhibit their subsequent growth. From a thermodynamic standpoint, the nucleation rate can be greatly enhanced by decreasing the nucleation energy barrier arising from the formation of the interface between the nuclei and the reaction solution.^{14, 39, 76} One way to minimize the nucleation barrier of forming a stable nucleus is to build a high supersaturation ratio (S) of metal atoms in the reaction volume. This can be achieved by applying a fast heat pulse to decompose the metal precursor rapidly to create a highly

supersaturated state leading to a very fast nucleation burst. Once small nuclei form, a fast cooling can be applied to quench these small nuclei from further growth. Although high temperature can hasten kinetics, it also speeds up transport, leading to the coagulation and sintering. In order to prevent nanoclusters from coagulation and sintering, a matrix should be used to anchor and stabilize these small nanoclusters. To this end, I develop an aerosol droplet mediated approach to in-situ generating sub- 5 nm Ni, Co and Cu nanoparticles with the presence of polymer or graphene matrix. The rapid thermal pulse given to the aerosol particles enables the formation of nuclei and growth, with subsequent rapid quenching to freeze in the structure.

Further, I use the aerosol droplet mediated approach towards scalable synthesis of high entropy alloy nanoparticles with atomic-level mixing of immiscible metal elements. Rather than pre-depositing metal salt mixture precursors onto a carbon support, I nebulize the precursors into aerosol droplets with a diameter less than 1 μm , and employ a fast heating and fast quenching treatment. As such each droplet contains precursors and operates as a nanoreactor, with very low thermal mass to enable rapid heating/cooling and small length scales to ensure no thermal and mass transfer gradients within the particle enabling one to produce a single high entropy alloy nanoparticle. The advantages of using aerosol droplets mediated technique are: 1) all metal salts are pre-confined into small droplets enabling incorporating different metals in same particles upon the heating and quenching process; 2) the small mass and volume nature of the aerosol droplets enables fast heating and fast cooling, which is crucially important to achieve kinetic control over the thermodynamic mixing regimes and creation of high entropy alloy nanoparticles; 3) metal salt ratios in the aerosol droplets reflect metal ratios in the precursor solution so that

component and composition of final products can be tuned by simply adjusting the type and ratio of metal salts in the precursor solution; 4) since this technique is a continuous process, scaling-up will be greatly simplified.

Besides, lasers present a flexible and powerful nanomanufacturing approach to provide both temporally and spatially resolved energy to generate nanoclusters.⁷⁷⁻⁷⁸ Laser-based manufacturing approaches shift the control and modulation of properties from the material to a programmable source, making them readily adaptable to industrial protocols.⁷⁹⁻⁸¹ Laser approaches to nanomaterial fabrication become especially consequential as one adapts to emerging manufacturing approaches like 3-D printing and writing.⁸²⁻⁸³ In this dissertation, I demonstrate a fast, thermal shock technique using a commercial CO₂ laser as the heating source to introduce an extremely short laser shock to trigger the formation of ultra-small, densely, and uniformly dispersed metal nanoclusters on carbon nanofiber matrices.

1.7. Scope of the Dissertation

This dissertation describes two techniques: aerosol processing and laser shock manufacturing, for scalable manufacturing of ultrasmall metal nanoparticles uniformly dispersed small nanoparticles in polymer and carbon-based matrices.

In Chapter 2, I discuss design and operation principles of the experimental setups for aerosol and laser shock technique to produce ultrasmall metal nanoparticles,

In Chapter 3, I demonstrate the formation of sub- 5 nm particles of Ni, Co and Cu nanoparticles in polymer matrix using an aerosol single-drop reactor approach. The rapid thermal pulse given to the aerosol particles enables the formation of nuclei and growth,

with subsequent rapid quenching to freeze in the structure. The role of temperature as well as precursor concentration of the resulting size and morphology are discussed. A characteristic time analysis and an analysis of the particle size distributions lead to the conclusion that growth is governed by nucleation and surface growth with little coagulation or Ostwald ripening. Finally, I note that this aerosol route is amenable to scale-up for large scale production of nanoclusters that can either be used as is within the polymer or released by solvent extraction, depending on application.

In Chapter 4, I report an aerosol-based thermal shock technique for in situ synthesis of well-dispersed metal nanoclusters in on-the-fly graphene aerosols. A rapid thermal shock to the graphene aerosol has been used to nucleate and grow the metal nanoclusters with subsequent quenching to freeze the newly formed nanoclusters in the graphene aerosol matrix. A characteristic time analysis comparison with experiment shows that the nanocluster formation is governed by nucleation and subsequent surface growth, and that the graphene retards coagulation, enabling unaggregated metal nanoclusters. The method is generic and I show the formation of sub-10 nm Ni, Co and Sn nanoclusters. This continuous aerosol-based thermal shock technique offers considerable potential for the scalable synthesis of well-dispersed and uniform metal nanoclusters stabilized within a host matrix. As an example of potential application I demonstrate very favorable catalytic properties.

In Chapter 5, I develop an electrospray-assisted printing technique coupled with post heating processing to fabricate high-capacity antimony nanoparticle embedded carbon sphere network (Sb@CSN) composite anode materials with Sb nanoparticles uniformly encapsulated by carbon sphere network for potassium ion batteries (PIBs). First-principles

computations and electrochemical characterizations confirm a reversible sequential phase transformation of KSb_2 , KSb , K_5Sb_4 , and K_3Sb during potassiation/depotassiation process. In a concentrated 4M potassium trifluoromethanesulfonimide (KTFSI)/Ethylene Carbonate (EC)/Diethyl Carbonate (DEC) (KTFSI/EC+DEC) electrolyte, the Sb@CSN anode delivers a high reversible capacity of 551 mAh/g at 100 mA/g for 100 cycles with an extremely slow capacity decay of only 0.06% per cycle from the 10th to 100th cycling; when up to a high current density of 200 mA/g, Sb@CSN anode still maintains a capacity of 504 mAh/g for 220 cycles. The Sb@CSN anodes demonstrate one of the best electrochemical performances for all K-ion batteries anodes reported to date. The exceptional performances of Sb@CSN should be attributed to the efficient capsulation of small Sb nanoparticles into conductive carbon network as well as the formation of a robust KF-rich solid electrolyte interface (SEI) layer on Sb@CSN anode in the concentrated 4M KTFSI/EC+DEC electrolyte.

In Chapter 6, I report an aerosol droplet-mediated technique toward scalable synthesis of high entropy alloy nanoparticles with atomic-level mixing of immiscible metal elements. An aqueous solution of metal salts is nebulized to generate $\sim 1 \mu\text{m}$ aerosol droplets, which when subjected to fast heating/quenching, result in decomposition of the precursors and freezing-in of the zero-valent metal atoms. Atomic-level resolution scanning transmission electron microscopy (STEM) coupled with energy dispersive X-ray spectroscopy (EDS) analysis reveals that all metal elements in the nanoparticles are homogeneously mixed at the atomic level. I believe this approach offers a facile and flexible aerosol droplet-mediated synthesis technique that will ultimately enable bulk processing starting from a particulate HEA.

In Chapter 7, Here I demonstrate an ultrafast laser shock technique to *in-situ* fabricate ultra-small metal nanoclusters supported on a carbon nanofiber (CNF) matrix with kinetically controllable size and surface density. An ultrafast laser shock heating on the metal precursor incorporated CNF matrix triggers the fast nucleation and growth of metal nanoclusters and a subsequent ultra-fast quenching freezes them onto the CNF structure. I find that a shorter laser shock enables the formation of metal nanoclusters with higher number densities and smaller sizes while longer laser shock leads to the further growth of metal nanoclusters and the achievement of their equilibrium shape. A characteristic time analysis suggests that the growth of metal nanoclusters is dominated by surface diffusion and sintering, and Ostwald ripening is mainly involved at the early stage of nanocluster formation. I also demonstrated that the catalytic performance of CNF matrix supported metal nanoclusters towards electrocatalytic hydrogen evolution is enhanced for metal nanoclusters with a smaller size and higher number density. This work provides a promising approach for rapid and scalable fabrication of ultra-small, high-density metal nanoclusters and nanocluster-based devices.

In Chapter 8, I summarize the important conclusions of my research and provide perspectives to guide future researches and potential applications.

Chapter 2: Experimental Design and Characterizations.

2.1. Aerosol assisted nanomanufacturing

Synthesis of metal nanoclusters in polymer matrix: In this dissertation, I develop an aerosol droplet mediated technique for continuous and scalable synthesis of ultrasmall metal nanoclusters decorated in the polymer matrix and graphene matrix. Below is a description of synthesis of metal nanoclusters embedded in the polymer matrix using this technique. Aerosol droplets containing metal salt and polymer molecules with desired mass ratio were created from a pneumatic Collision nebulizer with 5% hydrogen and 95% nitrogen mixture as the carrier gas. The precursor solutions were prepared by dissolving 425 mg of PVP polymer and a certain amount of metal salt in 25 ml deionized water. The metal salts used to obtain Ni, Co and Cu nanoparticles were $Ni(NO_3)_2 \cdot 6H_2O$, $Co(NO_3)_2 \cdot 6H_2O$, $Cu(NO_3)_2 \cdot 3H_2O$, respectively. The mass of the metal salt used was varied between 42.5 mg to 425 mg to prepare precursor solutions with different metal salt precursor to polymer mass ratios (0.1, 0.3, 0.5, 1.0). **Figure 2.1** shows schematically the basic concept behind the synthesis scheme. Most of the water solvent is removed from the droplets as they pass through a silica gel diffusion dryer, where they are carried to a tubular furnace (28 cm in length, 2 cm in diameter) for a residence time of ~ 1 s. The set temperature of the tube furnace varied from 400 °C to 800 °C. Within the heated flow, the dried polymer particles are molten, and the metal salt decomposed and reduced in H_2 to form metal nanoparticles in the polymer melt. Rapid quenching on a 0.4 μm pore Millipore HTPP membrane filter results in arresting of the nanoparticle growth.

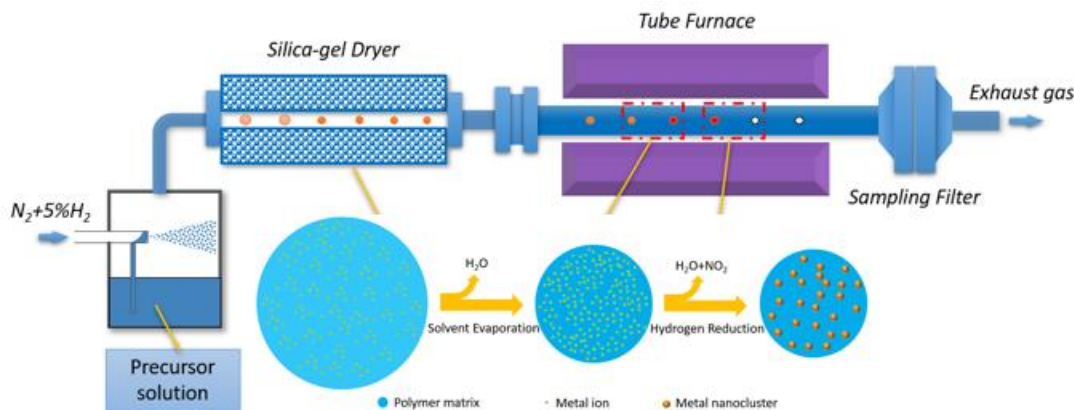


Figure 2.1. Schematic of aerosol assisted scalable manufacturing of ultrasmall metal nanoparticles.

Synthesis of metal nanoclusters in graphene oxide matrix: I further investigate this technique to produce ultrasmall metal nanoparticles decorated in the graphene matrix. The precursor solutions were prepared by adding 20 mL of the GO solution (6.5 mg/mL) and the required amount of metal salt into 84 mL of deionized water. The metal salts used to obtain Ni, Co, and Sn nanoclusters were $Ni(NO_3)_2 \cdot 6H_2O$, $Co(NO_3)_2 \cdot 6H_2O$, and $SnCl_2$. For the $SnCl_2$ GO precursor solution, dimethylformamide (DMF) was used as a solvent to dissolve $SnCl_2$. The mass of the metal salt used was varied between 130 to 520 mg to prepare solutions with different metal salt to graphene oxide mass ratios (1.0, 2.0, and 4.0). In a typical experiment, the precursor solution containing metal salt and graphene oxide is continuously nebulized into small aerosol droplets by the atomizer. The mixture gas of hydrogen and nitrogen then carries these droplets to pass through the diffusion dryer and the heating element. The solvent evaporates from the droplets as they pass through the diffusion dryer, producing a dry aerosol. The dry aerosol passes to a heating furnace with a nominal residence time in the high temperature region of ~ 300 ms where the thermal shock ($\sim 10^3$ K/s) induced decomposition and reduction in hydrogen leads to the nucleation

and growth of zero valent metal nanoclusters within a graphene matrix. Particles are captured on a filter resulting in a quenching rate of approximately 10^5 K/s.

GO was prepared using a modified version of the Hummer's method.⁸⁴ The detailed procedure is as follows: First, 1.5 g of graphite was placed in a 1000 mL Erlenmeyer Flask, to which 180 mL sulfuric acid and 20 mL phosphoric acid were added. The resulting suspension was placed in the water bath at 50°C, and 9 g potassium permanganate was gradually added into the suspension. After continuously stirring for 12 hours, the mixture was poured into 300 mL cold distilled water and 3 mL hydrogen peroxide (30%) was slowly added into the mixture while stirring, which made the color of the suspension turn from dark brown to yellow. The suspension was filtered and washed with diluted aqueous hydrogen chloride solution (300 mL, HCl: 10%) and subsequently distilled water (300 mL). The resulting solid was re-dispersed into 300 mL distilled water, stirred overnight and sonicated for 10 min so that the solid was exfoliated to GO sheets. Finally, the graphene oxide dispersion was purified by dialysis for around one week to remove the remaining metal ions and the acid.

Synthesis of high entropy alloy powders: I also demonstrate the formation of high entropy alloy nanoparticles using aerosol droplet mediated approach. The precursor solution was prepared by dissolving equimolar amount of metal salts into D.I. water. The experiment consists of a Collison nebulizer (BGI Inc.), a silica dryer, a silica tubular reactor heated by two combined tube furnace, and a membrane filter (Millipore, material: polycarbonate, pore size: 0.4 μ m). In a typical experiment, the prepared precursor solution was loaded into the atomizer and was nebulized into small aerosol droplets using 10% H₂/90% Ar mixture gas with a pressure of 30 psi . These droplets carried by the mixture

gas were first passing through the silica dryer, where the water solvent evaporated from the droplets. Following the water solvent removal, the resulting dry aerosol particles moved into the high-temperature tubular furnace reactor (diameter: 2 cm; heating length: 60 cm, set temperature: 1100 °C) where the fast heating led to the rapid decomposition and reduction of the metal salts to metals, and the subsequent fast cooling resulted to the HEA formation. The products were collected with a membrane filter collector, which was blew with cooling air to achieve fast quenching of the product. The aerosol flow rate was ~3 L/min, which was measured at the end of the sample collector. Thus, based on the geometry of the aerosol reactor and the gas flow rate, the calculated residence time of the droplets in the high temperature reactor was about 3 s.

2.2. Aerosol droplets as building blocks for functional nanostructured design

In this dissertation, I also use aerosol droplets as building blocks to create a 3D structure consisting of carbon sphere network supported metal nanoparticles, and investigate the excellent electrochemical performance of the resulting materials.

Electrospray-assisted Printing: Precursor solution is prepared by dissolving antimony chloride (340 mg) into DMF solvent (10 mL). Then, polyacrylonitrile (PAN, 160 mg) was added to the solution followed by vigorous stirring overnight. The obtained mixture solution was used as the precursor for electrospray. As shown in **Figure 2.2**, the precursor solution was loaded into a 10 mL syringe tube and pumped through a flat-top stainless-steel needle (inner diameter: 203.2 μm). A printing rate of 0.5 mL/hour and voltage differential of 20kV between the electrospray needle and the aluminum substrate were employed as the parameter for the electrospray-based printing. Under the electric field

generated by the voltage differential, the nebulized precursor solution from the needle fissioned into millions of small droplets, which served as the primary building blocks for porous 3D network construction. The solvent evaporated from the droplets when they were flying towards the substrates. By adjusting the distance between the needle and the substrate, the dry level of the on-the-fly droplets can be varied. Here, a distance of 10 cm between the needle and the substrate was used so that the aerosol particles would deposit on the substrate before they were completely dry. As such, the deposited aerosol particles were attached to one other to form a porous 3D network. The as-prepared sample was loaded into a tube furnace, heated up to 250 °C with a heating rate of 5 min/°C in the air atmosphere, and kept at 250 °C for 30 mins to stabilize the structure of the sample. Then, the sample was heated up to 600 °C with a heating rate of 2 °C /min under H₂/N₂ atmosphere and kept at 600 °C for 5 hours to obtain the desired electrode material.

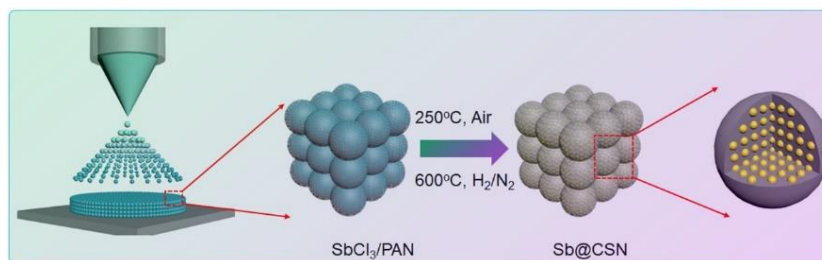


Figure 2.2. Schematic illustration of electro-spray-assisted strategy for fabricating Sb@CSN material.

2.3. Laser-assisted nanomanufacturing

In this dissertation, I also develop an ultrafast laser shock technique to produce high-density, extremely small metal nanoparticles uniformly decorated on carbon nanofiber thin film, and investigate the electrocatalytic performance of the resulting composite materials as catalysts for hydrogen generation evolution.

Synthesis of carbon nanofiber via electrospinning: First, Carbon nanofiber (CNF) thin film was first prepared as follows: Polyacrylonitrile was added to 10 mL DMF solvent followed by vigorous stirring overnight. The as-obtained solution was used as the precursor for electrospinning to prepare polyacrylonitrile (PAN) thin film. The precursor solution was loaded into a 10 mL syringe tube and pumped through a flat-top stainless-steel needle (inner diameter: 203.2 μm). A pumping rate of 0.5 mL/hour, a voltage differential of 12 kV and a distance of 15 cm between the needle and the aluminum substrate were employed for electrospinning. In order to prepare CNF films, the as-prepared PAN sample was loaded into a tube furnace, heated up to 250 $^{\circ}\text{C}$ with a heating rate of 5 $\text{min}/^{\circ}\text{C}$ in the air atmosphere, and kept at 250 $^{\circ}\text{C}$ for 2 hours. Then, the sample was heated up to 1000 $^{\circ}\text{C}$ with a heating rate of 2 $^{\circ}\text{C}/\text{min}$ under H_2/N_2 (v:v=5:95) atmosphere and kept at 1000 $^{\circ}\text{C}$ for 5 hours to obtain CNF thin films.

Metal precursor incorporation: The metal precursor (0.05M) was dropped onto carbon nanofiber thin films (2.5 mm x5.0 mm) using a pipette with a loading of ~ 100 $\mu\text{L}/\text{cm}^2$. The metal salt loaded thin film was air dried. The resulting weight percentage of Pt in CNF matrix is about 30%.

Ultrafast Laser shock experiment: The metal salt impregnated CNF thin film sample (2.5 mm x5.0 mm) was mounted on a homemade graphite holder, which was placed in the center of the box chamber filled with inert Ar gas (**Figure 2.3**). The freestanding thin film sample was heated by a continuous CO_2 laser, which was controlled by a computer. The duration, output energy power, and the size of the laser beam can be adjusted accordingly. The duration of the laser was varied from 50 ms to 60 s. The output power of the laser applied was 90% of the total laser power (80W). The size of the laser beam was

adjusted using a beam expander. In this experiment, the diameter of the laser beam was 4 mm. Therefore, the powder density of the laser beam was $\sim 400\text{W}/\text{cm}^2$ based on the output power and the size of the laser beam. The laser shock process was recorded with a high-speed color camera. The recorded color images were used to extract spatiotemporal temperature of the sample.

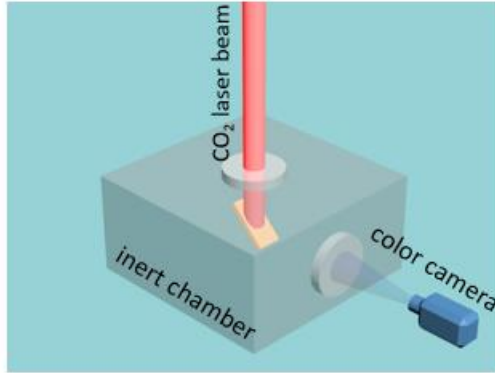


Figure 2.3. Schematic of laser shock synthesis of high-density ultrasmall metal nanoparticles uniformly decorated on carbon nanofiber thin film.

2.4. High speed color pyrometry

The temperature of the hot sample is estimated using Equation 1. By taking ratios of raw channel intensities, dependency on most variables associated with intensity is eliminated except for those regarding the channel gain (ψ_i), emissivity (ϵ), and spectral response (χ_i) of the camera at individual wavelengths and channels.⁸⁵ To estimate temperature of the hot surface, the graybody assumption has been modified to account for an optically thin flame by assuming that $\epsilon \sim 1/\lambda$, substituted into Planck's Law, and integrated over the entire spectrum to which the camera is sensitive (as shown in Equation 1 below).⁸⁶ When calibrated with a Newport Oriel 67000 Series Blackbody Infrared Light Source, calibration factors C_{gr} , C_{bg} , and C_{br} with data available in the article by Jacob and Kline *et al.*, and these factors were assumed valid from 773-4773K.⁸⁷ Through this,

calculation of temperature is reduced to matching of calibration factor-corrected channel intensity ratios to theoretical ratios. Three color ratios (green/red, blue/green, and blue/red) were simultaneously used to estimate temperature by minimizing their summed error from theoretical ratios. Further thresholding is used to eliminate summed errors corresponding to a temperature error greater than 110K. Only unsaturated pixels above the black level and within the error threshold are used to report mean and median temperature of the frame for a contiguous area of at least 10 acceptable pixels.

2.5. Catalytic performance tests.

Ni and Co nanoclusters decorated in graphene aerosols were chosen to demonstrate catalytic performance towards reduction of 4-nitrophenol by sodium borohydride. A volume of 20 mL 4-nitrophenol solution with a concentration of 0.1 mM was mixed with 5 mL of 0.2M sodium borohydride. The catalytic reaction was triggered with the addition of 5 ml of metal-rGO suspension containing 0.80 mg metal-rGO catalyst. The solution was continuously stirred and the reaction was allowed to proceed at room temperature. Immediately after catalyst addition, 300 μ L of the reaction solution was collected and diluted to 3 mL using D.I. water for time-resolved absorbance spectra measurement using a Perkin Elmer (Lambda 1050) UV-Vis spectrophotometer.

The electrocatalytic performance of CNF supported Pt nanoclusters toward hydrogen evolution reaction (HER) was tested. The freestanding metal nanoclusters decorated CNF film was directly used as the working electrode. Platinum foil was used as the counter electrode and a standard Ag/AgCl electrode as the reference electrode. HER tests were performed in a 0.5 M H₂SO₄ aqueous solution. The polarization tests were

performed by linear sweep voltammetry from 0 to -0.5 V (vs. RHE) with a scan rate of 2 mV/s.

2.6. Battery performance tests

Electrolytes Preparation: The salts of potassium trifluoromethanesulfonimide (KTFSI) and potassium hexafluorophosphate (KPF_6) was purchased from TCI and used as received. The solvents of Ethylene Carbonate (EC) and Diethyl Carbonate (DEC) were purchased from Sigma-Aldrich and used without any purification. The different electrolytes are prepared in Ar-filled glovebox as follows: a certain molar of salt dissolving into the mixed solvent of EC+DEC (V: V=1: 1) to obtain different electrolytes: 4M KTFSI/EC+DEC electrolyte (abbreviated as “4M KTFSI”), 1M KTFSI/EC+DEC electrolyte (abbreviated as “1M KTFSI”), and 1M KPF_6 /EC+DEC electrolyte (abbreviated as “1M KPF_6 ”).

Coin cells preparation: The Sb@CSN composite, conductive carbon (from SAFT) and sodium alginate with a mass ratio of 8:1:1 were mixed in certain amount of H_2O solvent to form homogeneous slurry by stirring for 2 hours. The slurry was coated onto a thin Cu foil and dried at 90 °C for 10 h in vacuum. The coin cells (CR2032) were assembled in the Ar-filled glove box with the as-prepared Sb@CSN composite as the working electrode, pure potassium metal foil as the counter electrode, polypropylene microporous (PP, Celgard) film as the separator.

Electrochemical Measurements: The galvanostatic charge/discharge tests were performed with Arbin Battery instrument (BT2000, Arbin Instruments, USA) at a voltage range of 0.01-2.0 V at room temperature. The galvanostatic intermittent titrations (GITT)

were also tested after 10 cycle's charge/discharge activation cycles on the Arbin station by alternating the current density with 100 mA/g for 20 min and rest intervals for 2h. Cyclic voltammetry (CV) measurements were performed on Gamry instrument (Reference 3000) with a scan rate of 0.1 mV/s in the range of 0.01 to 2.0 V. Electrochemical impedance spectroscopy (EIS) were also tested on the Gamry instrument with a frequency range of 10^5 to 10^{-2} Hz under the AC signal amplitude of 5 mV.

2.7. Characterization

In this dissertation, the morphology, microstructure, and composition of the synthesized materials were examined by various kinds of analytical tools including scanning electron microscopy (SEM), transmission electron microscopy (TEM), scanning transmission electron microscopy (STEM), Energy-dispersive X-ray spectroscopy (EDS), X-ray diffractometer (XRD), thermogravimetric analyzer (TGA), X-ray photoelectron spectroscopy (XPS), Raman spectroscopy (Raman), Fourier transform infrared spectroscopy (FTIR), Ultraviolet–visible spectrophotometer (UV vis).

Polymer supported metal nanoclusters: Morphologies and structures of metal polymer nanocomposites were examined by scanning electron microscopy (SEM, Hitachi SU-70) and transmission electron microscopy (TEM, JEOL JEM 2100 FEG). Elemental distribution in the nanocomposite particle was analyzed by Energy-dispersive X-ray spectroscopy (EDS) mapping on TEM. Phase and component identification was conducted by X-ray diffractometer (XRD, Bruker D8 diffractometer with Cu Ka radiation). The structure of the polymer molecules was characterized by Fourier transform infrared spectroscopy (FTIR). Thermogravimetric analysis (TGA) of PVP polymer was carried out

using a thermogravimetric analyzer (TA Instruments, USA) with a heating rate of 10 °C/min in argon gas.

Metal graphene nanocomposites: Morphologies and microstructures of metal-rGO nanocomposites were examined by transmission electron microscopy (JEOL JEM 2100 FEG) and scanning electron microscopy (Hitachi SU-70). Elemental distribution analysis in the aerosol particle was carried out with Energy-dispersive X-ray spectroscopy (EDS) in the TEM. The mean diameters and size distributions of the nanoclusters were determined by statistical analysis of the acquired TEM images, using Nano Measurer 1.2 image analysis software. Phase and component identification was done by X-ray diffractometer (Bruker D8 diffractometer with Cu K α radiation). Thermogravimetric analysis (TGA) of metal-rGO nanocomposites was carried out using a thermogravimetric analyzer (TA Instruments, USA) with a heating rate of 5 °C/min in air atmosphere. The absorbance spectra measurement was recorded using a Perkin Elmer (Lambda 1050) UV-Vis spectrophotometer equipped with a 4.5 mL quartz cuvette with a path length of 1 cm.

Antimony carbon nanocomposites: The Sb@CSN material was characterized by X-ray diffraction (XRD, Bruker Smart 1000 using a Cu K α line radiation source), thermogravimetry-differential scanning calorimetry (CAHN TG 2131, under Air with a heating rate of 5°C/min), Raman spectra (with 514.5 nm laser source), scanning electron microscopy (SEM, Hitachi SU-70 field emission scanning), high-resolution transmission electron microscopy (HRTEM, 2100F field emission), X-ray photoelectron spectroscopy (XPS, monochromatized ESCALAB 250 with Al K α source radiation, with an Ar⁺ sputtering gun). The electrolyte ignition and combustion experiment were recorded by high-speed digital camera with a Vision Research Phantom v 12.1 digital camera, and the

frame rate of 1,000 frames per second with a resolution of 640×480 pixel. A small piece of glass fiber membrane was soaked with about 0.5 mL electrolyte and fixed by an alligator clip, followed by immediate ignition with a butane lighter.

High entropy alloy nanoparticles: A JEOL ARM-200CF was used to image HEA nanoparticles deposited on lacey carbon Mo grid. High angle annular dark field (HAADF) and annular bright field (ABF) images were acquired by a spherical aberration corrected JEOL JEM-ARM 200CF STEM with a cold field emission gun operating at 200 kV, with 22 mrad convergence angle. Images were taken using an Orius CCD camera with 512×512 scanning resolution. Energy dispersive X-ray Spectroscopy (EDS) analyzes and elemental mapping were obtained in the STEM mode (ThermoFisher Scientific Titan Themis 300 instrument, fitted with X-FEG electron source, 3 lens condenser system and S-Twin objective lens) at 300 kV, utilizing ThermoFisher Scientific SuperX system equipped with $4 \times 30 \text{mm}^2$ window-less SDD detectors symmetrically surrounding the specimen with a total collection angle of 0.7 sr, by scanning selected area from the specimens. Elemental mapping by plotting the net X-ray counts was performed with an electron beam probe current of 550 pA at 1024×1024 frame resolution, dwell time of 30 $\mu\text{sec}/\text{pixel}$ and scanning multiple frames resulting in effective total acquisition time between 3 to 10 mins. EDS spectra were extracted from the elemental maps as well as by direct spectra acquisition from selected areas. Elemental concentrations were calculated using the Cliff-Lorimer ratio technique⁸⁸ using calculated k-factors, which have been verified experimentally to incorporate an error of less than $\pm 3\%$ by analyzing standard specimens with known composition of SiO_2 , SiC , TiO_2 and NiO and correcting for absorption. The minimum error in determining the elemental concentrations in the studied

specimens is estimated from the statistical uncertainty in measuring the X-ray peak intensities which was less than 5% relative. The EDS spectra were used to quantify the composition of the HEA particles deposited on lacey carbon Au grid.

CNF supported Pt nanoclusters: Morphologies and structures of metal nanoclusters supported on CNF matrix were examined by scanning electron microscopy (SEM, Hitachi SU-70) and transmission electron microscopy (TEM, JEOL JEM 2100 FEG). The mean diameters and size distributions of the nanoparticles were determined by statistical analysis of the acquired TEM images, using Nano Measurer 1.2 image analysis software.

Chapter 3: Growth of Sub- 5nm Metal Nanoclusters in Polymer Melt

Aerosol Droplets*

Abstract: Ultrasmall metal nanoparticles are inherently unstable because of their high specific surface area. This work investigates how growth and aggregation of these nanostructures can be circumvented by incorporating them into a polymer matrix in an on-the-fly growth process. I demonstrate the formation of sub- 5 nm particles of Ni, Co and Cu nanoparticles in polymer matrix using an aerosol single-drop reactor approach. The rapid thermal pulse given to the aerosol particles enables the formation of nuclei and growth, with subsequent rapid quenching to freeze in the structure. The role of temperature as well as precursor concentration of the resulting size and morphology are discussed. A characteristic time analysis and an analysis of the particle size distributions lead to the conclusion that growth is governed by nucleation and surface growth with little coagulation or Ostwald ripening. Finally, this aerosol route is amenable to scale-up for large scale production of nanoclusters that can either be used as is within the polymer or released by solvent extraction, depending on application.

* The results represent in this chapter have been previously published and are reprinted from: Yong Yang, Michelangelo Romano, Guangjie Feng, Xizheng Wang, Tao Wu, Scott Holdren, Michael R Zachariah; Growth of Sub-5 nm Metal Nanoclusters in Polymer Melt Aerosol Droplets. *Langmuir* 2019, 34 (2), 585-594

3.1. Introduction

Ultra-small metal nanoparticles with a diameter less than 5nm have been of great interest in recent years due to their unique size- and shape-dependent properties, enabling applications to the fields of plasmonics, photonics, catalyst, nanomedicine and magnetic storage, among others.¹⁻⁵ To synthesize these extremely small nanoparticles, at least in sufficient quantities to enable its utility, is challenging because their high mobility and meta-stable nature either results in aggregates or particle growth. One approach to potentially overcome this challenge is by encapsulating nanoparticles within a polymer matrix so that these nanoparticles are physically frozen in the polymer matrix or chemically stabilized via forming covalent bonds with polymer molecules, ultimately preventing nanoparticle agglomeration and oxidation.^{13, 89-90}

These hybrid materials are referred to as metal polymer nanocomposites. Fundamentally, the polymer serves as a framework for stabilizing nanoparticles. However, the strategic combination of nanoparticles and specific types of polymers can yield enhanced functionality for these composite materials.⁹¹ In many cases, nanoparticles incorporated within polymers have been demonstrated to increase the system's mechanical stability.⁹²⁻⁹³ Other synergistic effects have augmented the composite material's electrical and optical properties. For example, the introduction of metal nanoparticles into organic photovoltaics has led to improved efficiencies, stemming from the enhanced light absorption and scattering properties of the incorporated nanoparticles.⁹⁴ Furthermore, nanoparticles embedded within electrically conductive polymers have the potential to serve as innovative composite materials for electrodes within Li-ion batteries.⁹⁵

Synthesis of metal polymer nanocomposites have been accomplished by both ex situ and in situ composite stabilization. In ex situ stabilization, metal nanoparticles are first synthesized by processes such as colloidal chemistry, nanolithography, laser ablation, sputtering and ball-milling and subsequently introduced within a polymer matrix.^{13,96} One major difficulty in this approach is homogeneous incorporation of nanoparticles into polymer matrix and the prevention of aggregation. Alternatively, in situ techniques refer to the formation of nanoparticles directly within a polymer matrix. This fabrication method first incorporates metal-ion precursors into a polymer matrix, from which nanoparticles are generated in the polymer matrix via thermal reduction or decomposition of metal-ion precursors.⁹⁷⁻¹⁰² In essence, the polymer functions as a soft template for guiding the nucleation and growth of the metal nanoparticles. This method eliminates the need for surfactants and capping agents, yielding a higher nanoparticle number density and a more uniform nanoparticle distribution throughout the polymer matrix. However, most in situ and ex situ techniques reported in the literature typically generate metal polymer nanocomposites in small quantities. The difficult lies in increasing the production rate which for a bulk system typically involves inhomogeneous and slow heating and cooling rates. This typically leads to a wide size distribution, inhomogeneous dispersion and aggregation.⁶⁵

Ideally one would like to control the thermal pulse to trigger chemistry over a short time scale and do so homogeneously. One approach to accomplish this is to conduct the synthesis within an aerosol particle and use inherent rapid thermal equilibration of the particle to ensure precise control and homogeneous heating. Further because of the small thermal mass heating and cooling can be rapid, achieving higher temperatures for shorter

duration is plausible. Because such a process is continuous scaling becomes greatly simplified. Aerosol routes, such as aerosol spray pyrolysis (ASP) have been used to generate nanoparticles and nanocomposites.^{65, 103-105} In a typical ASP process, the precursor solution is continuously nebulized to produce aerosol droplets from hundred nanometers to several micrometers in diameter and these aerosol droplets, acting like small isolated reactors, pass through a heating element where the reaction in each aerosol reactor is triggered by a short thermal pulse to generate nanostructured materials upon solvent evaporation. Although the ASP technique has been used to produce and assemble a large range of materials (metals²⁶, alloys²⁷, metal oxide²⁸⁻³⁰, composites³¹⁻³³) with controllable size and morphologies, fabrication of nanoparticles with a diameter of sub- 50 nm, which is much smaller than that of the nebulized aerosol droplets, using this technique remains challenging. Recently, efforts have been made to produce small and monodisperse nanoparticles by introducing an inert solute into the aerosol droplets to guide the nucleation and growth of nanoparticles.³⁴⁻³⁵ For example, Xia et al. have introduced sodium chloride into the precursor solution to guide formation of sub- 10 nm NiO and ZnS nanoparticles.³⁴ Few studies have been reported on using this technique to synthesize metal polymer nanocomposites. One primary exception is Lee et al. who embedded silver nanoparticles in PVP matrix by thermal decomposition of silver nitrate.¹⁰⁶ However, encapsulation of non-noble metals cannot be achieved via this approach since thermal decomposition of salts of reactive metals would produce metal oxides. Seo et al. incorporated copper nanoparticles with diameters ranging from 30 nm to 50 nm in PVP matrix by reducing copper nitrate with ethanol as a reducing agent.

In this paper, our focus is the synthesis of high density unaggregated ultrasmall nanoparticles of zero valent metals with a very narrow size distribution. To our knowledge, this is the first demonstration of the formation of sub- 5nm metal nanoparticles (e.g. Ni, Co and Cu) incorporated into polymer particles (~several hundred nanometers to 1.5 micrometers) in a one-step ASP process. I demonstrate that this is a generic facile process to produce virtually any metallic nanoparticle and evaluate the role of temperature and metal precursor loading on particle properties.

3.2. Experimental section

3.2.1. Materials. Nickel nitrate hexahydrate ($\text{Ni}(\text{NO}_3)_2 \cdot 6\text{H}_2\text{O}$, $\geq 99\%$ pure), copper nitrate trihydrate ($\text{Cu}(\text{NO}_3)_2 \cdot 3\text{H}_2\text{O}$, $\geq 99\%$ pure), cobalt nitrate hexahydrate ($\text{Co}(\text{NO}_3)_2 \cdot 6\text{H}_2\text{O}$, $\geq 98\%$ pure) were all purchased from Sigma-Aldrich. Polyvinylpyrrolidone (PVP) powders with three different molecular weights (M.W. 1,300,000; 58,000; 8000, g/mol) were obtained from Alfa Aesar. All the chemicals were used as received.

3.2.2. Precursor preparation. The precursor solutions were prepared by dissolving 425 mg of PVP polymer and a certain amount of metal salt in 25 ml deionized water. The metal salts used to obtain Ni, Co and Cu nanoparticles were $\text{Ni}(\text{NO}_3)_2 \cdot 6\text{H}_2\text{O}$, $\text{Co}(\text{NO}_3)_2 \cdot 6\text{H}_2\text{O}$, $\text{Cu}(\text{NO}_3)_2 \cdot 3\text{H}_2\text{O}$, respectively. The mass of the metal salt used was varied between 42.5 mg to 425 mg to prepare precursor solutions with different metal salt precursor to polymer mass ratios (0.1, 0.3, 0.5, 1.0).

3.2.3. Aerosol Spray Pyrolysis. Aerosol droplets containing metal salt and polymer molecules with desired mass ratio were created from a pneumatic collision nebulizer with 5% hydrogen and 95% nitrogen mixture as the carrier gas. **Figure 3.1** shows schematically the basic concept behind the synthesis scheme. Most of the water solvent is removed from the droplets as they pass through a silica gel diffusion dryer, where they are carried to a tubular furnace (28 cm in length, 2 cm in diameter) for a residence time of ~ 1 s. The set temperature of the tube furnace varied from 400 °C to 800 °C. Within the heated flow, the dried polymer particles are molten, and the metal salt decomposed and reduced in H_2 to form metal nanoparticles in the polymer melt. Rapid quenching on a 0.4 μm pore Millipore HTPP membrane filter results in arresting of the nanoparticle growth.

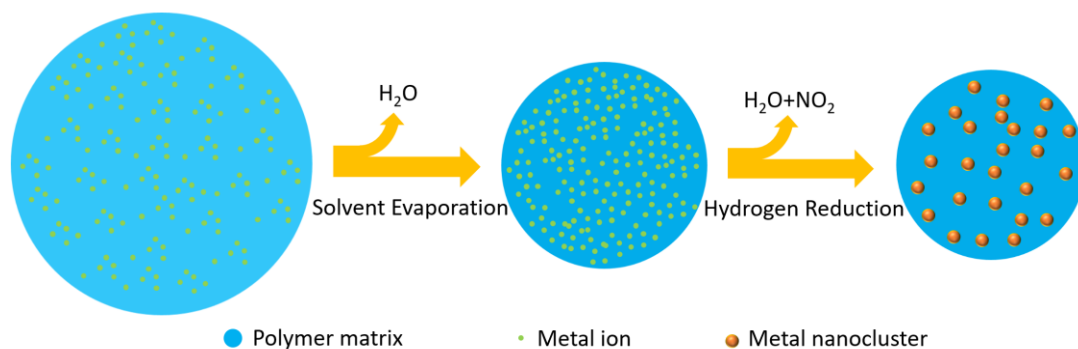


Figure 3.1. Schematic of formation of nanoclusters in aerosol polymer droplet.

3.2.4. Characterization. Morphologies and structures of metal polymer nanocomposites were examined by scanning electron microscopy (SEM, Hitachi SU-70) and transmission electron microscopy (TEM, JEOL JEM 2100 FEG). Elemental distribution in the nanocomposite particle was analyzed by Energy-dispersive X-ray spectroscopy (EDS) mapping on TEM. The mean diameters and size distributions of the nanoparticles were determined by statistical analysis of the acquired TEM images, using Nano Measurer 1.2 image analysis software.¹⁰⁷ Phase and component identification was conducted by X-ray diffractometer (XRD, Bruker D8 diffractometer with Cu K α radiation). The structure of the polymer molecules was characterized by Fourier transform infrared spectroscopy (FTIR). Thermogravimetric analysis (TGA) of PVP polymer was carried out using a thermogravimetric analyzer (TA Instruments, USA) with a heating rate of 10 °C/min in argon gas.

3.3. Results and Discussion

3.3.1. Formation of metal polymer nanocomposites. Figure 3.2 shows SEM images of metal polymer nanocomposites containing Ni, Co, and Cu nanoparticles respectively. Information about the precursor solutions and operation parameters used to generate these three types of nanocomposites is summarized in **Table 3.1**. As shown in Figure 3.2, all three nanocomposites have a spherical shape with a size distribution roughly ranging from several hundred nanometers to 1.5 micrometers. In particular, Ni and Co polymer nanocomposites shown in Figure 3.2(a) and 2(b) have a crumpled surface morphology. Similar surface morphologies have also been observed by others who have synthesized composite materials using the precursor containing polymer molecules and metal salts by ASP technique.^{31, 108} While I have no definitive conclusion about how the crumpled surface was formed, it may be related to the gas release during hydrogen reduction of metal nitrate (Eqn. 3.1, M represents metal element) in the presence of the high viscous polymer melt. Surface corrugation of the polymer particles appears to scale closely with the metal salt to PVP ratio. For example, Figure 3.2(c) shows Cu polymer nanocomposites formed using a much lower metal salt to PVP ratio (0.3) compared to the polymer nanocomposites in Figure 3.2(a) and 2(b) (1.0). The lower metal salt to PVP ratio formulation created particles with a smoother surface.

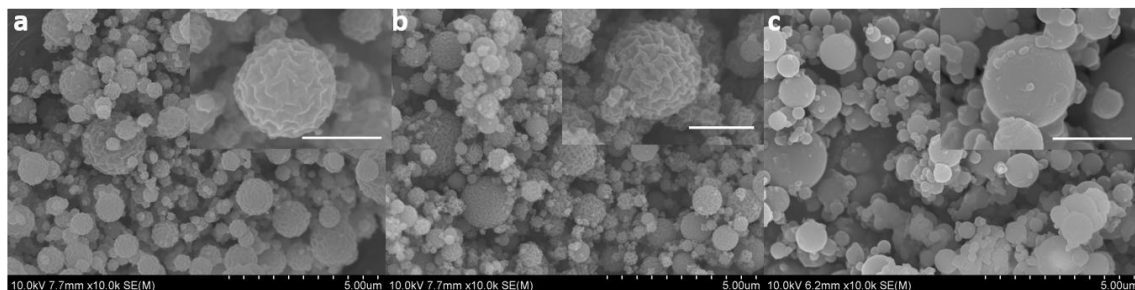


Figure 3.2. SEM images of metal polymer nanocomposites. (a) Ni PVP8k, (b) Co PVP58k, (c) Cu PVP8k. The length of the scale bar in the inset images is 1 μm .



Table 3.1. Synthetic conditions for spray pyrolysis

Nanocomposite	Metal salt	PVP molecular weight (g/mol)	Metal salt to PVP ratio	Pyrolysis temperature ($^{\circ}\text{C}$)	Residence time (s)
Ni PVP8k	$\text{Ni}(\text{NO}_3)_2 \cdot 6\text{H}_2\text{O}$	8000	1.0	600	1
Co PVP58k	$\text{Co}(\text{NO}_3)_2 \cdot 6\text{H}_2\text{O}$	58000	1.0	700	1
Cu PVP8k	$\text{Cu}(\text{NO}_3)_2 \cdot 3\text{H}_2\text{O}$	8000	0.3	600	1

Slow-heating TGA data of PVP shown in **Figure 3.12** demonstrates that PVP molecules are fully decomposed at temperatures above 460 $^{\circ}\text{C}$. However, aerosolized PVP particles, which were actually heated to much higher temperatures appear to survive due to their very short residence time in the reactor (~ 1 s.). FTIR analysis of 600 $^{\circ}\text{C}$ spray pyrolysed PVP particles (of different molecular weights) showed no discernable evidence of polymer degradation (see **Figure 3.13**). The PVP sample powders were also characterized by SEM. The sprayed PVP powders have a spherical shape with a smooth surface morphology as shown in **Figure 3.14**. However, despite the lack of any spectroscopic evidence for polymer chemistry under such short heating, I did notice that

spray-pyrolysed 1300k-PVP was more easily dissolved in water than compared to the commercial reagent PVP, suggesting the possibility of polymer cleavage leading to a lower average molecular weight after short heat shock.

The XRD patterns of the three metal polymer nanocomposite powders are shown in **Figure 3.15**. The broad and flat peak located at around 20° on each XRD pattern belongs to the PVP matrix. It was observed that nickel and copper nitrate were completely reduced to metallic nickel and copper by hydrogen gas at the reaction temperature of 600°C with a resident time of 1s. However, metallic cobalt was only obtained at a reaction temperature of 700°C . These results are consistent with other studies on fabricating pure metal powders by hydrogen reduction of metal salts via APS with similar operating conditions.^{26, 109-111} To test the stability of the metal nanoparticle incorporated in the PVP matrix, the Ni polymer nanocomposite was exposed to air for >1 month, and the metallic nickel phase was still observed by XRD (see Figure 3.15). This suggests that the PVP matrix is able to protect metal nanoparticles from oxidation.

The size and distribution of metal nanoparticles (Ni, Co, Cu) dispersed in polymer matrices were characterized by TEM as shown in **Figure 3** (see also Figure 3.16 for Scanning TEM and EDS mapping characterization). The three selected-area electron diffraction (SAD) patterns (inserts of Figure 3.3) confirm the presence of pure Ni, Co and Cu metals, respectively, which indicates the Ni, Co and Cu ions have been reduced to their metallic states by H_2 . This result is consistent with the aforementioned XRD data. As shown in Figure 3.3, monodispersed Ni, Co and Cu nanoparticles with an average diameter of 3.5 nm, 3.9 nm and 4.1 nm, respectively, are uniformly distributed in the polymer particles. The size difference between the different metal nanoparticles may be attributed

to both different mass fractions of metal nanoparticles in the polymer matrix and the various interactions between different metal nanoparticles and polymer molecules. With the full conversion of metal salts to metal elements and the complete release of the other byproducts such as water vapor and NO₂ from the polymer particles, the total mass and volume fractions of metal nanoparticles can be derived based on the metal salt to PVP ratio used to prepare the precursor solutions. The calculated total mass fractions of metal nanoparticles are listed in **Table 3.3**. Table 3.3 also includes the areal number concentrations and number average diameter of metal nanoparticles obtained by statistical analysis of metal nanoparticles in TEM images. The areal number concentration was calculated based on the number of particles divided by the corresponding nanocomposite particle area in the TEM images. As shown in Table 3.3, both mass fractions of Ni and Co metals in polymer matrices are around 16.8%. The formed Ni and Co nanoparticles have similar areal concentrations and diameters. This aligns well with our findings that the metal nanoparticle diameter increases with the metal salt concentration (discussed in more detail in section 3.3). However, the generated Cu nanoparticles also have a similar diameter compared to the Ni and Co nanoparticles even though a much lower mass fraction (7.9%) of copper was loaded in the PVP matrix. This suggests that additional factors affect the particle size besides the mass loading of metal salts. The similarity in size of the metal nanoparticles formed for the three different metals can be explained by differences in the polymer-nanoparticle surface interactions. Previous studies have shown that stronger polymer-nanoparticle surface interactions enabled formation of smaller nanoparticles.¹¹² Prior work has shown that the strength of the interaction between the polymer matrix and metal nanoparticles are related to the reactivity of the metal.¹¹³ Therefore, I believe that the

Cu-polymer interactions will be weaker compared to the Ni or Co-polymer interactions because Cu is less reactive. These weaker interactions allow the Cu to form larger nanoparticles with a lower mass loading. As a result, Cu nanoparticles with a similar diameter compared to Ni and Co nanoparticles were synthesized even though a lower mass fraction between metal and PVP was used in the precursor solution.

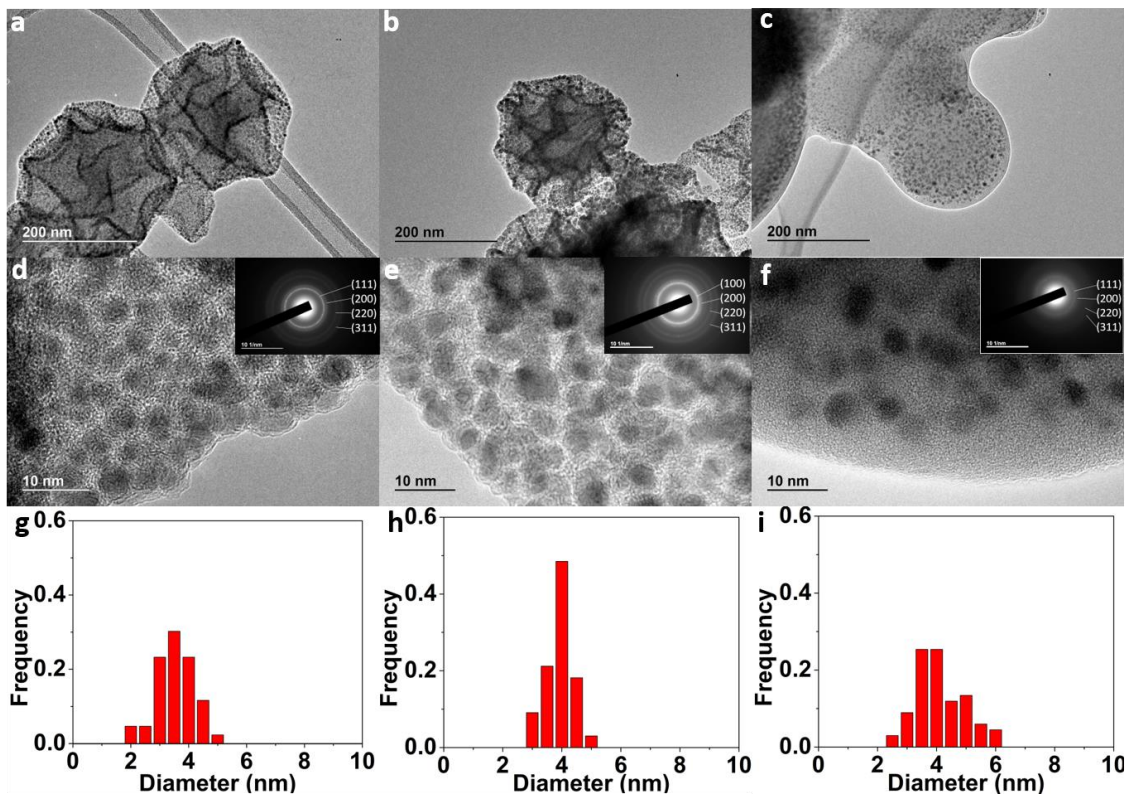


Figure 3.3. TEM images and metal nanocluster size distribution in metal polymer nanocomposites. (a)(d)(g) Ni PVP8k; (b)(e)(h) CoPVP58k; (c)(f)(i) CuPVP8k.

In the following, the Ni polymer nanocomposite system is used to demonstrate how temperature and metal salt to polymer ratio affect nucleation and growth.

3.3.2. Effect of temperature on the size and phase evolution of metal nanoparticles. The precursor solutions composed of nickel nitrate salt and PVP8k with a 1.0 mass ratio were spray-pyrolysed at different temperatures. It is known that under slow

heating (0.6 °C/min) and in the presence of H₂ nickel nitrate converts to metallic nickel at 270 °C.¹¹⁴ **Figure 3.4** shows, however, that at fast heating (short residence times) metallic nickel is only seen at temperatures of 600 °C or above.

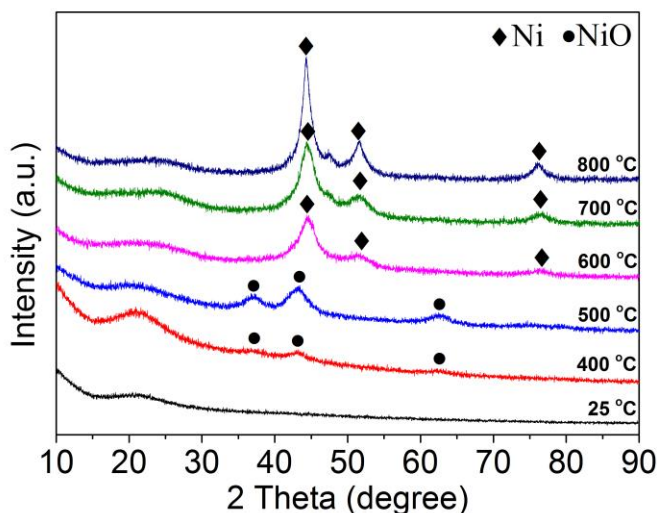


Figure 3.4. XRD of metal polymer nanocomposite synthesis under various reaction temperatures

The effect of reaction temperature from 400 °C to 800 °C on the morphology of the metal polymer nanocomposite and the growth of Ni nanoparticles in polymer matrix is shown in **Figure 3.5**. The mass ratio between nickel nitrate and polymer in precursor solutions was kept at 0.3. At 600 °C and above, a crumpled surface morphology is observed, presumably caused by gas release during a reduction reaction of the metal nitrate in the polymer melt. However, no crumpled texture was observed on the surface of the products produced at temperatures of 500 °C and below, where the conversion to Ni nanoparticles was not complete. This is confirmed by the observation that the volume fraction of nanoparticles formed at 500 °C (Figure 3.5.g) is smaller than that of nanoparticles formed at 600 °C (Figure 3.5.h).

From the TEM images shown in Figure 3.5, NiO nuclei with a diameter of less than 1 nm were formed at around 400 °C and grew to larger NiO nanoparticles with an average diameter of 1.5 nm at 500 °C. The ultra-small unaggregated Ni nanoparticles with an average diameter of 2.3 nm were generated at 600 °C. This result indicates that intra-drop coagulation (the process in which single particles diffuse together to form an agglomerate) is slow for the given residence time (~1 s). However, as seen in Figure 3.5(i)-(j) aggregation between nanoparticles is observed at higher reaction temperatures of 700 °C and 800 °C. This is consistent with high temperatures facilitating the diffusion of particles in the polymer melt and a likely decrease in polymer-metal interaction energy.¹¹⁵ The coagulation between nanoparticles leads to a decrease of the number concentration of the Ni nanoparticles in the temperature range from 700 °C to 800 °C as shown in **Figure 3.6**. The fact that the agglomerates are seen at all (primary particles 2~3 nm) indicates that coalescence (the process in which an agglomerate sinters together to gain a spherical morphology) is slow compared to the residence time. Results in Figure 3.6 show that the average size monotonically scales with reaction temperature at fixed residence time. This result clearly demonstrates that the use of a polymer encapsulant can be used as a reaction medium at temperatures well above its decomposition temperature, for short thermal pulses, enabling the nucleation, growth and stabilization of metal ultrafine nanoclusters.

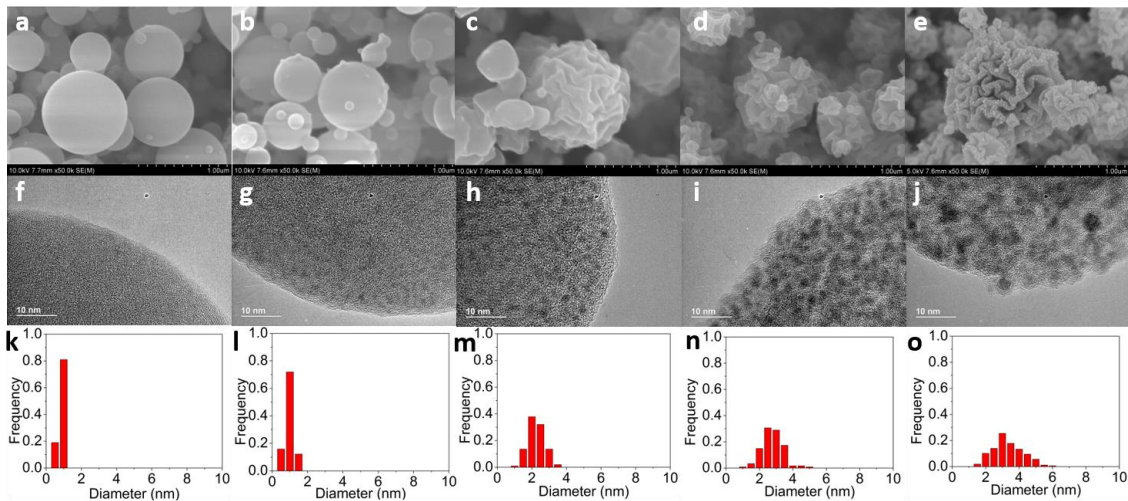


Figure 3.5. SEM and TEM images of Ni/NiO polymer nanocomposites synthesized at different reaction temperatures. (a)(f)(k) 400 °C, (b)(g)(l) 500 °C, (c)(h)(m) 600 °C, (d)(i)(n) 700 °C, (e)(j)(o) 800 °C.

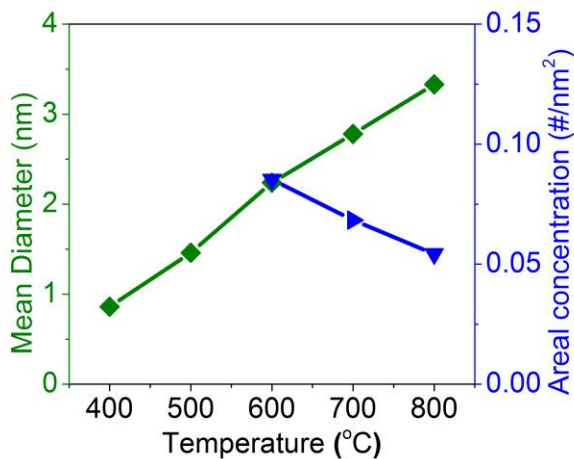


Figure 3.6. Size and number concentration evolution of Ni/NiO nanoparticles with reaction temperature

3.3.3 Effect of mass loading on the size of metal nanoparticles. By simply adjusting the mass of metal salt in the ASP precursor, the metal salt to polymer ratio in the sprayed droplet can be adjusted. The SEM images in **Figure 3.7(a)-(d)** show that the morphology of the nanocomposites changed with the metal salt to PVP ratio. The crumpled surface morphology is observed primarily for the high mass metal salt loading samples due

to the mass loss through gas release from the reduction reaction of nickel nitrate salt. Figure 3.7(e)-(i) show TEM micrographs and size distribution histograms of Ni nanoparticles synthesized with varying metal salt to polymer ratio. Clearly increasing the ratio yields larger particles in the polymer matrix. Interestingly, for all metal salt to polymer ratios investigated in this study, unaggregated and uniform nanoparticles were generated at a reaction temperature of 600 °C. The trends of the average diameter and the areal number concentration of Ni nanoparticles as a function of metal salt to polymer ratio are presented in **Figure 3.8**. The areal concentration increases initially with metal salt to polymer ratio ($0 < \text{ratio} < 0.5$), but at higher loadings ($0.5 < \text{ratio} < 1$) nanoparticle concentration in the polymer matrix is observed to decrease.

The most noticeable effects I observed from the metal salt loading are the consistent formation of unaggregated relatively monodisperse particles and the change in areal concentration. First, the formation of unaggregated, relatively monodisperse particles suggests that intra-droplet coagulation is slow for the given residence time of ~1s. A more detailed discussion of the mechanism and particle distribution will occur later in this paper. Second, as seen in Figure 3.8 the size scales with precursor concentration ($0 < \text{ratio} < 0.5$). This suggests that after the nucleation burst, metal atom diffusion and surface growth dominate. Third, the concentration peaks at a mass loading ratio of 0.5 and decreases shown in Figure 3.8. This suggests that highly concentrated nuclei are formed to enable coagulation and coalescence to take place at the early state of nanoparticle formation. However, coagulation and/or coalescence cannot be a dominant growth mechanism at the late stage of nanoparticle formation. Otherwise, monodisperse nanoparticles should not be observed as shown in Figure 3.7(h).

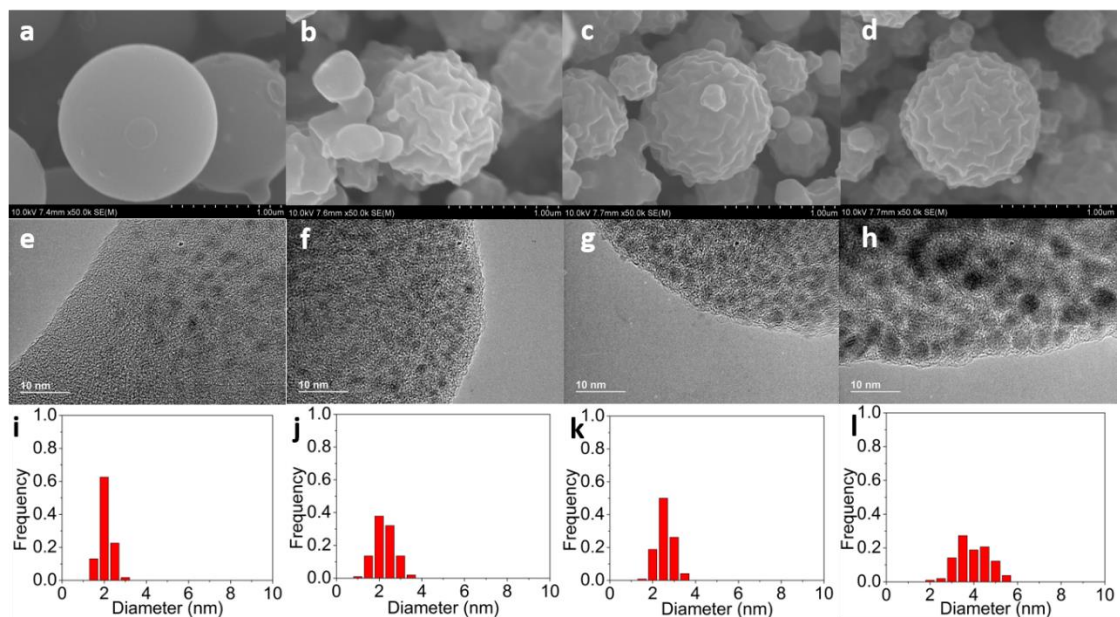


Figure 3.7. SEM and TEM images of metal polymer nanocomposites with different metal salt to PVP ratio. (a)(e)(i) 0.1 (b)(f)(j) 0.3, (c)(g)(k) 0.5, (d)(h)(l) 1.0

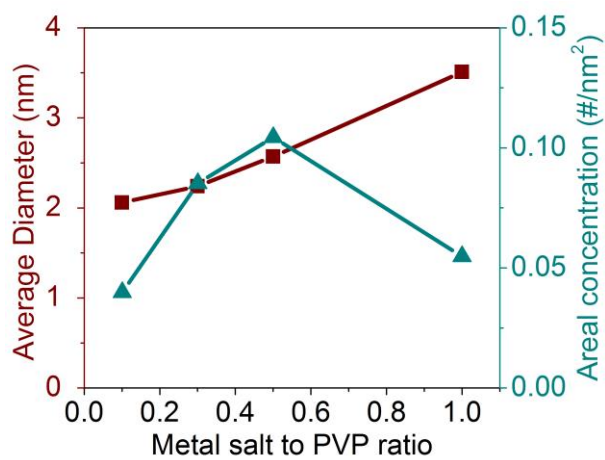


Figure 3.8. Average diameter and areal concentration of Ni nanoparticles as a function of metal salt to polymer ratio

3.3.4. Dynamics of nanoparticle growth in a polymer melt. The nucleation and growth mechanism of nanoparticles in small molecule solvents has been extensively studied for the past two decades.^{14, 39} However, only a few studies have focused on the formation mechanism of nanoparticles in a polymer melt.¹¹⁵⁻¹¹⁶ The aforementioned

experimental results in this study show that number concentration of metal nanoparticles decreases with increasing reaction temperature or metal salt to PVP ratio ($0.5 < \text{ratio} < 1$). This result suggests that pure surface growth (simple monomer attachment) might not be the only factor controlling the growth process. Two additional pathways for growth include Ostwald ripening and coagulation, both of which can lead to a decrease in concentration. The diffusivity of the nanoparticles in polymer melt can be estimated by the Stokes-Einstein equation:¹¹⁷

$$D = \frac{k_B T}{3\pi\eta d_p} \quad (3.2)$$

Where k_B is the Boltzmann constant, T is the absolute temperature, d_p is the particle's diameter, and η is the viscosity of the polymer.¹¹⁸ Experimental viscosity of PVP 8k with a temperature range from 140 °C to 185 °C has previously been measured.¹¹⁹ The viscosity at the high temperature region (up to 800 °C) was predicted by fitting and extrapolating the aforementioned experimental data¹¹⁹ using the Masuko and Magill model¹²⁰, which is shown in **Figure 3.17**. **Figure 3.18** shows the calculated diffusion coefficient of Ni nanoparticles as a function of diameter in the polymer melt at 600 °C.

In order to understand the dynamic behavior of nanoparticles in the polymer melt, the characteristic coagulation and coalescence times were estimated, and compared to the residence time of the aerosol droplets. The characteristic coagulation time is defined as the time required for the nanoparticles with an initial concentration of N_0 to achieve half of the initial concentration. The continuum Brownian coagulation coefficient is given in Eqn. 3.3:⁴⁰

$$K_{12} = 2\pi(D_1 + D_2)(d_{p1} + d_{p2}) \quad (3.3)$$

Where D_1, D_2 are diffusion coefficients for nanoparticles with a diameter of d_{p1} and d_{p2} , respectively. For nanoparticles with a narrow size distribution, such as what I observe, Eqn. 3.3 becomes:

$$K = 8\pi D d_p = \frac{8k_B T}{3\eta} \quad (3.4)$$

Where D is the diffusivity of the nanoparticles shown in Eqn. 3.2. Eqn. 3.4 indicates that the coagulation coefficient K is independent of the diameter for the monodispersed nanoparticles.

The characteristic coagulation time can then be written as:⁴⁰

$$\tau_c = \frac{2}{KN_0} \quad (3.5)$$

Where N_0 is the number concentration of nanoparticles in a polymer droplet. For samples with a constant metal salt to polymer ratio (0.3 is used for calculation), $N_0 \propto 1/d_p^3$ (d_p is the diameter of the Ni nanoparticles) based on the mass conservation of the nickel component in the polymer droplet.

The characteristic coalescence time for Ni nanoparticles was also estimated. The characteristic coalescence time is the time required for two contacted primary particles to rearrange and form a single spherical particle. The coalescence of Ni nanoparticles is sensitive to the phase (molten or solid) of the nanoparticles. Our calculation shows that a nanoparticle with a diameter of less than 1.5 nm is in liquid phase at the temperature of 600 °C. (see **Figure 3.19**) The characteristic coalescence time for Ni nanoparticles were computed based on the phase of Ni nanoparticles. When the size of nanoparticles was less than 1.5nm, the nanoparticles were in liquid phase. In this case, a viscous flow mechanism as shown in Eqn. 3.6 was used to calculate the coalescence time:⁴¹

$$\tau_l = \frac{\mu d_{eff}}{2\sigma_l} \quad (3.6)$$

Where μ is the viscosity of Ni nanoparticle, σ_l is the surface tension of Ni nanoparticle in liquid state; d_{eff} is the effective diameter of the coalescing particle pair, which is $6V_p/a_p$, V_p and a_p are volume and surface area of the coalescing particle pair, respectively. The data of all the properties mentioned here can be found in the supplemental.

If Ni nanoparticles are in the solid phase, the coalescence time for Ni nanoparticles can be described with the following equation:⁴²

$$\tau_s = \frac{3k_B T_p N}{64\pi\sigma_s D_{eff}} \quad (3.7)$$

Where T_p is the temperature of a particle pair undergoing coalescence, N is the number of atoms in the particle pair, σ_s is the surface tension of solid Ni nanoparticle D_{eff} is the effective atomic diffusion coefficient in the particle pair. The property data is given in the supplemental.

Figure 3.9 shows the characteristic coalescence, coagulation and residence time as a function of diameter. Interestingly, for nanoparticles with a diameter less than 1.5 nm, both the coagulation and coalescence times are less than the residence time, which suggests that both coagulation and coalescence should be occurring during the early stages of growth. This result is consistent with the previous discussion that coagulation of nuclei occurs at the early stage of nanoparticle formation at 600 °C, leading to the decrease of the areal concentration of Ni nanoparticles (see Figure 3.8). However, solidification of Ni as seen by the rapid jump in coalescence time above that of the residence time, implies that any coagulation event would lead to an aggregate. For the smaller particles, where the coagulation time is shorter than the residence time I might see aggregates, but our

observations show unaggregated particles. Despite the many approximations in these calculations, these results suggest that nanoparticles are not moving as independent entities in the polymer or else they would be forming agglomerates. It is more likely that as the nanoparticle moves, it carries with it a polymer layer, which retards its diffusion rate.¹²¹

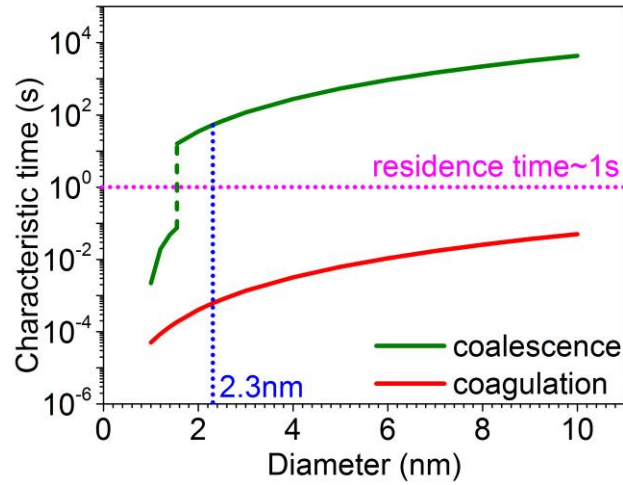


Figure 3.9. Characteristic sintering and coagulation time as a function of Ni nanoparticle diameter at 600 °C. The green dash line represents the transition of the melting point of Ni nanoparticles.

Experimental particle size distributions (PSD) are often used to deduce growth mechanisms.¹²²⁻¹²⁴ It is well known that the PSD for Brownian coagulation will approach an asymptotic (self-preserving) form regardless of the initial size distribution¹²⁵. This self-preserving PSD can be approximated by a lognormal distribution function with a geometric standard deviation of 1.44 for continuum regime.¹²⁶⁻¹²⁷ The self-preserving PSD is written as:

$$\frac{n(v)v}{N_{\infty}} = \frac{1}{3\sqrt{2\pi}\ln\sigma_g} \exp\left(\frac{-(\ln^2(v/v_g))}{18\ln^2\sigma_g}\right) \quad (3.8)$$

Where v is the particle volume, $n(v)$ is the number concentration, N_{∞} is the total number of particles, $v_g = \frac{1}{6}\pi d_g^3$ is the geometric number mean particle volume, d_g is the

geometric number mean particle diameter, σ_g is the geometric standard deviation of self-preserving PSD, 1.44. The scaled self-preserving PSD is plotted against the normalized particle diameter instead of normalized particle volume, v/v_g , which is shown in **Figure 3.10**.

On the other hand, if the growth of the ensemble is dominated by Ostwald ripening, the PSD is often approximated with the Lifshitz-slyozov-Wagner (LSW) model ¹²⁸. An analytical expression of the PSD in the asymptote is given as:^{122, 129}

$$f(\varphi) = A\varphi^2 \left(\frac{3}{3+\varphi}\right)^{7/3} \left(\frac{1.5}{1.5-\varphi}\right)^{11/3} \exp\left(\frac{-\varphi}{1.5-\varphi}\right) \quad (3.9)$$

Where φ is the ratio of the particle diameter to the average diameter and A is a function of time. There is a cut-off at $\varphi = 1.5$, above which $f(\varphi)$ becomes 0. Normalizing $f(\varphi)$ by the integral yields the famous PSD predicted by LSW model. The term A does not affect the shape of normalized $f(\varphi)$.

The experimental PSD of Ni nanoparticle generated with different reaction temperature and various metal salt to PVP ratio are shown in the Figure 3.10. The self-preserving PSD for Brownian coagulation and particle size distribution predicted by LSW model are also shown in Figure 3.10. Clearly the self-preserving model provides a poor representation of the experimental PSD. The peaks of all experimentally measured PSD are much narrower than that of the log-normally self-preserving PSD. Even though some coagulation was observed for the samples treated at 800 °C and the corresponding PSD became a little bit broader, its PSD still does not reach the self-preserving PSD by coagulation. As shown in **Table 3.2**, the geometric standard deviations for all cases are smaller than 1.44. the self-reserving limit. The poor representation by self-preserving coagulation model indicates that the coagulation is not a dominate growth mechanism. This

result is consistent with our prior discussion that the polymer layer on the surface of the nanoparticles might hinder the coagulation between nanoparticles. On the other hand, the experimental PSDs are also compared with the PSD predicted by LSW model. The size distribution predicted by Ostwald ripening is also not a good representation as the peak shapes are not correct. The experimental distributions are more symmetrical, while the LSW, far more skewed to larger sizes. I may conclude that after an initial nucleation burst, growth is predominately by surface addition of monomer, and that coagulation only takes place at the highest temperatures and loadings explored.

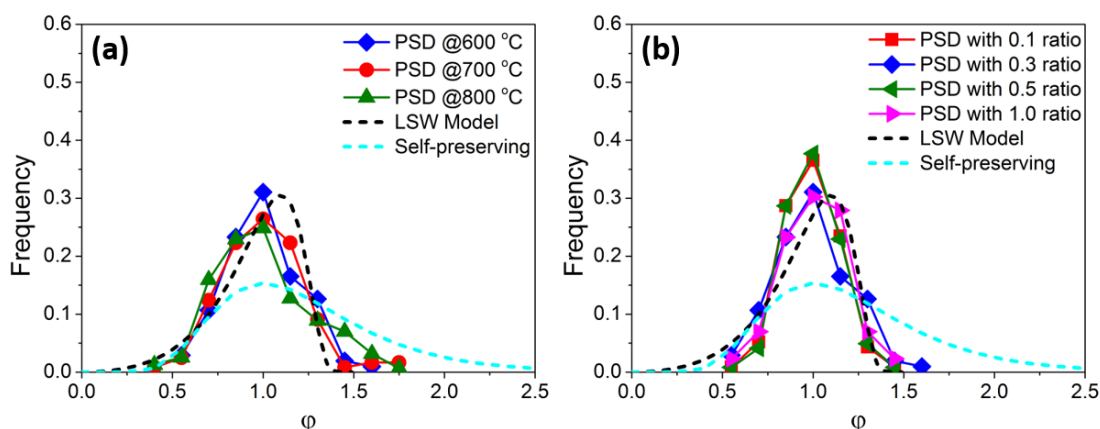


Figure 3.10. Scaled nanoparticle size distribution measured for three different reaction temperatures with a fixed metal salt to PVP ratio of 0.3 (a) and for four different metal salt to PVP ratios with a fixed reaction temperature of 600 °C (b). The dashed light blue line is the size distribution obtained for log-normally self-preserving size, and the dashed black line is the LSW size distribution.

Table 3.2. Geometric Standard deviations σ_g , for Ni nanoparticles generated at different conditions.

Metal salt to PVP ratio	σ_g	Reaction temperature	σ_g
0.1	1.18	600 °C	1.18
0.3	1.23	700 °C	1.26
0.5	1.16	800 °C	1.31
1.0	1.22	Self-preserving PSD	1.44

I schematically represent our best understanding of the experimental results in

Figure 3.11. Initially, Metal ions dispersed in polymer particle (Phase I) are rapidly

reduced to metal atoms by hydrogen at the elevated temperature of 600 °C. This process is rapid compared to the residence time of 1s. Studies have shown that diffusivity of gaseous molecules in a polymer matrix at elevated temperature is in the order of $10^{-4} \text{ cm}^2/\text{s}$ ¹¹³, thus one should not be limited by the diffusion rate of H₂ molecules. I estimate a diffusion time for a 1 μm polymer droplet to be < 5 μs. It has been found that the reduction of nickel oxides with a diameter of 10-20 μm by hydrogen is a first order reaction with a rate constant of 0.1 s⁻¹ at 600 °C. Therefore, the time for the half conversion of nickel oxides is in the order of 1s.¹³⁰ But this assumes that I first produce the oxide, which is a worst case scenario. Assuming the metal atoms were uniformly dispersed in polymer melt medium, homogenous nucleation will create a large number of small cluster nuclei. Initial coagulation between nuclei may occur, but the primary growth mechanism appears to be, based on the morphological evidence, surface addition of metal to existing nuclei. Isolated metal particles occur at temperatures sufficient to generate metal from the precursor, but not so high as to enable particles to have sufficient diffusion rates to coagulate to form aggregates (see at higher temperatures), given that the coalescence time is relatively long. It is likely that the polymer melt, retards coagulation growth beyond Brownian motion by an add-layer of polymer.

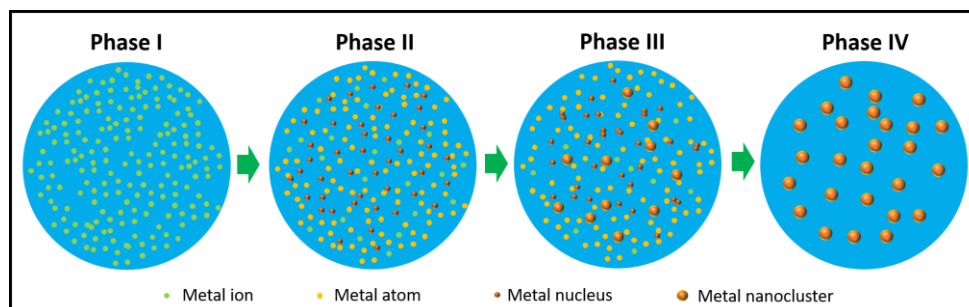


Figure 3.11. Schematic of the nucleation and growth of metal nanoparticles in polymer melt at 600 °C.

3.4. Conclusions

I demonstrate an aerosol single-drop reactor approach to grow and stabilize metal nanoclusters in a polymer matrix. The rapid thermal pulse given to the aerosol particles enables the formation of nuclei and growth, with subsequent rapid quenching to freeze in the structure. The size of metal nanoclusters can be controlled by adjusting the mass loading ratio of metal salt to polymer matrix, and the temperature of the tubular reactor. Based on the experimental observation and quantitative analysis, it is concluded that the growth is governed by nucleation and surface growth with little coagulation or Ostwald ripening. Finally, this aerosol route is amenable to scale-up for large scale production of nanoclusters that can either be used as is within the polymer or released by solvent extraction, depending on the application.

3.5. Supporting Information

Stability of PVP molecules against heat treatment. Component analysis of metal polymer nanocomposites. Scanning TEM, EDS mapping and line scanning characterization for Ni-PVP-8k nanocomposite. Property data used for the characteristic time analysis.

3.5.1. Stability of PVP molecules against heat treatment

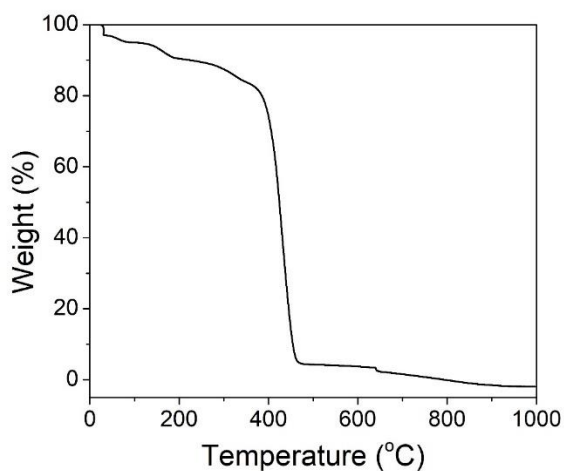


Figure 3.12. TGA of PVP polymer (MW. 8000g/mol) with a heating rate of 10C/min in Ar gas

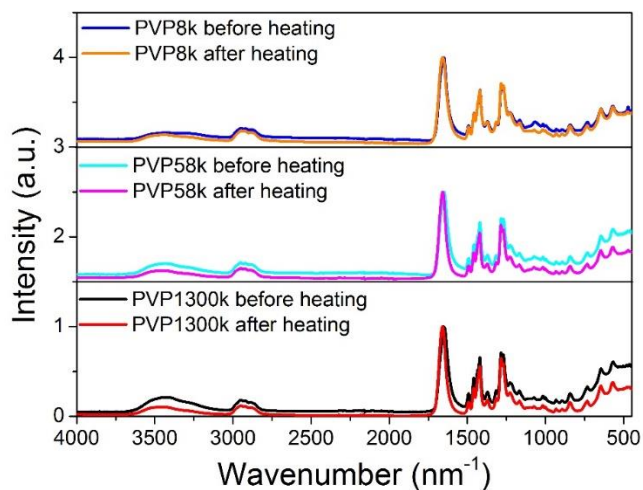


Figure 3.13. FTIR spectra of PVP polymers with different molecular weights before and after spray pyrolysis at 600 °C with 5% H₂ and 95%N₂ as carrier gas

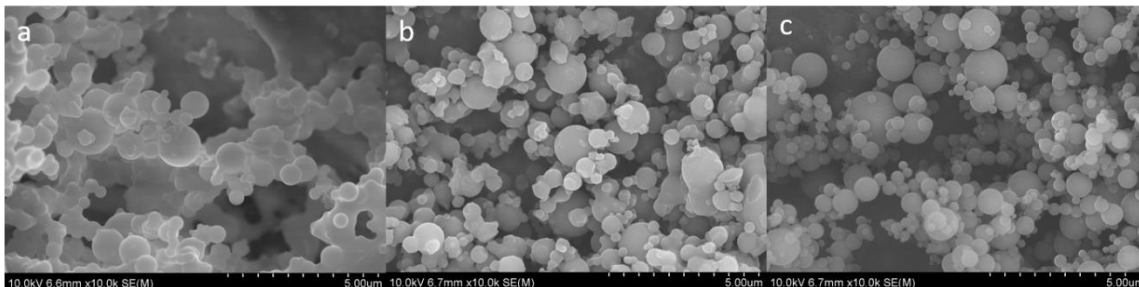


Figure 3.14. SEM images of PVP polymers with different molecular weights after spray pyrolysis: (a) 8000g/mol; (b) 58000g/mol; (c) 1300000g/mol

3.5.2. Component analysis of metal polymer nanocomposites

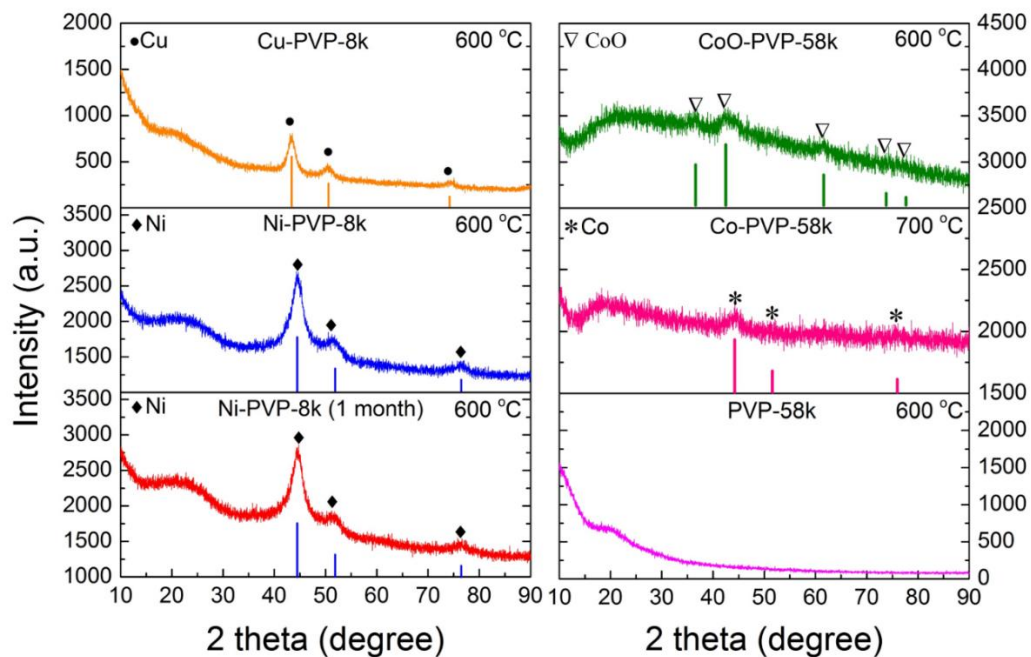


Figure 3.15. XRD Patterns of metal (Ni, Co, Cu) polymer nanocomposites

Table 3.3. Volume fraction of metal, areal concentration and average diameter of metal in polymer.

Nanocomposites	Mass fraction between metal and PVP matrix	Volume fraction of metal in PVP matrix	Areal concentration (#/nm ²)	Number average diameter (nm)
Ni PVP8k	16.8%	2.7%	0.052	3.5
Co PVP58k	16.8%	2.7%	0.046	3.9
Cu PVP8k	7.9%	1.0%	0.021	4.1

3.5.3. Scanning TEM, EDS mapping and line scanning characterization for Ni-PVP-8k nanocomposite.

STEM images shown in Figure 3.16 (a-c) indicates that ultrasmall Ni nanoparticles are uniformly distributed in the polymer matrix. The line scanning profile shown in Figure 3.16 (d) reveals these Ni nanoclusters has a diameter of ~5nm. EDS mappings in Figure 3.16(e-f) provide elemental distributions of Ni, C, O, and N elements, respectively. C, O and N belong to the PVP matrix. The weaker signal intensities of O and N elements compared to C elements is due to the lower molar ratio between O/N and C (1:6) in PVP molecules.

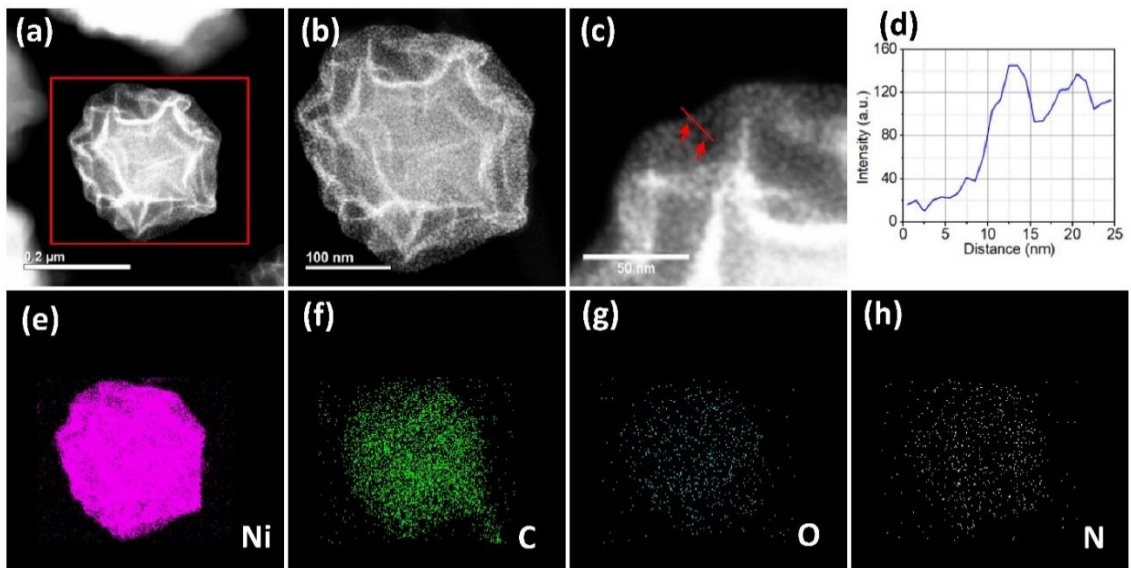


Figure 3.16. (a-c) STEM images of Ni PVP8k nanocomposite prepared at 600 °C from a precursor with a 1 to 1 metal salt to polymer ratio; (d) Line scanning profile of two nickel nanoparticles labeled with two red arrows in image (c); (e-f) EDS mapping of Ni, C, O and N elements, respectively.

3.5.4. Property data used for the characteristic time analysis

Viscosity of polymer melt:

Masuko and Magill model is

$$\log\left(\frac{\eta}{\eta_g}\right) = A \left[\exp\left(\frac{B(T_g - T)}{T}\right) - 1 \right] \quad (3.7)$$

They have shown that A and B are constants which are independent of materials. The average values for A and B in this model are

$$A = 15.29 \pm 1.04$$

$$B = 6.47 \pm 1.13$$

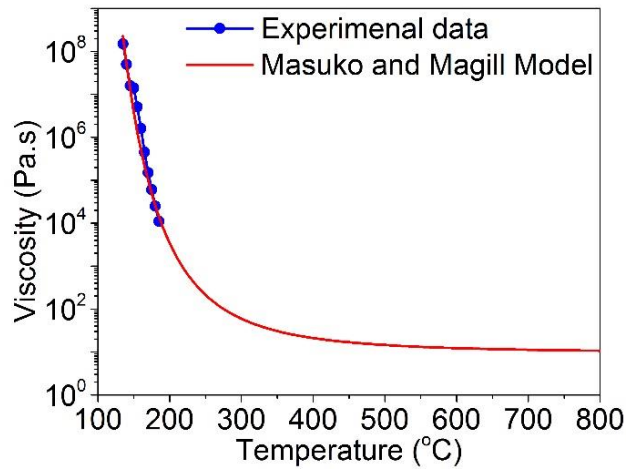


Figure 3.17. Viscosity of PVP polymer (MW. 8000g/mol) as a function of temperature. (Values of empirical constant A and B are 6.7 and 7.6 respectively in order to achieve a good fit.)

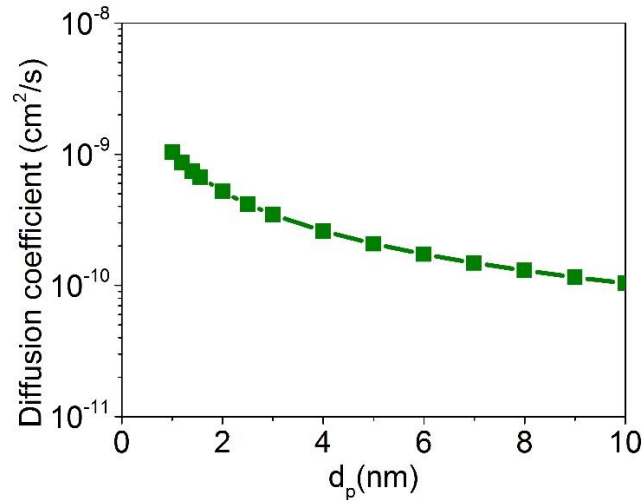


Figure 3.18. Diffusion coefficient of Ni nanoclusters as a function of diameter in polymer melt at 600 °C

Melting point of Ni nanoparticle, $T_{mp}(d_p)$

The melting point of Ni nanoparticles is size-dependent, which was approximated using the following empirical equation¹³¹:

$$T_{mp}(d_p) = T_m \left[1 - \frac{4}{L\rho_p d_p} (\sigma_s - \sigma_l \left(\frac{\rho_p}{\rho_l}\right)^{\frac{2}{3}}) \right] \quad (3.8)$$

Here, T_m is the bulk melting point (1728 K), L is the latent heat of melting (297000 J/kg), σ_s and σ_l are the surface tension (J/m²), $\sigma_s = 2.47$ N/m, $\sigma_l = 1.8$ N/m (surface tension of molten metals at their melting points¹³²), ρ_p and ρ_l are the respective solid and liquid phase densities (kg/m³), $\rho_p = 8900$ kg/m³ (assume it is temperature independent), $\rho_l = 7800$ kg/m³ (data obtained from¹³³, assume it is temperature independent.) Figure 3.19 shows how the melting point of Ni nanoparticle changes with its diameter. Our calculation in Figure 3.19 shows that the nanoparticle with a diameter of less than 1.5 nm is in liquid phase at the temperature of 600 °C.

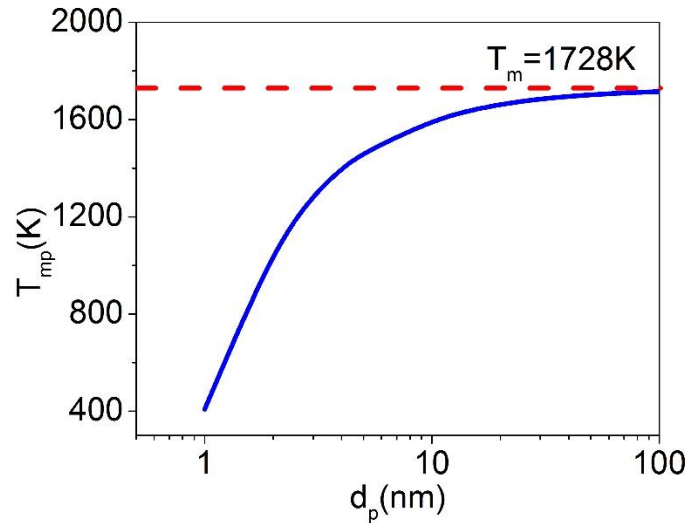


Figure 3.19. Variation of melting point as a function of Ni nanoparticle diameter.

Viscosity of Ni nanoparticle, μ

μ is the viscosity of Ni nanoparticle, which is given as⁴¹:

$$\mu = 1.8 \times 10^{-7} \frac{[M \cdot T_{mp}(d_p)]^{1/2} \exp\left(\frac{L}{RT_p}\right)}{v_m \exp\left[\frac{L}{RT_{mp}(d_p)}\right]} \quad (3.9)$$

Where L is the latent heat of melting (J/mol), 17200 J/mol (which is equal to 297000 J/kg), σ_l are the surface tension (J/m²), M is the molar weight, 5.87×10^{-3} kg/mol, R is the gas constant, 8.314 J/mol/K, v_m is the molar volume, 7.5×10^{-6} m³/mol.

Effective atomic diffusion coefficient, D_{eff}

Assuming volume diffusion is dominant, D_{eff} is predicted by the bulk self-diffusion coefficient of Ni, D_v , which is given by ¹³⁴:

$$D_v = 9.2 \times 10^{-5} \exp\left(-\frac{278 \text{ kJ/mol}}{RT}\right) \text{ m}^2 \text{ s}^{-1} \quad (3.10)$$

D_v is equal to $D_v = 2.1 \times 10^{-21}$ m²s⁻¹ at a temperature of 600 °C.

Chapter 4: Thermal Shock Synthesis of Metal Nanoclusters within On-the-fly Graphene Particles[†]

Abstract: Metal nanoclusters (1-10 nm) have drawn great attention due to their potential applications including energy storage, catalysis, nanomedicine and electronic devices. However, manufacturing ultra-small metal nanoparticles at high concentrations in an unaggregated state is not a solved problem. Here I report an aerosol-based thermal shock technique for in situ synthesis of well-dispersed metal nanoclusters in on-the-fly graphene aerosols. A rapid thermal shock to the graphene aerosol has been used to nucleate and grow the metal nanoclusters with subsequent quenching to freeze the newly formed nanoclusters in the graphene aerosol matrix. A characteristic time analysis comparison with experiment shows that the nanocluster formation is governed by nucleation and subsequent surface growth, and that the graphene retards coagulation, enabling unaggregated metal nanoclusters. The method is generic and it is shown the formation of sub-10 nm Ni, Co and Sn nanoclusters. This continuous aerosol-based thermal shock technique offers considerable potential for the scalable synthesis of well-dispersed and uniform metal nanoclusters stabilized within a host matrix. As an example of potential application I demonstrate very favorable catalytic properties.

[†] The results represent in this chapter have been previously published and are reprinted from: Yong Yang, Pankaj Ghildiyal, Michael R Zachariah; Thermal Shock Synthesis of Metal Nanoclusters within On-the-Fly Graphene Particles. *Langmuir* 2019, 35 (9), 3413-3420

4.1. Introduction

Metal nanoclusters (1-10 nm) with unique size- and shape-dependent properties have drawn attention due to their potential applications in electronics, catalysis, nanomedicine, and energy storage.^{6, 52, 54-55, 135-136} Technological utility of metal nanoclusters is hindered however by the difficulties of synthesizing and handling these ultra-small particles arising from their unstable and easy-aggregation nature. Although various kinds of synthesis approaches have been reported¹³⁵, manufacturing those small particles in large quantities to enable their utility is still challenging. Developing a fast, low-cost and scalable manufacturing technique for large scale production of metal nanoclusters is urgently required in order to achieve their industrial applications.

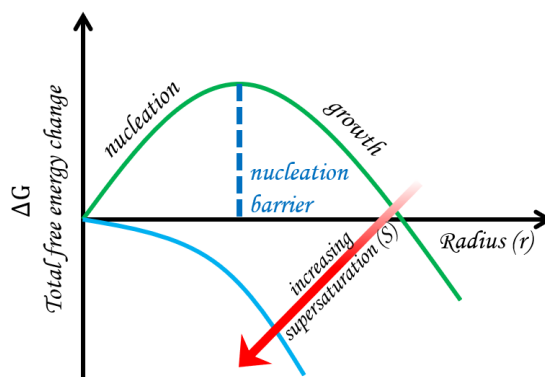


Figure 4.1. Gibbs free energy change as a function of particle radius

In order to synthesize smaller nanoclusters with a higher number concentration, one needs to promote the nucleation rate of nanoclusters and inhibit their subsequent growth. From a thermodynamic standpoint, the nucleation rate can be greatly enhanced by decreasing the nucleation energy barrier arising from the formation of the interface between the nuclei and the reaction solution.^{14, 39, 76} As shown in **Figure 4.1**, one way to minimize the nucleation barrier of forming a stable nucleus is to build a high

supersaturation ratio (S) of metal atoms in the reaction volume. This can be achieved by applying a fast heat pulse to decompose the metal precursor rapidly to create a highly supersaturated state leading to a very fast nucleation burst. Once small nuclei form, a fast cooling can be applied to quench these small nuclei from further growth. Although high temperature can hasten kinetics, it also speeds up transport, leading to the coagulation and sintering. In order to prevent nanoclusters from coagulation and sintering, a matrix should be used to anchor and stabilize these small nanoclusters.¹³⁷ Recently, Yao et al. demonstrated a thermal shock technique to generate metal nanoclusters and nanoalloys decorated on carbon nanofiber thin films.^{36, 61} The rapid heating and fast nanocluster formation were achieved by electrically Joule heating the conductive carbon matrix. However, the Joule heating assisted thermal shock technique is limited to electrically conductive matrices and is not amenable to bulk production of nanoclusters.

In the current work, I adapt the thermal shock technique by aerosolizing the metal precursor and graphene matrix and applying an extremely short thermal shock on aerosol particles to trigger the formation of nanoclusters within the aerosol. I employ graphene as the aerosol matrix within which nucleation and quenching can be implemented. In this work I demonstrate the formation of sub-10 nm nickel (Ni), cobalt (Co), and tin (Sn) nanoclusters in the reduced graphene oxide (rGO) matrix. I have also investigated the effect of reaction temperature and metal salt loading on the formation of the nanoclusters in the graphene aerosols. A characteristic time analysis leads to the conclusion that nanocluster formation is governed by nucleation and subsequent surface growth. Finally, I note that this one-step continuous aerosol-based thermal shock technique offers considerable

potential for the manufacturing processing of well-dispersed and uniform nanoclusters stabilized within a host matrix.

4.2. Experimental Section

4.1.1. Materials

Nickel nitrate hexahydrate ($\text{Ni}(\text{NO}_3)_2 \cdot 6\text{H}_2\text{O}$, $\geq 99\%$ pure), cobalt nitrate hexahydrate ($\text{Co}(\text{NO}_3)_2 \cdot 6\text{H}_2\text{O}$, $\geq 98\%$ pure), tin chloride (SnCl_2) 4-nitrophenol ($\geq 99\%$ pure), sodium borohydride (NaBH_4 , 99%) were all purchased from Sigma-Aldrich. All the chemicals were used as received.

4.2.2. Synthesis of graphene oxide (GO)

GO was prepared using a modified version of the Hummer's method.⁸⁴ The detailed procedure is as follows: First, 1.5 g of graphite was placed in a 1000 mL Erlenmeyer Flask, to which 180 mL sulfuric acid and 20 mL phosphoric acid were added. The resulting suspension was placed in the water bath at 50°C , and 9 g potassium permanganate was gradually added into the suspension. After continuously stirring for 12 hours, the mixture was poured into 300 mL cold distilled water and 3 mL hydrogen peroxide (30%) was slowly added into the mixture while stirring, which made the color of the suspension turn from dark brown to yellow. The suspension was filtered and washed with diluted aqueous hydrogen chloride solution (300 mL, HCl: 10%) and subsequently distilled water (300 mL). The resulting solid was re-dispersed into 300 mL distilled water, stirred overnight and sonicated for 10 min so that the solid was exfoliated to GO sheets. Finally, the graphene oxide dispersion was purified by dialysis for around one week to remove the remaining metal ions and the acid.

4.2.3. Precursor Preparation

The precursor solutions were prepared by adding 20 mL of the GO solution (6.5 mg/mL) and the required amount of metal salt into 84 mL of deionized water. The metal

salts used to obtain Ni, Co, and Sn nanoclusters were $\text{Ni}(\text{NO}_3)_2 \cdot 6\text{H}_2\text{O}$, $\text{Co}(\text{NO}_3)_2 \cdot 6\text{H}_2\text{O}$, and SnCl_2 . For the SnCl_2 GO precursor solution, dimethylformamide (DMF) was used as a solvent to dissolve SnCl_2 . The mass of the metal salt used was varied between 130 to 520 mg to prepare solutions with different metal salt to graphene oxide mass ratios (1.0, 2.0, and 4.0).

4.2.4. Aerosol-based Thermal shock Technique

Aerosol-based thermal shock technique was used to generate metal nanoclusters stabilized in the graphene matrix. The experiment consists of a collision-type atomizer, a silica gel diffusion dryer, a heating element, and a membrane filter collector. In a typical experiment, the precursor solution containing metal salt and graphene oxide is continuously nebulized into small aerosol droplets by the atomizer. The mixture gas of hydrogen and nitrogen then carries these droplets to pass through the diffusion dryer and the heating element. The solvent evaporates from the droplets as they pass through the diffusion dryer, producing a dry aerosol. The dry aerosol passes to a heating furnace with a nominal residence time in the high temperature region of ~ 300 ms where the thermal shock ($\sim 10^3$ K/s) induced decomposition and reduction in hydrogen leads to the nucleation and growth of zero valent metal nanoclusters within a graphene matrix. Particles are captured on a filter resulting in a quenching rate of approximately 10^3 K/s.

4.2.5. Catalytic Reaction Evaluation

Ni and Co nanoclusters decorated in graphene aerosols were chosen to demonstrate catalytic performance towards reduction of 4-nitrophenol by sodium borohydride. A volume of 20 mL 4-nitrophenol solution with a concentration of 0.1 mM was mixed with 5 mL of 0.2M sodium borohydride. The catalytic reaction was triggered with the addition

of 5 ml of metal-rGO suspension containing 0.80 mg metal-rGO catalyst. The solution was continuously stirred and the reaction was allowed to proceed at room temperature. Immediately after catalyst addition, 300 μ L of the reaction solution was collected and diluted to 3 mL using D.I. water for time-resolved absorbance spectra measurement using a Perkin Elmer (Lambda 1050) UV-Vis spectrophotometer.

4.2.6. Characterization

Morphologies and microstructures of metal-rGO nanocomposites were examined by transmission electron microscopy (JEOL JEM 2100 FEG) and scanning electron microscopy (Hitachi SU-70). Elemental distribution analysis in the aerosol particle was carried out with Energy-dispersive X-ray spectroscopy (EDS) in the TEM. The mean diameters and size distributions of the nanoclusters were determined by statistical analysis of the acquired TEM images, using Nano Measurer 1.2 image analysis software. Phase and component identification was done by X-ray diffractometer (Bruker D8 diffractometer with Cu Ka radiation). Thermogravimetric analysis (TGA) of metal-rGO nanocomposites was carried out using a thermogravimetric analyzer (TA Instruments, USA) with a heating rate of 5 $^{\circ}$ C/min in air atmosphere. The absorbance spectra measurement was recorded using a Perkin Elmer (Lambda 1050) UV-Vis spectrophotometer equipped with a 4.5 mL quartz cuvette with a path length of 1 cm.

4.3. Results and Discussion

4.3.1. Thermodynamic and Kinetic Considerations

Here, I first consider if a fast heating pulse (~ 1 s) is able to decompose metal precursor rapidly to create a high supersaturation ratio of metal atoms for a very fast nucleation burst and nanoparticle formation. Assuming the Gibbs Free energy droplet model can describe the thermodynamics of nanoparticle formation¹⁴, the critical radius can be evaluated as:

$$r_c = \frac{2\sigma V_m}{RT \ln S} \quad (4.1)$$

where σ is the surface tension of the nanoparticles; V_m is the molar volume of bulk and S is the saturation ratio.

Figure 4.2a shows that increasing the saturation ratio S decreases the critical radius of the nanoparticles at a constant temperature, assuming the surface tension is a size-independent parameter. I observe that as the saturation ratio reaches an order of $\sim 10^7$, the critical radius approaches the radius of a nickel atom, ~ 0.2 nm. In this scenario, each metal atom might become a stable nucleus if a sufficiently high saturation ratio is created. Therefore, it is critically important to generate a higher saturation ratio ($>10^7$) in a short time to enable formation of smaller nuclei with a higher number concentration.

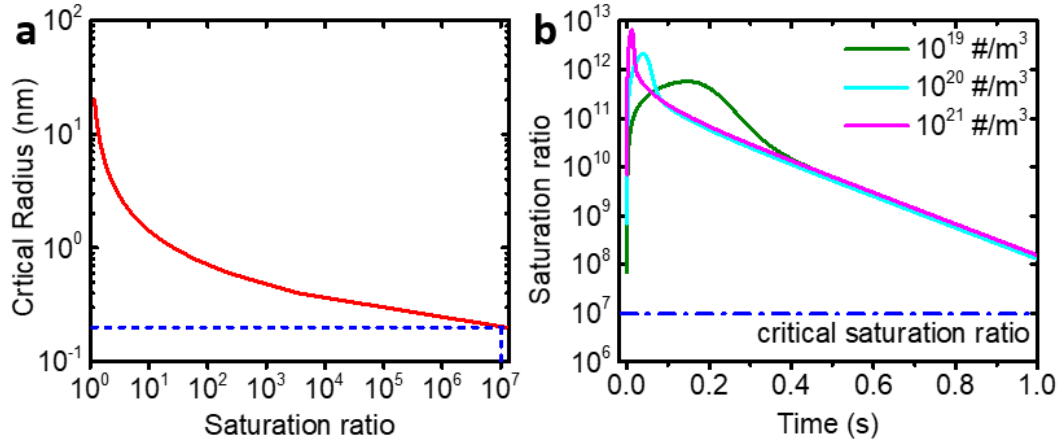


Figure 4.2. a) Nucleus critical radius as a function of metal atom saturation ratio; b) time resolved saturation ratio with different initial concentrations of metal ion loadings (10^{19} , 10^{20} , and 10^{21} #/m³).

In order to estimate if such high saturation ratios are achievable kinetically in the experiment, I calculate the saturation ratio change of the monomer in a confined reaction volume of the aerosol particle with 1 s heating pulse at 600 °C, ignoring the heating and quenching processes. This thermal shock is assumed to trigger metal salt reduction into monomer metal atoms and nucleation of the nanoclusters, accelerated by the high saturation ratio built during the thermal shock. The temporal change in saturation ratio is affected by four processes: (a) generation of monomer from the hydrogen reduction of metal ions, (b) consumption of monomer due to nuclei formation, (c) evaporation of monomer atoms from the surface of the stable nuclei, and (d) the consumption of monomer due to monomer condensation onto the surface of the existing nuclei, which is described by the following equation, derived from a moment model formulation of nucleation and surface growth ⁴⁰:

$$\frac{dS}{dt} = \frac{R_H}{n_s} - \frac{Jk^*}{n_s} - (S - 1) \frac{B_1 A}{2v_1 n_s} \quad (4.2)$$

Here, R_H is the reaction rate of metal salt precursor to zero-valent metal atoms; A is the total surface area of all the nuclei in the reaction volume; both R_H and A are time-dependent variables; k^* is the number of monomers in a single particle with a critical radius r_c ; n_s is the monomer concentration at saturation condition; $B_1 = 2n_1v_1\left(\frac{kT}{2\pi m_1}\right)^{1/2}$ where n_1 is the monomer number concentration; v_1 and m_1 is volume and mass of the monomer, respectively; J is the rate of particle formation by homogenous nucleation, which is given as follows ⁴⁰:

$$J = \frac{Kn_1s_1}{3} \sqrt{\frac{\theta}{\pi}} \exp\left(-\frac{4}{27} \frac{\theta^3}{(\ln S)^2}\right) \quad (4.3)$$

Where $K = n_1\left(\frac{kT}{2\pi m_1}\right)^{1/2}$; θ is dimensionless surface tension of the stable nuclei $\theta = \frac{s_1\sigma}{kT}$; s_1 is the surface area of a monomer. The values for all the property parameters (**Table 4.2**) and the details of the calculation can be found in the Supporting Information.

Figure 4.2c shows the variation in saturation ratio with the duration of thermal shock for three different initial number concentrations of the metal salt precursors loaded into the reaction volume. One can see that for all three metal salt loadings (10^{19} , 10^{20} , and 10^{21} #/m³), the 1s thermal shock of 600 °C is sufficient to create a supersaturated state ($S > 10^7$) of metal atoms in a short time, which leads to a nucleation burst and formation of smaller nuclei with a high number concentration. For the calculations I ignored the presence of the graphene matrix, which would be expected to further lower the nucleation barrier and thus promote nucleation.¹³⁸

4.3.2. Preparation of Metal Nanoclusters with the Aerosol-based Thermal Shock Technique

Figure 4.3a shows a schematic representation of the aerosol-based thermal shock method used to fabricate metal nanoclusters in the graphene aerosols. Ni nanoclusters were chosen as the model to investigate synthesis-structure relationship in the proposed method. The precursor solution was prepared by mixing nickel nitrate and GO sheets with a fixed mass ratio (1.0, 2.0, or 4.0) into D. I. water. After 10 min sonication, the precursor was transferred into a collision-type atomizer, which was used to nebulize the precursor into small aerosol droplets. The small aerosol droplets were carried by a mixture gas (5% H₂/95% N₂) through a silica gel diffusion dryer and a high-temperature heating zone. Figure 4.3a shows the temporal evolution of the aerosol particles containing nickel nitrate and graphene oxide sheets: the thermal shock in the high-temperature zone triggers thermal decomposition, reduction and subsequent nucleation and growth of nickel nanoclusters in the graphene aerosol nanoreactors. Unlike wet chemistry with a slow heating and cooling rate, the small mass of each graphene aerosol nanoreactor enables rapid heating ($\sim 10^3$ K/s) and-cooling rates ($\sim 10^3$ K/s), which triggers the formation of small metal nanoclusters and prevents further growth of the nanoclusters.²⁴ This thermal shock approach enables the chemistry in the aerosol nanoreactors to be bracketed to the approximate 1 s residence time, and is a significantly shorter reaction timescale as compared to traditional wet chemistry approaches.¹³⁹⁻¹⁴⁰

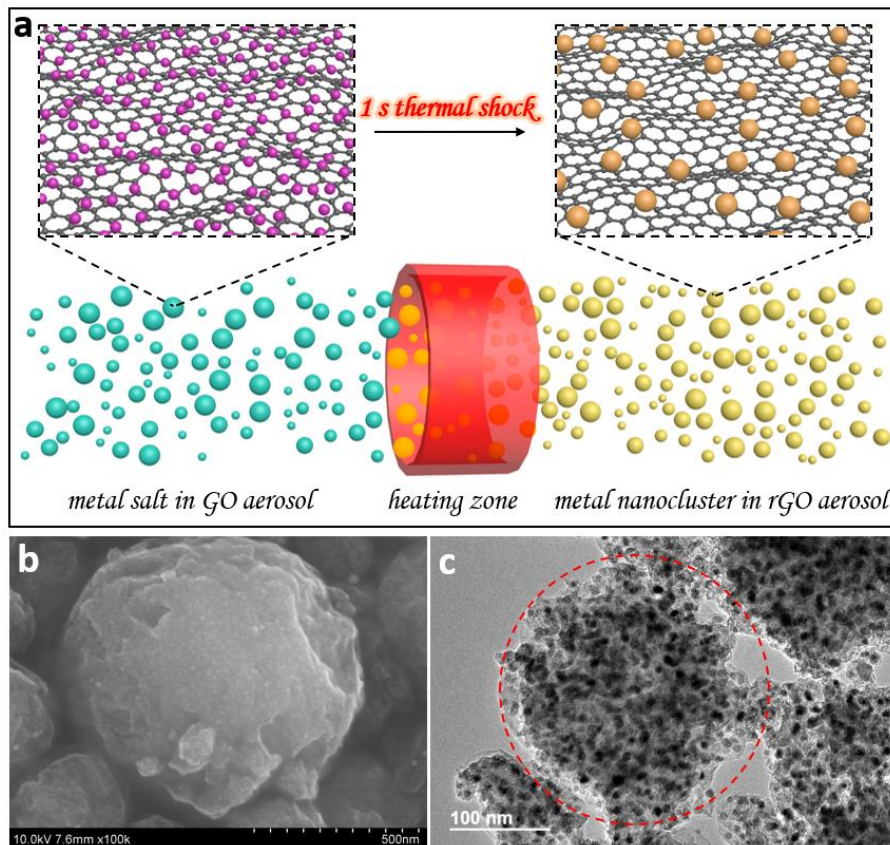


Figure 4.3. Synthesis of metal nanoclusters via aerosol-based thermal shock technique: a) a schematic representation of the in-situ growth of metal nanoclusters in the one-the-fly graphene aerosol nanoreactors; b) SEM image of a nickel nanoclusters incorporated graphene aerosol particle (reaction temperature: 600 °C; residence time: ~1 s); c) TEM image of Ni nanoclusters incorporated graphene aerosol particles; the structure with the red dash circle depicts one single aerosol particle.

Figure 4.3b,c shows the morphology of the resulting aerosol particles as observed by scanning electron microscopy (SEM) and transmission electron microscopy (TEM), respectively. The product shows a crumpled morphology. This crumpled surface was probably caused by the capillary compression during the solvent evaporation from the aerosol droplet.¹⁴¹⁻¹⁴² This observation is consistent with several other groups who have also observed that water evaporation from the aerosol droplets results in a crumbled surface in the final of aerosol products.³¹ As shown in Figure 4.3c, Ni nanoclusters with an average diameter of 6.7 nm were formed and uniformly distributed in the graphene matrix. The

formation of the metallic nickel was confirmed by XRD as shown in **Figure 4.9a**. I observe the complete reduction of nickel nitrate to metallic nickel in hydrogen, with a sub-1s thermal shock at 600 °C and above. At lower temperatures however, nickel nitrate was thermally decomposed to nickel oxide as shown in Figure 4.9b. It is known that hydrogen gas can reduce nickel ion to metallic nickel at a temperature as low as 260 °C under a slow heat treatment.¹⁴³ However, the rapidity of our process presumably requires higher temperature to achieve the necessary kinetic rates.

To investigate the effect of the high-temperature treatment on the GO matrix, Raman spectra in Figure 4.9c show the as-prepared GO features the two characteristic peaks around 1342 and 1598 cm^{-1} corresponding to the D and G bands, respectively.¹⁴⁴ The D band represents the defect-induced features while the G band corresponds to sp^2 hybridized graphitic carbon atoms. I find that heat treatment at 600 °C in the inert environment for 30 min results in only a minor change in the intensity ratio (I_D/I_G) implying that while heat treatment is known to self-heal, I see only a minor change in defect state¹⁴⁵⁻¹⁴⁶. A more significant change is observed in the Ni nanocluster incorporated rGO aerosols, which actually show an increase in defect states. This suggests the presence of the newly formed Ni nanoclusters occupied the defects in the rGO and prevents them from self-healing during the high-temperature treatment.¹⁴⁶⁻¹⁴⁷ These defects on the rGO sheets serve as the anchoring sites for the stabilization of the nanoclusters. This observation is consistent with molecular dynamics simulation showing that small metal particles are confined and retarded from aggregating on graphene sheets by slit defects, even at very high temperatures.¹⁴⁵

The microstructure of the in-situ synthesized Ni nanoclusters embedded in the graphene aerosols were examined by TEM, Scanning TEM, and energy dispersive X-ray (EDS) mapping. **Figure 4.4a** shows Ni nanoclusters uniformly distributed in the graphene matrix. The high-resolution TEM image shown in Figure 4b reveals that the lattice fringes of the nanocrystal are separated by 1.76 Å, which corresponds to the (200) plane of the metallic nickel. Figure 4c shows selected area electron diffraction (SAED) pattern of the Ni nanoclusters. The SAED pattern indicates the presence of the metallic nickel phase, which is consistent with the XRD of the nanocomposite as mentioned previously. Together, the SAED pattern, XRD profile, and high-resolution TEM image confirm that Ni nanoclusters are crystalline. The component analysis on a single Ni-rGO aerosol particle as shown in Figure 4.4d was carried out using EDS mapping. Figure 4e shows the corresponding scanning TEM of the same aerosol particle. The distributions of Ni and carbon illustrated in Figure 4.4f and 4.4g reveal that Ni nanoclusters are uniformly distributed over the graphene aerosol particle.

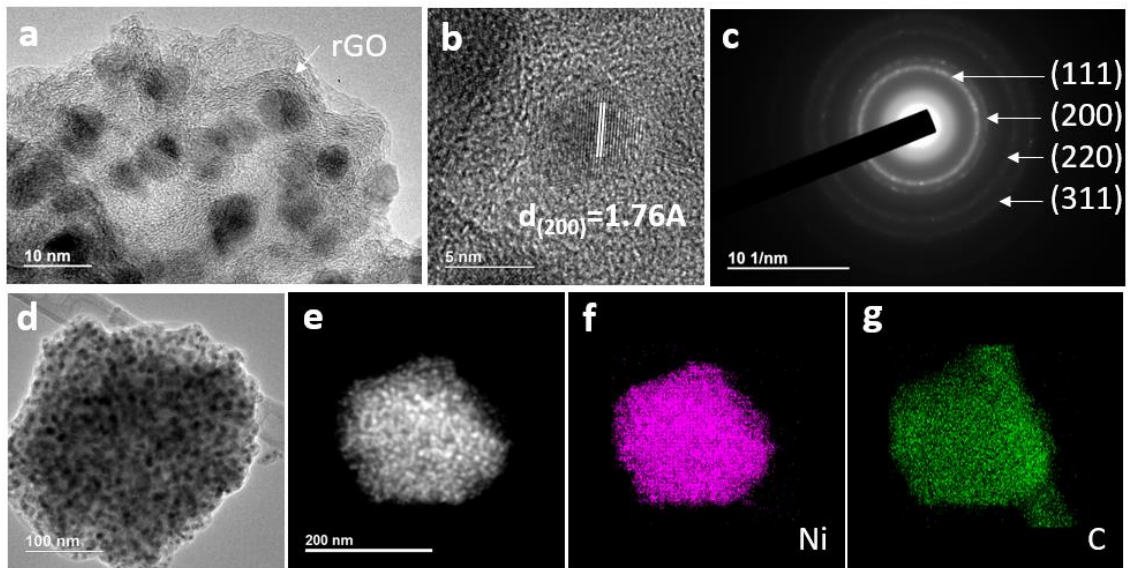


Figure 4.4. Microstructure of the Ni nanoclusters graphene aerosol particles: a) TEM image of Ni nanocluster dispersed graphene aerosol, b) High-resolution TEM of one single

Ni nanocluster, c) SAD pattern of the Ni nanocluster dispersed graphene particle. d-g) TEM, Scanning TEM images of one single Ni graphene particle and the corresponding EDS mappings for nickel and carbon.

4.3.3. Effect of Temperature and Metal Salt Loading on the Size and Distribution of Metal Nanoclusters in Graphene Aerosols

The effect of temperature is seen in **Figure 4.5** which exhibits TEM images of the Ni nanoclusters generated at various reaction temperatures (600, 800, and 1000 °C) at the same precursor ratio (metal salt: GO =1). The histograms and Gaussian fit show the resulting size distributions. The goodness of the Gaussian fits rather than a more traditional log-normal fit implies that the growth is not driven by coagulation. The result as shown in Figure 4.5 indicates that lower temperatures lead to smaller nanoclusters with a relatively narrower size distribution whereas higher temperatures enable the formation of larger nanoclusters with a broader size distribution.

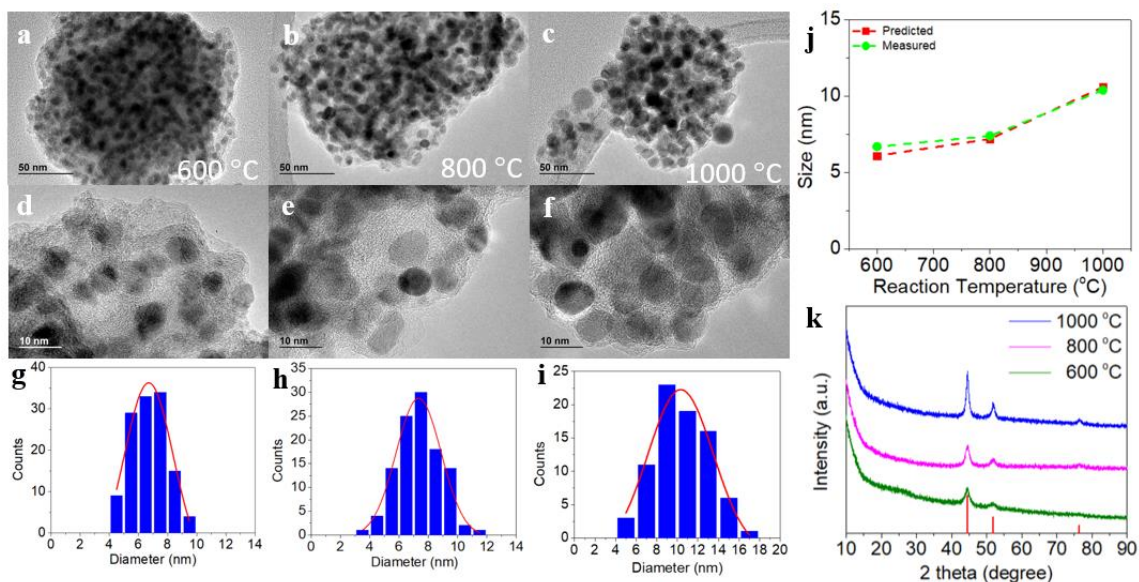


Figure 4.5. Effect of the reaction temperature on the formation of Ni nanoclusters: a-f) TEM images of Ni graphene aerosols and g-i) histograms of the size distributions of the Ni nanoclusters synthesized at different temperatures (600, 800, 1000 °C); the red curves represent gaussian fits to the size distributions. j) effect of the reaction temperature on the average size of Ni nanoclusters: the data points labeled as “measured” are the size of Ni

nanoclusters determined by statistical analysis of the TEM images; the data points labeled as “predicted” are the size predicted using Scherrer equation based on the XRD; k) XRD patterns for Ni-rGO nanocomposites generated at different temperatures.

Figure 4.5j summarizes the average size of the Ni nanoclusters as a function of reaction temperature. It is clear that the average size of Ni nanoclusters (labelled as “measured”) increases with increasing reaction temperatures. This trend is supported by the result of the XRD patterns (Figure 4.5k) of Ni nanoclusters incorporated graphene aerosols. As shown in Figure 4.5k, the peak intensity of Ni nanoclusters increases with the reaction temperature. The size of Ni nanoclusters generated at each temperature was predicted based on each XRD pattern using the Scherrer equation and is comparable with the statistically measured average size as shown in Figure 4.5j. These observations are consistent with prior studies by Jang and coworkers, who have observed a similar reaction temperature-dependent increase in the diameter of platinum nanoclusters generated in graphene matrix.¹⁴⁸

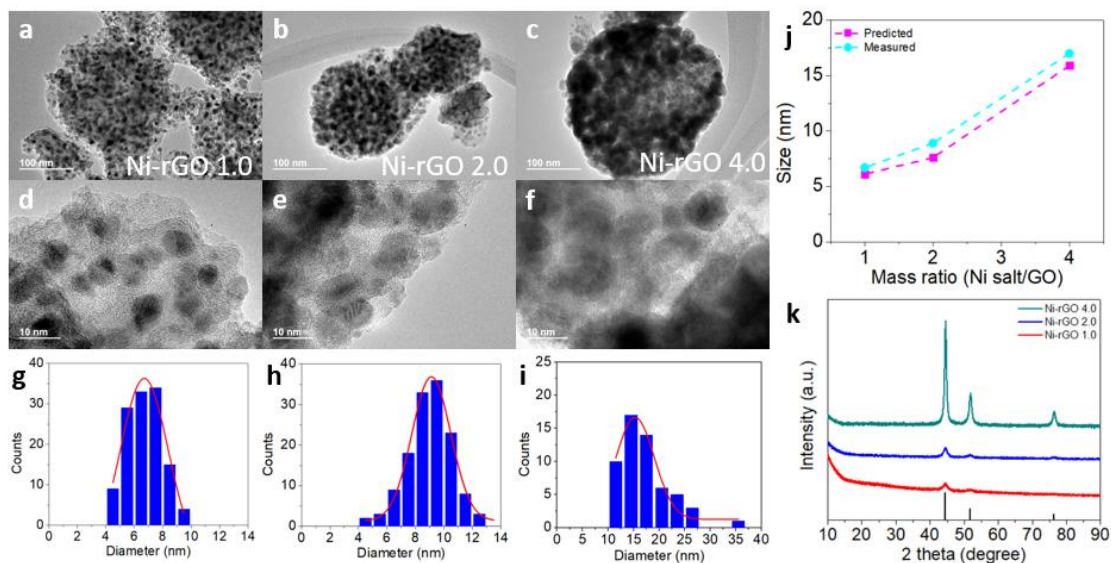


Figure 4.6. Effect of the metal salt loading on the size of Ni nanoclusters: a-f) TEM images of Ni graphene aerosols and g-i) histograms of the size distributions of the Ni nanoclusters synthesized at different mass loadings (1.0, 2.0, 4.0); j) effect of the mass ratio between Ni salt and GO on the size of Ni nanoclusters; k) XRD patterns of Ni-rGO nanocomposites generated at different mass ratios.

The effect of the metal salt loading ratio (1.0, 2.0, and 4.0) on the size and distribution of Ni nanoclusters were also investigated. **Figure 4.6** shows TEM images of the Ni nanoclusters formed with different mass loading ratios of the metal salt to GO at a constant reaction temperature of 600 °C. The size of the Ni nanoclusters increases with increasing mass loading of nickel nitrate salt, with a broader size distribution. It is evident that the average size of Ni nanoclusters, as seen in Figure 4.6j, increases with increasing salt mass loading ratio. Again, this observation is consistent with the results from XRD using the Scherrer equation. Noticeably, the average size of Ni nanoclusters produced with a 4.0 mass loading ratio increased dramatically as compared to previous mass loadings. Since the total mass of Ni nanoclusters should be proportional to the mass of nickel nitrate salt loaded. Using the diameter of Ni-rGO 1.0 of 6.7 nm, the diameter of Ni nanocluster for Ni-rGO 4.0 should be 10.8 nm, but what I observe is 15.6 nm. This suggests that the number concentration of Ni nanoclusters decreased with increasing mass loading through coagulation and coalescence, which I explore in more detail below.

4.3.4. Other Metal Nanoclusters Generated with the Aerosol-based Thermal Shock Technique

Since hydrogen reduction of metal salts is universal, the synthesis of nanoclusters in the graphene matrix with the aerosol-based thermal shock method can be easily extended to other non-noble metals. I demonstrate in **Figure 4.7** the in-situ formation of Co and Sn nanoclusters in graphene aerosols. The mass loading between the metal salt and the graphene oxide used to prepare the precursor was adjusted to ensure that the molar amount of each metal ion loaded is the same with that of nickel ions used in the nickel salt and GO

(mass ratio 1:1) precursor. The XRD profiles (see **Figure 4.10**) confirm the formation of metallic cobalt and tin at 1000 and 600 °C, respectively. SEM images (Figure 4.7) show both Co-rGO and Sn-rGO aerosols also have a crumpled morphology and TEM images (Figure 4.7) indicate Co and Sn nanoclusters are uniformly distributed in the graphene particles. Figure 4.7d and 4.7h show the size distributions of Co and Sn nanoclusters with an average size of 10.2 and 3.6 nm, respectively. The size of Co nanoclusters generated at 1000 °C is comparable to the size of Ni nanoclusters (10.4 nm) generated at the same reaction temperature. However, Sn nanoclusters generated at 600 °C (See Figure 4.7f-h) are smaller than Ni nanoclusters obtained at a corresponding operation condition (See Figure 4.6a, 4.6d and 4.6g). This observation might be explained with the following argument. Compared with Ni²⁺ ion, Sn²⁺ ion is more easily reduced by hydrogen since it has a less negative standard electrode potential. At the same heating rate, Sn atoms are generated at a faster rate leading to more nuclei, which are thus correspondingly smaller. This explanation is supported by the observation that the concentration of Sn nanoclusters shown in Figure 4.7g is higher than that of Ni nanoclusters shown in Figure 4.6d.

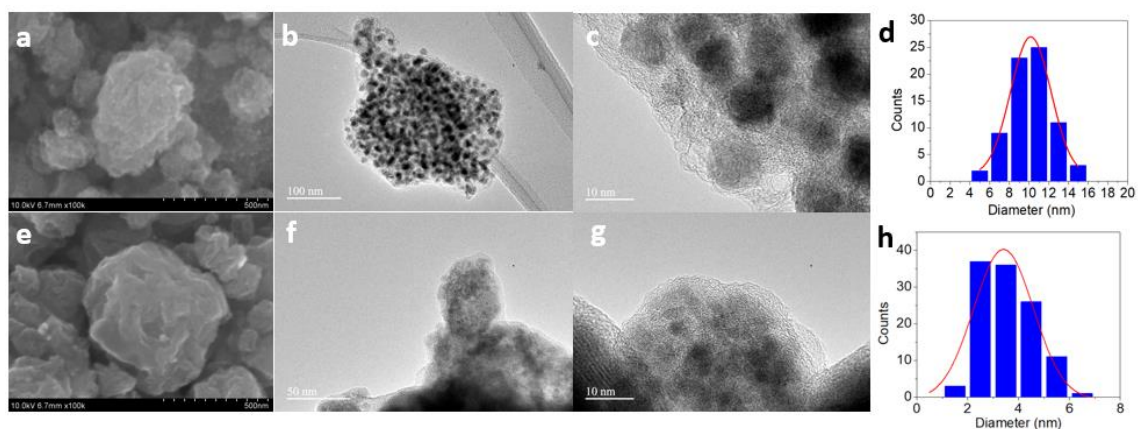


Figure 4.7. Co and Sn nanoclusters generated with the aerosol based thermal shock technique: a) SEM, b-c) TEM, d) histogram of the size distribution of Co nanoclusters decorated in graphene particles; e) SEM, f-g) TEM, h) histogram of the size distribution of Sn nanoclusters generated in graphene particles.

4.3.5. Example Application

Metal particles, particularly ultra-fine particles, are known to be good catalysts. Here, I investigated the catalytic properties of our metal nanocluster incorporated graphene aerosol particles towards the reduction of 4-nitrophenol by sodium borohydride. This reduction reaction has been widely used as a gold standard for investigating the catalytic properties of various nanoclusters. I report on the catalytic properties of our Ni and Co nanoclusters/graphene materials as examples of the utility of this aerosol-based thermal shock synthesis approach and the resulting materials. As shown in **Table 4.1**, the results indicate our metal rGO nanocomposites show favorable catalytic activities compared with previously reported. More detailed discussion is described in the Supporting Information.

Table 4.1. Comparison of catalytic activity of the catalysts for the reduction of 4-NP with NaBH₄

catalyst	size [nm]	M_{cat}^a [mg]	volume [mL]	K_{app} [$10^{-3}s^{-1}$]	κ^b [$10^{-3}Lg^{-1}s^{-1}$]	κ/S_p^c [$10^{-3}Lm^{-2}s^{-1}$]	reference
Ni-rGO	6.7	0.80	30	4	150	1.49	this work
Ni-rGO	17.2	2.0	40	7.66	153.2	3.90	149
Ni-rGO	25	6.0	100	0.65	10.8	0.40	150
Co-rGO	10	0.80	30	17	638	9.43	this work
Co-rGO	4	5.0	100	1.37	27.4	0.16	151
Co-rGO	95	6.0	100	0.45	7.5	1.05	150

^{a)} M_{cat} : mass of the nanocomposite catalyst (mg)

^{b)} κ : catalytic activity, which is equal to $\frac{K_{app}}{M_{cat}/Volume}$ ($Lg^{-1}s^{-1}$)

^{c)} S_p : specific surface area of metal nanoparticle, $\frac{6}{\rho_p D_p}$ (m^2/g), ρ_p density of bulk cobalt,

D_p diameter of metal nanoparticle

4.3.6 Growth Mechanism of Nanoclusters in a Graphene Aerosol particle

Here, I use a simple characteristic time analysis to explore the likely growth mechanism of nanoclusters in the graphene matrix, and discuss the role of the coagulation, coalescence and surface growth on the nanocluster formation. In order to simplify the problem, I assume that the chemistry to form the zero-valent metal atoms is not rate limiting. Although no direct data was found to support this assumption, it has been reported that the hydrogen reduction of nickel oxide particles with a diameter of 10~20 μm is a first order reaction with a rate constant of 7 s^{-1} , which renders a time required for the half conversion of nickel oxides in the order of 0.1 s. However, the reduction rate of nickel ions dispersed in the graphene matrix with a much smaller dimension would proceed much faster.¹³⁰ Considering a 200 nm ($d_{aerosol}$) graphene aerosol containing uniformly dispersed Ni nanoclusters with a diameter, d_p and a number concentration, N_0 , respectively. The mass ratio, ϕ between metallic nickel and rGO matrix for Ni-rGO 1.0 nanocomposites is 1, obtained from TGA result (See **Figure 4.11**) so that the number of Ni nanoclusters, N_0 is correlated with the diameter d_p as follows: $N_0 \propto 1/d_p^3$. The characteristic coagulation time is defined as the time required for the nanoclusters with the initial concentration of N_0 to achieve half of its value. For nanoclusters with a narrow size distribution, the characteristic coagulation time can be estimated by using⁴⁰:

$$\tau_{coag} = \frac{2}{KN_0} \quad (4.4)$$

Here, $K = 8\pi Dd_p$ is the Brownian coagulation coefficient, where D is the stokes diffusivity temporarily ignoring the presence of the graphene matrix, estimated by the Stokes-Einstein equation¹¹⁷:

$$D = \frac{k_B T}{3\pi\eta d_p} \quad (4.5)$$

Where k_B is the Boltzmann constant, T is the absolute temperature, d_p is the particle's diameter, and η is the viscosity of the air at the temperature T .

I can also estimate the characteristic coalescence time for Ni nanoclusters, which is defined as the time required for two contacted primary particles to form a single spherical particle. In our previous study, I have shown that the coalescence of Ni nanoclusters is sensitive to the phase of the nanoclusters. Our calculation shows that Ni nanoclusters with a diameter of less than 1.5 nm are in a liquid like phase at 600 °C,²⁴ enabling the use of a viscous flow mechanism for coalescence time⁴¹:

$$\tau_{coales,l} = \frac{\mu d_{eff}}{2\sigma_l} \quad (4.6)$$

Where μ is the viscosity of Ni nanocluster, σ_l is the surface tension of Ni nanocluster in liquid state; d_{eff} is the effective diameter of the coalescing particle pair, which is $6V_p/a_p$, V_p and a_p are volume and surface area of the coalescing particle pair, respectively.

For nanoclusters in the solid phase, the coalescence time can be estimated with the following equation⁴²:

$$\tau_{coales,s} = \frac{3k_B T N}{64\pi\sigma_s D_{eff}} \quad (4.7)$$

Where T is the temperature of a particle pair undergoing coalescence, N is the number of atoms in the particle pair, σ_s is the surface tension of solid Ni nanocluster, D_{eff} is the effective atomic diffusion coefficient in the particle pair. All property data mentioned above can be found in the Supporting Information (**Table 4.3**).

As shown in **Figure 4.8**, in the absence of the graphene matrix, the characteristic coagulation time of the Ni nanoclusters is extremely short compared to the residence time

of the aerosol particle in the tube furnace. This if the particles were free to coagulate they would achieve the self-preserving log-normal size distribution with a geometric standard deviation of 1.44.⁴⁰ However, our observed geometric standard deviations (shown in the **Table 4.4**) are smaller, and thus our size distribution narrower and range from 1.2 to 1.29. This indicates that the graphene matrix, inhibits nanocluster mobility, and thus suppresses coagulation. As discussed in the previous section, higher mass loadings and higher temperatures might facilitate the coagulation between nanoclusters, resulting in the further growth of nanoclusters decreasing the number concentrations and increasing the width of the size distributions. The experimental observation of aggregation occurs at the point where the characteristic coalescence time exceeds that of the coagulation time. As shown in Figure 4.8, the computed coalescence time for anything larger than ~ 1.5 nm is much larger than both the coagulation and residence time. This indicates, that the actual coagulation times must be quite large, else one would see aggregates, and implies that the mobility of nanoclusters even at 600 °C are effectively frozen to the graphene substrate.

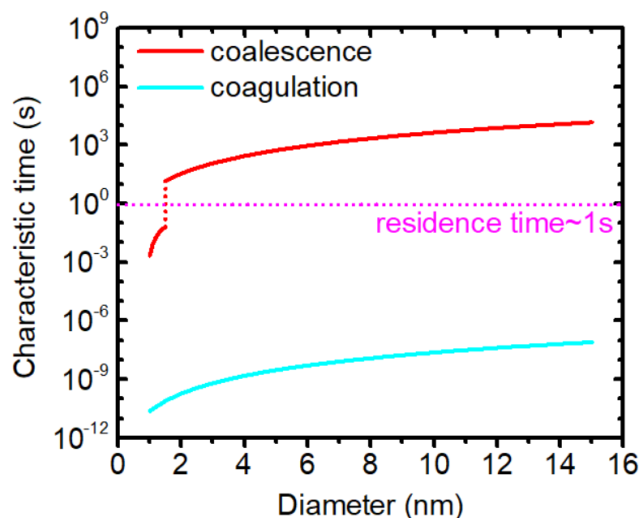


Figure 4.8. Characteristic coagulation and coalescence times of monodispersed Ni nanoclusters at 600 °C without the presence of the graphene matrix.

4.4. Conclusions

I demonstrate a rapid and continuous aerosol-based thermal shock processing technique to *in situ* synthesize well-dispersed metal nanoclusters in the graphene matrix. The aerosol particles containing graphene oxide sheets acts as nanoreactors for the reduction of metal precursor and the growth of metal nanoclusters. With this fast heating and quenching, the metal precursor was quickly reduced and nucleated into metallic nanoclusters. The size and morphology of the metal nanoclusters can be controlled by varying the reaction temperature and the mass loading of metal salt in the graphene aerosol nanoreactors. Smaller nanoclusters with a narrower size distribution were obtained with a lower reaction temperature and lower mass loading. A characteristic time analysis leads to the conclusion that the nanocluster formation is governed by nucleation and subsequent surface growth, and the coagulation and coalescence might only be involved in the nucleation stage. Finally, this one-step continuous aerosol-based thermal shock technique offers considerable potential for the manufacturing processing of well-dispersed and uniform nanoclusters stabilized within a graphene matrix.

4.5. Supporting Information

Moment model for saturation ratio calculation; XRD, Raman, and TGA profiles; property data for characteristic time analysis; Geometric standard deviations for Ni nanoclusters generated at different conditions; Catalytic properties of metal nanoclusters in graphene aerosol particles.

4.5.1. Moment model for saturation ratio calculation

A moment model⁴⁰ was used to calculate how the saturation ratio S of metal atoms changes with the duration of the thermal shock. In order to calculate time resolved-saturation ratio, one needs to solve the follow set of differential equations simultaneously:

$$\frac{dS}{dt} = \frac{R_H}{n_s} - \frac{Jk^*}{n_s} - (S - 1) \frac{B_1 A}{2v_1 n_s} \quad (4.8)$$

$$\frac{dA}{dt} = Jk^{*2/3} S_1 + 2\pi B_1 (S - 1) M_1 \quad (4.9)$$

$$\frac{dM_1}{dt} = Jr_c + (S - 1) B_1 N \quad (4.10)$$

$$\frac{dN}{dt} = J \quad (4.11)$$

Here, R_H is the reaction rate of metal salt precursor to zero-valent metal atoms; A is the total surface area of all the nuclei in the reaction volume; M_1 is the first moment which is defined as $M_1 = \int_{d^*}^{\infty} n_d d_p d(d_p)$ where $d^* = 2r_c = \frac{4\sigma V_1}{k_B T \ln S}$, n_d is number concentration of particle with a diameter of d_p ; N is the number concentration of nuclei; R_H and A are time-dependent variables; k^* is the number of monomers in a single particle with a critical radius r_c ; n_s is the monomer concentration at saturation condition; $B_1 = 2n_1 v_1 \left(\frac{k_B T}{2\pi m_1}\right)^{1/2}$ where n_1 is the monomer number concentration; v_1 and m_1 is volume and mass of the monomer,

respectively; J is the rate of particle formation by homogenous nucleation, which is given as follows ⁴⁰:

$$J = \frac{Kn_1s_1}{3} \sqrt{\frac{\theta}{\pi}} \exp\left(-\frac{4}{27} \frac{\theta^3}{(\ln S)^2}\right) \quad (4.12)$$

Where $K = n_1 \left(\frac{kT}{2\pi m_1}\right)^{1/2}$; θ is dimensionless surface tension of the stable nuclei $\theta = \frac{s_1\sigma}{kT}$; s_1 is the surface area of a monomer.

Although no direct data of hydrogen reduction of metal salt was found, it has been reported that the hydrogen reduction of nickel oxide particles with a diameter of 10~20 μm is a first order reaction with a rate constant of 7 s^{-1} , which renders a time required for the half conversion of nickel oxides in the order of 0.1 s. However, the reduction rate of nickel ions dispersed in the graphene matrix with a much smaller dimension (~200 nm in diameter) would proceed much faster.¹³⁰ Since it is known that the reaction rate of hydrogen reduction reaction of metal salt to metallic nickel, one can calculate the time-dependent saturation ratio of nickel atoms during the thermal pulse.

$$R = k_1 n \quad (4.13)$$

Where k_1 is the estimated rate constant for hydrogen reduction of metal salt to zero-valent metal atoms; n is the number concentration of metal salt precursor in the graphene particles with an initial value of n_0 . Three initial metal salt loadings investigated are: 10^{19} , 10^{20} , and 10^{21} \#/m^3 . Therefore, the number concentration of metal salt $n = n_0 e^{-k_1 t}$; the concentration of the monomer generated from the hydrogen reduction of metal salt $n_1 = n_0 - n$.

The values for all the property parameters and the details of the calculation can be found in the Supporting Information.

Table 4.2. Property data used to calculate saturation ratio.

parameter	definition	value
k_B	Boltzmann constant	$1.38 \times 10^{-23} \text{ m}^2\text{kgs}^2\text{K}^{-1}$
T	reaction temperature	873 K
σ	surface tension of Ni nanocluster in liquid state, σ_l	1.8 N/m
v_1	nickel atom (monomer) volume	$1.09 \times 10^{-29} \text{ m}^3$
m_1	nickel atom (monomer) mass	$9.74 \times 10^{-26} \text{ kg}$
k_1	estimated rate constant of hydrogen reduction of metal salt to metal atoms	7 s^{-1}
n_s	monomer concentration at saturation condition	$1.06 \times 10^7 \text{ \#/m}^3$

4.5.2. XRD, Raman and TGA profiles

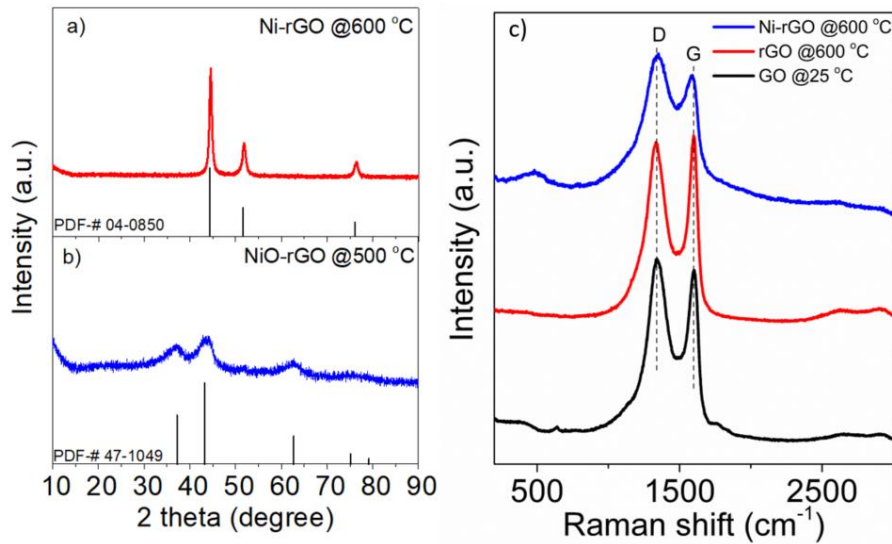


Figure 4.9. XRD and Raman characterizations of Ni nanoclusters decorated graphene nanocomposite: XRD profiles of (a) Ni nanocluster incorporated graphene aerosol particles (4:1 mass ratio of nickel nitrate salt to GO), b) NiO incorporated graphene aerosol particles. c) Raman spectra of the Ni nanocluster incorporated graphene aerosol particles (1:1 mass ratio of nickel nitrate salt to GO), reduced graphene oxide sheets (graphene oxide sheets heated at 600 °C for 30 min in the argon gas); as-prepared graphene oxide sheets prepared using the modified Hummer's method. (a 632 nm He-Ne laser was used for the Raman spectrum measurement)

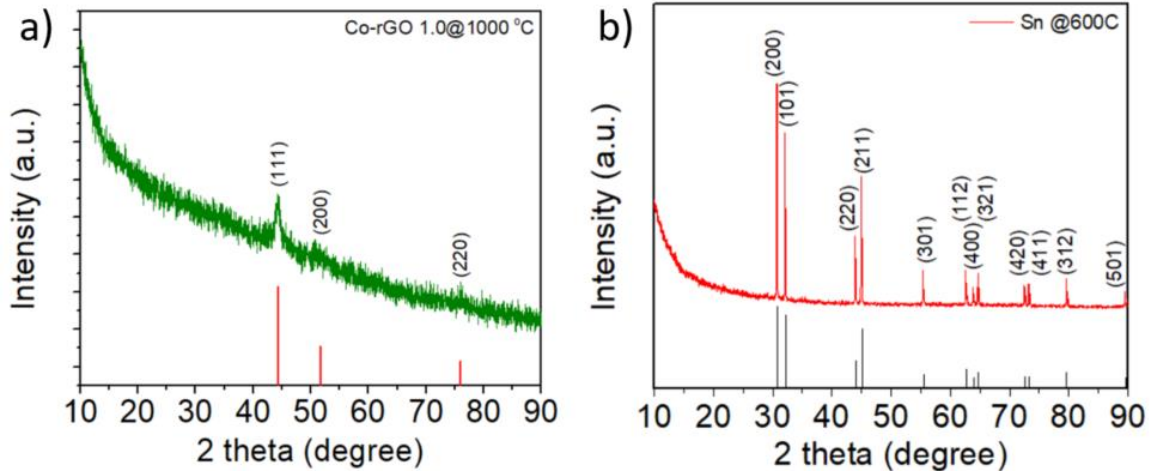


Figure 4.10. a) XRD profile of Co-rGO nanocomposite generated using aerosol spray pyrolysis approach at 1000 °C; b) XRD profile of Sn powder generated using aerosol spray pyrolysis approach at 600 °C. Please note that the XRD profile of Sn powder confirms the formation of the complete reduction of tin chloride to metallic tin at a temperature of 600 °C.

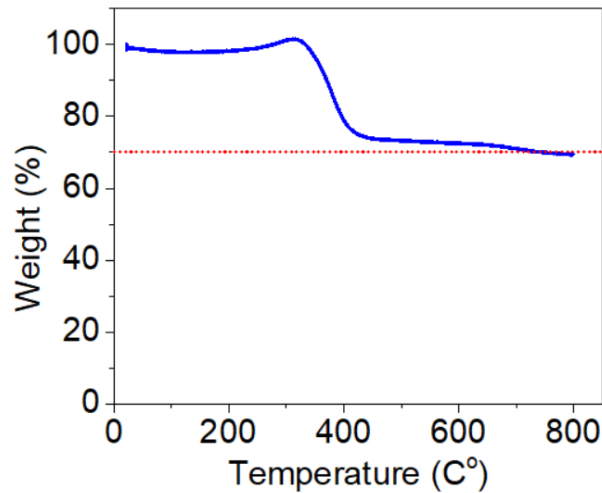


Figure 4.11. TGA profile of Ni-rGO 1.0 nanocomposite generated at 1000 °C. (TGA was operated under air atmosphere with a heating rate of 5°C/min.) The mass ratio between nickel and rGO matrix calculated based the TGA profile is ~1.0. Note that the final product in the TGA test is nickel oxide (Ni_2O_3).

4.5.3. Property data for Characteristic time analysis

N_0 , number concentration of nickel nanoclusters with a diameter of d_p in a 200nm

($d_{aerosol}$) graphene aerosol:

$$N_0 = \frac{\left(\frac{1}{6}\pi d_{aerosol}^3\right) \left(\frac{m_{Ni}}{\rho_{Ni}}\right) \left(\frac{m_{rGO}}{\rho_{rGO}}\right)}{\frac{1}{6}\pi d_p^3} \times \frac{1}{\left(\frac{1}{6}\pi d_{aerosol}^3\right)} \quad (4.14)$$

Where m_{Ni} and m_{rGO} are the masses of nickel metal and rGO matrix, respectively; note that $m_{Ni}=m_{rGO}$; ρ_{Ni} and ρ_{rGO} are densities of nickel metal (the bulk density of nickel metal was used for the calculation.) and rGO matrix (the density is 1.91 g/cm^3 , the data is obtained from Graphee Inc.).

Table 4.3. Property data used for the characteristic time analysis.

parameter	definition	value
k_B	Boltzmann constant	$1.38 \times 10^{-23} \text{ m}^2\text{kgs}^2\text{K}^{-1}$
T	temperature	873 K
η	viscosity of the air at 600 °C	$3.93 \times 10^{-5} \text{ N/m}$
μ	viscosity of Ni nanocluster at 600 °C	See below
σ_l	surface tension of Ni nanocluster in liquid state	1.8 N/m
σ_s	surface tension of solid Ni nanocluster	2.47 N/m
D_{eff}	effective atomic diffusion coefficient in the particle pair at 600 °C ¹³⁴	$2.1 \times 10^{-21} \text{ m}^2\text{s}^{-1}$

Viscosity of the air, η is given by Sutherland's formula:¹⁵²

$$\eta = \lambda \frac{T^{\frac{3}{2}}}{T+C} \quad (4.15)$$

Where $\lambda = \frac{\mu_0(T_0+C)}{T_0^{\frac{3}{2}}}$ is a constant for the gas, $\mu_0 = 1.87 \times 10^{-5} \text{ N/m}$, $T_0 = 291.15 \text{ K}$,

$C = 120$, which is Sutherland's constant for the gaseous material.

Viscosity of Ni nanocluster, μ ^{24, 41}

μ is the viscosity of Ni nanocluster, which is given as:

$$\mu = 1.8 \times 10^{-7} \frac{[M \cdot T_{mp}(d_p)]^{1/2} \exp\left(\frac{L}{RT_p}\right)}{v_m \exp\left[\frac{L}{RT_{mp}(d_p)}\right]} \quad (4.16)$$

Where L is the latent heat of melting (J/mol), 17200 J/mol (which is equal to 297000 J/kg), $T_{mp}(d_p)$ is the melting point of the Ni nanoclusters with a diameter of d_p , M is the molar weight, 5.87×10^{-3} kg/mol, R is the gas constant, 8.314 J/mol/K, v_m is the molar volume, 7.5×10^{-6} m³/mol.

4.5.4. Geometric standard deviations σ_g for Ni nanoclusters

Table 4.4. Geometric standard deviations σ_g for Ni nanoclusters generated at different conditions.

Metal salt to GO ratio	σ_g	Reaction temperature	σ_g
1.0	1.20	600 °C	1.20
2.0	1.20	800 °C	1.23
4.0	1.28	1000 °C	1.29

4.5.5. Catalytic properties of metal nanoclusters in graphene particles.

Metal particles are known to be good catalysts, particularly ultra-fine particles. The ability to anchor particles in and within an accessible matrix enables these particles to function while still preserving their metastable state. Here, I investigated the catalytic properties of our metal nanocluster incorporated graphene aerosols towards the reduction of 4-nitrophenol by sodium borohydride. I report on the catalytic properties of our Ni-rGO and Co-rGO materials as examples of the utility of this aerosol-based thermal pulse synthesis approach and the resulting materials. I adopted experimental conditions as applied by Kastner¹⁵³ of the catalytic performance of poly(acrylic acid) stabilized Ag nanoclusters towards the reduction of 4-nitrophenol by sodium borohydride. A total volume of 5 ml sodium borohydride with a concentration of 0.2 M was first added into 20 ml 4-nitrophenol solution with a concentration of 0.1 mM. The addition of the sodium borohydride with a basic pH made the color of the solution turn yellow due to the formation

of the 4-nitrophenolate ions.¹⁵³ As shown in Figure 4.12a, the absorbance spectrum of 4-nitrophenolate exhibits a characteristic peak located at around 400 nm. The reduction of 4-nitrophenolate by sodium borohydride was monitored by the spectro-temporal evolution of the absorbance peak of 4-nitrophenolate. Without the addition of the catalyst, the reduction reaction was extremely slow and there was no obvious color change even after several days. The reaction was triggered with the addition of 5 ml Ni or Co nanoclusters decorated rGO catalyst with a concentration of 0.16 mg/ml. As shown in Figure 4.12b and 4.12d, the absorbance peak of 4-nitrophenolate decreases with the reaction time due to the catalytic process of 4 nitrophenolate to 4-aminophenolate with the presence of Ni and Co nanoclusters, respectively.

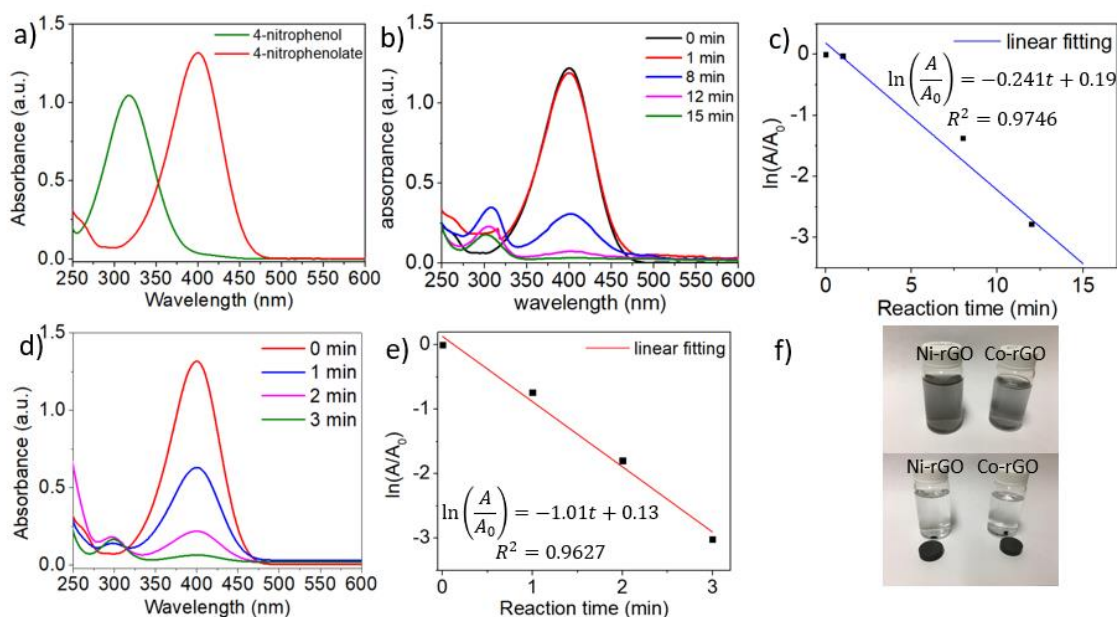


Figure 4.12. Catalytic properties of metal nanoclusters in graphene particles: a) Absorbance spectra of 4-nitrophenol and 4-nitrophenolate; b) time-resolved absorbance spectra of 4-nitrophenolate and c) peak absorbance versus the reaction time with Ni nanoclusters (6.7 nm, generated at 600 °C) as the catalyst; d) time-resolved absorbance spectra of 4-nitrophenolate and e) peak absorbance versus the reaction time with Co nanoclusters (10 nm, generated at 1000 °C) as the catalyst; f) the post-reaction solutions containing the catalysts with and without the presence of a magnet.

Since an excess amount of sodium borohydride (the molar ratio between sodium borohydride molecules and 4-nitrophenol: 1000:1) was used, the reduction of 4-nitrophenolate with sodium borohydride can be treated as a pseudo first-order reaction. A_t is the real-time peak intensity of the absorbance of 4-nitrophenolate with an initial value of A_0 . A first order plot shown in Figure 4.12c and e yields observed first order rate constant rates, $K_{app} = 17 \times 10^{-3}$ and $17 \times 10^{-3} s$ for Ni and Co catalysts, respectively. A direct comparison with prior work is difficult even for the same catalyst, as K_{app} varies with both the mass loading of the catalyst and the reaction volume. In order to address this issue, the catalytic activity κ was used, which takes into account the mass of the catalyst and the volume of the reaction solution. κ is defined as the ratio of K_{app} to the concentration of the catalyst added (in mass per volume).¹⁵³⁻¹⁵⁴ The determined values of κ for the Ni-rGO and Co-rGO nanocomposite are 0.150 and 0.638 $Lg^{-1}s^{-1}$, respectively. Compared to previous studies concerning the catalytic properties of Ni and Co nanoclusters decorated graphene nanocomposites prepared by other techniques, our metal-rGO nanocomposites shows favorable catalytic activities.¹⁴⁹⁻¹⁵¹

Chapter 5: Extremely Stable Antimony-Carbon Composite Anodes for Potassium-ion Batteries[‡]

Abstract: Potassium-ion batteries (PIBs) have been considered as promising alternatives to lithium-ion batteries due to the high natural K abundance of 2.09 wt.% (vs. 0.0017 wt.% for Li) and low K/K⁺ redox potential of -2.93 V (vs. -2.71 V for Na/Na⁺). However, PIB electrodes still suffer huge challenges due to the large K-ion radius and slow reaction dynamics. Herein, I report a high-capacity Sb@CSN composite anode with Sb nanoparticles uniformly encapsulated by carbon sphere network (CSN) for PIBs. First-principles computations and electrochemical characterizations confirm a reversible sequential phase transformation of K₂Sb, KSb, K₅Sb₄, and K₃Sb during potassiation/depotassiation process. In a concentrated 4M KTFSI/EC+DEC electrolyte, the Sb@CSN anode delivers a high reversible capacity of 551 mAh/g at 100 mA/g for 100 cycles with an extremely slow capacity decay of only 0.06% per cycle from the 10th to 100th cycling; when up to a high current density of 200 mA/g, Sb@CSN anode still maintains a capacity of 504 mAh/g for 220 cycles. The Sb@CSN anodes demonstrate one of the best electrochemical performances for all K-ion batteries anodes reported to date. The exceptional performances of Sb@CSN should be attributed to the efficient capsulation of small Sb nanoparticles into conductive carbon network as well as the formation of a robust KF-rich SEI layer on Sb@CSN anode in the concentrated 4M KTFSI/EC+DEC electrolyte.

[‡] The results represent in this chapter have been previously published and are reprinted from: Extremely Stable Antimony-carbon Composite Anodes for Potassium-ion Batteries; Jing Zheng #, Yong Yang #, Xiulin Fan, Guangbin Ji, Xiao Ji, Haiyang Wang, Singyuk Hou, Michael Zachariah, Chunshen Wang; Energy Environ. Sci., 2019, 12, 615-623. # Author Contributions: J. Z and Y. Y contributed equally to this work.

5.1. Introduction

With the continuously increasing consumption of traditional nonrenewable energy sources along with severe global environmental issues, developing efficient and renewable energy storage technologies has been more urgently required. Lithium-ion batteries (LIBs) as efficient electrical energy storage technology has been successfully developed and widely used in various types of electronic devices and electric vehicles.¹⁵⁵⁻¹⁵⁶ However, the broad utilization of LIBs in large-scale energy storage systems is still significantly hindered by the limited and unevenly distributed availability of Li in the earth's crust (0.0017 wt.%).¹⁵⁷⁻¹⁵⁸ In the past decades, many efforts have been devoted to developing alternative batteries using earth-abundant and cheap materials. Recently, sodium-ion batteries (SIBs) and potassium-ion batteries (PIBs) have received increasing attention because of their high abundance (2.36 and 2.09 wt.% for Na and K, respectively) and low cost.¹⁵⁹ Especially for PIBs, its lower redox potential (-2.93 V) for K/K^+ than Na/Na^+ (-2.71 V vs. SHE) guarantees a higher operation voltage and higher energy density, making it as a promising candidate for high-energy-density and low-cost electrical energy storage applications.

Significant advances have been achieved in developing high-performance PIBs cathode materials such as amorphous FePO_4 ,¹⁶⁰ FeSO_4F ,¹⁶¹ Prussian blue,¹⁶² Prussian Green,¹⁶³ and organic material¹⁶⁴. The research on anode materials mainly focus on carbonaceous materials, such as hard carbon,¹⁶⁵ soft carbon,¹⁶⁶ graphite,¹⁶⁷⁻¹⁶⁸ and reduced graphene oxide¹⁶⁹. However, these carbonaceous materials have a low capacity of less than 300 mAh/g. Metal anode through alloying/de-alloying reaction with K can provide a much higher specific capacity than that of intercalation type anode.¹⁷⁰ As a result, adding metal into carbon materials can significantly enhance the capacity of carbonaceous

materials. Recently, Sn-carbon composite prepared by mechanical ball-milling of Sn powder with graphite was reported for PIBs. However, the capacity of Sn-C composite anode quickly drops from 288 mAh/g at 1st cycle to a low value of 150 mAh/g after 30th cycling even at a low current density of 25 mA/g.¹⁷¹ Such rapid capacity decay is caused by the large volume change during alloy/de-alloy processes, which leads to obvious electrical disconnection between the electrode material and current collector.¹⁷² Although encapsulation of Sn nanoparticles into carbon skeleton¹⁷³, mesoporous nanostructured carbon¹⁷⁴, or nanocrystalline materials¹⁷⁵ can mitigate the damage from volume expansion/contraction during cycles, the capacity of Sn@C anodes is still declined during the charge/discharge cycles due to high mobility of Sn nanoparticles. Alternatively, antimony (Sb) with a low mobility has been investigated for PIBs anodes. As in Li-ion and Na-ion batteries,^{176,177} Sb can also form K₃Sb¹⁷⁸ by reacting with K. However, Sb-based anode prepared by simply ball-milling of a mixture of carbon black and “bulk” antimony powder can only provide a capacity of 250 mAh/g for 50th cycles, similar to the Sn@C anode in PIBs.¹⁷⁹ Furthermore, electrolytes are also critical for stabilizing PIBs anodes because the nature of solid electrolyte interphase (SEI) layer on the anode significantly affects the cycling performance of PIBs.¹⁸⁰ However, to our best of knowledge, only limited study on the SEI design via rational electrolyte regulation have been reported.¹⁸¹⁻¹⁸² Therefore, in order to achieve a high capacity and excellent cycle stability for Sb-based K storage process, nanostructure improvements as well as electrolyte design should be concerned simultaneously.

Herein, a novel class of Sb-based composite is prepared via a scalable electrospray-assisted strategy. This approach enables Sb nanoparticles to be uniformly encapsulated by

an interconnecting carbon sphere network (Sb@CSN), which not only works as a buffering matrix to mitigate the deleteriously mechanical damage from the large volume changes during alloy/de-alloy cycling, but also acts as a highly conductive framework for fast electron transport. More importantly, I also regulate the components of ester-based electrolytes to promote the formation of KF-rich SEI layer on Sb@CSN anode. Surprisingly, the Sb@CSN composite in the optimized 4M KTFSEI/EC+DEC electrolyte delivers excellent reversible capacity of 551 mAh/g at 100 mA/g over 100 cycles with a low capacity decay of 0.06% per cycle from the 10th to 100th cycling and 504 mAh/g even at a high current density of 200 mA/g over 220 cycling. Sb@CSN composite anodes also show an excellent rate performance by providing high capacity of 589 mAh/g at 50 mA/g and still maintaining 530 mAh/g even at 200 mA/g. These outstanding performances should be attributed to the novel nanostructure of Sb nanoparticles uniformly encapsulated into conductive carbon network and the formation of a more stable and robust KF-rich SEI layer on Sb@CSN in the optimized 4M KTFSEI/EC+DEC electrolyte. To our best knowledge, the Sb@CSN composites in our work show one of the highest capacity and longest cycle life in all reported PIBs anodes to date.

5.2. Experimental section

Materials and Synthesis: Antimony chloride (340 mg) was first dissolved into 10 mL N, N-dimethylformamide (DMF). Then, polyacrylonitrile (PAN, 160 mg) was added to the solution followed by vigorous stirring overnight. The as-obtained mixture was used as the precursor for electrospray. The precursor solution was loaded into a 10 mL syringe tube and pumped through a flat-top stainless-steel needle (inner diameter: 203.2 μm). A pumping rate of 0.5 mL/hour, a voltage of 20 kV and a distance of 10 cm between the needle and the aluminum substrate were employed for the electrospray process. The as-prepared sample was loaded into a tube furnace, heated up to 250 $^{\circ}\text{C}$ with a heating rate of 5 $\text{min}/^{\circ}\text{C}$ in the air atmosphere, and kept at 250 $^{\circ}\text{C}$ for 30 mins. Then, the sample was heated up to 600 $^{\circ}\text{C}$ with a heating rate of 2 $^{\circ}\text{C}/\text{min}$ under H_2/N_2 (v:v=5:95) atmosphere and kept at 600 $^{\circ}\text{C}$ for 5 hours to obtain the desired Sb@CSN material.

Computational Method: To study the electrochemical process during the K insertion into Sb at an atomic scale, first-principle computations based on density functional theory (DFT)¹⁸³⁻¹⁸⁴ are performed using the Vienna *Ab Initio* Simulation Package (VASP).¹⁸⁵ The Projector Augmented Wave (PAW)¹⁸⁶ method with an energy cut-off of 520 eV is used to describe the ion-electron interaction on a well-converged k-point mesh. The Perdew-Burke-Ernzerhof (PBE) functional in the Generalized Gradient Approximation (GGA)¹⁸⁷ is employed to calculate the exchange-correlation energy. The equilibrium voltage plateaus are computed by Nernst equation using the calculated DFT energies of all relevant equilibrium phases in K-Sb phase diagram from the Materials Project.¹⁸⁸ The geometry optimizations are performed using the conjugated gradient

method, and the convergence threshold is set to be 10^{-5} eV in energy and 0.01 eV/Å in force. Visualization of the structures is made by using VESTA software.¹⁸⁹

Structural Characterization: The Sb@CSN material was characterized by X-ray diffraction (XRD, Bruker Smart 1000 using a Cu $K\alpha$ line radiation source), thermogravimetry-differential scanning calorimetry (CAHN TG 2131, under Air with a heating rate of $5^{\circ}\text{C}/\text{min}$), Raman spectra (with 514.5 nm laser source), scanning electron microscopy (SEM, Hitachi SU-70 field emission scanning), high-resolution transmission electron microscopy (HRTEM, 2100F field emission), X-ray photoelectron spectroscopy (XPS, monochromatized ESCALAB 250 with Al $K\alpha$ source radiation, with an Ar^+ sputtering gun). The electrolyte ignition and combustion experiment were recorded by high-speed digital camera with a Vision Research Phantom v 12.1 digital camera, and the frame rate of 1,000 frames per second with a resolution of 640×480 pixel. A small piece of glass fiber membrane was soaked with about 0.5 mL electrolyte and fixed by an alligator clip, followed by immediate ignition with a butane lighter.

Electrolytes Preparation: The salts of potassium trifluoromethanesulfonimide (KTFSI) and potassium hexafluorophosphate (KPF_6) was purchased from TCI and used as received. The solvents of Ethylene Carbonate (EC) and Diethyl Carbonate (DEC) were purchased from Sigma-Aldrich and used without any purification. The different electrolytes are prepared in Ar-filled glovebox as follows: a certain molar of salt dissolving into the mixed solvent of EC+DEC (V: V=1: 1) to obtain different electrolytes: 4M KTFSI/EC+DEC electrolyte (abbreviated as “4M KTFSI”), 1M KTFSI/EC+DEC electrolyte (abbreviated as “1M KTFSI”), and 1M KPF_6 /EC+DEC electrolyte (abbreviated as “1M KPF_6 ”).

Coin cells preparation: The Sb@CSN composite, conductive carbon (from SAFT) and sodium alginate with a mass ratio of 8:1:1 were mixed in certain amount of H₂O solvent to form homogeneous slurry by stirring for 2 hours. The slurry was coated onto a thin Cu foil and dried at 90 °C for 10 h in vacuum. The coin cells (CR2032) were assembled in the Ar-filled glove box with the as-prepared Sb@CSN composite as the working electrode, pure potassium metal foil as the counter electrode, polypropylene microporous (PP, Celgard) film as the separator.

Electrochemical Measurements: The galvanostatic charge/discharge tests were performed with Arbin Battery instrument (BT2000, Arbin Instruments, USA) at a voltage range of 0.01-2.0 V at room temperature. The galvanostatic intermittent titrations (GITT) were also tested after 10 cycle's charge/discharge activation cycles on the Arbin station by alternating the current density with 100 mA/g for 20 min and rest intervals for 2h. Cyclic voltammetry (CV) measurements were performed on Gamry instrument (Reference 3000) with a scan rate of 0.1 mV/s in the range of 0.01 to 2.0 V. Electrochemical impedance spectroscopy (EIS) were also tested on the Gamry instrument with a frequency range of 10⁵ to 10⁻² Hz under the AC signal amplitude of 5 mV.

5.3. Results and discussion

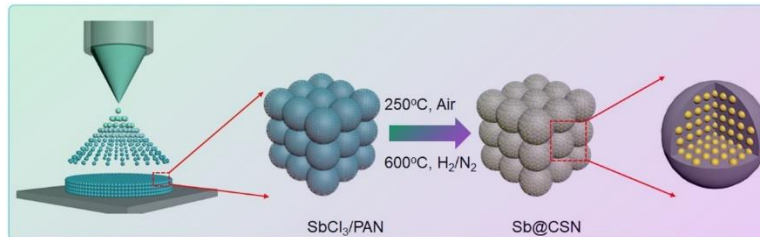


Figure 5.1. Schematic illustration of electro-spray-assisted strategy for fabricating Sb@CSN material.

Sb@CSN materials were synthesized using a scalable electro-spray-assisted strategy, as illustrated in **Figure 5.1**. Under the controllable high-voltage electrostatic field between the needle and the substrate collector, the precursor solution containing polyacrylonitrile (PAN) and SbCl₃ was nebulized to generate high concentrations of highly charged microdroplets when dried in free flight, which served as the primary building blocks for porous 3D network construction. The formed PAN nanospheres with evenly-distributed SbCl₃ (marked as SbCl₃/PAN) was collected from the substrate and then thermally stabilized and reduced to generate uniform metal Sb nanoparticles which were well confined into in-situ formed carbon spheres network (CSN) to obtain Sb@CSN material.

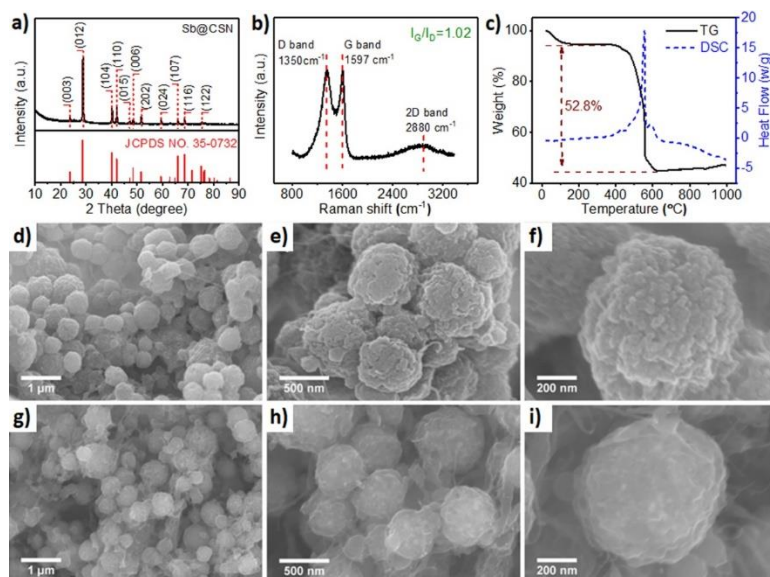


Figure 5.2. a) XRD pattern, b) Raman spectra, and c) TG-DSC curves for Sb@CSN material; SEM images of the d-f) as-prepared SbCl₃/PAN precursor and g-i) Sb@CSN composite.

Figure 5.2 demonstrates the structure and morphology of Sb@CSN composite material revealed by XRD, TG-DSC, Raman, and SEM analysis. As shown in Figure 5.2a, the XRD pattern of the Sb@CSN material is consistent with hexagonal Sb (JCPDS no. 35-0732), without any other phases or impurities, indicating that Sb³⁺ was reduced completely to metallic Sb during the synthesis process. Using the Scherrer equation to the (012) peaks of Sb, the average size of Sb crystallites was calculated at around 18 nm. On the other side, Raman spectrum was used to reveal the structure property of the carbon in Sb@CSN composites. The Raman spectrum in Figure 5.2b shows that the three bands at 1350, 1597, and 2880 cm⁻¹, corresponding to D, G and 2D bands; moreover, the intensity ratio between the G and D band (I_G/I_D) is 1.02, suggesting a high degree of graphitization for the carbon in Sb@CSN, which should offer better electro-conductivity.¹⁹⁰ To evaluate the content of Sb in the prepared Sb@CSN material, TG-DSC analysis was carried out in air from room temperature to 1000 °C, as displayed in Figure 5.2c. The slight weight loss at around 100

°C resulted from adsorbed solvent evaporation; the main weight loss at around 500 °C is due to carbon oxidation. According to oxygen-antimony binary phase diagram (**Figure 5.8a**), a small peak in the DCS curve at around 590 °C is attributed to the oxidation of Sb nanoparticles to form Sb_2O_4 .¹⁹¹ As a result, the mass loading of Sb for prepared Sb@CSN material can be calculated at around 37.8 wt.%.

The morphology of the SbCl_3/PAN precursor and Sb@CSN before and after heat treatment is shown in Figure 5.2d-f and Figure 5.2g-i, respectively. The as-prepared SbCl_3/PAN precursor in Figure 5.2d-f demonstrates uniform spheres which interconnects to form a three-dimensional (3D) network. Notably, these spheres have a crumpled surface, probably formed by the capillary compression during the solvent evaporation from the aerosol droplets.²⁴ This crumpled surface microstructure can be very beneficial for boosting the surface area of the carbon network. After carbonization, the obtained Sb@CSN maintains a similar microstructure and morphology, indicating that the unique structure of the prepared material can be maintained after the heat treatment. Figure 5.2g-i illustrates the interconnection between each primary carbon sphere embedded with secondary Sb nanoparticles (Figure 5.8b-c), which enables the continuous 3D conductive network to provide a fast electronic and ionic transfer path and effectively accommodate the volume changes.

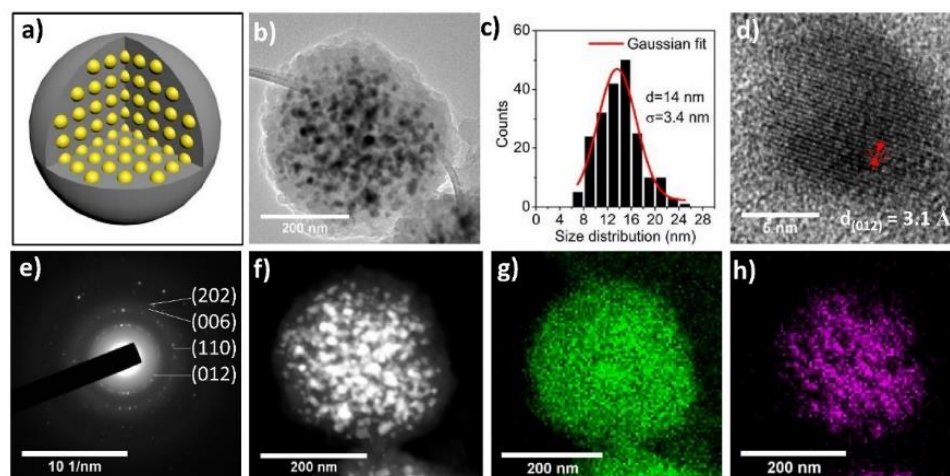


Figure 5.3. a) Schematic illustration of uniform Sb nanoparticles confined in a carbon sphere (Sb@CSN); b) TEM image of an individual Sb@CSN sphere and c) corresponding size distribution curve of Sb nanoparticles from image b); d) HRTEM image, e) selected-area electron diffraction pattern, and f-h) EDS images for one individual Sb@CSN sphere, g) for C and h) for Sb element.

The microstructure and morphology of Sb@CSN was also examined by TEM analysis, as shown in **Figure 5.3**. Figure 5.3a represents a schematic illustration of uniform Sb nanoparticles confined in a carbon sphere. The corresponding TEM image in Figure 5.3b indicates that the Sb nanoparticles are well-encapsulated and uniformly distributed in the carbon sphere. The size distribution curve in Figure 5.3c indicates a relatively narrow size distribution for Sb nanoparticles in prepared Sb@CSN material, with an average size of 14 nm and a standard deviation of 3.4 nm, which is consistent with the XRD results. The HRTEM image shown in Figure 5.3d suggests that the Sb nanoparticle has a good crystalline structure, confirmed by the 3.1 Å distance of lattice fringes corresponding to the (012) plane of the metallic Sb. The selected-area electron diffraction pattern (SAED) in Figure 5.3e exhibits typical SAD pattern of metallic Sb. The lack of diffraction rings corresponding to Sb₂O₄ suggests that carbon matrix serves as an effective barrier to prevent

the Sb nanoparticles from oxidizing. The element mapping images in Figure 5.3f-h suggests a uniform distribution of Sb nanoparticles in the carbon sphere matrix.

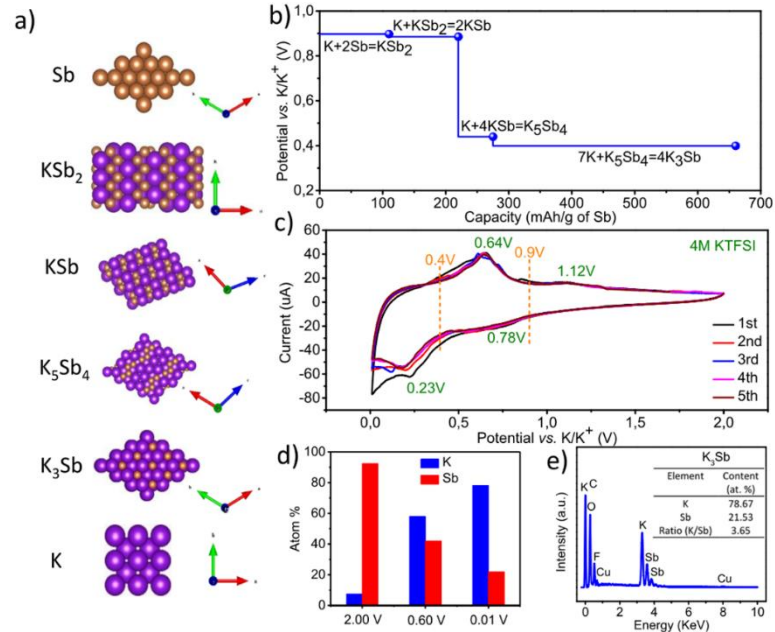


Figure 5.4. a) Crystal structure of K and stage structure evolutions from Sb to K₃Sb during potassiation process; b) DFT calculated equilibrium voltages (vs. K/K⁺) for the potassiation process; c) CV curves for Sb@CSN electrode at scan rate of 0.05 mV/s; d) Relative atom% of K and Sb from EDS with different discharge cut-off voltage; e) EDS element analysis for K₃Sb with discharge cut-off voltage of 0.01 V. (Cells from d-f are all in 4M KTFSI electrolyte)

According to the potassium-antimony binary phase diagram (**Figure 5.9a**), there are four intermediate phases from KSb₂, KSb, K₅Sb₄ to K₃Sb along with the increasing of K content, and the corresponding crystalline structures are exhibited in **Figure 5.4a**. The equilibrium potential for the reaction process of K with Sb was obtained using first-principles computations based on density functional theory (DFT). As can be seen from Figure 5.4b, the thermodynamic equilibrium potentials of KSb₂ and KSb are 0.89 V and 0.849 V, respectively. Similarly, the two adjacent equilibrium potentials of K₅Sb₄ and K₃Sb

are 0.439 V and 0.398 V, respectively. The K concentration in K_xSb interphases corresponds to the $X= 0.5, 1.0, 1.25,$ and 3.0 with a theoretical capacity of 108, 216, 270, 660 mAh/g, occupying the total capacity percentage of 16.4%, 16.4%, 8.2%, and 59.1%, respectively. Furthermore, two prominent potential platforms can be clearly found in the calculated potential profile, corresponding to the equilibrium potentials of the above-mentioned interphases. A dramatic potential drop from around 0.9 V to 0.4 V when the capacity excess 216 mAh/g; subsequently, the potential profile slowly decreases from 0.439 V to 0.398 V, with the formation of K_3Sb .

Electrochemical behavior of $Sb@CSN$ anode was evaluated using cyclic voltammetry (CV) at a scan rate of 0.05 mV/s in coin cells using K as counter electrode and 4M KTFSI/EC+DEC (abbreviated as “4M KTFSI”) as electrolyte. As displayed in Figure 5.4c, two pairs of redox peaks at approximate 0.4 V and 0.9 V potentials can be observed in the CV curve during the alloying/de-alloying process, in consistence with the calculated intermediate K_xSb phases located at around 0.9 V and 0.4 V in Figure 5.4b. The alloying peak located at around 0.78 V in potassiation process should be attributed to the stepwise alloying reaction of Sb to form KSb_2/KSb . Furthermore, the similar equilibrium reaction voltage between these two intermediates leads to an appearance of the overlap broad peak at 0.78 V. Another reduction peak centered at about 0.23 V is also an overlap broad peak, which was resulted from the approximate formation voltage for both K^+ insertion in C and the step formation of K_5Sb_4 and K_3Sb alloys.¹⁹² Based on the potential-capacity curve in Figure 5.4b, the formation of K_3Sb occupied a large proportion of theoretical capacity (58.5%), which is the reason why the peak at 0.23 V is larger than that of 0.78 V. The peaks voltage both at 0.78 V and 0.23 V are slightly lower than that of the

corresponding value from theoretical calculation, which is primarily due to the overpotential. On the reversed anodic scan, there is a distinct anodic peak at 0.64 V and a minor oxidation peak at 1.12 V, which is due to the extraction reaction of K during depotassiation reaction. In similar manner, the peaks of K_3Sb and K_5Sb_4 overlap with each other to form a new broad apparent peak at 0.64 V but an inconspicuous peak of KSb and KSb_2 at 1.12 V. In the same situation of overpotential, these oxidation peaks gradually shifted to higher potentials when compared with the theoretical values. Owing to SEI film formation during the first cathodic scan, a lower current peak at the initial cycle is observed, slightly distinguished from subsequent cycles where the SEI layer has already formed.¹⁹³ However, after the second and subsequent reduction/oxidation scans, the CV curves keep stable in their shapes and current intensities. Therefore, the CV curves demonstrate that the $Sb@CSN$ material can perform reversibly alloy/de-alloy reaction with K at potential region of 0.01-2.0 V.

Energy dispersive spectroscopy (EDS) elemental mapping was carried out to investigate the chemical composition of the formed interphases during charging/discharging process. Figure 5.4d shows the atomic percentages of K/Sb from the $Sb@CSN$ electrode taken at different cut-off voltages (2.0, 0.6, and 0.01 V) during the 5th discharge process. The ratio of K/Sb can provide insight into the composition of the alloy interphase at each cut-off voltage. Obviously, along with the increasing discharge depth from 2 V to 0.01 V, the atomic ratio of K to Sb increases, indicating deeper K alloying reaction with Sb. Notably, the ratio of K/Sb maintains a constant value of 3.65 in EDS elemental mapping when the cut-off voltage is 0.01 V (Figure 5.4e), slightly higher than that of the K_3Sb , which is probably attributed to the unclean-washed potassium salt from

the electrolyte. Furthermore, as shown in Figure 5.9b-f, the elements of C, K and Sb have an even distribution in nanometer scale among Sb@CSN electrode even at the highest discharge depth of 0.01 V.

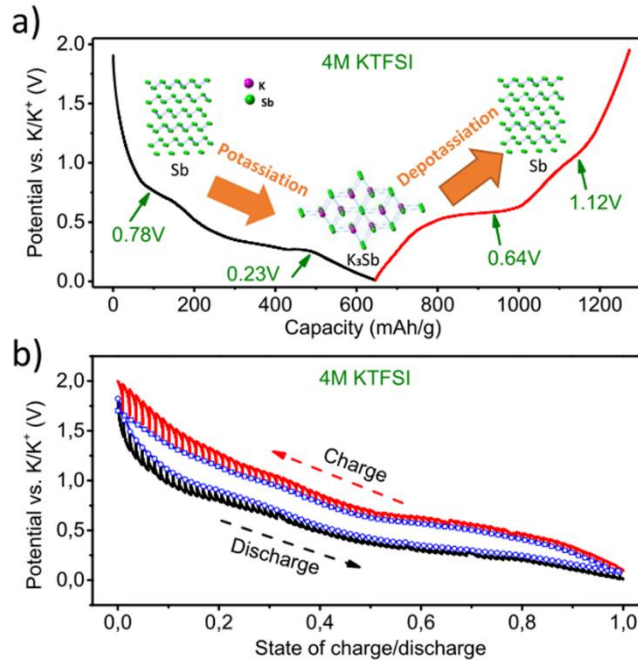


Figure 5.5. Electrochemical K storage properties for Sb@CSN in the 4M KTFSI electrolyte. a) Typical 2nd charge/discharge profile at 50 mA/g; b) quasi-equilibrium voltage profile from galvanostatic intermittent titration technique (GITT) at 100 mA/g.

Figure 5.5a shows the galvanostatic charge/discharge behavior of Sb@CSN in 4M KTFSI concentrated electrolyte at a low current density of 50 mA/g in the second cycle after the formation of SEI. The mass capacities of Sb were calculated by subtracting the corresponding capacity contributed from CSN. The CSN material without any Sb provide 110 to 180 mAh/g capacity at current of 50-200 mA/g, as shown in **Figure 5.10**. In this work, evidently, the voltage profile exhibits two prominent discharge voltage plateaus, located at about 0.78 V ending with a capacity of about 216 mAh/g and 0.23 V ending with ~646 mAh/g, corresponding to the potassiation reaction of Sb to KSb_2/KSb and

K_5Sb_4/K_3Sb , respectively; and two charge platforms were found at 0.64 V and 1.12V, which can be attributed to the extraction reaction of K from K_3Sb to Sb. Both the platform voltages and intensity of these two discharging/charging plateaus are in good agreement with the above-mentioned CV experimental results and calculated voltage profile. **Figure 5.11** shows the first galvanostatic charge–discharge profile of the Sb@CSN anode at the same current and electrolyte. In the first charge/discharge cycle, Sb@CSN anode delivered an initial alloying and de-alloying capacity of 1049 and 640 mAh/g, respectively, leading to a low coulombic efficiency (CE) of 61%. It can be ascribed to the formation reaction of irreversible SEI layer on the surface of electrode, which is consistent with the reported results of Sb anode.¹⁹⁴ The quasi-thermodynamic equilibrium potential and K^+ diffusivity coefficient in Sb@CSN was measured using the galvanostatic intermittent titration technique (GITT) after 10 charge/discharge activation cycles, as indicated in Figure 5.5b.¹⁹⁵ The cell was discharged/charged at a current pulse of 100 mA/g for a duration period of 20 min, followed by an open-circuit stand for 120 min to allow fully relaxation back to its quasi-equilibrium potential. The quasi-equilibrium potential at different normalized K insertion/extraction levels are indicated by the blue dotted lines in GITT. The potential difference between end of charge/discharge and end of relaxation period represents the overpotential at the corresponding depotassiation/potassiation stage.¹⁹⁶ It can be observed that the overpotential for the depotassiation and potassiation process is as low as 0.15 V even at a high current of 100 mA/g, suggesting a fast K^+ diffusion in Sb@CSN material. Furthermore, the four successive GITT curves displayed in **Figure 5.12** demonstrated a reversible potassiation/depotassiation process with a repeatable overpotential of as low as

0.15 V. These results strongly suggest that a fast and reversible depotassiation/potassiation dynamics can be achieved for the prepared Sb@CSN material in the 4M KTFSI electrolyte.

The cycle stability for the as-prepared Sb@CSN material was investigated in 1M KTFSI/EC+DEC (abbreviated as “1M KTFSI”) dilute and 4M KTFSI concentrated electrolytes, respectively. **Figure 5.6a** presents the cycling stability and its corresponding CE during 100 cycles charge/discharge cycles at 100 mA/g in 1M and 4M KTFSI electrolyte. Specifically, the capacity of the Sb@CSN anode in 4M KTFSI electrolyte exhibits exceptional reversibility and cycling stability, maintaining a stable capacity of 551 mAh/g over 100 cycles with a high average CE of > 98% and a low capacity decay of 5.3% from 10th to 100th cycling; while the capacity of Sb@CSN material in 1M KTFSI electrolyte fades rapidly, only 286 mAh/g left at 100th cycles with fluctuant average CE of 95%. Similarly, the capacity of Sb@CSN anode in the common dilute 1M KPF₆/EC+DEC electrolyte also delivers a rapid capacity loss, with a discharge capacity of 603 mAh/g at 2nd cycling but only 256 mAh/g after 100 cycles, as indicated in **Figure 5.13**, suggesting the significant improvement of the electrochemical K-storage performance of Sb@CSN material by electrolyte optimization. Furthermore, the cycled Sb@CSN material also maintained complete sphere morphology with uniform Sb nanoparticles well-defined encapsulated in the carbon sphere (**Figure 5.14**), indicating excellent structure stability and efficient relief of the huge volume change (456.7%) during electrochemical reactions. These advanced properties should be ascribed to the well-designed carbon sphere matrix which can not only provide more space from its porous structure and defects to accommodate the volume change,¹⁹⁷ but also possesses excellent flexibility and good

adhesion to Sb nanoparticles to remarkably stabilize the Sb nanoparticles and reduce the strain during the volume change process, protecting the CSN from cracking.¹⁹⁸

The impedance changes during charge/discharge cycles were measured using the electrochemical impedance spectroscopy (EIS). **Figure 5.15** show the impedance of Sb@CSN before and after 100 cycles in 1M and 4M KTFSI electrolyte. The fresh Sb@CSN shows similar impedance in both 1M and 4M KTFSI electrolyte with a depressed semicircle for electron-involved reaction and a slop line for diffusion. It is worth noting that the initial charge transfer resistance in 4M electrolyte is higher than that in 1M electrolyte before cycling, which should be attributed to the higher viscosity of 4M KTFSI concentrated electrolyte that leads to a lower Li^+ conductivity and slow Li^+ mobility in the electron-involved reaction. After the 100 charge/discharge cycles, only a small increase in electron-involved reaction impedance is observed for Sb@CSN in 4M KTFSI electrolyte, while a large electron-involved reaction impedance increase is demonstrated in 1M KTFSI electrolyte. This result can be probably attributed to the formation of robust potassium solid electrolyte interface (SEI) layer on Sb@CSN in the 4M electrolyte.

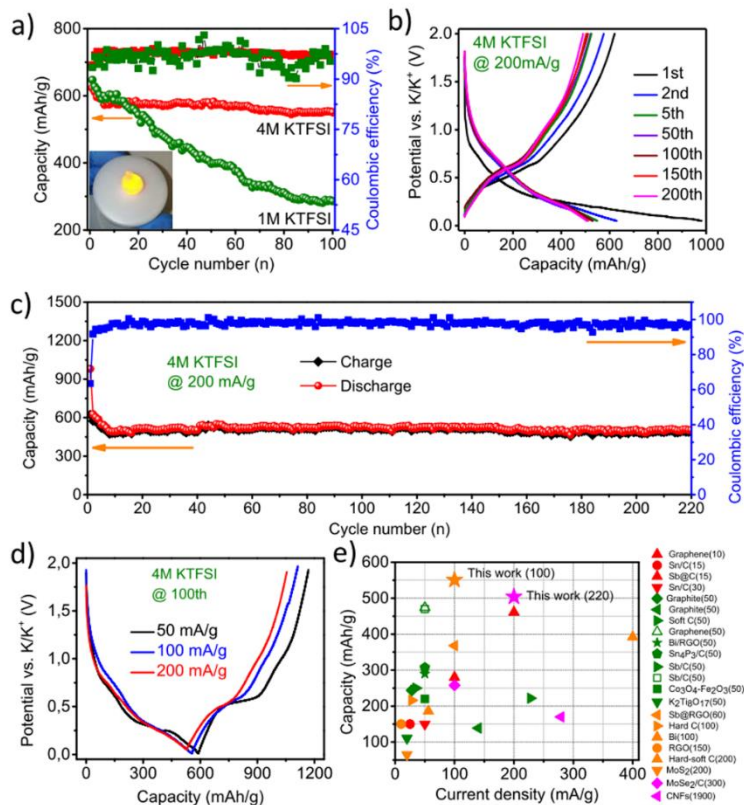


Figure 5.6. Electrochemical performance for Sb@CSN anode: a) cycling performance at 100 mA/g in 1M KTF SI and 4M KTF SI electrolyte (Inset: Lighting electronic candle with a coin cell in 4M KTF SI electrolyte after 100 cycles); b) charge/discharge curves and c) its corresponding cycling performance at 200 mA/g in 4M KTF SI electrolyte; d) The 50th charge/discharge curves under various current densities from 50 to 200 mA/g; e) Capacity comparison of Sb@CSN anode with previous reported anodes in PIBs, the numbers in brackets is the cycle numbers, the color code represents the cycling number range: red is < 50 cycles, olive is 50 cycles, orange is 50 to 200 cycles, magenta is > 200 cycles.

The long-term cycling stability of Sb@CSN composite in 4M KTF SI electrolyte at a high current density of 200 mA/g was also evaluated. As shown in Figure 5.6b-c, Sb@CSN at 200 mA/g in 4M KTF SI still provide a high discharge capacity of 626 mAh/g at 2nd cycle, which is very close to its theoretical capacity of 660 mAh/g (corresponding to the formation of K₃Sb). The capacity slightly decreases in the initial 10 cycles and then stabilizes at 504 mAh/g over 200th cycles. Correspondingly, the CE increases in the first 10 cycles and then approaches to a consistent value of 98%. These results manifest a

reversible alloying-dealloying process between the formation of Sb and K_3Sb even at such a high current density. Furthermore, Figure 5.6d displays the charge-discharge profiles at various current densities after 50 cycles. The charge/discharge capacity only slightly decreases when increasing the current density from 50, 100 to 200 mA/g, along with a slight capacity decay from 589 mAh/g, 566 mAh/g to 530 mAh/g, respectively, which indicates excellent rate capability for the unique nanostructured Sb@CSN in 4M KTFSI electrolyte. Moreover, the voltage plateaus at various current densities show small differences, indicating only minor electrochemical polarization augment when increasing to a higher current.

Figure 5.6e and **Table 5.1** compared the electrochemical performance of the Sb@CSN in 4M KTFSI electrolyte with reported K-ion battery anodes, including carbon-based anodes, metal alloy anodes, metal oxide (sulfide) anodes. It can be found that the Sb@CSN can achieve a high specific capacity of 551 mAh/g at 100 mA/g over 100 cycles with a capacity decay of 0.06% per cycle from the 10th to 100th cycling and 504 mAh/g at a high current density of 200 mA/g even after 220 cycles, which are much better than all reported K-ion battery anodes. Such excellent performance should be attributed to (i) the carbon sphere network which not only acts as the efficient conductive skeleton but also as the buffering for huge volume expansion of Sb nanoparticle during alloying/de-alloying reaction process, (ii) the small Sb crystallite with an average size of 14 nm which benefits to decrease K^+ diffusion distance, and (iii) the concentrated 4M KTFSI electrolyte employed here which can promote the formation of robust SEI to obtain good reversibility for the alloying/de-alloying reaction process.

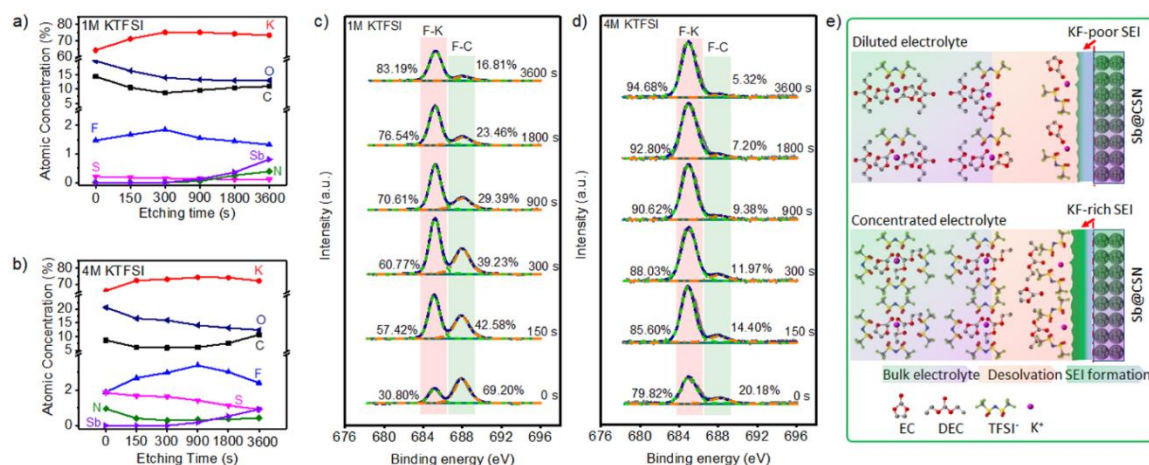


Figure 5.7. a, b) Atomic percentage concentrations of different elements with increasing etching time and c, d) corresponding high-resolution F1s XPS spectra for the Sb@CSN electrode in a, c) 1M KTFSI and b, d) 4M KTFSI electrolyte; e) Illustration of the influence of dilute and concentrated electrolytes on the formation of SEI layer.

The SEI compositions formed on Sb@CSN electrodes in 4M KTFSI and 1M KTFSI electrolytes were analyzed using X-ray photoelectron spectroscopy (XPS) coupled with Ar⁺ etching technique. As demonstrated in **Figure 5.7a** and **b**, the signal of Sb element at the etching time demonstrated that the SEI in 4M KTFSI electrolyte is thinner than that in 1M KTFSI electrolyte (**Table 5.2**). Moreover, the SEI layer formed in 4M KTFSI electrolyte delivers an obviously lower C at.% and higher F at.% than that formed in the 1M KTFSI electrolyte, indicating that F-rich and inorganic-dominated SEI layer is preferred to be formed in the 4M concentrated electrolyte.¹⁹⁹ Figure 5.7c and d show the high resolution F1s XPS spectra for the electrode surface in 1M KTFSI and 4M KTFSI electrolyte, respectively. Two main signal peaks centered at 685.0 and 688.1 eV in the both electrolytes are assigned to F-K bonds and F-C bonds, respectively.²⁰⁰ It can be found that at the outside surface (corresponding to etching time of 0 s) of Sb@CSN electrode in 1M KTFSI electrolyte, 69.20 at.% of F element exists as organic F-C bonds, suggesting an organic property of this surface. With the increasing etching time, the content of F-C bonds

decreases gradually to 16.81 at. %, indicating the changes of SEI composition from organic sublayer to organic-inorganic hybrid sublayer. By contrast, the content of F-C bonds in the SEI layer formed in 4M KTFSI electrolyte is distinctly lower than that formed in 1M KTFSI electrolyte at all the etching times, resulting to a F-K dominated bonding property for the F element in the SEI layer. These results suggest a more inorganic SEI layer with abundant KF phase was formed in the concentrated 4M KTFSI electrolyte, well consistent with the previous report.¹⁸¹ The high concentrated KTFSI electrolyte can weaken the solvent reduction and lead the reduction of KTFSI to mainly induce the formation of KF-rich SEI.

As demonstrated in Figure 5.7e, during the formation of SEI layer, K^+ , $TFSI^-$ and solvent molecules should first reach to the electrode/electrolyte interface and then react irreversibly. It's much easier for the concentrated electrolyte to provide more $TFSI^-$ ions with abundant F element to reach the interface and then participate the SEI formation reaction in a faster kinetic way than in the 1M diluted electrolyte. Accompanied by the condition of concentrated K^+ , a denser and thinner KF-rich SEI layer was preferred to be formed in 4M KTFSI electrolyte. Such a robust KF-rich SEI layer can not only protect the active materials from further reacting with the electrolyte, but also accommodate the volume change of Sb@CSN, thus leading to excellent K-storage performance for such a material. In addition, the high concentrated KTFSI also reduce the solubility of KF in electrolyte, further stabilizing the KF-rich SEI for excellent long-term cycling property.

The high concentrated electrolyte can also reduce the flammability. The flammability of electrolytes was evaluated by soaking a piece of glass fiber membrane with 0.5 mL electrolyte and then immediately igniting it with butane lighter, as illustrated in

Figure 5.16. The flame for the 4M KTFSI electrolyte is much smaller and darker than that of the dilute electrolyte and the same concentrated 4M KClO_4 electrolyte. After the combustion, the glass fiber in 4M KTFSI electrolyte is black due to the fire retardation and incomplete combustion resulting from the stable and high concentrated KTFSI salt. By contrast, it is white for the dilute electrolyte, indicating the complete combustion of the electrolyte. For the 4M KClO_4 electrolyte, an obvious explosion can be observed due to the strong oxidization property of KClO_4 . Therefore, the high concentrated 4M KTSFI electrolyte is suitable for highly secure batteries with less fire-severity and lower fire-catching properties.

5.4. Conclusions

In summary, Sb@CSN composite anode with evenly-distributed and small Sb nanoparticles confined in carbon sphere network has been successfully prepared for K-ion battery anode via unique electrospray-assisted strategy. Sb@CSN anode in the concentrated 4M KTFSI electrolyte shows a high reversible capacity of 551 mAh/g at 100 mA/g over 100 cycles with a capacity decay of 0.06% per cycle from the 10st to 100th cycling and 504 mAh/g after 220 cycles even at a high current density of 200 mA/g. It also shows excellent rate performance by providing 589 mAh/g at 50 mA/g and 530 mAh/g at 200 mA/g. Such a unique material in this concentrated electrolyte demonstrates one of the best capacity performances among all K-ion battery anode materials. These excellent K-storage performances should be ascribed to the formation of stable and robust KF-rich SEI layer along with the novel nanostructure of Sb nanoparticles uniformly encapsulated into the conductive carbon network. These discoveries provide valuable guidance for rationally developing advanced alloy-based electrode materials for high-performance PIBs applications.

5.5. Supporting Information

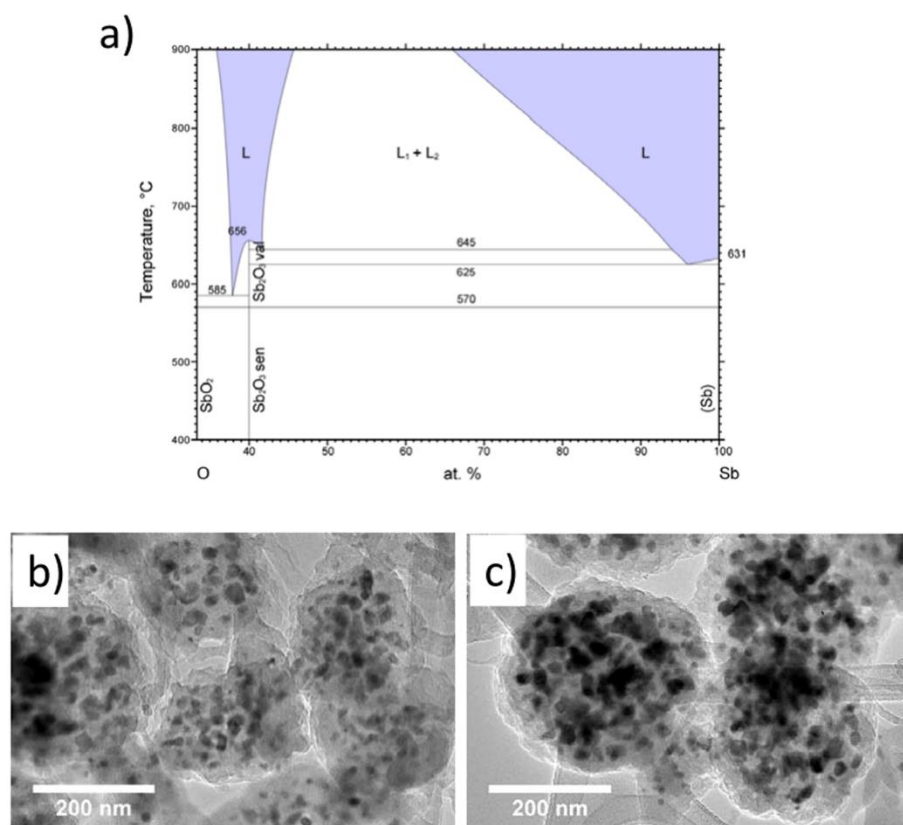


Figure 5.8. a) Oxygen-antimony binary phase diagram²⁰¹; b-c) TEM images of Sb nanoparticles in associated carbon sphere network.

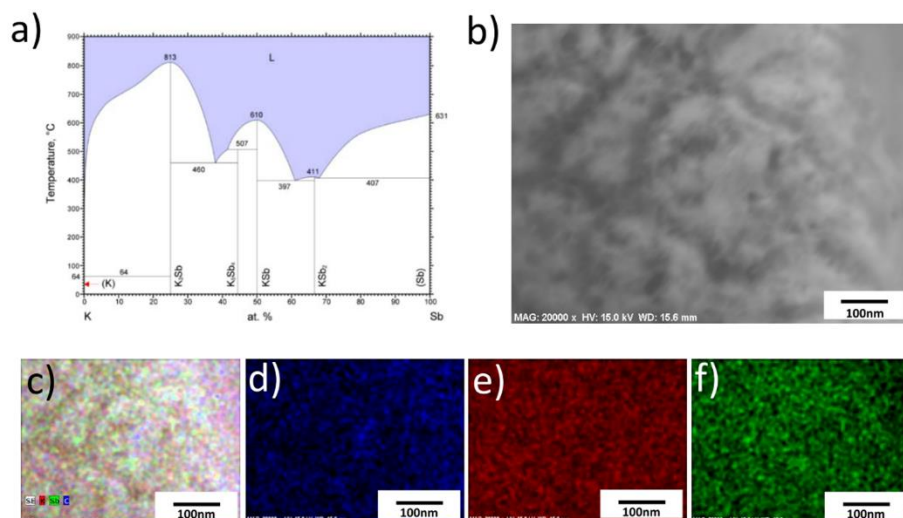


Figure 5.9. a) Potassium-antimony binary phase diagram; b) SEM image and c-f) the corresponding EDS elemental mapping of Sb@CSN electrode at discharge cut-off voltage of 0.01 V in 4M KTFSI electrolyte.

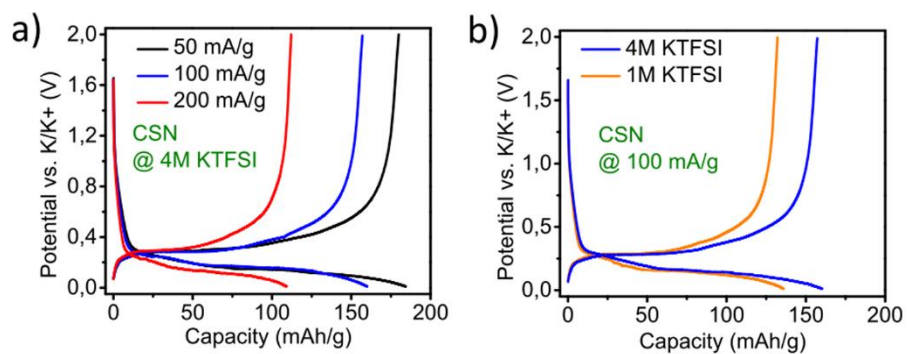


Figure 5.10. Charge/discharge curves for CSN material a) in 4M KTFSI electrolyte with different current densities, b) in different electrolytes.

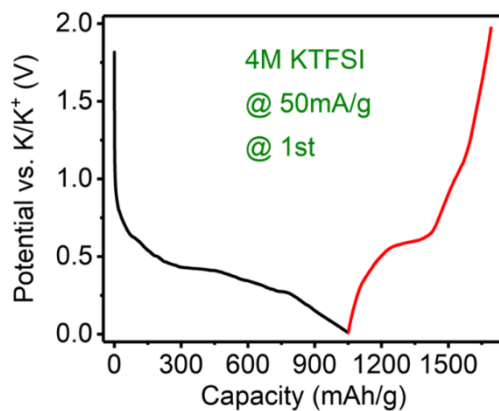


Figure 5.11. 1st charge/discharge voltage profile for Sb@CSN electrode at 50 mA/g in 4M KTFSI electrolyte.

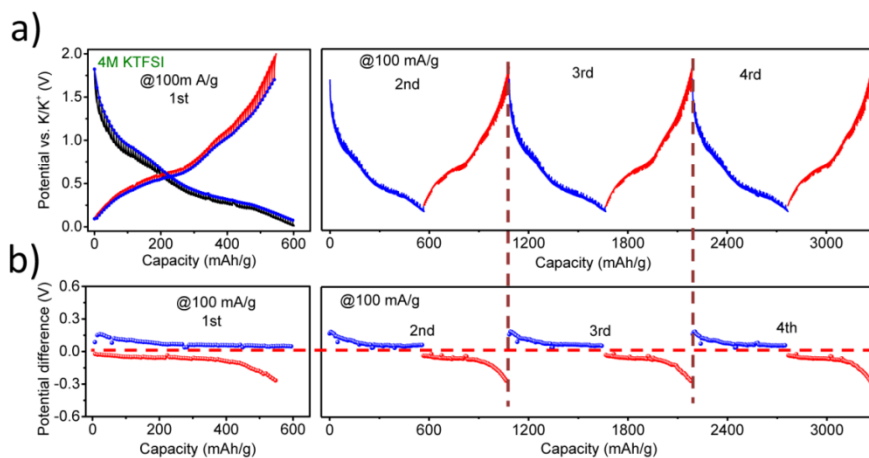


Figure 5.12. a) four successive GITT curves after 10 activation cycles; b) the potential difference curves for the successive GITT curves in 4M KTFSI electrolyte (Potential difference= rest end potential - rest initial potential).

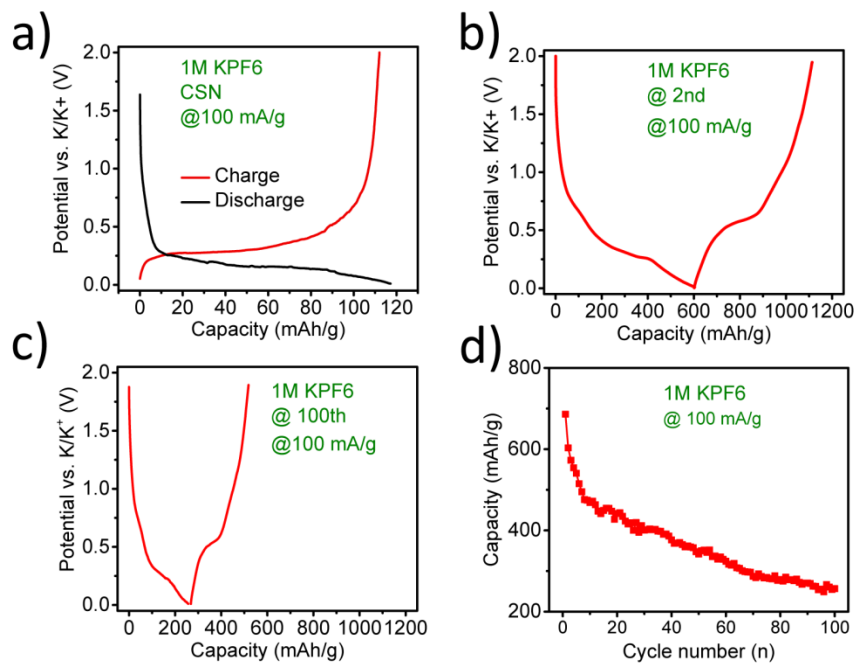


Figure 5.13. Electrochemical performance in 1M KPF₆ electrolyte: a) charge/discharge curves for CSN material; charge/discharge curves for Sb@CSN anode at b) 2nd and c) 50th cycling; d) its corresponding cycling performance.

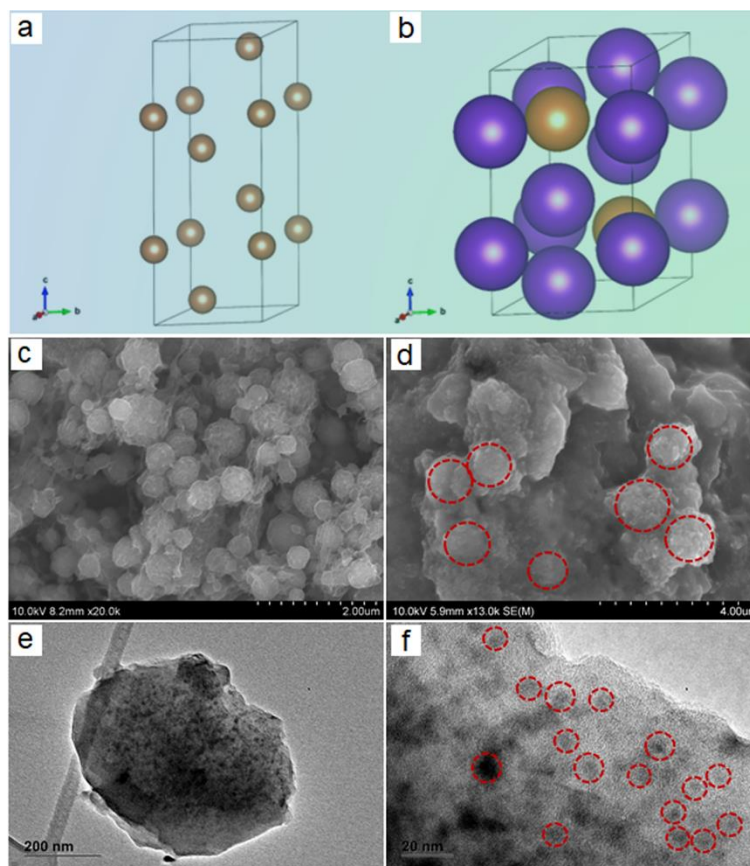


Figure 5.14. a, b) Crystal structures of a) Sb (space group: $R3m[166]$) and b) K_3Sb (space group: $P63/mmc[194]$); c, d) SEM images of c) fresh prepared Sb@CSN and d) cycled Sb@CSN; e, f) TEM images of cycled Sb@CSN.

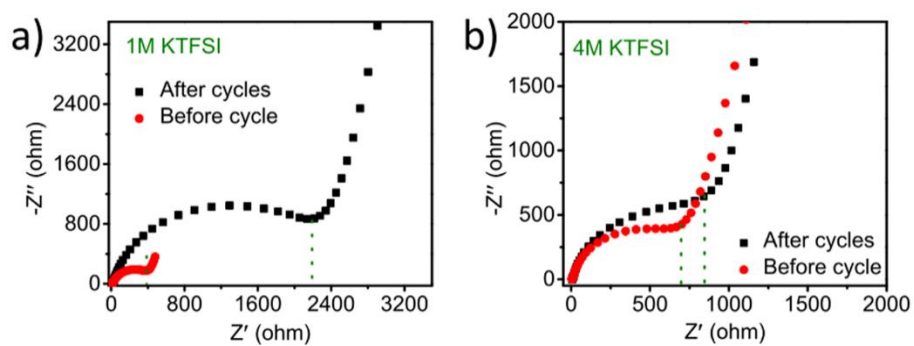


Figure 5.15. EIS curves before and after 100 cycling at 100 mA/g in a) 1M KTFSI and b) 4M KTFSI electrolyte.

Table 5.1. A comparison summary of potassium storage performances for the most common anodes materials in the previous reports.

Samples	Current density (mA/g)	Cycle number	Capacity (mAh/g)	Reference
Graphene	100	10	280	202
Sn/C	150	15	25	171
Sb@C	200	15	461	203
Sn/C	25	30	150	204
Graphite	28	50	244	168
Graphite	140	50	139	167
Soft C	228	50	222	167
Graphene	50	50	474	205
Bi/RGO	50	50	290	204
Sn ₄ P ₃ /C	50	50	307	206
Sb/C	35	50	250	179
Sb/C	50	50	470	204
Co ₃ O ₄ -Fe ₂ O ₃	50	50	220	207
K ₂ Ti ₈ O ₁₇	20	50	110	208
Sb@RGO	100	60	368	209
Hard C	28	100	216	210
Bi microparticle	400	100	392	211
Sb@CSN	100	100	551	This work
RGO	10	175	150	169
Hard-soft C	56	200	186	212
MoS ₂	20	200	65	213
Sb@CSN	200	220	504	This work
MoSe ₂ /C	100	300	258	214
CNFs	279	1900	170	215

Table 5.2. Atomic percentage concentrations of different elements with increasing etching time for the SEI layers on Sb@CSN electrode formed in 1M KTFSI and 4M KTFSI electrolytes.

Electrolytes	Etching times	C(at.%)	K(at.%)	F(at.%)	S(at.%)	N(at.%)	O(at.%)	Sb(at.%)
1M KTFSI	0s	14.3	64.2	1.47	0.21	0	19.8	0
	150s	10.5	71.3	1.67	0.18	0	16.3	0
	300s	8.71	75.3	1.84	0.15	0	13.9	0
	900s	9.62	75.3	1.55	0.14	0.05	13.2	0.11
	1800s	10.5	74.4	1.44	0.1	0.25	13	0.36
	3600s	11	73.5	1.32	0.11	0.39	13	0.81
4M KTFSI	0s	8.67	65.99	1.89	1.86	0.95	20.63	0
	150s	6.18	72.44	2.69	1.67	0.41	16.6	0
	300s	5.93	73.19	2.98	1.63	0.3	15.97	0
	900s	6.13	74.43	3.39	1.42	0.33	14.12	0.18
	1800s	7.56	74.22	3.02	1.13	0.36	13.18	0.53
	3600s	10.72	72.18	2.41	0.92	0.43	12.42	0.92

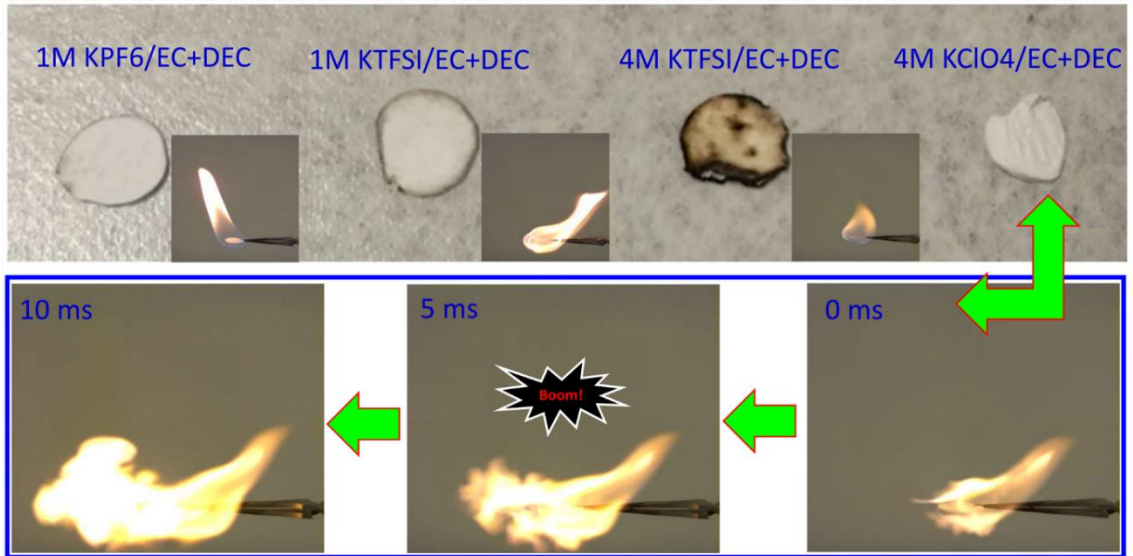


Figure 5.16. Ignition and combustion experiments for different electrolytes used in PIBs.

Chapter 6: Aerosol synthesis of high entropy alloy nanoparticles[§]

Abstract: Homogeneously mixing multiple metal elements within a single particle may offer new material property functionalities. High entropy alloys (HEA), nominally defined as structures containing 5 or more well-mixed metal elements, are being explored at the nanoscale, but scaleup to enable their industrial application is an extremely challenging problem. Here, I report an aerosol droplet-mediated technique toward scalable synthesis of high entropy alloy nanoparticles with atomic-level mixing of immiscible metal elements. An aqueous solution of metal salts is nebulized to generate $\sim 1 \mu\text{m}$ aerosol droplets, which when subjected to fast heating/quenching, result in decomposition of the precursors and freezing-in of the zero-valent metal atoms. Atomic-level resolution scanning transmission electron microscopy (STEM) coupled with energy dispersive X-ray spectroscopy (EDS) analysis reveals that all metal elements in the nanoparticles are homogeneously mixed at the atomic level. I believe this approach offers a facile and flexible aerosol droplet-mediated synthesis technique that will ultimately enable bulk processing starting from a particulate HEA.

[§] The results represent in this chapter have been submitted to a peer-review journal and are under review: Yong Yang, Boao Song, Xiang Ke, Feiyu Xu, Krassimir Bozhilov, Liangbing Hu, Reza Shahbazian-Yassar, Michael R. Zachariah, Aerosol Synthesis of High Entropy Alloy Nanoparticles. 2019, *under review*.

6.1. Introduction

Combining multiple metals into one single particle at nanoscale enables the formation of multicomponent metal nanoparticles with unique physical and chemical properties.⁶⁶ The electronic interactions between different metal components, make them potentially promising materials for a broad range of applications in the fields of catalysis, plasmonics, nanomedicine, and electronics.⁶⁷ Among all the multicomponent metallic nanostructures investigated, the attention on high entropy alloy nanoparticles have been growing dramatically. High entropy alloys represent such nanostructures, defined as five or more well-mixed metal elements in near equimolar ratios.⁶⁸ The maximized interactions between different metal atoms leads to the formation of the unique architectures with a high configurational entropy of mixing, resulting in advanced properties, including high mechanical strengths at high temperature, high corrosion resistance, and high oxidation resistance, among others.⁶⁹

To date, the primary techniques used to produce multicomponent metal nanoparticles, either in an alloyed or phase-separated state, are wet-chemistry based approaches, including bulk solution synthesis⁷⁰, microfluidic method⁷¹, and microemulsion⁷². However, forming metallic nanostructures containing more than three metal elements using traditional wet-chemistry approaches becomes challenging due to the increasing difficulty arising from balancing diverse reduction kinetics of different metal precursors. This often results in site-selective nucleation of each metal and the formation of nanoparticles with components and structures varying from particle to particle. In order to address this issue, a site-specific lithography-based synthesis technique has been recently reported to fabricate multicomponent metal nanoparticles containing five metal

elements by confining the corresponding metal precursors in a small reaction volume on a desired site followed by hydrogen reduction procedures at elevated temperatures.⁷³ Although this technique has greatly expanded the composition and structure diversities of multicomponent metal nanoparticles, phase-separated nanostructures were always generated when incompatible metal elements (like Cu and Co) were used. The reason is that the slow heating and slow quenching applied in the hydrogen reduction procedures in this technique caused multi-component nanoparticles to reach their thermodynamically favorable phase-separation state. Alternatively, melting processing has been developed to create bulk-size multicomponent alloys with uniformly mixed metal atoms - high entropy alloy, via melting and quenching physically mixed multiple metals.⁷⁴ However, a recent study on atomic distributions of Al_{1.3}CoCrCuFeNi alloy generated via the melting technique reveals that Cu rich precipitates were formed in the final product.⁷⁵ Furthermore, although melt processing has been successful in the synthesis of bulk high entropy alloys as structural materials, generating high entropy alloys at the nanoscale is extremely difficult with this technique.

Recently a carbothermal shock (CTS) technique was developed to incorporate multiple immiscible metal elements into a single nanoparticle.³⁶ This technique involves an ultrafast electric heating step to thermally decompose carbon matrix-supported metal salt mixtures into liquid metals particles and a subsequent ultrafast quenching step to produce solid state high entropy alloys nanoparticles containing well-mixed immiscible metal elements. With this technique, I was able to alloy up to eight metal elements into single-phase solid-solution nanoparticles uniformly dispersed on carbon supports. Although I have demonstrated the advantage of the technique over size and composition

control on high entropy alloys nanoparticle synthesis, this joule heating assisted thermal shock technique is limited to electrically conductive matrices and is not suitable for large-scale production of high entropy alloy nanoparticles.

Building on that work however, I provide an aerosol droplet mediated approach towards scalable synthesis of high entropy alloy nanoparticles with atomic-level mixing of immiscible metal elements. Rather than pre-depositing metal salt mixture precursors onto a carbon support, I nebulize the precursors into aerosol droplets with a diameter less than 1 μm , and employ a fast heating and fast quenching treatment. As such each droplet contains precursors and operates as a nanoreactor, with very low thermal mass to enable rapid heating/cooling and small length scales to ensure no thermal and mass transfer gradients within the particle enabling one to produce a single high entropy alloy nanoparticle. I demonstrate aerosol-mediated formation of five-element high entropy alloy nanoparticle containing Ni, Co, Cu, Fe, Pt, Pd, chosen as example elements because of their applications in a broad range of fields including catalysis, magnetics, electronics. Atomic-level resolution scanning transmission electron microscopy (STEM) coupled with energy dispersive X-ray spectroscopy (EDS) analysis reveals that all metal elements (containing incompatible metals like Co and Cu) in the nanoparticles are mixed together on an atomic level. The advantages of using aerosol droplets mediated technique are: 1) all metal salts are pre-confined into small droplets enabling incorporating different metals in same particles upon the heating and quenching process; 2) the small mass and volume nature of the aerosol droplets enables fast heating and fast cooling, which is crucially important to achieve kinetic control over the thermodynamic mixing regimes and creation of high entropy alloy nanoparticles; 3) metal salt ratios in the aerosol droplets reflect metal

ratios in the precursor solution so that component and composition of final products can be tuned by simply adjusting the type and ratio of metal salts in the precursor solution; 4) since this technique is a continuous process, scaling-up will be greatly simplified.

6.2. Experimental section

Materials. Nickel nitrate hexahydrate ($\text{Ni}(\text{NO}_3)_2 \cdot 6\text{H}_2\text{O}$, $\geq 99\%$ pure), cobalt nitrate hexahydrate ($\text{Co}(\text{NO}_3)_2 \cdot 6\text{H}_2\text{O}$, $\geq 99\%$ pure), iron nitrate nonahydrate ($\text{Fe}(\text{NO}_3)_3 \cdot 9\text{H}_2\text{O}$, $\geq 99\%$ pure), copper nitrate trihydrate ($\text{Cu}(\text{NO}_3)_2 \cdot 3\text{H}_2\text{O}$, $\geq 99\%$ pure), nickel nitrate hexahydrate ($\text{Ni}(\text{NO}_3)_2 \cdot 6\text{H}_2\text{O}$, $\geq 99\%$ pure), palladium chloride (PdCl_2 , $\geq 99\%$ pure), chloroplatinic acid (H_2PtCl_6 , 99%) were all purchased from Sigma-Aldrich. All the chemicals were used as received.

Precursor preparation. The precursor solution was prepared by dissolving equimolar amount of metal salts into D.I. water. The total concentration of the metal salts in the solutions was 0.02M.

Aerosol droplet mediated synthesis technique. HEAs were synthesized using one-step aerosol spray pyrolysis technique. A schematic of the aerosol reactor including details of the geometry, flow rates, operation pressure, temperature profiles can be found in **Figure 6.5**. The experiment consists of a Collison nebulizer (BGI Inc.), a silica dryer, a silica tubular reactor heated by two combined tube furnace, and a membrane filter (Millipore, material: polycarbonate, pore size: 0.4 μm). In a typical experiment, the prepared precursor solution was loaded into the atomizer and was nebulized into small aerosol droplets using 10% H_2 /90% Ar mixture gas with a pressure of 30 psi . These droplets carried by the mixture gas were first passing through the silica dryer, where the water solvent evaporated from the droplets. Following the water solvent removal, the resulting dry aerosol particles moved into the high-temperature tubular furnace reactor (diameter: 2 cm; heating length: 60 cm, set temperature: 1100 $^\circ\text{C}$) where the fast heating led to the rapid decomposition and reduction of the metal salts to metals, and the subsequent

fast cooling resulted to the HEA formation. The products were collected with a membrane filter collector, which was blew with cooling air to achieve fast quenching of the product. The aerosol flow rate was ~ 3 L/min, which was measured at the end of the sample collector. Thus, based on the geometry of the aerosol reactor and the gas flow rate, the calculated residence time of the droplets in the high temperature reactor was about 3 s.

Finite element simulation of temperature profile of the gas flow in the tubular reactor: In order to estimate the temperature profiles of the aerosol gas flow in the tubular reactor, a finite-element simulation of the aerosol synthesis process was implemented using COMSOL Multiphysics software. The model including the tubular reactor and sample collector with the aerosol flow were constructed. I assumed that the temperature on the surface of the tubular reactor in the heating zone (length: 60 cm) was 1100 °C and the sample collector cooled with the cold air remained a temperature of 25 °C on its surface. With a gas flow rate of 3 lpm. The calculated Reynold number was ~ 30 . I expect the flow to be laminar, thus non-isothermal laminar flow module in the software was used for the model.

Characterization. The morphology, microstructure, and composition of the HEA nanoparticles were examined by SEM, TEM, STEM, EDS and XRD. SEM images were taken with a NS450 scanning electron microscope at an acceleration voltage of 18 kV. A JEOL ARM-200CF was used to image HEA nanoparticles deposited on lacey carbon Mo grid. High angle annular dark field (HAADF) and annular bright field (ABF) images were acquired by a spherical aberration corrected JEOL JEM-ARM 200CF STEM with a cold field emission gun operating at 200 kV, with 22 mrad convergence angle. Images were taken using an Orius CCD camera with 512×512 scanning resolution. Energy dispersive

X-ray Spectroscopy (EDS) analyzes and elemental mapping were obtained in the STEM mode (ThermoFisher Scientific Titan Themis 300 instrument, fitted with X-FEG electron source, 3 lens condenser system and S-Twin objective lens) at 300 kV, utilizing ThermoFisher Scientific SuperX system equipped with $4 \times 30 \text{ mm}^2$ window-less SDD detectors symmetrically surrounding the specimen with a total collection angle of 0.7 sr, by scanning selected area from the specimens. Elemental mapping by plotting the net X-ray counts was performed with an electron beam probe current of 550 pA at 1024×1024 frame resolution, dwell time of 30 $\mu\text{sec}/\text{pixel}$ and scanning multiple frames resulting in effective total acquisition time between 3 to 10 mins. EDS spectra were extracted from the elemental maps as well as by direct spectra acquisition from selected areas. Elemental concentrations were calculated using the Cliff-Lorimer ratio technique⁸⁸ using calculated k-factors, which have been verified experimentally to incorporate an error of less than $\pm 3\%$ by analyzing standard specimens with known composition of SiO_2 , SiC , TiO_2 and NiO and correcting for absorption. The minimum error in determining the elemental concentrations in the studied specimens is estimated from the statistical uncertainty in measuring the X-ray peak intensities which was less than 5% relative. The EDS spectra were used to quantify the composition of the HEA particles deposited on lacey carbon Au grid. The XRD analysis was performed on the nanoparticles collected on the membrane filter. The size distribution of HEA particles was analyzed using dynamic mobility analyzer (TSI, model 3081) coupled with a condensation particle counter (TSI, model 3776) on-line size analysis system (DMA-CPC).

6.3. Results and discussion

6.3.1. Methodology

Figure 6.1a exhibits a schematic of aerosol droplet-mediated approach toward scalable synthesis of high entropy alloy nanoparticles. Here, synthesis of NiCoCuFePt HEA nanoparticles is chosen to investigate synthesis-structure relationship. A detailed description including the reactor design and the operation parameters can be found in Experimental Section and in **Figure 6.5**. In a typical experiment, the precursor solution containing five types of metal salts with equal molar ratios mixed in D.I. water was nebulized to create aerosol droplets using a collision-type atomizer. The nebulized aerosol droplets, carried by a 10% H₂/90% Ar gas mixture, were passed through a silica dryer for water solvent removal, and the resulting dried aerosol particles composed of five mixed metal salt species were carried through a high-temperature reaction zone (~1100 °C) in which a rapid temperature increase (thermal shock) triggers rapid thermal decomposition and hydrogen reduction of the metal salts to metal, leading to the formation of high entropy alloy nanoparticles upon fast quenching. Particles exiting the reactor were collected on a membrane filter collector. The calculated residence time of the aerosol particles in the heating zone based on the geometry of the reactor and the flow rate is about 3 s.

Figure 6.1b shows the elemental distributions within a single NiCoCuFePt HEA nanoparticle with a ~60 nm diameter. I observe that Ni, Co, Cu, Fe, Pt elements are uniformly distributed in the nanoparticle and all five elements shown in the mixed EDS map are overlapped with each other, suggesting that HEA nanoparticles were successfully synthesized using the aerosol droplet-mediated approach. X-ray Diffraction pattern (XRD) (**Figure 6.6**) on the bulk samples suggests that the synthesized particles have a single-phase

structure without phase separation. This observation is further corroborated by the EDS data(**Figure 6.7**) which indicates the main phase of the particle is metallic containing all five metals (Ni, Co, Cu, Fe, Pt) with negligible oxygen content. The quantitative EDS analysis reveals that the composition of the HEA nanoparticle has deviated from the ideal composition with all five metals having a 20% atomic percentage. The atomic ratios in the synthesized nanoparticles are 19.16 % for Ni, 19.19 % for Co, 11.45 % for Cu, 24.59 % for Fe, 25.60 % for Pt. In particular, the percentage of Cu element is relatively low compared with the other metal elements in the nanoparticle. Similar result has also been observed on the high entropy alloy nanoparticles synthesized with the previously mentioned carbothermal shock approach.³⁶ The possible reason is the differences in vapor pressures between the various metals, with Cu having the highest vapor pressure (**Figure 6.8**). However, in our previous study, I employed a precursor compensation approach to balance the atomic ratio of volatile metals, (i.e. add more of one component) which is a commonly used strategy when volatile metals are involved in the synthesis.³⁶

The size of the dried aerosol particles containing multiple metal salts after water solvent removal was measured on-the-fly with a differential mobility analyzer (DMA) coupled with condensation particle counter (CPC). The operation principles can be found in our previous publication.¹⁹ The result shown in **Figure 6.9** indicates that the aerosol distribution has an average size of 92.0 nm with a 1.77 geometric standard deviation. The extremely small mass and volume of aerosol particles enables fast heating and fast quenching, which is crucially important to achieve kinetic control over the thermodynamic mixing regimes and creation of high entropy alloy nanoparticles. A simple heat transfer calculation indicates that a cold particle (25 °C) with a diameter of 100 nm can reach the

ambient in a few nanoseconds once introduced into high temperature environment (1100 °C), and vice versa.²¹⁶ Therefore, the aerosol particles were always at the local gas temperature, and the heating and cooling rates of the aerosol droplets became the heating and cooling rates of the aerosol gas flow in the tubular reactor. In order to estimate the temperature profiles of the gas flow in the tubular reactor, a finite-element simulation of the aerosol synthesis process was implemented using COMSOL Multiphysics software, and the result (**Figure 6.10**) suggests that the heating and cooling rates of the flow were about 10^3 K/s and 10^5 K/s, respectively, demonstrating the excellent fast heating and fast cooling nature of the aerosol process compared to the bulk batch reactors. In particular, the extremely high cooling rate is comparable to the cooling rate demonstrated in our carbon thermal shock work. The reason why such a high cooling rate was achieved is that once the high-temperature gas flow moved out of the heating zone, it was effectively quenched by the cold stainless-steel collector with a relatively large inner surface area.

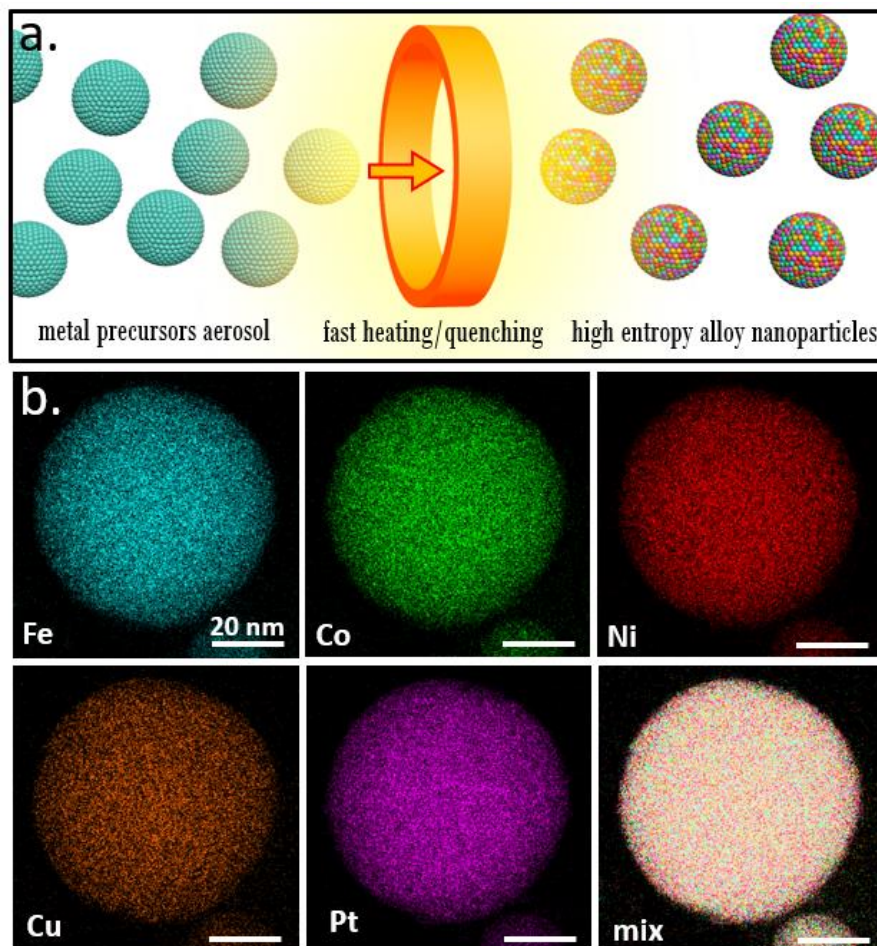


Figure 6.1. Aerosol droplet-mediated technique for scalable synthesis of high entropy alloy nanoparticles: a) schematic of the evolution of aerosol droplets during the high temperature treatment; b) EDS mappings for a single high entropy alloy nanoparticle.

6.3.2. Microstructure and composition analysis

Figure 6.2a and 6.2b show the morphology of the HEA nanoparticles examined using SEM and high angle annular dark field STEM (HAADF-STEM), respectively. The SEM image and the corresponding low-magnification HAADF-STEM image show these particles have a spherical morphology. The size distribution of the nanoparticles measured by DMA-CPC on-line size analysis system is shown in Figure 6.2c. The result shows that the nanoparticles have a number average diameter of ~ 58.6 nm, which is smaller than the average size (92 nm) of aerosol particles before the heat treatment. The decrease of particle

size is due to shrinking and densification of the aerosol nanoreactors caused by thermal decomposition and hydrogen reduction of metal salts to metals. However, the generated HEA nanoparticles have geometric standard deviation of 1.88, slightly larger than that of the corresponding metal salt aerosol particles without heat treatment. One possible reason is that gas byproducts released from the thermal decomposition and hydrogen reduction of the on-the-fly aerosol particles were trapped in the aerosol particles, causing the formation of voids in the nanoparticles, widening the size distribution of the final HEA particles. The presence of the void microstructure in the nanoparticles is observed in the collected STEM images, which is shown in **Figure 6.11**.

The microstructure of HEA nanoparticles was analyzed using atomic-scale STEM. Figure 6.2d and 6.2e display a HAADF-STEM image and a corresponding annular bright field STEM (ABF-STEM) image of a HEA nanoparticle to be investigated. In order to examine how all five metal atoms (Ni, Co, Cu, Fe, Pt) mix with each other in the single HEA nanoparticle, atomic-scale HAADF-STEM was performed on the red squares labeled regions of the corresponding HEA nanoparticle. The results shown in Figure 6.2f and 6.2h indicate that the nanoparticle has a crystalline structure with some atomic planes distortions. The atomic plane distortion might be attributed to difference between radii (ranging from 123 to 138 pm) of the five different metal atoms used (**Table 6.1**). The formation of the crystalline structure also indicates that the crystallization process was relatively fast compared to the residence time of the aerosol particles. Moreover, As shown in Figure 6.2g, the fast Fourier transform (FFT) analysis recorded along $\langle 100 \rangle$ zone axis shows six diffraction spots rendering two d-spacings of 1.98 and 1.33 Å, belonging to two lattice planes (200) and (220), respectively, suggesting that the HEA nanoparticle is compatible

with FCC crystalline structure. This observation is in accordance with the XRD data shown in **Figure 6.6**, and is also consistent with the result obtained for the high entropy alloy nanoparticles fabricated using the carbothermal shock technique reported in our previous study.³⁶

Note that the five-element high entropy alloy nanoparticles investigated here contains four metal elements with similar atomic masses (Ni, Co, Cu, Fe) and one element with relatively large atomic mass (Pt) (**Table 6.2**). Typically, atoms having a large atomic mass have larger interaction cross-section and result in higher brightness in Z-contrast STEM image. As shown in Figure 6.2f and 6.2i, there are a lot of bright dots randomly distributed in the matrix. These bright dots could be attributed to Pt atoms in the high entropy alloy nanoparticle. The uniform distribution of Pt atoms reflects the atomic-level mixing of the metal elements in the nanoparticle. This result suggests that Pt atoms did not cluster together leading to phase separation but instead, they remain mix perfectly randomly with four other types of metal atoms in the HEA nanoparticles during the high-temperature treatment.

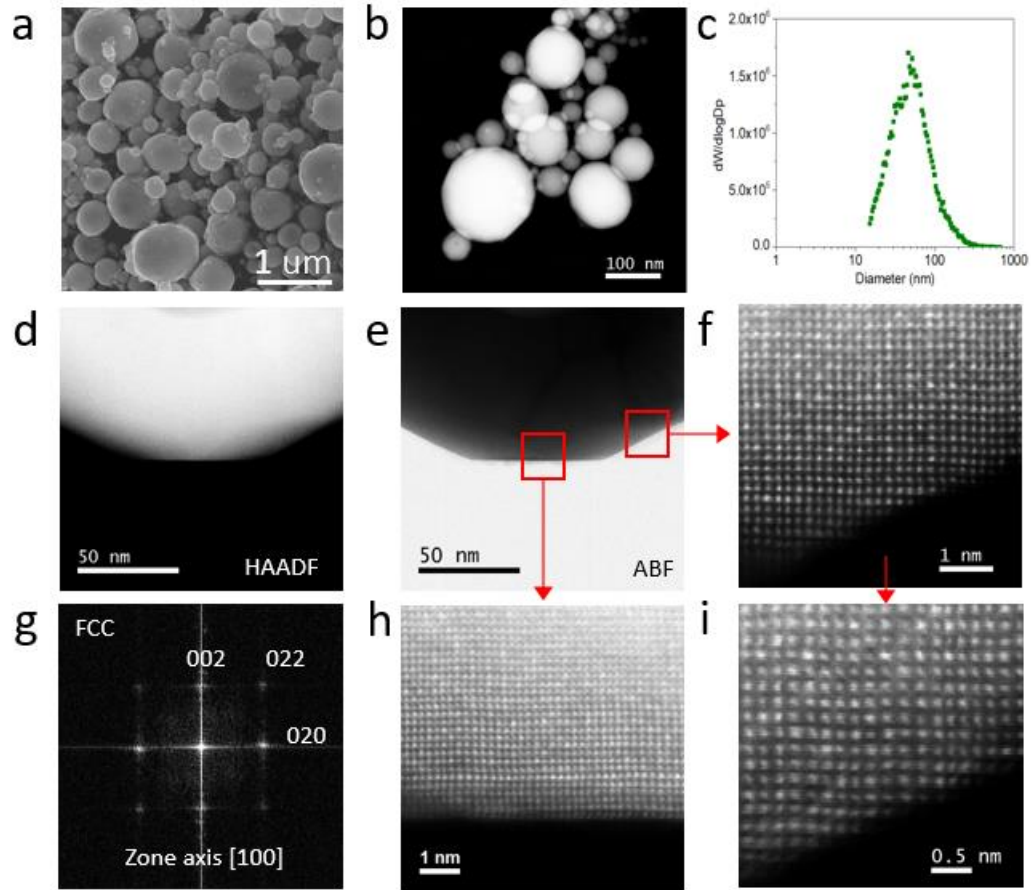


Figure 6.2. Morphology and microstructure of HEA nanoparticles: a) SEM image of high entropy alloy nanoparticles; b) low-magnification HAADF-STEM image of high entropy alloy nanoparticles; c) size distribution of high entropy alloy nanoparticles measured by DMA-CPC on-line size analysis system; d-e) HAADF and annular bright field (ABF) STEM for a single high entropy alloy nanoparticle; f, h, and i) atomic STEM of the high entropy alloy nanoparticle; g) FFT analysis on high entropy alloy nanoparticle.

Since it is difficult to distinguish Ni, Co, Cu, Fe atoms in the atomic-scale STEM images as shown above, I measure the atomic ratios for the five atoms at various areas (**Figure 6.3a**) of the same nanoparticles using the data collected by EDS mapping analysis so as to further investigate how different types of atoms mix in the single nanoparticle. The result shown in Figure 6.3b indicates that for all the nine regions examined, the atomic percentage of each element is similar with that of the same element in the whole particle (19.16 % for Ni, 19.19 % for Co, 11.45 % for Cu, 24.59 % for Fe, 25.60% for Pt),

confirming the compositional uniformity throughout the whole nanoparticle. Furthermore, I also investigated how particle size affects elemental composition in each particle. One example of EDS mapping data containing multiple particles with different sizes is exhibited in **Figure 6.12**. I measured the elemental compositions for each particle with the corresponding size and the results are plotted in the Figure 6.3c. The calculated average elemental composition is listed as follows: Ni: 20.55%+1.65%; Co: 22.53%+2.01%; Cu: 11.93%+3.04%; Fe: 23.54%+2.63%; Pt: 21.45%+2.29%. This result demonstrates that the compositional variation ($< \sim 3.00\%$) of the atomic percentage of each element for different particles are very small, indicating particle size does not affect the atomic ratios in different particles. This $\sim 3\%$ compositional variations of the HEA nanoparticles synthesized here is much better than the compositional uniformity of our previously reported carbothermal shock technique (10%)³⁶ and lithography-based technique (50%)⁷³. The compositional uniformity of HEA nanoparticles generated here might be attributed to the small confinement volume and the homogeneous nature of thermal field all particle experience, unlike bulk processing which may have significant thermal gradients. Considering that physical and chemical properties of HEA nanoparticles are greatly affected by their elemental compositions, the HEA nanoparticles with such small variations synthesized by our aerosol technique demonstrates great potential for a broad range of applications.

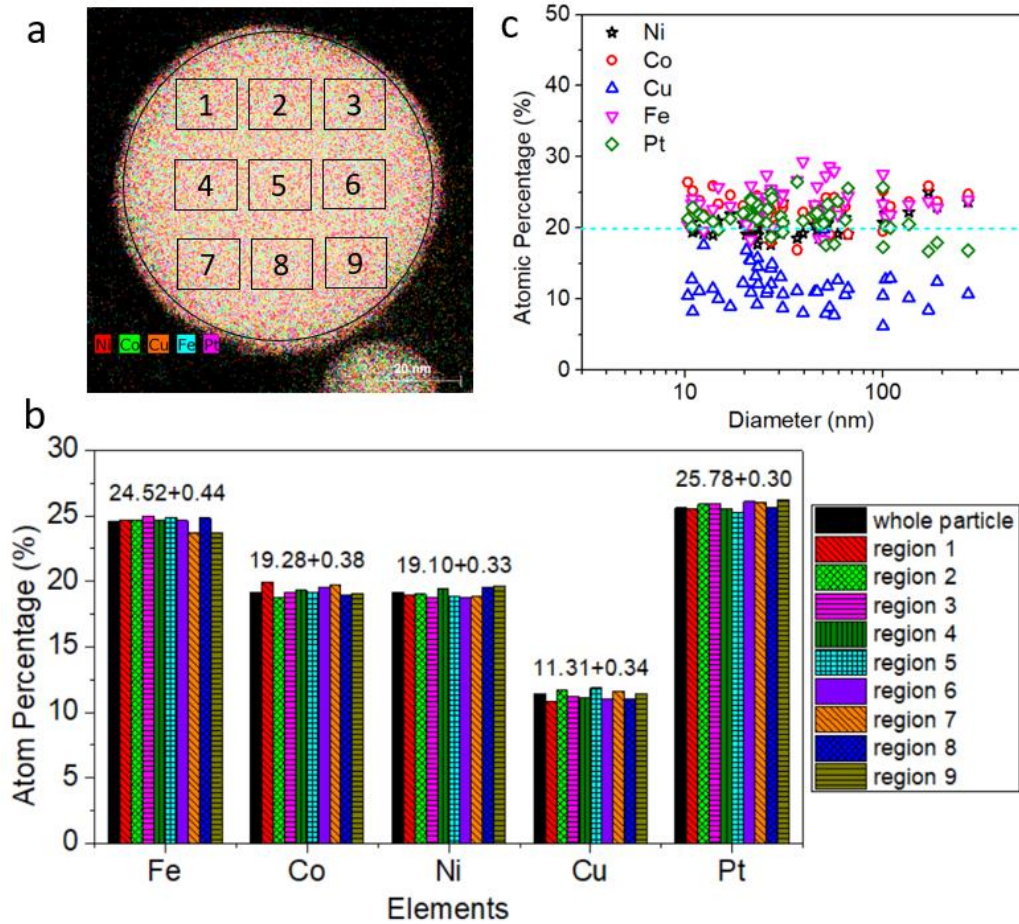


Figure 6.3. Composition analysis of HEA nanoparticles: a) HAADF EDS image of high entropy alloy nanoparticle; b) atomic percentages for five elements at different regions of the HEA nanoparticle in a; c) statistical distributions for atomic percentages of each elements for nanoparticles with different diameters.

6.3.3. Generality of the aerosol technique.

I demonstrate that aerosol assisted process technique is a generic approach toward synthesis of high entropy alloy nanoparticles. Here, I investigate synthesis of HEA nanoparticles with various combinations of elements including Fe, Co, Ni, Cu, Pd, Pt. Table 6.2 shows the standard reduction potentials for all the metal ions used in this study. Since most of metal element investigated in this study have relatively low standard

potentials, thermal heating is required to reduce metal salt precursors by hydrogen gas. Hydrogen reduction of metal nitrate precursors in our experiment can be written as:



The conversion of metal salt precursor to metallic particles contains two steps: diffusion of hydrogen molecules into the aerosol particles and reduction of metal salt precursors by hydrogen molecules. Since the residence time of the particles in the high-temperature reaction zone is extremely fast (~1 s), I examine if both the diffusion of hydrogen molecules and the hydrogen reactions are kinetically favorable. Previous study has shown that hydrogen molecules can diffuse through the interstitials in metals. The diffusion coefficient of hydrogen interstitials in FCC Fe metal is $D \sim 7 \times 10^{-5} \text{ cm}^2/\text{s}$ at room temperature (25 °C)²¹⁷, which yields a characteristic diffusion length of $\sim 2 \times 10^5 \text{ nm}$ ($d^2 = 6Dt$)¹⁴ for hydrogen diffusion within 1 s. Since the diameter of the particles ($< 10^3 \text{ nm}$) is much smaller than the characteristic diffusion distance of hydrogen molecules, and the diffusion process considered is at higher temperature (1100 °C), the diffusion of hydrogen is not a rate limiting step. Previous slow heating experiments have reported that most of the metal salt precursor can be reduced to metals at temperatures ranging from 200-550 °C.²¹⁸ Among all the metal salt precursors investigated in this study, iron is the most reactive metal and has the lowest standard reduction potential. Although I cannot find the kinetic parameters for metal salt reduction, researchers have studied the reduction of iron oxide powders by hydrogen at elevated temperatures.²¹⁹ The reduction of metal salt precursor was estimated based on this study. Assume the reduction of metal salt precursor particles following a shrink core model with a reaction kinetics described by the equation $(1 - (1 - \alpha)^{1/3})^2 = k(T)t$, where α is the conversion, $k(T)$ is the reaction rate at a reaction temperature T .²¹⁹

The complete conversion time for iron nitrate is less than 0.04 s at a reaction temperature of 1100 °C, which is much faster than our residence time. Hence, elevated temperature fastens the kinetics of the hydrogen reduction of metal salt precursors and enables the completion of the conversion of metal salt to metallic phase in less than one second.

Figure 4a shows the miscibility between binary elemental combinations, the data obtained from ASM alloy phase diagram database. The result suggests, for example, that Cu prefers to separate with Fe, Co, or Ni thermodynamically. It is shown that the aerosol assisted processing technique enables the uniform mixing of different elements via kinetically controlled synthesis even through these elements are not mixable thermodynamically. In this study, I have successfully synthesized FeCoNiCuPt, FeCoNiPdPt, and FeCoNiCuPd high entropy alloy nanoparticles. The elemental distributions for each type of high entropy alloy nanoparticles are investigated using EDS analysis as shown in Figure 6.4b-d, confirming the uniform mixing for all elements for each type of high entropy alloy nanoparticle.

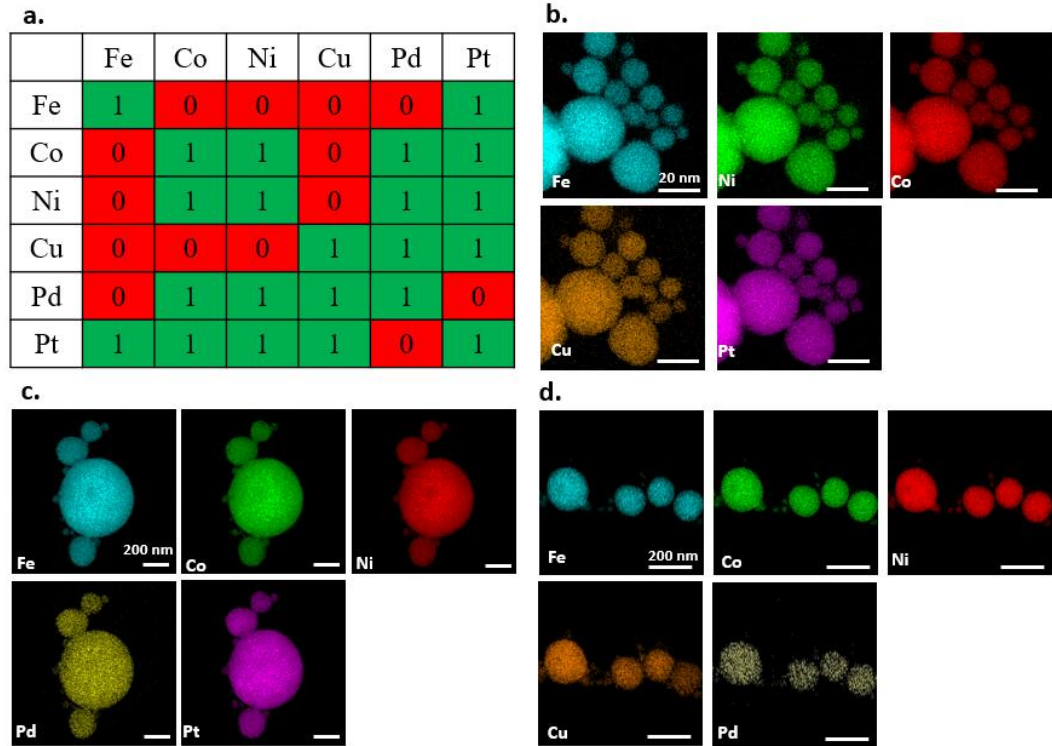


Figure 6.4. Aerosol processing: a generic approach for high entropy alloy nanoparticle synthesis. a) miscibility between binary elemental combinations with a 1:1 ratio, data obtained from ASM Alloy Phase Diagram Database (1 represents the formation of an alloy or intermetallic, 0 represents two metals are immiscible.); several types of high entropy alloy nanoparticles synthesized: b) NiCoFeCuPt, c) NiCoFePdPt, and d) NiCoCuFePd.

6.4. Conclusions.

I have demonstrated an aerosol droplet-mediated technique toward scalable synthesis of high entropy alloy nanoparticles with atomic-level mixing of immiscible metal elements. The aqueous solution containing desired different metal salts was nebulized into millions of aerosol droplets with a diameter of less than 1 μm , and fast heating and fast quenching treatment was exerted on these on-the-fly droplets with each droplet acting as a nanoreactor to produce a single high entropy alloy nanoparticle. Atomic-level STEM study coupled with EDS analysis reveals that all metal elements in the nanoparticles are mixed together on an atomic level. I believe this facile and flexible aerosol droplet-mediated synthesis technique advances the field of high entropy alloy nanoparticles and also demonstrates the potential to transcend fundamental research to industrial application.

6.5. Supporting information

Aerosol reactor design and flow dynamics analysis; XRD pattern of high entropy alloy nanoparticles; EDS spectrum for high entropy alloy nanoparticles; Vapor pressures for different metals; Size distribution of dried aerosol particles containing metal salt mixtures measured by DMA-CPC system; Temperature profile of the aerosol gas flow simulated by COMSOL; HAADF and BF images of NiCoFeCuPt HEA nanoparticles showing the hollow sphere shape; Physical properties of different metal investigated in this study; Standard reduction potentials for different metals; Estimation on yield and production rate of the aerosol process.

6.5.1. Aerosol reactor design and flow dynamics analysis.

Figure 6.5 shows a schematic of our aerosol reactor to include details of the geometry, flow rates, operation pressure, temperature profiles for our reactor system (Figure 6.5) as suggested by the Reviewer. In particular, the total length of the tubular reactor (silica tube, inner diameter: 2 cm) is about 70 cm with a 60 cm long zone in the middle heated by two combined tube furnaces. There was a 5 cm long region on each end of the tube, which was not heated by heating coils of the furnaces. The temperature of the furnaces is set to 1100 °C. With a measured gas flow rate of ~3 L/min, the residence time for aerosol droplets passing through the heating zone was ~3 s.

Based on the aerosol flow rate and the geometry of the tubular reactor, I calculated Reynold number for the aerosol flow in the tubular reactor using the following equation:

$$Re = \frac{\rho v D}{\mu} \quad (6.1)$$

where, ρ is the density of Ar at 1373 K, v is the velocity of the flow in in the tubular reactor, D is the diameter of the tube, μ is the viscosity of argon at 1373 K. The calculated Re is

~ 30 , so one expect the flow to be Laminar. Since these particles are small (i.e small Stokes #) there is no difference between particle velocity and gas flow velocity, so there is no convective heat transfer term to the particles.

Considering the extremely small size and mass of the droplets, heat transfer time are on the order of microseconds, and thus larger than the characteristic residence or temperature variation in reactor. Thus, the heating and cooling rates of the aerosol droplets become the heating and cooling rates of the aerosol gas flow in the tubular reactor. The particles are thus always at the local gas temperature.

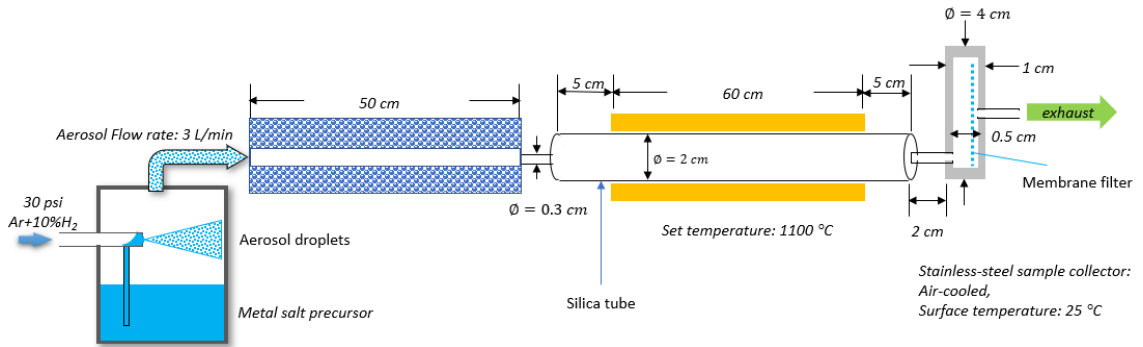


Figure 6.5. Schematic of the aerosol reactor with detailed geometry and operation parameters.

6.5.2. XRD Pattern of high entropy alloy nanoparticles

The data was collected using the sample deposited on the membrane filter.

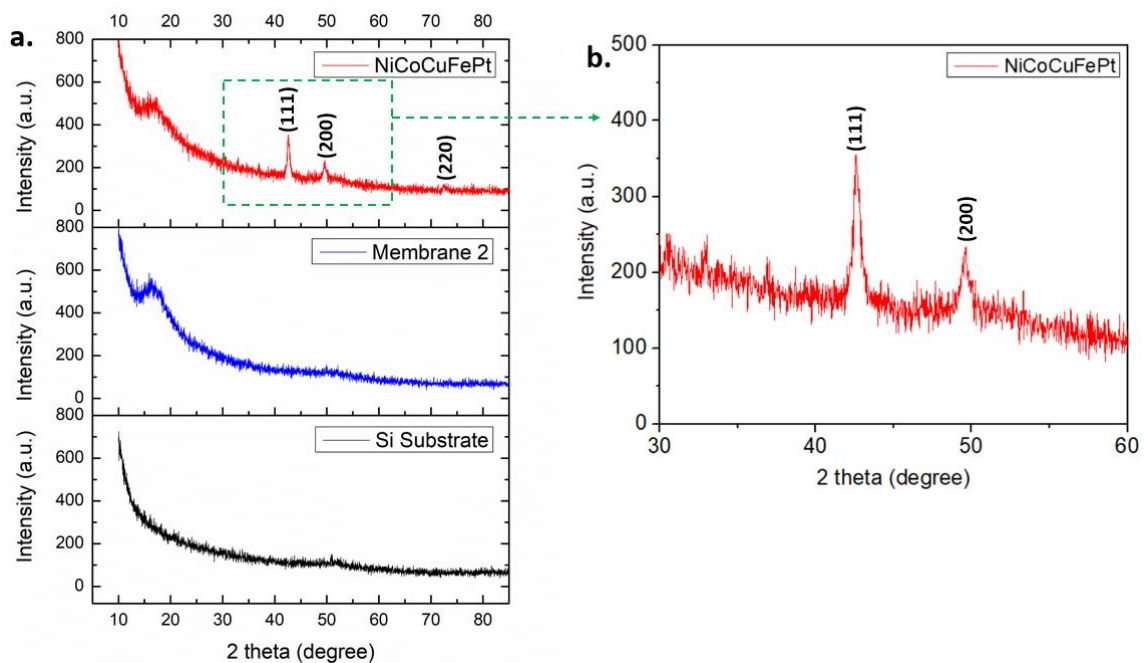


Figure 6.6. a) XRD patterns of NiCoCuFePt high entropy alloy nanoparticles (data collected from the samples containing the polycarbonate membrane filter), polycarbonate membrane filter, and zero-diffraction Si plate substrate, respectively; b) zoom-in XRD pattern of NiCoCuFePt high entropy alloy nanoparticles.

6.5.3. EDS spectrum to demonstrate the formation of metallic phase

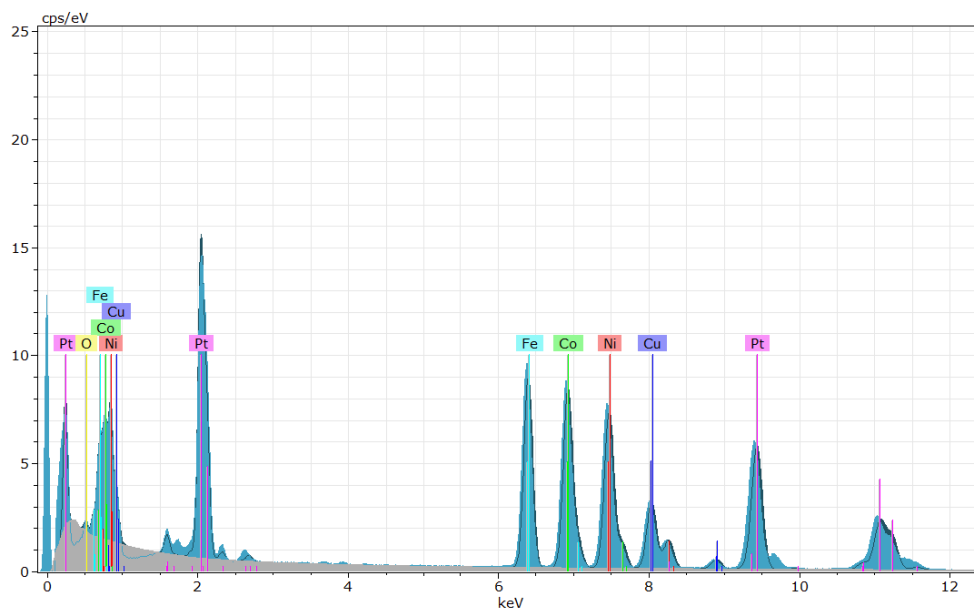


Figure 6.7. EDS spectrum for NiCoCuFePt high entropy alloy nanoparticle.

6.5.4. Vapor pressure for different metals

The equation used to calculate the vapor pressure of metallic elements, P, can be written as:

$$\log(P/atm) = A + \frac{B}{T} + C \cdot \log(T) + D/T^3 \quad (6.2)$$

where A, B, C, D are coefficient constants which are related to specific metals.²²⁰

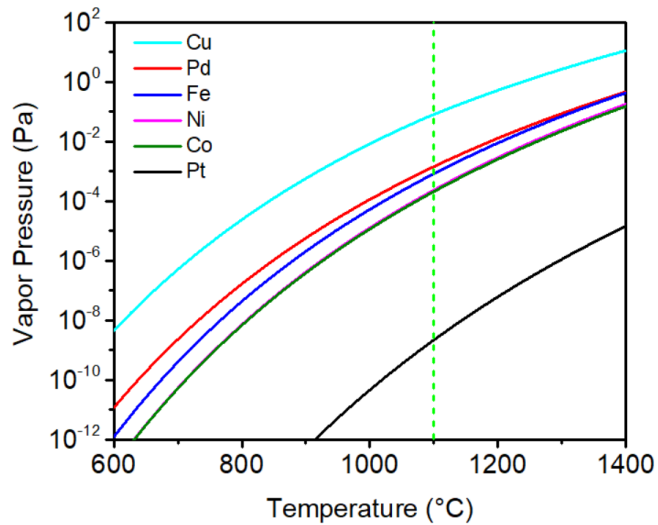


Figure 6.8. Vapor pressures of metallic elements in solid state.

6.5.5. Size distribution of dried aerosol particles containing metal salt mixtures measured by DMA-CPC system.

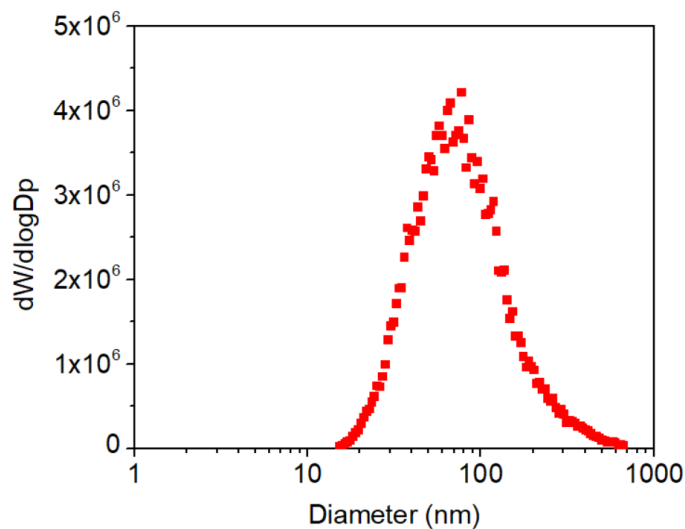


Figure 6.9. Size distribution of dried aerosol particles containing metal salt mixtures measured by DMA-CPC system. (mobility size: 92.0 nm, total concentration: $2.51848e+006\#/cc$)

6.5.6. Temperature profile of the aerosol gas flow simulated by COMSOL.

In order to estimate the temperature profiles of the aerosol gas flow in the tubular reactor, a finite-element simulation of the aerosol synthesis process was implemented using COMSOL Multiphysics software. The model including the tubular reactor and sample collector with the aerosol flow were constructed. I assumed that the temperature on the surface of the tube reactor in the heating zone is 1100 °C, based on prior measurements by others.²²¹ Their experimental results showed that the temperature profile in the heating zone was relatively flat and close to the set temperature.

The temperature profile of the gas in the tubular reactor is displayed in **Figure 6.10**. The temperature along the centerline of the tube shown in **Figure 6.10** indicates that the heating rate of the gas along the centerline is 1000 K/s (the calculated travelling velocity of the gas flow is ~0.2 m/s). The cooling rate is estimated based on the travelling velocity (~8 m/s) of the gas flow in the tubing with a much smaller diameter (0.3 cm vs. 2 cm) and

a temperature difference between point A and point B (1000 K) with a travel distance of ~ 4 cm, and renders a value of ~ 100000 K/s.

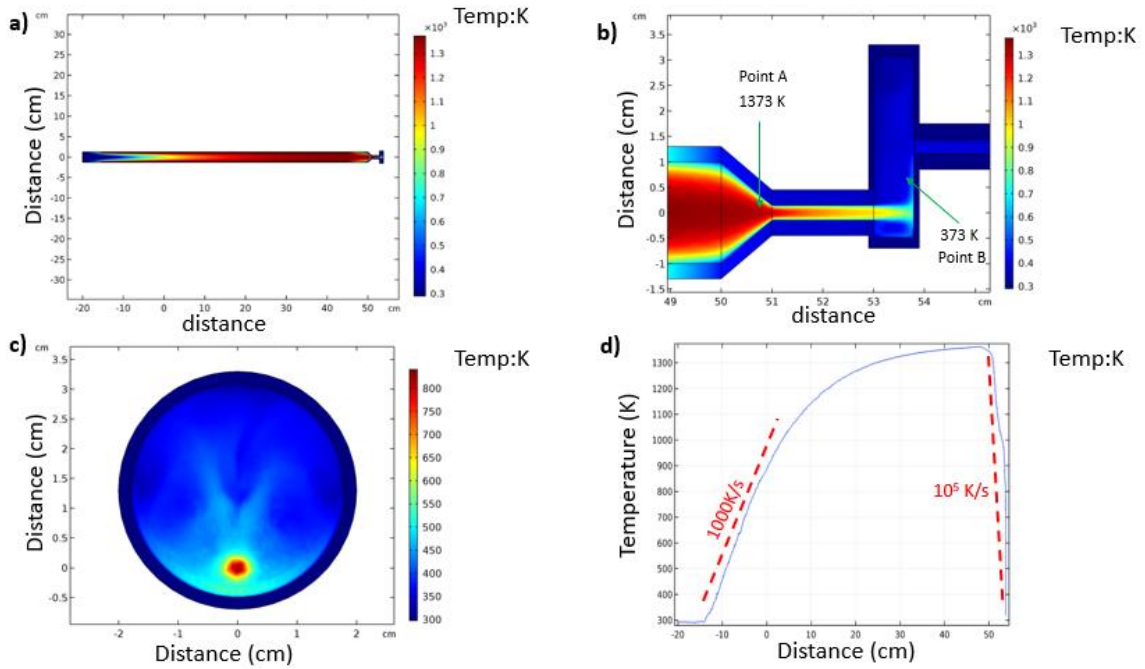


Figure 6.10. Temperature profiles of the gas flow in the aerosol reactor simulated with COMSOL: a) overall temperature profile of the aerosol reactor, b) temperature profile of the gas flow in the sample collector, c) temperature profile of the gas flow in the sample collector in the radial direction; d) temperature profile along the centerline of the gas flow.

6.5.7. STEM: hollow structure.

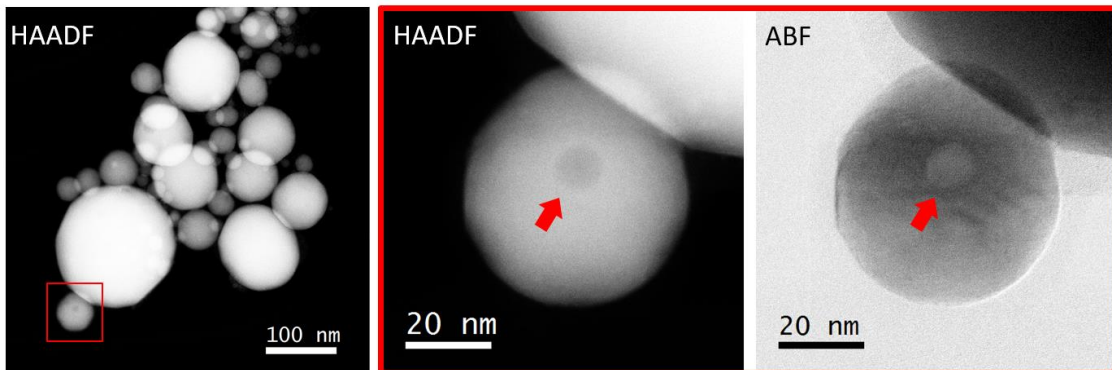


Figure 6.11. HAADF and ABF images of NiCoFeCuPt HEA nanoparticles showing the hollow sphere shape.

6.5.8. EDS maps containing multiple NiCoFeCuPt HEA nanoparticles with different sizes.

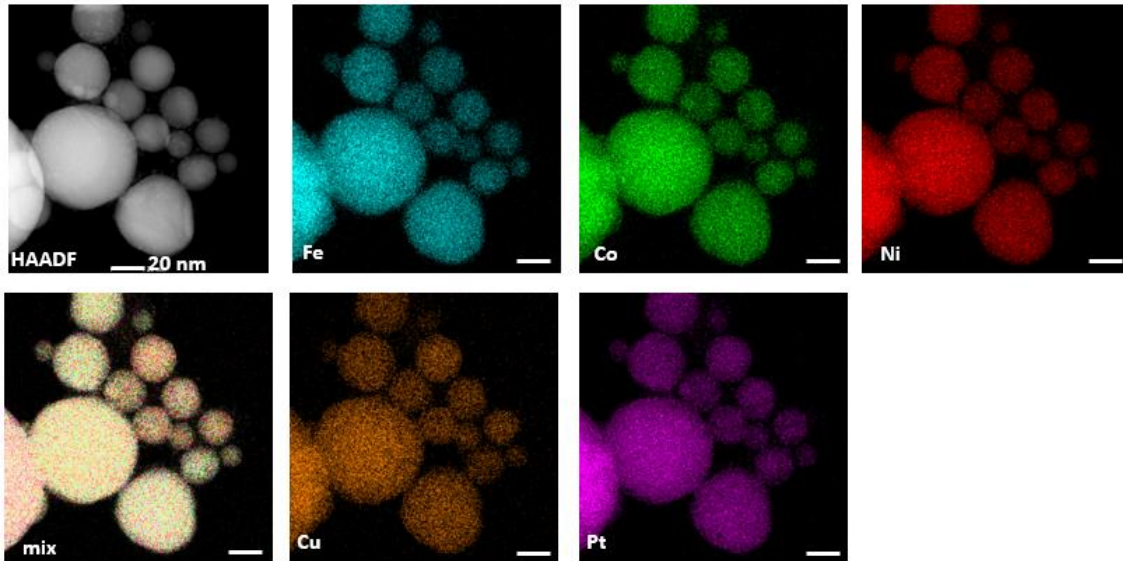


Figure 6.12. HAADF image and EDS maps containing multiple NiCoFeCuPt HEA nanoparticles with different sizes.

Table 6.1. Physical properties of different metal investigated in this study

Metals	Atomic weight	Atom radius (pm)	Crystal structure	Melting point (K)
Fe	55.8	126	BCC/FCC	1811
Co	58.9	125	HCP	1768
Ni	58.7	124	FCC	1728
Cu	63.5	132+/-4	FCC	1358
Pd	106.4	137	FCC	1828
Pt	195.1	139	FCC	2041

Table 6.2. Standard reduction potentials for different metals

Metals	Reaction	E ⁰ (volts)
Fe	$\text{Fe}^{2+} + 2\text{e}^- \rightleftharpoons \text{Fe(s)}$	-0.44V
Co	$\text{Co}^{2+} + 2\text{e}^- \rightleftharpoons \text{Co(s)}$	-0.282
Ni	$\text{Ni}^{2+} + 2\text{e}^- \rightleftharpoons \text{Ni(s)}$	-0.25
H ₂	$2\text{H}^+ + 2\text{e}^- \rightleftharpoons \text{H}_2(\text{g})$	0
Cu	$\text{Cu}^{2+}(\text{aq}) + 2\text{e}^- \rightarrow \text{Cu(s)}$	0.339
Fe	$\text{Fe}^{3+} + \text{e}^- \rightleftharpoons \text{Fe}^{2+}$	0.77
Pd	$\text{Pd}^{2+} + 2\text{e}^- \rightleftharpoons \text{Pd(s)}$	0.915
Pt	$\text{Pt}^{2+} + 2\text{e}^- \rightleftharpoons \text{Pt(s)}$	1.18

6.5.9. Estimation on yield and production rate of the aerosol process.

In order to achieve better estimation on the production rate and the yield, I ran the experiment with the same operation parameters using the nickel nitrate solution (0.5M) as the precursor solution, and it was observed that the consumption rate of the solution was ~20 ml in three hours. Ideally, 100% conversion of the sprayed nitrate salt would produce 4.0 g of nickel metal nanoparticles. The amount of the nanoparticles collected was 0.2 g. Therefore, for the 0.5M nickel nitrate precursor, the production rate was 0.2 g/3 hours = 0.07 g/hour=70 mg/hour. The yield of the particles was about 0.2 g/4 g = 5 %. However there is considerable deposit at the exit of the reactor due to Thermophoresis as the reviewer has indicated. Larger production reactors would decrease this loss considerable, as would better design including a vertically oriented reactor to minimize buoyancy effects leading to particle losses to walls.

Chapter 7: Laser Shock-Assisted Ultrafast Synthesis of Supported Metal Nanoclusters with Kinetically Tunable Size and Surface Density**

Abstract: Matrix-supported metal nanoclusters (1-10 nm) with unique size- and shape-dependent properties have drawn for their potential applications in electronics, catalysis, energy storage, and sensors. However, synthesis of matrix-supported ultra-small nanoclusters at high concentration and in an unaggregated state is challenging. Here I demonstrate an ultrafast laser shock technique to *in-situ* fabricate ultra-small metal nanoclusters supported on a carbon nanofiber (CNF) matrix with kinetically controllable size and surface density. An ultrafast laser shock heating on the metal precursor incorporated CNF matrix triggers the fast nucleation and growth of metal nanoclusters and a subsequent ultra-fast quenching freezes them onto the CNF structure. I find that a shorter laser shock enables the formation of metal nanoclusters with higher number densities and smaller sizes while longer laser shock leads to the further growth of metal nanoclusters and the achievement of their equilibrium shape. A characteristic time analysis suggests that the growth of metal nanoclusters is dominated by surface diffusion and sintering, and Ostwald ripening is mainly involved at the early stage of nanocluster formation. I also demonstrated that the catalytic performance of CNF matrix supported metal nanoclusters towards electrocatalytic hydrogen evolution is enhanced for metal nanoclusters with a smaller size and higher number density. This work provides a promising approach for rapid and scalable fabrication of ultra-small, high-density metal nanoclusters and nanocluster-based devices.

** The results represent in this chapter have been submitted to a peer-review journal and are under review: Yong Yang, Yonggang Yao, Dylan Kline, Tangyuan Li, Haiyang Wang, Liangbing Hu, Michael R. Zachariah, Laser Shock-Assisted Ultrafast Synthesis of Supported Metal Nanoclusters with Kinetically Tunable Size and Surface Density. 2019, under review

7.1. Introduction

Matrix-supported Metal nanoclusters (1-10 nm) have shown potential for applications in electronics, catalysis, energy storage, and sensors.^{6, 55, 135} Although many techniques have been developed to decorate metal nanoclusters onto the supporting matrices¹³⁶, achieving a higher surface density while maintaining an ultra-small size and uniform dispersity is extremely difficult because of the metastable nature and the rapid aggregation of nanoclusters. Simply increasing the nanocluster surface density by adding more nanoclusters onto the host matrix often leads to nanocluster aggregation, uneven dispersion, and further growth of nanoclusters into larger sizes. Further, most of those reported techniques only produce supported nanoclusters in small quantities and are therefore not suitable for immediate technological applications. Hence, there is a need to develop an effective, facile, and industrially-scalable technique to synthesize supported metal nanoclusters with an ultra-small size and extremely high surface density.

From a thermodynamic standpoint, one strategy to produce nanoclusters with a smaller size and a higher number density is to promote nucleation and simultaneously limit growth. This can be achieved by employing a fast thermal pulse to rapidly decompose the metal precursor to create a highly supersaturated state, leading to a fast nucleation burst. Subsequent ultrafast cooling can then quench the growth of small nuclei and form ultra-small nanoclusters. Recently, Yao et al. demonstrated a thermal shock technique to generate high-surface density, ultrasmall metal nanoclusters and nanoalloys decorated on carbon nanofiber thin films.^{36, 38} Rapid heating and fast nanocluster formation was achieved by electrically heating a conductive carbon matrix. Despite being an ultrafast technique, this Joule heating-assisted thermal shock technique is limited to electrically conductive

matrices and is not amenable to bulk production of supported ultra-small nanoclusters with high surface densities.

Lasers present a flexible and powerful nanomanufacturing approach to provide both temporally and spatially resolved energy to generate nanoclusters.^{77-78, 222} Laser-based manufacturing approaches shift the control and modulation of properties from the material to a programmable source, making them readily adaptable to industrial protocols. Laser approaches to nanomaterial fabrication become especially consequential as one adapts to emerging manufacturing approaches like 3-D printing and writing.⁸²⁻⁸³ In this work, I demonstrate a fast, thermal shock technique using a commercial CO₂ laser as the heating source to introduce an extremely short laser shock to trigger the formation of ultra-small, densely, and uniformly dispersed metal nanoclusters on carbon nanofiber matrices. This approach is a facile way to precisely tune nanocluster size, surface density, and shape. I observe that a shorter laser pulse enables the formation of smaller nanoclusters with high number densities. Conversely, a longer laser shock leads to the further growth of metal nanoclusters and the achievement of their equilibrium shape. A characteristic time analysis suggests that the growth of metal nanoclusters is primarily dominated by coagulation and sintering, with Ostwald ripening mainly involved at the early stage of nanoparticle formation. As an example application, I demonstrate size-dependent catalytic properties of Pt nanoclusters for electrocatalytic hydrogen evolution. This further demonstrates the ability of this approach for an easy and fast tuning of material properties through a simple modulation of laser parameters. This technique represents a promising approach for rapid and scalable fabrication of tunable, ultra-small, high-density metal nanoclusters and nanocluster-based devices.

7.2. Experimental section

Carbon nanofiber (CNF) preparation Polyacrylonitrile was added to 10 mL DMF solvent followed by vigorous stirring overnight. The as-obtained solution was used as the precursor for electrospinning to prepare polyacrylonitrile (PAN) thin film. The precursor solution was loaded into a 10 mL syringe tube and pumped through a flat-top stainless-steel needle (inner diameter: 203.2 μm). A pumping rate of 0.5 mL/hour, a voltage differential of 12 kV and a distance of 15 cm between the needle and the aluminum substrate were employed for electrospinning. In order to prepare CNF films, the as-prepared PAN sample was loaded into a tube furnace, heated up to 250 $^{\circ}\text{C}$ with a heating rate of 5 $\text{min}/^{\circ}\text{C}$ in the air atmosphere, and kept at 250 $^{\circ}\text{C}$ for 2 hours. Then, the sample was heated up to 1000 $^{\circ}\text{C}$ with a heating rate of 2 $^{\circ}\text{C}/\text{min}$ under H_2/N_2 (v:v=5:95) atmosphere and kept at 1000 $^{\circ}\text{C}$ for 5 hours to obtain CNF thin films.

Metal salt loading onto CNF: The metal precursor (0.05M). was dropped onto carbon nanofiber thin films (2.5 mm x5.0 mm) using a pipette with a loading of $\sim 100 \mu\text{L}/\text{cm}^2$. The metal salt loaded thin film was air dried. The resulting weight percentage of Pt in CNF matrix is about 30%.

Laser induced Thermal Shock: The metal salt impregnated CNF thin film sample (2.5 mm x5.0 mm) was mounted on a homemade graphite holder, which was placed in the center of the box chamber filled with inert Ar gas. The freestanding thin film sample was heated by a continuous CO_2 laser, which was controlled by a computer. The duration, output energy power, and the size of the laser beam can be adjusted accordingly. The output power of the laser applied was 90% of the total laser power (80W). The laser shock process

was recorded with a high-speed color camera. The recorded color images were used to extract spatiotemporal temperature of the sample.

Spatiotemporal Temperature Mapping The temperature of the hot sample is estimated using Equation 1. By taking ratios of raw channel intensities, dependency on most variables associated with intensity is eliminated except for those regarding the channel gain (ψ_i), emissivity (ϵ), and spectral response (χ_i) of the camera at individual wavelengths and channels.⁸⁵ To estimate temperature of the hot surface, the graybody assumption has been modified to account for an optically thin flame by assuming that $\epsilon \sim 1/\lambda$, substituted into Planck's Law, and integrated over the entire spectrum to which the camera is sensitive (as shown in Equation 1 below).⁸⁶ When calibrated with a Newport Oriel 67000 Series Blackbody Infrared Light Source, calibration factors C_{gr} , C_{bg} , and C_{br} with data available in the article by Jacob and Kline *et al.*, and these factors were assumed valid from 773-4773K.⁸⁷ Through this, calculation of temperature is reduced to matching of calibration factor-corrected channel intensity ratios to theoretical ratios. Three color ratios (green/red, blue/green, and blue/red) were simultaneously used to estimate temperature by minimizing their summed error from theoretical ratios. Further thresholding is used to eliminate summed errors corresponding to a temperature error greater than 110K. Only unsaturated pixels above the black level and within the error threshold are used to report mean and median temperature of the frame for a contiguous area of at least 10 acceptable pixels.

Catalytic Test. The electrocatalytic performance of the samples toward hydrogen evolution reaction (HER) was tested. The freestanding metal nanoclusters decorated CNF film was directly used as the working electrode. Platinum foil was used as the counter

electrode and a standard Ag/AgCl electrode as the reference electrode. HER tests were performed in a 0.5 M H₂SO₄ aqueous solution. The polarization tests were performed by linear sweep voltammetry from 0 to -0.5 V (vs. RHE) with a scan rate of 2 mV/s.

Characterization. Morphologies and structures of metal nanoclusters supported on CNF matrix were examined by scanning electron microscopy (SEM, Hitachi SU-70) and transmission electron microscopy (TEM, JEOL JEM 2100 FEG). The mean diameters and size distributions of the nanoparticles were determined by statistical analysis of the acquired TEM images, using Nano Measurer 1.2 image analysis software.

7.3. Results and Discussion

Thermodynamic and Kinetic Criteria. Here, I first use classical nucleation theory to investigate if an ultrafast laser shock is able to produce a supersaturated metal atom vapor condition for a fast nucleation burst and nanocluster formation. Thermodynamically, a nucleation process can be described by the Gibbs Free energy droplet model¹⁴, where the critical radius, r_c , of a stable nucleus is expressed as:

$$r_c = \frac{2\sigma V_m}{RT \ln S} \quad (7.1)$$

Here, S is the saturation ratio of the Pt vapor; σ is the surface tension of Pt nanoclusters in the liquid phase; and V_m is the molar volume of bulk metallic Pt. Eqn 7.1. indicates that increasing the saturation ratio S of Pt vapor decreases the critical radius of the nanoclusters (**Figure 7.1a**), assuming a size-independent surface and constant temperature. In an extreme case, one can imagine a saturation ratio high enough to cause each single atom to become a stable nucleus. **Figure 7.1b** shows that this scenario becomes feasible when $S > 10^5$, when the critical radius approaches the radius of a platinum single atom (~0.2 nm). Ideally, creating a highly saturated condition for metal atoms in a short time should allow a fast nucleation and formation of stable nuclei with an ultra-small size. A subsequent fast cooling step would then freeze and stabilize these clusters onto a host matrix with high density and dispersity.

I examine if a CO₂ laser is fast enough to create such high saturation ratios in an extremely short time. In order to estimate these timescales, a crucial parameter to consider is the saturation ratio change of the monomer (Pt atoms) in the CNF matrix during laser shock heating. This saturation ratio change is mainly affected by four primary processes: (a) generation of Pt atoms from thermal decomposition of H₂PtCl₆, (b) consumption of Pt

atoms due to nucleus formation, (c) evaporation of Pt atoms from the surface of the stable nuclei, and (d) consumption of vapor phase Pt atoms due to Pt condensation onto the surface of the existing nuclei. These processes can be well described by the moment model as follows^{25, 40}:

$$\frac{dS}{dt} = \frac{R_H}{n_s} - \frac{Jk^*}{n_s} - (S - 1) \frac{B_1 A}{2v_1 n_s} \quad (7.2)$$

Here, R_H is the reaction rate of metal salt precursor decomposition to zero-valent metal atoms; A is the total surface area of all the nuclei in the reaction volume; both R_H and A are time-dependent variables; k^* is the number of monomers in a single particle with a critical radius r_c ; n_s is the monomer concentration at saturation condition; $B_1 = 2n_1 v_1 \left(\frac{kT}{2\pi m_1}\right)^{1/2}$ where n_1 is the monomer number concentration; v_1 and m_1 is volume and mass of the monomer, respectively; J is the rate of particle formation by the nucleation. For a homogenous nucleation process, J is given as follows⁴⁰:

$$J_{homo} = \frac{Kn_1 s_1}{3} \sqrt{\frac{\Phi}{\pi}} \exp\left(-\frac{4}{27} \frac{\Phi^3}{(\ln S)^2}\right) \quad (7.3)$$

Where $K = n_1 \left(\frac{kT}{2\pi m_1}\right)^{1/2}$; Φ is dimensionless surface tension of the stable nuclei $\Phi = \frac{s_1 \sigma}{kT}$; s_1 is the surface area of a monomer. However, the presence of the carbon nanofibers would be expected to further lower the nucleation barrier and promote heterogenous nucleation, which can be expressed as:¹³⁸

$$J_{hetero} = \frac{Kn_1 s_1}{3} \sqrt{\frac{\Phi}{\pi}} \exp\left(-\frac{4}{27} \frac{\Phi^3}{(\ln S)^2}\right) \cdot f(\theta). \quad (7.4)$$

where $f(\theta) = 1/4(2 + \cos\theta)(1 - \cos\theta)^2$, which is the reduction factor and θ is the contact angle between the metal and carbon surface. Therefore, I use J_{hetero} in Eqn. 7.2 for

the saturation ratio calculation. The values for all the property parameters and the details of the calculation can be found in the Supporting Information (**Table 7.1**).

Figure 7.1c shows the calculated change in saturation ratio of Pt atoms with the duration of the laser shock. It is observed that for two metal precursor loadings investigated (10^{21} , 10^{22} #/m³), a short laser shock is fast enough to create a supersaturated state ($S > 10^5$) of Pt atoms, enabling a rapid nucleation burst and formation of extremely small nanoclusters which are also thermodynamically favorable. Note that particle coagulation and particle sintering are not considered in the calculation, and the role of coagulation and sintering on nanoparticle growth will be discussed later.

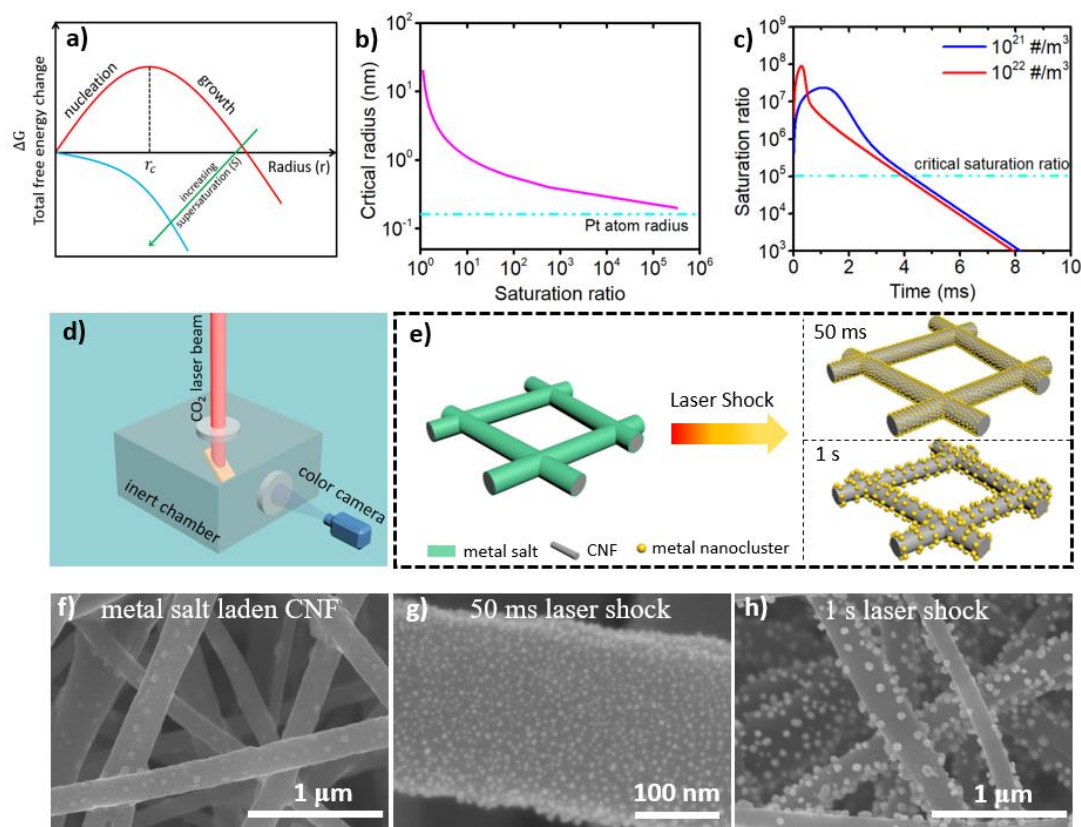


Figure 7.1. Laser induced thermal shock technique for nanocluster synthesis. a-c) relationship between the critical nucleus radius and the saturation ratio of metal atoms. d) schematic of apparatus; e) effect of laser shock duration on nanocluster size and number density; f) SEM image of H_2PtCl_6 coated CNF film; g-h) CNF supported Pt nanoclusters synthesized by 50 ms and 1 s laser shocks, respectively.

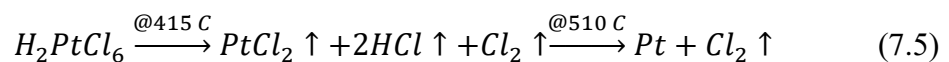
Laser induced thermal shock technique: Figure 7.1d shows the experimental system for the laser shock technique fabrication of carbon nanofiber supported metal nanoclusters. Pt nanoclusters were chosen as the model system to investigate the process-structure relationship. In a typical experiment, the metal precursor was impregnated onto carbon nanofibers by depositing the precursor solution onto a carbon nanofiber thin film. After drying at ambient conditions, the metal precursor impregnated CNF thin film sample was mounted onto a custom graphite substrate located in the center of an inert Ar gas-filled chamber. Photothermal shock on the thin film sample was carried out using a CO₂ laser (SYNRAD, ti series) operating at 10.6 μm with an output power of 70W. The heating process was recorded by a high-speed color camera (Vision Research Phantom Micro) and a spatiotemporal temperature map of the thin film sample was obtained based on the recorded camera video.⁸⁷ A pulse generator was used to simultaneously trigger the CO₂ laser beam irradiation and the high-speed camera recording process.

Figure 7.1e shows a schematic of synthesis of CNF supported metal nanoclusters by the laser shock technique. A surface layer of metal salt precursor is uniformly coated on the carbon nanofiber matrix. Laser shock heating triggers rapid thermal decomposition of the metal salt and subsequent nucleation of metal nanoclusters. Fast quenching stabilizes these small nanoclusters on the surface of the carbon nanofiber matrix and prevents further growth. By simply controlling the duration of the laser shock, one is able to synthesize metal nanocluster with tunable size and surface density. As shown in Figure 7.1e, a shorter laser shock leads to formation of smaller nanoclusters (represented by gold color spheres) with a higher surface number density. On the other hand, a longer laser shock promotes

further nanocluster growth, resulting in the formation of large-size particles with a lower surface number density.

The microstructure evolution of supported Pt nanoclusters carbon nanofibers before and after the laser shock treatment was investigated using scanning electron microscopy. Figure 7.1f shows a uniform coating of the metal precursor (H_2PtCl_6) on the surface of carbon nanofibers. The incident high-power laser beam absorbed by the thin film sample quickly heats the sample to an extremely high temperature (~ 1550 K), causing thermal decomposition of the precursor and formation of nanoclusters anchored on the carbon nanofibers. Figure 7.1g depicts that 50 ms laser shock produces uniformly dispersed Pt nanoclusters with an average diameter of 3.8 nm and a surface number concentration of $\sim 10^{16}$ #/m². Meanwhile, a 1 s laser shock synthesizes Pt nanoclusters with a larger average diameter of 54 nm and a lower surface number concentration of $\sim 10^{14}$ #/m². An elongated laser shock pulse accelerates the diffusion small clusters on the carbon nanofiber surface at elevated temperatures, leading to further growth of nanoclusters and a concomitant decrease in their surface density. These results demonstrate that by simply adjusting the pulse duration of the laser shock, nanoparticles supported on the carbon nanofibers with different size and number density can be generated. Particularly, decreasing the laser shock duration enables the formation of smaller nanoclusters with higher number densities.

I further investigated the thermal decomposition of metal salt precursor during the ultrafast heating treatment. Previous thermogravimetric analysis with a slow heating rate (10 K/s) revealed that chloroplatinic acid decomposes to volatile $PtCl_2$ at 415 °C, which further decomposes to metallic Pt at 510 °C.²²³



Temperature-Jump/Time-of-Flight Mass Spectrometry (T-Jump/TOFMS, see **Figure 7.5**) was used to study precursor decomposition under a fast heating rate (10^5 K/s). The principle and details of T-Jump/TOFMS can be found in the experimental section and in our previous studies.⁵⁴ Briefly, a small amount of metal salt precursor was deposited onto a platinum wire probe. Once loaded into the TOFMS vacuum chamber, the platinum wire probe coated with metal salt precursor was resistively heated by a direct current voltage supply which delivers a rapid heating rate as fast as 10^5 K/s. In this manner, the heating process mimics the heating rate employed in a laser shock experiment. The mass spectra detected by the TOFMS is shown in **Figure 7.6** (also refer to **Table 7.2**), confirming the release of volatile $PtCl_2$ during the thermal decomposition of the metal salt precursor. Particularly, $PtCl_2^+$ species was released at a time of 1.1 ms and a temperature of 437 °C, which is comparable to the release temperature of volatile $PtCl_2$ under a slow heating regime (415 °C). Note that the signal intensity for HCl, Cl are much stronger than $PtCl_2$ and no Pt signal was detected by TOFMS. Since the release temperature of $PtCl_2$ is similar under both ultrafast and slow heating regimes, it is reasonable to believe that volatile $PtCl_2$ was quickly reduced to Pt atoms and re-condensed onto Pt wire at a temperature slightly higher than 510 °C. Heating the sample to even higher final temperature (1550 K) in an extremely short time further hastens the kinetics of metal salt decomposition and enables the formation of Pt atoms in a relatively short time. The weak signal of $PtCl_2$ also implies its extremely short lifetime under this ultrafast heating regime. This indicates that $PtCl_2$ is rapidly reduced to Pt atoms, which nucleate and deposit on the surface of the Pt wire. Results from SEM-EDS (**Figure 7.7**) further confirm the complete conversion of metal salt precursor to metallic phase particles with a 50 ms laser pulse.

Spatiotemporal temperature mapping: The spatiotemporal dynamics of the rapid thermal shock of the thin film sample induced by the CO₂ laser at high powers was explored by high-speed two-dimensional color camera pyrometry.⁸⁷ As shown in **Figure 7.2a**, the light signal emitted from the laser-heated CNF thin film first passes through a Bayer mosaic color filter array, which is then used for selective bandpass transmission of light (red, green, blue). Red, green, or blue sensitivities are recorded by the CMOS sensor of the camera at each pixel, and RGB intensities at each channel are then recovered by demosaicing the image. The raw channel intensity ratios (green/red, blue/green, and blue/red) are used to determine temperature after appropriate calibration using procedures described previously.^{85, 87}

The video of the entire laser heating process captured by the color camera and the time-resolved two-dimensional temperature profile of the thin film are shown in the supplementary video. Figure 7.2b-c show the snapshot images of the heated sample at selected time points of the 1 s laser shock and the corresponding temperature maps. The time-resolved temperature maps suggest that the thermal energy provided by laser shock quickly spreads to the entire film uniformly, leading to an equilibrium temperature of 1550 K in about 50 ms. The uniform temperature distribution in the film is attributed to the high thermal conductivity of the carbon nanofiber matrix. Once the laser shock was terminated, the thin film sample rapidly cools. The temperature profile of the sample at each time was calculated by averaging all the effective temperature values at each pixel of the two-dimensional temperature map and is shown in Figure 7.2c. It is observed that a 1 s laser shock irradiated on CNF film renders extremely fast heating (10^4 K/s) and cooling rates (10^5 K/s). The extremely high heating rate rapidly reduces the metal salt to metal atom

vapor to build a supersaturated state for nanocluster nucleation. Fast heating and cooling rates were achieved because of the high output power of the laser beam and the small mass of the thin film sample. These rates induced by laser shock are similar to those achieved via electrical Joule heating and are much higher than those achieved in traditional wet chemistry approaches. Additionally, compared with joule heating, the laser shock approach is more amenable to scale-up such as roll-to-roll manufacturing as this approach is not limited to conductive matrices, thus enabling the use of ceramics and polymers.

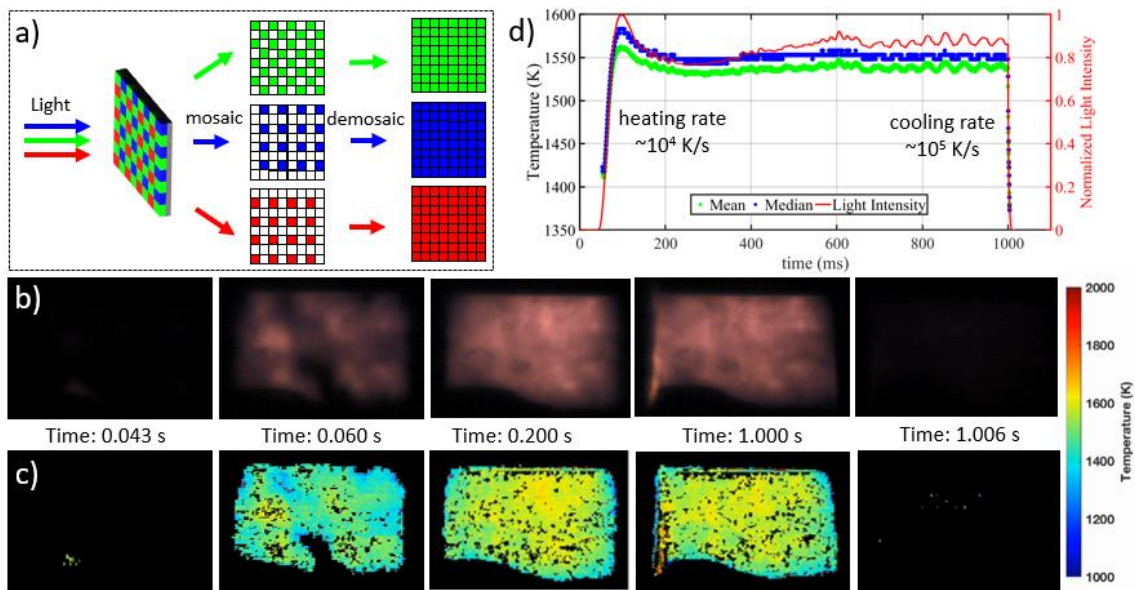


Figure 7.2. Spatiotemporal temperature mapping; a) principle of recording a color image with a Bayer filter; b-c) time-resolved color images of the sample during the laser shock process and the corresponding time-resolved temperature maps of the sample during the laser shock process; d) temperature profile of the thin film sample;

Microstructural analysis: The microstructure of CNF supported Pt nanoclusters was examined by transmission electron microscopy (TEM). **Figure 3a** exhibits Pt nanoclusters stabilized by CNF generated with a 50 ms laser shock pulse. The TEM image of the labeled area with red dash square show that ~ 4 nm Pt nanoclusters are uniformly dispersed on CNF with a high surface number density. In particular, there are some

particles located right outside of the carbon nanofiber projected area in Figure 7.3b, indicating that these nanoclusters anchor on the surface of carbon nanofiber instead of being encapsulated inside the nanofiber. This observation is consistent with the morphology of CNF supported nanoclusters shown in the SEM image of Figure 7.1g. High resolution TEM image in Figure 7.3c shows that these nanoclusters have a crystalline structure with a d-spacing of 2.27 Å, corresponding to the (111) of Pt crystal. The selected-area electron diffraction pattern (SAD) in Figure 7.3d matches well with that of Pt metal, further confirming the presence of the metallic phase of Pt nanoclusters with a single crystalline structure. It is interesting to note that a crystalline structure is observed even for laser shock heating with ultrafast cooling rates (10^5 K/s). This suggests that the crystallization process from liquid Pt droplets occurs faster even at such high cooling rates. Previous studies have shown that a crystallinity can be achieved for liquid iron nanodroplets with a diameter of 10 nm when cooled down from 1600 K to room temperature even with a cooling rate as high as 10 K/s.²¹⁶ Therefore, the laser shock approach allows sufficient time for crystallization to occur from liquid Pt droplets.

Figure 7.3e shows the corresponding scanning transmission electron microscopy (STEM) image of CNF supported metal nanoclusters shown in the TEM image of Figure 7.3a. Figure 7.3f-h shows EDS analysis of Pt nanoclusters on the carbon nanofiber. EDS map for carbon element shows smooth features and the edge of the nanofiber is relatively darker because this part is thin, and less signal is collected from this area. EDS map for platinum element indicates platinum particles are uniformly distributed on the surface of the carbon nanofiber. It is observed that the height of Pt EDS map is slightly larger than that of the carbon nanofiber matrix, indicating Pt clusters anchoring on the surface of the

nanofiber. This observation is further confirmed by the mixed EDS map shown in Figure 7.3h, which renders bright green edges and no presence of the carbon nanofiber matrix.

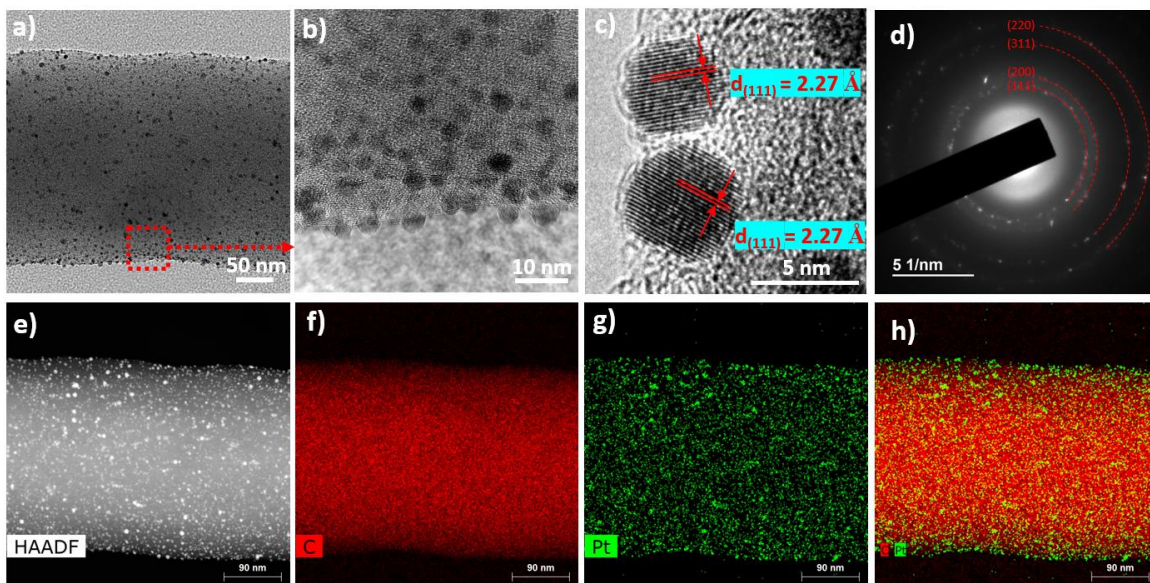


Figure 7.3. Microstructure analysis of CNF supported Pt nanoclusters synthesized by 50 ms laser induced thermal shock. a-c) TEM images of supported Pt nanoclusters; d) Selected-area electron diffraction pattern of Supported Pt nanoclusters; e-h) Scanning TEM of supported Pt nanoclusters and their corresponding EDS mappings.

I further investigated the effect of the laser shock duration on nanocluster size and surface number density. The microstructural evolution of Pt nanoclusters with increase of the laser shock and their corresponding size distribution histograms are shown in **Figure 7.4a-h**. The size distributions and the surface density of the nanoclusters were obtained by statistical analysis of SEM images shown in Figure 7.4a-d. Figure 7.4i shows that the particle diameter increases with a corresponding decrease in surface number concentration. Longer laser shock pulse cause further growth of nanoclusters and a decrease in surface density through nanoparticle diffusion and sintering. Interestingly, nanoparticles generated with 1 s laser pulse or smaller, are uniformly dispersed on the CNF surface and no agglomerates are observed. However, nanoparticles are observed to aggregate around the

junctions between CNFs, which suggests that particle diffusion might be faster than particle sintering. More detailed analysis on nanoparticle growth mechanism will be explored in the following section.

Interestingly, I observe that increasing laser shock duration not only leads to a larger particle size but also generates different particle shape and morphology. Figure 7.4c shows that nanoclusters produced with a 50 ms are primarily spherical in shape. On the other hand, a much longer laser pulse of 60 s generates faceted Pt nanocrystals with a typical octahedral morphology, as shown in **Figure 7.8**. Pt nanocrystals with a thermodynamic equilibrium shape are usually bounded by three low-index crystal planes, (100), (110), (111), with surface tensions following the order, $\gamma_{(111)} < \gamma_{(100)} < \gamma_{(110)}$.²²⁴ Pt NPs should therefore take an octahedral shape in order to maximize the expression of (111) facets and minimize total surface energy. Previous studies have demonstrated the formation of similar 5 nm octahedral platinum nanoparticles by colloidal synthetic routes.²²⁵ However, 5 nm nanoparticles generated with a 50 ms laser shock pulse have a spherical morphology. This observation can be primarily attributed to the rapid nature of the process which favors the kinetic formation of particles over the thermodynamically-favorable morphology. It is well known that the melting point of metal nanoparticles decreases with their size.²⁴ At elevated temperatures during laser heating, Pt nanoparticles as small as 5 nm must therefore be in a liquid state. The surface energies for different facets, thus, become similar so that these nanoparticles grow with no preferential facets²¹⁶, resulting in a spherical morphology. Ultrafast quenching then freezes these spherical nanoparticles and prevents them from reaching the thermodynamically equilibrium shape. For a longer laser pulse, however, the nanoparticles grow into large sizes with their melting

point approaching that of bulk Pt. Since the temperatures reached by laser shock are much lower than bulk melting point of Pt, the surface tension for different facets are energetically distinguishable. These particles, therefore, grow with preferential orientations to stable (111) planes, leading to a thermodynamically equilibrium shape, octahedron.

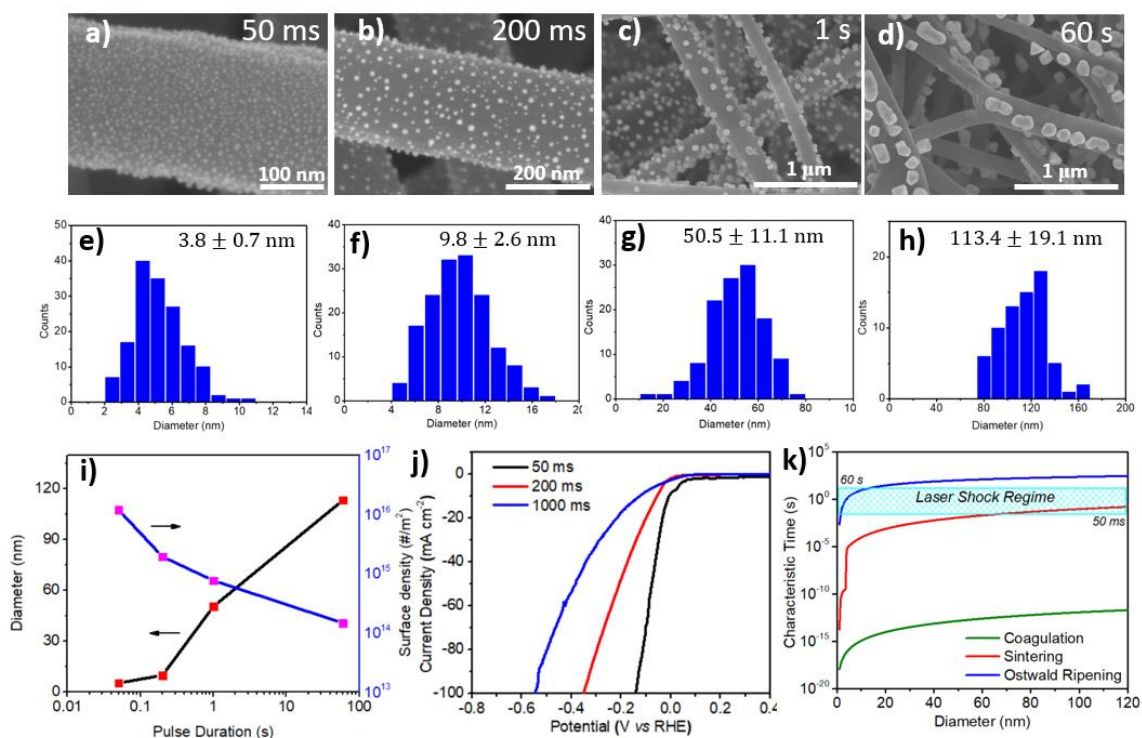


Figure 7.4. Effect of the duration of laser induced thermal shock on the nanocluster size and number density supported on the carbon nanofibers. a-d) SEM images of metal nanoclusters with different laser shock pulses (50ms, 0.2s, 1s, 60s) and e-h) their corresponding histograms of size distribution; i) variations of particle diameter and number density with laser pulse; j) polarization curve of CNF supported Pt nanoclusters; k) characteristic times for coagulation, sintering, Ostwald Ripening of monodispersed Pt nanoclusters on the carbon nanofiber surface at 1550 K.

Example Application: Electricity generated from renewable energy such as solar and wind must be stored durably for off-grid applications. Electrochemical water splitting to produce hydrogen and oxygen provides a promising solution to convert the electrical energy to chemical energy in the form of chemical bonds.⁴⁹ Platinum has been proved to

be an excellent catalyst to catalyze the reduction of protons to H₂ at high reaction rates and low overpotentials.²²⁶ Here, the electrocatalytic performance of Pt nanoclusters generated with the laser shock technique toward hydrogen evolution reaction was evaluated. The linear sweep voltammetry polarization curves of the thin film samples treated with different laser shock durations are shown in Figure 7.4j. **Table 7.3** summarizes the overpotentials of the three samples at the current densities of 50 mA cm⁻². It is clear that the sample with the shortest laser shock treatment has the best electrocatalytic performance. This is likely because a short laser pulse enables the formation of the smallest nanoclusters with high surface number densities, maximizing the active sites for the electrocatalytic reaction. In particular, the results show that Pt nanoclusters prepared with a 50 ms laser shock has an overpotential of 76 mV at a current density of 50 mA cm⁻². This result is comparable to that of commercial 40 wt% Pt/C composite electrode previously reported²²⁷, demonstrating promising catalytic performance of the Pt nanoclusters generated with our laser shock technique.

Nanoparticle Growth Mechanism: Here, I use a simple characteristic time analysis to investigate the likely growth mechanism of nanoclusters on the surface of carbon nanofibers, and discuss the role of Brownian coagulation, sintering, and Ostwald ripening on nanocluster formation. In this case, Ostwald Ripening describes the process of metal atoms releasing from smaller particles, moving into the gas phase, and attaching onto larger particles.

Consider a CNF thin film matrix with a surface area, A , and a thickness, L , containing uniformly dispersed Pt nanoclusters with a diameter, d_p , and a number concentration, N_0 . The number concentration N_0 is correlated with the diameter d_p as

follows: $N_0 \propto 1/d_p^3$. The characteristic coagulation time is defined as the time required for the nanoclusters with the initial concentration of N_0 to achieve half of its value. For nanoclusters with a narrow size distribution, the characteristic coagulation time can be estimated by using the following equation⁴⁰:

$$\tau_{coag} = \frac{2}{KN_0} \quad (7.8)$$

Here, $K = 8\pi Dd_p$ is the continuum Brownian coagulation coefficient, where D is the diffusion coefficient of Pt nanoclusters on the surface of the carbon nanofiber. To be in line with previous transport theory, I relate the surface diffusion coefficient D of nanoparticle with the Einstein-Stokes Equation of three-dimensional diffusivity, D_∞ , by using a hydrodynamic wall-correction factor, λ .²²⁸⁻²²⁹

$$D = \frac{D_\infty}{\lambda} \quad (7.9)$$

Einstein-Stokes Equation of the three-dimensional diffusivity, D_∞ , is expressed as:

$$D_\infty = \frac{kT}{6\pi\eta d_p} \quad (7.10)$$

Where k is Boltzmann constant; η is the viscosity of air at the temperature T ; and d_p is the particle diameter.

I can further estimate the characteristic sintering time for Pt nanoclusters, which is defined as the time required for two contacted primary particles to form a single spherical particle. In our previous study, I have shown that the sintering of metal nanoparticles is sensitive to the phase of the nanoparticles.²⁴ Our calculation shows that Pt nanoparticles with a diameter of less than 5.2 nm are in liquid phase at 1550 K. Therefore, a viscous flow mechanism was used to calculate the sintering time of the particles in liquid phase⁴¹:

$$\tau_{sinter,l} = \frac{\mu d_{eff}}{2\sigma_l} \quad (7.11)$$

Where μ is the viscosity of Pt nanoparticle, σ_l is the surface tension of Pt nanoparticle in liquid state; d_{eff} is the effective diameter of the sintering particle pair, which is $6V_p/a_p$, V_p and a_p are volume and surface area of the sintering particle pair, respectively.

For nanoparticles in the solid phase, the sintering time can be estimated as follows⁴²:

$$\tau_{sinter,s} = \frac{3k_B T N}{64\pi\sigma_s D_{eff}} \quad (7.12)$$

Where T is the temperature of a particle pair undergoing sintering, N is the number of atoms in the particle pair, σ_s is the surface tension of solid Pt nanoparticle, D_{eff} is the effective atomic diffusion coefficient of the particle pair.

Another possible mechanism for nanoparticle growth is Ostwald ripening. Ostwald ripening involves the dissolvment of smaller particles and the redeposition of the dissolved species on the surfaces of the larger particles that are far more thermodynamically favorable. The sublimation time is used to estimate the characteristic time for Ostwald ripening. The time to sublime a particle with a diameter of d_p can be derived as:⁴³

$$\tau_{sublim} = \frac{2B}{A} \left\{ E_0 \left(\frac{B}{d_p} \right) - E_1 \left(\frac{B}{d_p} \right) \right\} \quad (7.13)$$

Where the definition for the constants A , B , $E_0(x)$, $E_1(x)$ can be found in the supporting information. All property data mentioned above can be found in the Supporting Information (**Table 7.4**).

The characteristic times for coagulation, sintering, and Ostwald ripening as a function of nanoparticle diameter are shown in Figure 7.4k with the laser shock duration ranging from 50 ms to 60 s. At early stages of nanoparticle growth when particle size is less than 10 nm, I observe that all three characteristic times are shorter than the laser shock

duration. This implies that all three growth mechanisms are involved in the initial stages of nanoparticle growth. Small particles diffuse, coagulate, and sinter together to form large particles. Meanwhile, small particles might sublime and disappear, and released metal atoms transport and deposit on relatively larger particles. Once the particles grow to a size of 10 nm and above, the characteristic time for Ostwald ripening becomes longer than the laser shock duration, suggesting that Ostwald ripening is no longer a dominant force, leaving the primary growth mechanisms as sintering and coagulation. As shown in Figure 7.4k, the characteristic coagulation time of the Pt nanoparticles is much shorter than the characteristic sintering time, suggesting that one should see the aggregated particles at any stage of particle growth. However, no aggregated particles are observed in the SEM images shown in Figure 7.4a-c, indicating that particle coagulation on CNF surface might be slower than that demonstrated in Figure 7.4k. Previous Raman Spectrometry analysis on the CNF matrix prepared using a similar procedure has shown that there is relatively strong defect-induced D band, suggesting that there is an abundance of defects on the CNF surface.³⁶ Molecular dynamics simulations show that these surface defects can provide anchoring sites to stabilize the nanoparticles and significantly retard their diffusion and coagulation on CNF surface.¹⁴⁵ A longer laser shock (~60 s) may help remove these defects, which is confirmed by Raman spectrometry result demonstrating no presence of the defect-induced D band for annealed fibers.³⁶ A decrease in surface defects by laser heating, therefore, leads to accelerated diffusion of Pt nanoclusters on CNF surface. This explains the aggregation-dominated formation of larger Pt nanoparticles (Figure 7.4d) where a 60 s laser pulse was used.

7.4. Conclusions

I demonstrate an ultrafast laser induced thermal shock technique to fabricate carbon nanofiber supported ultra-small metal nanoclusters with high surface density. An ultrafast laser shock heating on the metal precursor incorporated CNF matrix triggers fast nucleation and growth of metal nanoclusters and a subsequent ultra-fast quenching freezes them onto the CNF structure. Shorter thermal pulse enables the formation of smaller nanoclusters with higher number densities. Longer thermal shock enables the further growth of metal nanoparticles and the achievement of their equilibrium shape. A characteristic time analysis suggested that the growth of metal nanoclusters is dominated by coagulation and sintering, and Ostwald ripening is mainly involved at the early stage of nanoparticle formation. As an example of application, I demonstrate very favorable catalytic property of Pt nanoclusters for electrocatalytic hydrogen evolution. This work provides a promising approach for rapid and scalable fabrication of ultra-small metal nanoclusters and nanocluster-based devices.

7.5. Supporting Information

Moment model for saturation ratio calculation; data collected from Temperature Jump/Time of Flight Mass Spectrometry (T-Jump/TOFMS); EDS spectrums of metal precursor laden CNF samples before and after 50 ms laser shock treatment; size-dependent melting point of Pt nanoparticle; property data for characteristic time analysis; high speed color camera video for temperature measurement.

7.5.1. Moment model for saturation ratio calculation

A moment model⁴⁰ was used to calculate how the saturation ratio S of metal atoms changes with the duration of the laser shock. A set of differential equations was solved simultaneously in order to calculate time resolved-saturation ratio:

$$\frac{dS}{dt} = \frac{R_H}{n_s} - \frac{Jk^*}{n_s} - (S - 1) \frac{B_1 A}{2v_1 n_s} \quad (7.14)$$

$$\frac{dA}{dt} = Jk^{*2/3} S_1 + 2\pi B_1 (S - 1) M_1 \quad (7.15)$$

$$\frac{dM_1}{dt} = Jr_c + (S - 1) B_1 N \quad (7.15)$$

$$\frac{dN}{dt} = J \quad (7.17)$$

Here, R_H is the thermal decomposition rate of metal salt precursor to zero-valent metal atoms; A is the total surface area of all the nuclei in the reaction volume; M_1 is the first moment which is defined as $M_1 = \int_{d^*}^{\infty} n_d d_p d(d_p)$ where $d^* = 2r_c = \frac{4\sigma V_1}{k_B T \ln S}$, n_d is number concentration of particle with a diameter of d_p ; N is the number concentration of nuclei; R_H and A are time-dependent variables; k^* is the number of monomers in a single particle with a critical radius r_c ; n_s is the monomer concentration at saturation condition; $B_1 = 2n_1 v_1 \left(\frac{k_B T}{2\pi m_1}\right)^{1/2}$ where n_1 is the monomer number concentration; v_1 and m_1 is volume and

mass of the monomer, respectively; J is the rate of particle formation by homogenous nucleation, which is given as follows ⁴⁰:

$$J_{homo} = \frac{Kn_1s_1}{3} \sqrt{\frac{\Phi}{\pi}} \exp\left(-\frac{4}{27} \frac{\Phi^3}{(\ln S)^2}\right) \quad (7.18)$$

Where $K = n_1 \left(\frac{kT}{2\pi m_1}\right)^{1/2}$; Φ is dimensionless surface tension of the stable nuclei $\Phi = \frac{s_1\sigma}{kT}$; s_1 is the surface area of a monomer.

The presence of the carbon nanofibers would be expected to further lower the nucleation barrier and promote the heterogenous nucleation, which is given as: ¹³⁸

$$J_{hetero} = \frac{Kn_1s_1}{3} \sqrt{\frac{\Phi}{\pi}} \exp\left(-\frac{4}{27} \frac{\Phi^3}{(\ln S)^2}\right) \cdot f(\theta) \quad (7.19)$$

where $f(\theta) = 1/4(2 + \cos\theta)(1 - \cos\theta)^2$, which is the reduction factor and θ is the contact angle between the metal and carbon surface. Therefore, J_{hetero} was used in Eqn. 7.14 for the saturation ratio calculation.

Although no direct data of thermal decomposition/reduction of H_2PtCl_6 was found, it has been reported that the thermal decomposition/reduction of metal oxide (NiO) to zero-valence metal is a first order reaction with an activation energy of 85 kJ/mol and a rate constant of 7 s^{-1} at 873 K, ^{25, 130} which are used to estimate the rate constant, k_1 , for the thermal decomposition of H_2PtCl_6 to zero-valent metal atoms at 1550 K. The thermal decomposition rate of H_2PtCl_6 can be written as:

$$R_H = k_1 n \quad (7.20)$$

Where n is the number concentration of metal salt precursor in the carbon nanofiber matrix with an initial value of n_0 . Three initial metal salt loadings investigated are: 10^{20} , 10^{21} , and 10^{22} #/m^3 . Therefore, the number concentration of metal salt $n = n_0 e^{-k_1 t}$; the

concentration of the monomer generated from the thermal decomposition of metal salt

$$n_1 = n_0 - n.$$

Table 7.1. Property data used to calculate saturation ratio.

parameter	definition	value
k_B	Boltzmann constant	$1.38 \times 10^{-23} \text{ m}^2 \text{ kg s}^2 \text{ K}^{-1}$
T	reaction temperature	1550 K
σ	surface tension ¹³² of Pt nanocluster in liquid state, σ_1	1.8 N/m
v_1	platinum atom (monomer) volume	$1.09 \times 10^{-29} \text{ m}^3$
m_1	platinum atom (monomer) mass	$2.34 \times 10^{-25} \text{ kg}$
k_1	estimated rate constant of thermal decomposition of metal salt to metal atoms at 1550 K	$1.15 \times 10^3 \text{ s}^{-1}$
n_s	monomer concentration at saturation condition	$2.73 \times 10^{13} \text{ \#/m}^3$
ω	Contact angle between liquid Pt and carbon ²³⁰⁻²³¹	53°

7.5.2. Temperature Jump/Time of Flight Mass Spectrometry

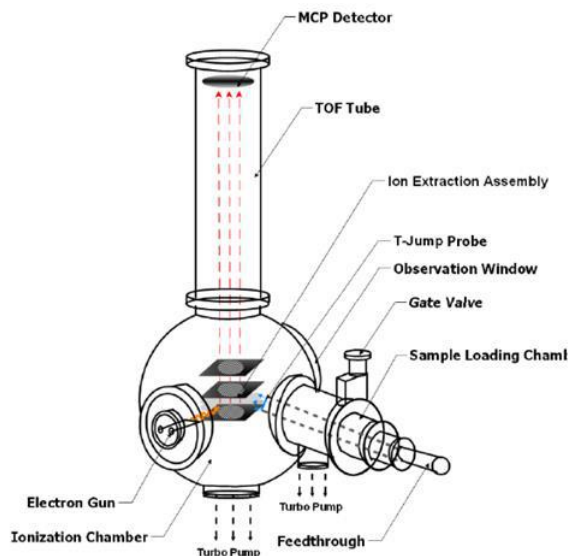


Figure 7.5. Temperature Jump/Time of Flight Mass Spectrometry (T-Jump/TOFMS) Apparatus Schematic⁵⁴

Table 7.2. Release time, release temperature for different species detected by time of flight mass spectrometry.

species	release time (ms)	release temperature (°C)	heating rate
PtCl ₂ ⁺	1.1	437	3.60E+05
CClH ₂ ⁺	0.4	187	3.80E+05
C ₂ ClH ₃ ⁺	0.4	187	3.80E+05
HCl ⁺	0.4	187	3.80E+05
Cl ⁺	0.4	187	3.80E+05

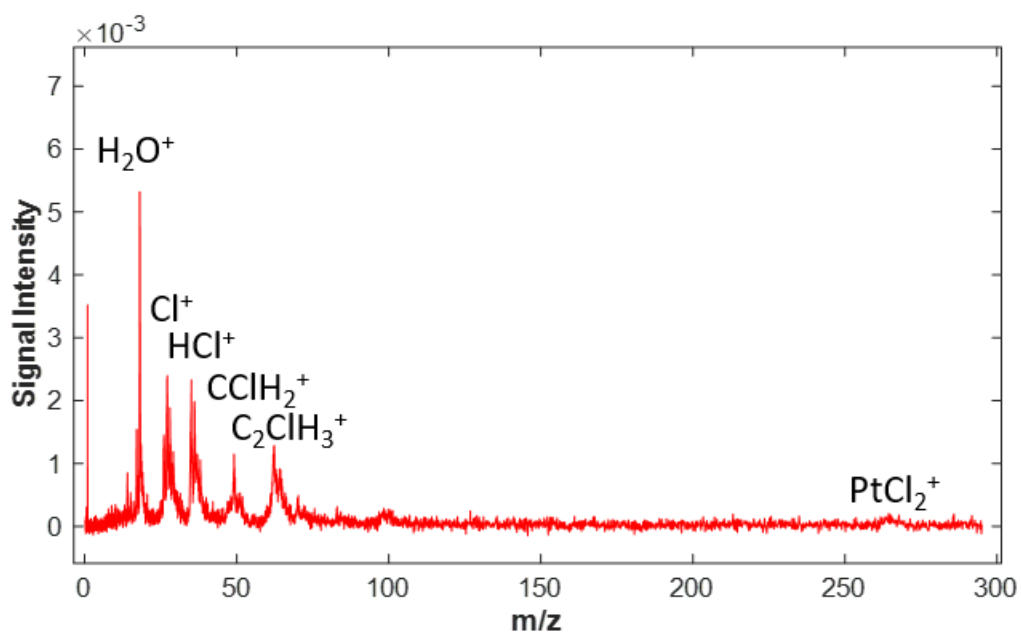


Figure 7.6. Mass spectrum results for metal salt during ultrafast heating detected by time of flight mass spectrometry.

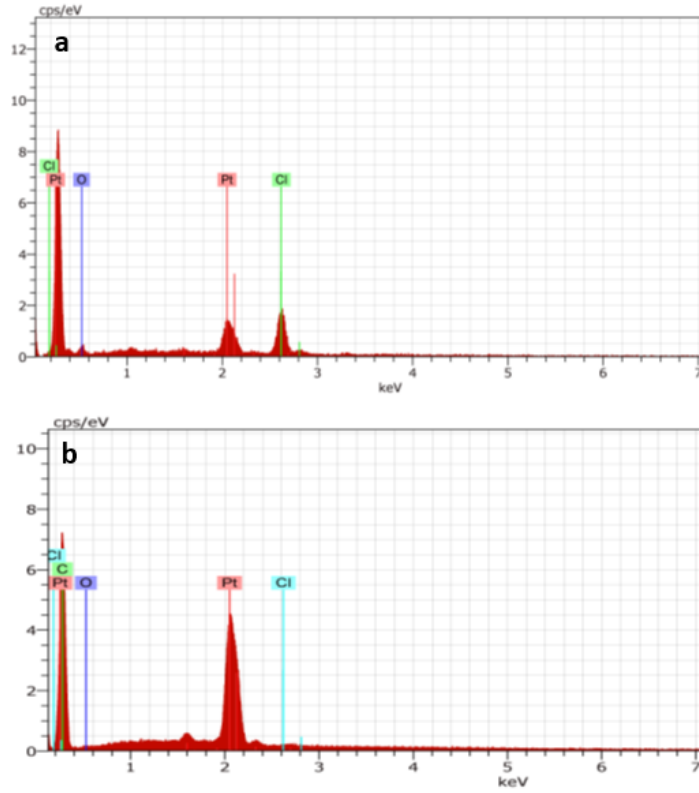


Figure 7.7. EDS spectra of CNF supported Pt nanoclusters before (a) and after (b) 50ms laser shock treatment.

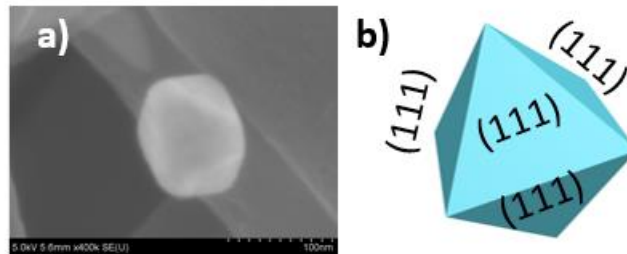


Figure 7.8. SEM image of a single particle generated with a 60 s laser pulse.

7.5.3. Size-dependent melting point of Pt nanoparticle

The melting point of Pt nanoparticles is size-dependent, which was approximated using the following empirical equation¹³¹:

$$T_{mp}(d_p) = T_m \left[1 - \frac{4}{L\rho_p d_p} (\sigma_s - \sigma_l \left(\frac{\rho_p}{\rho_l} \right)^{\frac{2}{3}}) \right] \quad (7.21)$$

Here, T_m is the bulk melting point (2041 K), L is the latent heat of melting (100000 J/kg), σ_s and σ_l are the surface tension (J/m²), $\sigma_s = 2.37$ N/m, $\sigma_l = 1.8$ N/m (surface tension of molten metals at their melting points¹³²), ρ_p and ρ_l are the respective solid and liquid phase densities (kg/m³), $\rho_p = 21450$ kg/m³ (assume it is temperature independent), $\rho_l = 19770$ kg/m³ (assume it is temperature independent.) **Figure 7.9** shows the melting point of Pt nanoparticle changes with its diameter and nanoparticles with a diameter of less than 5.2 nm are in liquid phase at the temperature of 1550 K.

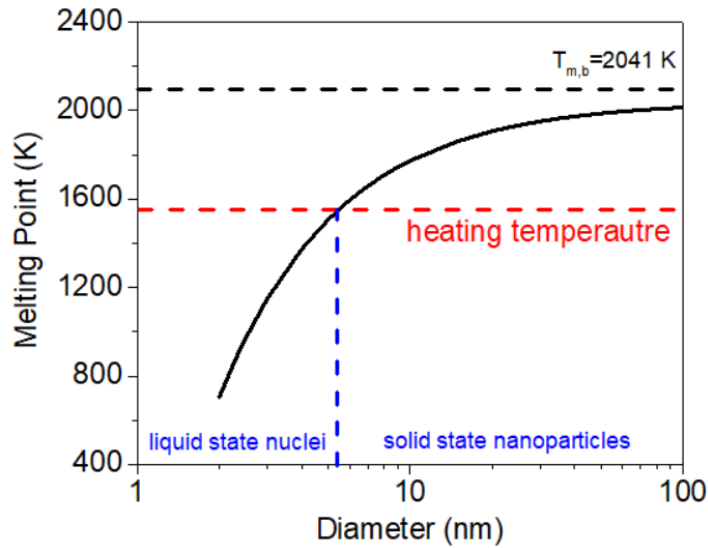


Figure 7.9. Metal point of Pt nanoparticle versus particle diameter.

7.5.4. Catalytic Property of CNF supported Pt nanoclusters.

Table 7.3. Overpotentials for CNF supported Pt nanoclusters at various current densities applied.

Current density	50 (mA cm ⁻²)	100 (mA cm ⁻²)
Commercial 40% Pt/C ²²⁷	~80 mV	~125 mV
Pt-CNF-50 ms	76 mV	144 mV
Pt-CNF-200 ms	208 mV	352 mV
Pt-CNF-1000 ms	384 mV	546 mV

7.5.5. Property data for characteristic time analysis

Hydrodynamic wall-correction factor can be written as:

$$\lambda = \left[1 - \frac{9}{16} \left[\frac{R}{Z} \right] + \frac{1}{8} \left[\frac{R}{Z} \right]^3 - \frac{45}{256} \left[\frac{R}{Z} \right]^4 - \frac{1}{16} \left[\frac{R}{Z} \right]^5 \right]^{-1} \quad (7.22)$$

Where R is particle radius and Z is the distance from the center of the particle to the surface of the carbon nanofiber. Here I assume nanoparticles have a spherical shape with an R/Z value of 1.

Parameters for sublimation rate calculation:

Ostwald ripening involves the dissolution of smaller particles and the redeposition of the dissolved species on the surfaces of the larger particles that are far more thermodynamically favorable. At elevated temperatures, the metal atoms release from small particles and migrate onto large particles in the gas phase due to a vapor pressure difference between two particles with different sizes caused by Kelvin effect, which is described below:⁴³

$$\ln \frac{P_{d_p}}{P_{\infty}} = \left(\frac{M_{d_p}}{TR\rho} \right) \left(\frac{2\sigma_s}{d_p} \right) \quad (7.23)$$

Where M_{d_p} is the molecular weight, R is the gas constant, ρ is the density of the solid, T is the temperature, P_{d_p} is the vapor pressure above a particle of diameter d_p , P_{∞} is the equilibrium vapor pressure of the sublimating species over a flat surface, σ_s is the surface tension of the solid.

In a typical Ostwald ripening process, metal atoms sublime from smaller particles and attach to larger ones. The sublimation rate of the smaller particles can be written as:

$$\frac{d(d_p)}{dt} = n_v V_a \quad (7.24)$$

Where V_a is the volume of platinum atom; n_v is the total number of platinum atoms leaving the surface per unit time, which can be derived using kinetic collision theory:

$$n_v = \alpha n_c = \frac{1}{4} \alpha n \left(\frac{8RT}{\pi M d_p} \right)^{1/2} \quad (7.25)$$

Where α is the sticking coefficient for metal atom arriving at the surface and n is the number of metal atoms in the vapor. n can be related to the vapor pressure (Eqn. 7.23) by applying ideal gas law.

Combining Eqns. 7.23 to S7.25, the time to sublime a particle with a diameter of d_p can be derived as:

$$\tau_{sublimation} = \frac{2B}{A} \left\{ E_0 \left(\frac{B}{d_p} \right) - E_1 \left(\frac{B}{d_p} \right) \right\} \quad (7.26)$$

Where the definition for the constants A , B , $E_0(x)$, $E_1(x)$ can be found in the supporting information. The sublimation time is used to estimate the characteristic time for Ostwald ripening.

The constant A , B , $E_0(x)$, $E_1(x)$ used for calculating sublimation rate of a Pt nanoparticle are defined as:

$$A = \alpha \left(\frac{M d_p}{2\pi R \rho} \right)^{1/2} \frac{P_\infty}{T^{1/2}} \quad (7.27)$$

$$B = \frac{2M_r \gamma}{\rho R T} \quad (7.28)$$

$$E_0 = \frac{\exp(-x)}{x} \quad (7.29)$$

$$E_1 = \int_x^\infty \frac{\exp(-y)}{y} dy \quad (7.30)$$

Table 7.4. Property data used for the characteristic time analysis.

parameter	definition	value
k_B	Boltzmann constant	$1.38 \times 10^{-23} \text{ m}^2 \text{ kg s}^2 \text{ K}^{-1}$
T	temperature	1550K
η	viscosity of the air at 1550 K	$5.53 \times 10^{-5} \text{ N/m}$
μ	viscosity of Pt nanocluster at 1550 K	See below
σ_l	surface tension of Pt nanocluster in liquid state	1.8 N/m
σ_s	surface tension of solid Pt nanocluster	2.37 N/m
D_{eff}	effective atomic diffusion coefficient in the particle pair at 1550 K ¹³⁴	$1.06 \times 10^{-14} \text{ m}^2 \text{ s}^{-1}$

Viscosity of the air, η is given by Sutherland's formula:¹⁵²

$$\eta = \xi \frac{T^{\frac{3}{2}}}{T+C} \quad (7.31)$$

Where $\xi = \frac{\mu_0(T_0+C)}{T_0^{\frac{3}{2}}}$ is a constant for the gas, $\mu_0 = 1.87 \times 10^{-5} \text{ N/m}$, $T_0 = 291.15 \text{ K}$,

$C = 120$, which is Sutherland's constant for the gaseous material.

Viscosity of Pt nanocluster, μ ^{24, 41}

μ is the viscosity of Pt nanocluster, which is given as:

$$\mu = 1.8 \times 10^{-7} \frac{[M \cdot T_{mp}(d_p)]^{1/2} \exp\left(\frac{L}{RT_p}\right)}{v_m \exp\left[\frac{L}{RT_{mp}(d_p)}\right]} \quad (7.32)$$

Where L is the latent heat of melting (J/mol), 19500 J/mol (which is equal to 100000 J/kg), $T_{mp}(d_p)$ is the melting point of the Pt nanoclusters with a diameter of d_p , M is the molar weight, $195.08 \times 10^{-3} \text{ kg/mol}$, R is the gas constant, 8.314 J/mol/K, v_m is the molar volume, $9.1 \times 10^{-6} \text{ m}^3/\text{mol}$.

Chapter 8: Summary and Future Work

In this dissertation, I have described two ultrafast high temperature processing techniques for the large-scale production of ultrasmall metal nanoparticles with high densities decorated in the proper host matrices: aerosol based thermal pulse technique and laser induced thermal shock technique. Also, the fast heating and fast quenching nature of the aerosol based thermal shock enables me to produce well-mixed high entropy alloy nanoparticles containing unmixable metal elements. Further investigation of the aerosol droplets mediated approach leads to the fabrication of functional nanostructures for battery design using aerosol droplets as the building block. Now, I will summarize the important conclusion of my work and suggest areas for further study.

8.1. Summary

I have developed an aerosol single-drop reactor approach to grow and stabilize metal nanoclusters in a polymer matrix. The rapid thermal pulse given to the aerosol particles enables the formation of nuclei and growth, with subsequent rapid quenching to freeze in the structure. The size of metal nanoclusters can be controlled by adjusting the mass loading ratio of metal salt to polymer matrix, and the temperature of the tubular reactor. Based on the experimental observation and quantitative analysis, I conclude that the growth is governed by nucleation and surface growth with little coagulation or Ostwald ripening. Finally, it is noted that this aerosol route is amenable to scale-up for large scale production of nanoclusters that can either be used as is within the polymer or released by solvent extraction, depending on the application.

Based on this success in produce polymer matrix supported ultrasmall metal nanoparticle, I have applied the method to to *in situ* synthesize well-dispersed metal nanoclusters in the graphene matrix. The aerosol particles containing graphene oxide sheets acts as nanoreactors for the reduction of metal precursor and the growth of metal nanoclusters. With this fast heating and quenching, the metal precursor was quickly reduced and nucleated into metallic nanoclusters. The size and morphology of the metal nanoclusters can be controlled by varying the reaction temperature and the mass loading of metal salt in the graphene aerosol nanoreactors. Smaller nanoclusters with a narrower size distribution were obtained with a lower reaction temperature and lower mass loading. A characteristic time analysis leads to the conclusion that the nanocluster formation is governed by nucleation and subsequent surface growth, and the coagulation and coalescence might only be involved in the nucleation stage. Finally, I note that this one-step continuous aerosol-based thermal shock technique offers considerable potential for the manufacturing processing of well-dispersed and uniform nanoclusters stabilized within a graphene matrix.

Next, I showed that by using aerosol droplets as building blocks to design functional nanostructure as excellent energy storage materials . I successfully fabricated Sb@CSN composite anode with evenly-distributed and small Sb nanoparticles confined in carbon sphere network for K-ion battery anode via unique electrospray-assisted strategy. Sb@CSN anode in the concentrated 4M KTFSI electrolyte shows a high reversible capacity of 551 mAh/g at 100 mA/g over 100 cycles with a capacity decay of 0.06% per cycle from the 10st to 100th cycling and 504 mAh/g after 220 cycles even at a high current density of 200 mA/g. It also shows excellent rate performance by providing 589 mAh/g at

50 mA/g and 530 mAh/g at 200 mA/g. Such a unique material in this concentrated electrolyte demonstrates one of the best capacity performances among all K-ion battery anode materials. These excellent K-storage performances should be ascribed to the formation of stable and robust KF-rich SEI layer along with the novel nanostructure of Sb nanoparticles uniformly encapsulated into the conductive carbon network. These discoveries provide valuable guidance for rationally developing advanced alloy-based electrode materials for high-performance PIBs applications.

Then, I showed that the fast heating and fast quenching nature of the aerosol droplet-mediated technique enabled scalable synthesis of high entropy alloy nanoparticles with atomic-level mixing of immiscible metal elements. The aqueous solution containing desired different metal salts was nebulized into millions of aerosol droplets with a diameter of less than 1 μm , and fast heating and fast quenching treatment was exerted on these on-the-fly droplets with each droplet acting as a nanoreactor to produce a single high entropy alloy nanoparticle. Atomic-level STEM study coupled with EDS analysis reveals that all metal elements in the nanoparticles are mixed together on an atomic level. This facile and flexible aerosol droplet-mediated synthesis technique advances the field of high entropy alloy nanoparticles and also demonstrates the potential to transcend fundamental research to industrial application.

Finally, I demonstrated an ultrafast laser induced thermal shock technique to fabricate carbon nanofiber supported ultra-small metal nanoclusters with high surface density. An ultrafast laser shock heating on the metal precursor incorporated CNF matrix triggers fast nucleation and growth of metal nanoclusters and a subsequent ultra-fast quenching freezes them onto the CNF structure. Shorter thermal pulse enables the

formation of smaller nanoclusters with higher number densities. Longer thermal shock enables the further growth of metal nanoparticles and the achievement of their equilibrium shape. A characteristic time analysis suggested that the growth of metal nanoclusters is dominated by coagulation and sintering, and Ostwald ripening is mainly involved at the early stage of nanoparticle formation. As an example of application, I demonstrate very favorable catalytic property of Pt nanoclusters for electrocatalytic hydrogen evolution. This work provides a promising approach for rapid and scalable fabrication of ultra-small metal nanoclusters and nanocluster-based devices.

8.2. Future Work

8.2.1. Laser shock synthesis of multi-component metal nanoparticles

In this dissertation, I developed the laser shock approach to fabricate ultra-small, densely, and uniformly dispersed ultrasmall metal nanoparticles on carbon nanofiber matrices. This approach is a facile way to precisely tune nanocluster size, surface density, and shape. Compared to the aerosol based thermal shock approach, this technique provides high flexibility to tune the duration of the thermal pulse (50 ms vs. 1 s) towards the sample and also renders a much faster cooling rate (10^5 K/s vs. 10^3 K/s). Therefore, it is plausible to generate size-tunable multi-component metal nanoparticles decorated on the carbon nanofiber thin film matrix with the laser shock technique. Furthermore, the current experimental setup can be easily modified for roll-to roll manufacturing of multi-component metal nanoparticles.

8.2.2. Kinetics oxidation of high entropy alloy nanoparticles.

Multiple principal element alloys (MPEAs), also called high-entropy alloys (HEAs), have received a great deal of research of interest due to their outstanding mechanical

properties such as high toughness and strength, impressive fatigue resistance as well as excellent wear resistance in comparison with traditional alloys.^{68, 232} However, scientific and technological attention on the oxidation and surface phenomena of the MPEAs is insufficient compared to the development of studying and improving their mechanical properties. The poor understanding of the high temperature surface oxidation of the MPEAs has become a serious issue towards their practical utilization.

Even though the research on the high-temperature surface oxidation of MPEAs has drew growing attention, a comprehensive understanding of the oxidation and surface phenomena of the MPEAs is still lacking. In order to achieve a better understanding on the surface oxidation mechanism of the MPEAs, several things need to be considered. First, most reported studies on surface oxidation behaviors of MPEAs heavily rely on the microstructure results obtained using SEM/EDS and XRD. Unfortunately, these instruments have limited spatial resolution and sensitivity so that they are not able to reveal the detailed elemental distributions and compositions of MPEAs. Second, the temporal evolution of the protective oxide layer formation during heat treatment has not been investigated so far, which is crucially important to study the surface oxidation mechanism of MPEAs. In fact, the evolution of the protective oxide layer on the surface of MPEAs can be studied using newly developed in-situ heating TEM. However, this observation requires to prepare MPEA samples in a nanoscale dimension, which is much smaller than the samples prepared with the currently used melting and casting approaches. Therefore, new technique needs to be developed to synthesize nanosized MPEAs with atomically mixed elements. Third, quite often, the sample synthesis process is separated with the post heat treatment, which unavoidably introduces the surface oxidation on samples to be

studied and affects final results. In order to avoid the surface oxidation during sample transportation, one needs to combine the synthesis and characterization instruments together to build an on-line analysis for investigating surface oxidation kinetics of MPEAs in a more precise way.

Bibliography

1. Olson, J.; Dominguez-Medina, S.; Hoggard, A.; Wang, L.-Y.; Chang, W.-S.; Link, S., Optical characterization of single plasmonic nanoparticles. *Chemical Society Reviews* **2015**, *44* (1), 40-57.
2. Boisselier, E.; Astruc, D., Gold nanoparticles in nanomedicine: preparations, imaging, diagnostics, therapies and toxicity. *Chemical society reviews* **2009**, *38* (6), 1759-1782.
3. Lu, A. H.; Salabas, E. e. L.; Schüth, F., Magnetic nanoparticles: synthesis, protection, functionalization, and application. *Angewandte Chemie International Edition* **2007**, *46* (8), 1222-1244.
4. Ozbay, E., Plasmonics: merging photonics and electronics at nanoscale dimensions. *science* **2006**, *311* (5758), 189-193.
5. Choi, K. M.; Na, K.; Somorjai, G. A.; Yaghi, O. M., Chemical environment control and enhanced catalytic performance of platinum nanoparticles embedded in nanocrystalline metal–organic frameworks. *J. Am. Chem. Soc* **2015**, *137*, 7810-7816.
6. Zheng, J.; Yang, Y.; Fan, X.; Ji, G.; Ji, X.; Wang, H.; Hou, S.; Zachariah, M. R.; Wang, C., Extremely stable antimony–carbon composite anodes for potassium-ion batteries. *Energy & Environmental Science* **2019**, *12* (2), 615-623.
7. Puentes, V. F.; Gorostiza, P.; Aruguete, D. M.; Bastus, N. G.; Alivisatos, A. P., Collective behaviour in two-dimensional cobalt nanoparticle assemblies observed by magnetic force microscopy. *Nat Mater* **2004**, *3* (4), 263-268.
8. Chen, J.; Wiley, B.; Li, Z. Y.; Campbell, D.; Saeki, F.; Cang, H.; Au, L.; Lee, J.; Li, X.; Xia, Y., Gold nanocages: engineering their structure for biomedical applications. *Advanced Materials* **2005**, *17* (18), 2255-2261.
9. Tan, J.; Yang, Y.; El Hadri, H.; Li, M.; Hackley, V. A.; Zachariah, M. R., Fast quantification of nanorod geometry by DMA-spICP-MS. *Analyst* **2019**, *144* (7), 2275-2283.
10. Pillai, S.; Catchpole, K.; Trupke, T.; Green, M., Surface plasmon enhanced silicon solar cells. *Journal of applied physics* **2007**, *101* (9), 093105.
11. Li, W.; Liang, C.; Zhou, W.; Qiu, J.; Zhou, Z.; Sun, G.; Xin, Q., Preparation and characterization of multiwalled carbon nanotube-supported platinum for cathode catalysts of direct methanol fuel cells. *The Journal of Physical Chemistry B* **2003**, *107* (26), 6292-6299.
12. Hadeif, F., An Introduction to Nanomaterials. In *Environmental Nanotechnology*, Springer: 2018; pp 1-58.

13. Faupel, F.; Zaporojtchenko, V.; Strunskus, T.; Elbahri, M., Metal - polymer nanocomposites for functional applications. *Advanced engineering materials* **2010**, *12* (12), 1177-1190.
14. Park, J.; Joo, J.; Kwon, S. G.; Jang, Y.; Hyeon, T., Synthesis of monodisperse spherical nanocrystals. *Angewandte Chemie International Edition* **2007**, *46* (25), 4630-4660.
15. Charitidis, C. A.; Georgiou, P.; Koklioti, M. A.; Trompeta, A.-F.; Markakis, V., Manufacturing nanomaterials: from research to industry. *Manufacturing Review* **2014**, *1*, 11.
16. McMahan, B. W.; Yu, J.; Boatz, J. A.; Anderson, S. L., Rapid Aluminum Nanoparticle Production by Milling in NH₃ and CH₃NH₂ Atmospheres: An Experimental and Theoretical Study. *ACS Applied Materials & Interfaces* **2015**, *7* (29), 16101-16116.
17. Jacob, R.; Zong, Y.; Yang, Y.; Li, S.; Zachariah, M. R. In *Size-Resolved Burn Rate Measurements of Metal NanoParticles*, 54th AIAA Aerospace Sciences Meeting, 2016; p 0687.
18. Jacob, R. J.; Zong, Y.; Yang, Y.; Li, S.; Zachariah, M. R. In *Measurements of Size Resolved Burning of Metal Nanoparticles for Evaluation of Combustion Mechanism*, Proceedings of the 54th AIAA Aerospace Sciences Meeting, San Diego, CA, USA, 2016; pp 4-8.
19. Zong, Y.; Jacob, R. J.; Li, S.; Zachariah, M. R., Size Resolved High Temperature Oxidation Kinetics of Nano-Sized Titanium and Zirconium Particles. *The Journal of Physical Chemistry A* **2015**, *119* (24), 6171-6178.
20. Polonskyi, O.; Kylián, O.; Drábik, M.; Kousal, J.; Solař, P.; Artemenko, A.; Čechvala, J.; Choukourov, A.; Slavínská, D.; Biederman, H., Deposition of Al nanoparticles and their nanocomposites using a gas aggregation cluster source. *Journal of materials science* **2014**, *49* (9), 3352-3360.
21. Turkevich, J.; Stevenson, P. C.; Hillier, J., A study of the nucleation and growth processes in the synthesis of colloidal gold. *Discussions of the Faraday Society* **1951**, *11*, 55-75.
22. Brust, M.; Walker, M.; Bethell, D.; Schiffrin, D. J.; Whyman, R., Synthesis of thiol-derivatised gold nanoparticles in a two-phase liquid-liquid system. *J. Chem. Soc., Chem. Commun.* **1994**, (7), 801-802.
23. Sun, Y.; Xia, Y., Shape-controlled synthesis of gold and silver nanoparticles. *Science* **2002**, *298* (5601), 2176-2179.
24. Yang, Y.; Romano, M.; Feng, G.; Wang, X.; Wu, T.; Holdren, S.; Zachariah, M. R., Growth of Sub-5 nm Metal Nanoclusters in Polymer Melt Aerosol Droplets. *Langmuir* **2018**, *34* (2), 585-594.

25. Yang, Y.; Ghildiyal, P.; Zachariah, M. R., Thermal Shock Synthesis of Metal Nanoclusters within On-the-Fly Graphene Particles. *Langmuir* **2019**, *35* (9), 3413-3420.
26. Shatrova, N.; Yudin, A.; Levina, V.; Dzidziguri, E.; Kuznetsov, D.; Perov, N.; Issi, J.-P., Elaboration, characterization and magnetic properties of cobalt nanoparticles synthesized by ultrasonic spray pyrolysis followed by hydrogen reduction. *Materials Research Bulletin* **2017**, *86*, 80-87.
27. Liang, Y.; Hou, H.; Yang, Y.; Glicksman, H.; Ehrman, S., Conductive one-and two-dimensional structures fabricated using oxidation-resistant Cu–Sn particles. *ACS applied materials & interfaces* **2017**, *9* (40), 34587-34591.
28. Wu, C.; Lee, D.; Zachariah, M. R., Aerosol-based self-assembly of nanoparticles into solid or hollow mesospheres. *Langmuir* **2009**, *26* (6), 4327-4330.
29. Kim, S.; Liu, B.; Zachariah, M., Ultrahigh Surface Area Nanoporous Silica Particles via an Aero-Sol– Gel Process. *Langmuir* **2004**, *20* (7), 2523-2526.
30. Firmansyah, D. A.; Kim, T.; Kim, S.; Sullivan, K.; Zachariah, M. R.; Lee, D., Crystalline phase reduction of cuprous oxide (Cu₂O) nanoparticles accompanied by a morphology change during ethanol-assisted spray pyrolysis. *Langmuir* **2009**, *25* (12), 7063-7071.
31. Atkinson, J. D.; Fortunato, M. E.; Dastgheib, S. A.; Rostam-Abadi, M.; Rood, M. J.; Suslick, K. S., Synthesis and characterization of iron-impregnated porous carbon spheres prepared by ultrasonic spray pyrolysis. *Carbon* **2011**, *49* (2), 587-598.
32. Suh, W. H.; Suslick, K. S., Magnetic and porous nanospheres from ultrasonic spray pyrolysis. *Journal of the American Chemical Society* **2005**, *127* (34), 12007-12010.
33. Chen, Y.; Guo, F.; Jachak, A.; Kim, S.-P.; Datta, D.; Liu, J.; Kulaots, I.; Vaslet, C.; Jang, H. D.; Huang, J., Aerosol synthesis of cargo-filled graphene nanosacks. *Nano letters* **2012**, *12* (4), 1996-2002.
34. Xia, B.; Lenggoro, I. W.; Okuyama, K., Novel Route to Nanoparticle Synthesis by Salt-Assisted Aerosol Decomposition. *Advanced Materials* **2001**, *13* (20), 1579-1582.
35. Didenko, Y. T.; Suslick, K. S., Chemical aerosol flow synthesis of semiconductor nanoparticles. *Journal of the American Chemical Society* **2005**, *127* (35), 12196-12197.
36. Yao, Y.; Huang, Z.; Xie, P.; Lacey, S. D.; Jacob, R. J.; Xie, H.; Chen, F.; Nie, A.; Pu, T.; Rehwoldt, M.; Yu, D.; Zachariah, M. R.; Wang, C.; Shahbazian-Yassar, R.; Li, J.; Hu, L., Carbothermal shock synthesis of high-entropy-alloy nanoparticles. *Science* **2018**, *359* (6383), 1489-1494.
37. Yao, Y.; Huang, Z.; Xie, P.; Li, T.; Lacey, S. D.; Jiao, M.; Xie, H.; Fu, K. K.; Jacob, R. J.; Kline, D. J., Ultrafast, Controllable Synthesis of Sub-Nano Metallic Clusters through Defect Engineering. *ACS applied materials & interfaces* **2019**, *11* (33), 29773-29779.

38. Yao, Y.; Huang, Z.; Xie, P.; Li, T.; Lacey, S. D.; Jiao, M.; Xie, H.; Fu, K. K.; Jacob, R. J.; Kline, D. J.; Yang, Y.; Zachariah, M.; Wang, C.; Shahbazian-Yassar, R.; Hu, L., Ultrafast, Controllable Synthesis of Sub-Nano Metallic Clusters through Defect Engineering. *ACS applied materials & interfaces* **2019**, *11* (33), 29773-29779.
39. Thanh, N. T.; Maclean, N.; Mahiddine, S., Mechanisms of nucleation and growth of nanoparticles in solution. *Chemical reviews* **2014**, *114* (15), 7610-7630.
40. Friedlander, S. K., Smoke, Dust, and Haze: Fundamentals of Aerosol Dynamics. Topics in Chemical Engineering. Oxford University Press, New York: 2000.
41. Mukherjee, D.; Sonwane, C.; Zachariah, M., Kinetic Monte Carlo simulation of the effect of coalescence energy release on the size and shape evolution of nanoparticles grown as an aerosol. *The Journal of chemical physics* **2003**, *119* (6), 3391-3404.
42. Wu, M.; Windeler, R.; Steiner, C.; Börs, T.; Friedlander, S., Controlled synthesis of nanosized particles by aerosol processes. *Aerosol Science and Technology* **1993**, *19* (4), 527-548.
43. Asoro, M. A.; Kovar, D.; Ferreira, P. J., In situ transmission electron microscopy observations of sublimation in silver nanoparticles. *ACS nano* **2013**, *7* (9), 7844-7852.
44. Wang, M.; Zhang, W.; Liu, Y.; Yang, Y.; Wang, C.; Wang, Y., Electrochemical performance of patterned LiFePO₄ nano-electrode with a pristine amorphous layer. *Applied Physics Letters* **2014**, *104* (17), 171604.
45. Xu, Y.; Liu, Q.; Zhu, Y.; Liu, Y.; Langrock, A.; Zachariah, M. R.; Wang, C., Uniform nano-Sn/C composite anodes for lithium ion batteries. *Nano letters* **2013**, *13* (2), 470-474.
46. Zheng, J.; Ji, G.; Fan, X.; Chen, J.; Li, Q.; Wang, H.; Yang, Y.; DeMella, K. C.; Raghavan, S. R.; Wang, C., High-Fluorinated Electrolytes for Li-S Batteries. *Advanced Energy Materials* **2019**, *9* (16), 1803774.
47. Dahn, J. R.; Zheng, T.; Liu, Y.; Xue, J., Mechanisms for lithium insertion in carbonaceous materials. *Science* **1995**, *270* (5236), 590-593.
48. Winter, M.; Besenhard, J. O., Electrochemical lithiation of tin and tin-based intermetallics and composites. *Electrochimica Acta* **1999**, *45* (1-2), 31-50.
49. Gao, M.-R.; Liang, J.-X.; Zheng, Y.-R.; Xu, Y.-F.; Jiang, J.; Gao, Q.; Li, J.; Yu, S.-H., An efficient molybdenum disulfide/cobalt diselenide hybrid catalyst for electrochemical hydrogen generation. *Nature communications* **2015**, *6*, 5982.
50. Egan, G. C. Understanding the reaction mechanism of aluminum nanocomposite thermites. University of Maryland, College Park, 2015.

51. Wang, H.; DeLisio, J. B.; Holdren, S.; Wu, T.; Yang, Y.; Hu, J.; Zachariah, M. R., Mesoporous Silica Spheres Incorporated Aluminum/Poly (Vinylidene Fluoride) for Enhanced Burning Propellants. *Advanced Engineering Materials* **2018**, *20* (2).
52. Wang, H.; Rehwoldt, M. C.; Wang, X.; Yang, Y.; Zachariah, M. R., On the promotion of high temperature AP decomposition with silica mesoparticles. *Combustion and Flame* **2019**, *200*, 296-302.
53. Wang, X.; Wu, T.; Wang, H.; DeLisio, J. B.; Yang, Y.; Zachariah, M. R., Boron ignition and combustion with doped δ -Bi₂O₃: Bond energy/oxygen vacancy relationships. *Combustion and Flame* **2018**, *197*, 127-133.
54. Rehwoldt, M. C.; Yang, Y.; Wang, H.; Holdren, S.; Zachariah, M. R., Ignition of Nanoscale Titanium/Potassium Perchlorate Pyrotechnic Powder: Reaction Mechanism Study. *The Journal of Physical Chemistry C* **2018**, *122* (20), 10792-10800.
55. Wang, H.; DeLisio, J. B.; Holdren, S.; Wu, T.; Yang, Y.; Hu, J.; Zachariah, M. R., Mesoporous Silica Spheres Incorporated Aluminum/Poly (Vinylidene Fluoride) for Enhanced Burning Propellants. *Advanced Engineering Materials* **2018**, *20* (2), 1700547.
56. Jacob, R. J.; Hill, K. J.; Yang, Y.; Pantoya, M. L.; Zachariah, M. R., Pre-stressing aluminum nanoparticles as a strategy to enhance reactivity of nanothermite composites. *Combustion and Flame* **2019**, *205*, 33-40.
57. Gao, L.; Yue, W.; Tao, S.; Fan, L., Novel Strategy for Preparation of Graphene-Pd, Pt Composite, and Its Enhanced Electrocatalytic Activity for Alcohol Oxidation. *Langmuir* **2013**, *29* (3), 957-964.
58. Guo, S.; Dong, S.; Wang, E., Three-Dimensional Pt-on-Pd Bimetallic Nanodendrites Supported on Graphene Nanosheet: Facile Synthesis and Used as an Advanced Nanoelectrocatalyst for Methanol Oxidation. *ACS Nano* **2010**, *4* (1), 547-555.
59. Wang, Y.; Zhen, S. J.; Zhang, Y.; Li, Y. F.; Huang, C. Z., Facile Fabrication of Metal Nanoparticle/Graphene Oxide Hybrids: A New Strategy To Directly Illuminate Graphene for Optical Imaging. *The Journal of Physical Chemistry C* **2011**, *115* (26), 12815-12821.
60. Liu, J.; Fu, S.; Yuan, B.; Li, Y.; Deng, Z., Toward a Universal "Adhesive Nanosheet" for the Assembly of Multiple Nanoparticles Based on a Protein-Induced Reduction/Decoration of Graphene Oxide. *Journal of the American Chemical Society* **2010**, *132* (21), 7279-7281.
61. Yao, Y.; Chen, F.; Nie, A.; Lacey, S. D.; Jacob, R. J.; Xu, S.; Huang, Z.; Fu, K.; Dai, J.; Salamanca-Riba, L.; Zachariah, M. R.; Shahbazian-Yassar, R.; Hu, L., In Situ High Temperature Synthesis of Single-Component Metallic Nanoparticles. *ACS Central Science* **2017**, *3* (4), 294-301.

62. Qin, J.; He, C.; Zhao, N.; Wang, Z.; Shi, C.; Liu, E.-Z.; Li, J., Graphene Networks Anchored with Sn@Graphene as Lithium Ion Battery Anode. *ACS Nano* **2014**, *8* (2), 1728-1738.
63. Wang, J.; Zhang, X.-B.; Wang, Z.-L.; Wang, L.-M.; Zhang, Y., Rhodium–nickel nanoparticles grown on graphene as highly efficient catalyst for complete decomposition of hydrous hydrazine at room temperature for chemical hydrogen storage. *Energy & Environmental Science* **2012**, *5* (5), 6885-6888.
64. Kundu, P.; Nethravathi, C.; Deshpande, P. A.; Rajamathi, M.; Madras, G.; Ravishankar, N., Ultrafast Microwave-Assisted Route to Surfactant-Free Ultrafine Pt Nanoparticles on Graphene: Synergistic Co-reduction Mechanism and High Catalytic Activity. *Chemistry of Materials* **2011**, *23* (11), 2772-2780.
65. Motl, N. E.; Mann, A. K.; Skrabalak, S. E., Aerosol-assisted synthesis and assembly of nanoscale building blocks. *Journal of Materials Chemistry A* **2013**, *1* (17), 5193-5202.
66. Chen, P.-C.; Liu, M.; Du, J. S.; Meckes, B.; Wang, S.; Lin, H.; Dravid, V. P.; Wolverton, C.; Mirkin, C. A., Interface and heterostructure design in polyelemental nanoparticles. *Science* **2019**, *363* (6430), 959-964.
67. Takahashi, M.; Koizumi, H.; Chun, W.-J.; Kori, M.; Imaoka, T.; Yamamoto, K., Finely controlled multimetallic nanocluster catalysts for solvent-free aerobic oxidation of hydrocarbons. *Science advances* **2017**, *3* (7), e1700101.
68. Yeh, J. W.; Chen, S. K.; Lin, S. J.; Gan, J. Y.; Chin, T. S.; Shun, T. T.; Tsau, C. H.; Chang, S. Y., Nanostructured high-entropy alloys with multiple principal elements: novel alloy design concepts and outcomes. *Advanced Engineering Materials* **2004**, *6* (5), 299-303.
69. Ye, Y.; Wang, Q.; Lu, J.; Liu, C.; Yang, Y., High-entropy alloy: challenges and prospects. *Materials Today* **2016**, *19* (6), 349-362.
70. Buck, M. R.; Bondi, J. F.; Schaak, R. E., A total-synthesis framework for the construction of high-order colloidal hybrid nanoparticles. *Nature chemistry* **2012**, *4* (1), 37.
71. Nie, Z.; Li, W.; Seo, M.; Xu, S.; Kumacheva, E., Janus and ternary particles generated by microfluidic synthesis: design, synthesis, and self-assembly. *Journal of the American Chemical Society* **2006**, *128* (29), 9408-9412.
72. Ganguli, A. K.; Ganguly, A.; Vaidya, S., Microemulsion-based synthesis of nanocrystalline materials. *Chemical Society Reviews* **2010**, *39* (2), 474-485.
73. Chen, P.-C.; Liu, X.; Hedrick, J. L.; Xie, Z.; Wang, S.; Lin, Q.-Y.; Hersam, M. C.; Dravid, V. P.; Mirkin, C. A., Polyelemental nanoparticle libraries. *Science* **2016**, *352* (6293), 1565-1569.

74. Li, Z.; Pradeep, K. G.; Deng, Y.; Raabe, D.; Tasan, C. C., Metastable high-entropy dual-phase alloys overcome the strength–ductility trade-off. *Nature* **2016**, *534* (7606), 227.
75. Santodonato, L. J.; Zhang, Y.; Feygenson, M.; Parish, C. M.; Gao, M. C.; Weber, R. J.; Neufeind, J. C.; Tang, Z.; Liaw, P. K., Deviation from high-entropy configurations in the atomic distributions of a multi-principal-element alloy. *Nature communications* **2015**, *6*, 5964.
76. Zhang, R.; Khalizov, A.; Wang, L.; Hu, M.; Xu, W., Nucleation and growth of nanoparticles in the atmosphere. *Chemical Reviews* **2011**, *112* (3), 1957-2011.
77. Davari, S. A.; Gottfried, J. L.; Liu, C.; Ribeiro, E. L.; Duscher, G.; Mukherjee, D., Graphitic coated Al nanoparticles manufactured as superior energetic materials via laser ablation synthesis in organic solvents. *Applied Surface Science* **2019**, *473*, 156-163.
78. Muñeton Arboleda, D.; Santillán, J. M.; Mendoza Herrera, L. J.; van Raap, M. B. F. n.; Mendoza Zelis, P.; Muraca, D.; Schinca, D. C.; Scaffardi, L. B., Synthesis of Ni nanoparticles by femtosecond laser ablation in liquids: Structure and sizing. *The Journal of Physical Chemistry C* **2015**, *119* (23), 13184-13193.
79. Feng, G.; Li, Z.; Jacob, R. J.; Yang, Y.; Wang, Y.; Zhou, Z.; Sekulic, D. P.; Zachariah, M. R., Laser-induced exothermic bonding of carbon fiber/Al composites and TiAl alloys. *Materials & Design* **2017**, *126*, 197-206.
80. Feng, G.; Li, Z.; Xu, X.; Shen, Z.; Yang, Y., Glass-Copper anodic bonding through activated Sn-0.6 Al solder. *Journal of Materials Processing Technology* **2018**, *254*, 108-113.
81. Feng, G.; Li, Z.; Zhou, Z.; Yang, Y.; Sekulic, D. P.; Zachariah, M. R., Microstructure and mechanical properties of Cf/Al-TiAl laser-assisted brazed joint. *Journal of Materials Processing Technology* **2018**, *255*, 195-203.
82. Ghildiyal, P.; Yang, Y.; Kline, D. J.; Holdren, S.; Zachariah, M., Ultrafast, Scalable Laser Photothermal Synthesis and Writing of Uniformly-Dispersed Metal Nanoclusters in Polymer Films. *Nanoscale* **2019**.
83. Kunwar, P.; Hassinen, J.; Bautista, G.; Ras, R. H.; Toivonen, J., Direct laser writing of photostable fluorescent silver nanoclusters in polymer films. *ACS nano* **2014**, *8* (11), 11165-11171.
84. Hummers Jr, W. S.; Offeman, R. E., Preparation of graphitic oxide. *Journal of the american chemical society* **1958**, *80* (6), 1339-1339.
85. Densmore, J. M.; Biss, M. M.; McNesby, K. L.; Homan, B. E., High-speed digital color imaging pyrometry. *Applied Optics* **2011**, *50* (17), 2659-2665.
86. Kalman, J.; Hedman, T., On the Origin and Use of the Emissivity Approximations for Alumina Particles. *Propellants, Explosives, Pyrotechnics* **2016**, *41* (5), 793-797.

87. Jacob, R. J.; Kline, D. J.; Zachariah, M. R., High speed 2-dimensional temperature measurements of nanothermite composites: Probing thermal vs. Gas generation effects. *Journal of Applied Physics* **2018**, *123* (11), 115902.
88. Cliff, G.; Lorimer, G. W., The quantitative analysis of thin specimens. *Journal of Microscopy* **1975**, *103* (2), 203-207.
89. Zhang, J.; Xu, S.; Kumacheva, E., Polymer microgels: reactors for semiconductor, metal, and magnetic nanoparticles. *Journal of the American Chemical Society* **2004**, *126* (25), 7908-7914.
90. Ramesh, G.; Porel, S.; Radhakrishnan, T., Polymer thin films embedded with in situ grown metal nanoparticles. *Chemical Society Reviews* **2009**, *38* (9), 2646-2656.
91. Firestone, M. A.; Hayden, S. C.; Huber, D. L., Greater than the sum: Synergy and emergent properties in nanoparticle–polymer composites. *MRS Bulletin* **2015**, *40* (09), 760-767.
92. Kutvonen, A.; Rossi, G.; Puisto, S. R.; Rostedt, N. K.; Ala-Nissila, T., Influence of nanoparticle size, loading, and shape on the mechanical properties of polymer nanocomposites. *The Journal of chemical physics* **2012**, *137* (21), 214901.
93. Zaragoza, J.; Babhadiashar, N.; O'Brien, V.; Chang, A.; Blanco, M.; Zabalegui, A.; Lee, H.; Asuri, P., Experimental investigation of mechanical and thermal properties of silica nanoparticle-reinforced poly (acrylamide) nanocomposite hydrogels. *PLoS one* **2015**, *10* (8), e0136293.
94. Sygletou, M.; Tzourmpakis, P.; Petridis, C.; Konios, D.; Fotakis, C.; Kymakis, E.; Stratakis, E., Laser induced nucleation of plasmonic nanoparticles on two-dimensional nanosheets for organic photovoltaics. *Journal of Materials Chemistry A* **2016**, *4* (3), 1020-1027.
95. Wu, H.; Yu, G.; Pan, L.; Liu, N.; McDowell, M. T.; Bao, Z.; Cui, Y., Stable Li-ion battery anodes by in-situ polymerization of conducting hydrogel to conformally coat silicon nanoparticles. *Nature communications* **2013**, *4*.
96. Porta, M.; Nguyen, M. T.; Ishida, Y.; Yonezawa, T., Highly stable and blue-emitting copper nanocluster dispersion prepared by magnetron sputtering over liquid polymer matrix. *RSC advances* **2016**, *6* (107), 105030-105034.
97. Slistan-Grijalva, A.; Herrera-Urbina, R.; Rivas-Silva, J.; Avalos-Borja, M.; Castellón-Barraza, F.; Posada-Amarillas, A., Synthesis of silver nanoparticles in a polyvinylpyrrolidone (PVP) paste, and their optical properties in a film and in ethylene glycol. *Materials Research Bulletin* **2008**, *43* (1), 90-96.
98. Porel, S.; Singh, S.; Harsha, S. S.; Rao, D. N.; Radhakrishnan, T., Nanoparticle-embedded polymer: in situ synthesis, free-standing films with highly monodisperse silver nanoparticles and optical limiting. *Chemistry of Materials* **2005**, *17* (1), 9-12.

99. Jin, W. J.; Lee, H. K.; Jeong, E. H.; Park, W. H.; Youk, J. H., Preparation of Polymer Nanofibers Containing Silver Nanoparticles by Using Poly (N-vinylpyrrolidone). *Macromolecular rapid communications* **2005**, *26* (24), 1903-1907.
100. Zhang, J.; Xu, S.; Kumacheva, E., Photogeneration of fluorescent silver nanoclusters in polymer microgels. *Advanced Materials* **2005**, *17* (19), 2336-2340.
101. Ramesh, G.; Sreedhar, B.; Radhakrishnan, T., Real time monitoring of the in situ growth of silver nanoparticles in a polymer film under ambient conditions. *Physical Chemistry Chemical Physics* **2009**, *11* (43), 10059-10063.
102. Hariprasad, E.; Radhakrishnan, T., In situ fabricated polymer–silver nanocomposite thin film as an inexpensive and efficient substrate for surface-enhanced Raman scattering. *Langmuir* **2013**, *29* (42), 13050-13057.
103. Athanassiou, E. K.; Grass, R. N.; Stark, W. J., Chemical aerosol engineering as a novel tool for material science: from oxides to salt and metal nanoparticles. *Aerosol Science and Technology* **2010**, *44* (2), 161-172.
104. Bang, J. H.; Suslick, K. S., Applications of ultrasound to the synthesis of nanostructured materials. *Advanced materials* **2010**, *22* (10), 1039-1059.
105. Yang, Y.; Romano, M.; Zachariah, M. In *Synthesis and stabilization of ultrasmall-metal nanoparticles (Ni, Co, Cu) within a polymer matrix via a one-step aerosol spray pyrolysis*, 256th ACS National Meeting, Washington, DC, American Chemical Society: Washington, DC, 2017.
106. Lee, K. H.; Rah, S. C.; Kim, S.-G., Formation of monodisperse silver nanoparticles in poly (vinylpyrrolidone) matrix using spray pyrolysis. *Journal of Sol-Gel Science and Technology* **2008**, *45* (2), 187-193.
107. Wang, X.; Zhou, W.; DeLisio, J. B.; Egan, G. C.; Zachariah, M. R., Doped δ -bismuth oxides to investigate oxygen ion transport as a metric for condensed phase thermite ignition. *Physical Chemistry Chemical Physics* **2017**, *19* (20), 12749-12758.
108. Seo, J. Y.; Kang, H. W.; Jung, D. S.; Lee, H. M.; Park, S. B., One-step synthesis of copper nanoparticles embedded in carbon composites. *Materials Research Bulletin* **2013**, *48* (4), 1484-1489.
109. Gürmen, S.; Stopić, S.; Friedrich, B., Synthesis of nanosized spherical cobalt powder by ultrasonic spray pyrolysis. *Materials Research Bulletin* **2006**, *41* (10), 1882-1890.
110. Jung, K. Y.; Lee, J. H.; Koo, H. Y.; Kang, Y. C.; Park, S. B., Preparation of solid nickel nanoparticles by large-scale spray pyrolysis of Ni (NO₃)₂ · 6H₂O precursor: Effect of temperature and nickel acetate on the particle morphology. *Materials Science and Engineering: B* **2007**, *137* (1), 10-19.

111. Majumdar, D.; Shefelbine, T.; Kodas, T.; Glicksman, H., Copper (I) oxide powder generation by spray pyrolysis. *Journal of materials research* **1996**, *11* (11), 2861-2868.
112. Tannenbaum, R.; Zubris, M.; Goldberg, E. P.; Reich, S.; Dan, N., Polymer-directed nanocluster synthesis: control of particle size and morphology. *Macromolecules* **2005**, *38* (10), 4254-4259.
113. Faupel, F.; Willecke, R.; Thran, A., Diffusion of metals in polymers. *Materials Science and Engineering: R: Reports* **1998**, *22* (1), 1-55.
114. Brockner, W.; Ehrhardt, C.; Gjikaj, M., Thermal decomposition of nickel nitrate hexahydrate, $\text{Ni}(\text{NO}_3)_2 \cdot 6\text{H}_2\text{O}$, in comparison to $\text{Co}(\text{NO}_3)_2 \cdot 6\text{H}_2\text{O}$ and $\text{Ca}(\text{NO}_3)_2 \cdot 4\text{H}_2\text{O}$. *Thermochimica Acta* **2007**, *456* (1), 64-68.
115. Kane, R.; Cohen, R.; Silbey, R., Semiconductor nanocluster growth within polymer films. *Langmuir* **1999**, *15* (1), 39-43.
116. Dan, N.; Zubris, M.; Tannenbaum, R., Effect of polymeric media on the kinetics of nanocluster nucleation and growth. *Macromolecules* **2005**, *38* (22), 9243-9250.
117. Einstein, A., Über die von der molekularkinetischen Theorie der Wärme geforderte Bewegung von in ruhenden Flüssigkeiten suspendierten Teilchen. *Annalen der physik* **1905**, *322* (8), 549-560.
118. Rubinstein, M.; Colby, R. H., Polymer physics 2003. *NEW YORK: Oxford University*.
119. Gupta, S. S.; Meena, A.; Parikh, T.; Serajuddin, A., Investigation of thermal and viscoelastic properties of polymers relevant to hot melt extrusion-I: Polyvinylpyrrolidone and related polymers. *Journal of Excipients & Food Chemicals* **2014**, *5* (1).
120. Masuko, T.; MAGILL, J. H., A Comprehensive Expression for Temperature Dependence of Liquid Viscosity. *Nihon Reoroji Gakkaishi (Journal of the Society of Rheology, Japan)* **1988**, *16* (1), 22-26.
121. Griffin, P. J.; Bocharova, V.; Middleton, L. R.; Composto, R. J.; Clarke, N.; Schweizer, K. S.; Winey, K. I., Influence of the bound polymer layer on nanoparticle diffusion in polymer melts. *ACS Macro Letters* **2016**, *5* (10), 1141-1145.
122. Woehl, T. J.; Park, C.; Evans, J. E.; Arslan, I.; Ristenpart, W. D.; Browning, N. D., Direct observation of aggregative nanoparticle growth: Kinetic modeling of the size distribution and growth rate. *Nano Lett* **2014**, *14* (1), 373-378.
123. Sholl, D. S.; Skodje, R. T., Late-stage coarsening of adlayers by dynamic cluster coalescence. *Physica A: Statistical Mechanics and its Applications* **1996**, *231* (4), 631-647.

124. Simonsen, S. B.; Chorkendorff, I.; Dahl, S.; Skoglundh, M.; Sehested, J.; Helveg, S., Direct observations of oxygen-induced platinum nanoparticle ripening studied by in situ TEM. *Journal of the American Chemical Society* **2010**, *132* (23), 7968-7975.
125. Friedlander, S.; Wang, C., The self-preserving particle size distribution for coagulation by Brownian motion. *Journal of Colloid and interface Science* **1966**, *22* (2), 126-132.
126. Lee, K.; Chen, J.; Gieseke, J., Log-normally preserving size distribution for Brownian coagulation in the free-molecule regime. *Aerosol Science and Technology* **1984**, *3* (1), 53-62.
127. Lee, K., Change of particle size distribution during Brownian coagulation. *Journal of Colloid and Interface Science* **1983**, *92* (2), 315-325.
128. Lifshitz, I. M.; Slyozov, V. V., The kinetics of precipitation from supersaturated solid solutions. *Journal of physics and chemistry of solids* **1961**, *19* (1-2), 35-50.
129. Wong, E. M.; Bonevich, J. E.; Searson, P. C., Growth kinetics of nanocrystalline ZnO particles from colloidal suspensions. *The Journal of Physical Chemistry B* **1998**, *102* (40), 7770-7775.
130. Richardson, J. T.; Scates, R.; Twigg, M. V., X-ray diffraction study of nickel oxide reduction by hydrogen. *Applied Catalysis A: General* **2003**, *246* (1), 137-150.
131. Buffat, P.; Borel, J. P., Size effect on the melting temperature of gold particles. *Physical review A* **1976**, *13* (6), 2287.
132. Keene, B., Review of data for the surface tension of pure metals. *International Materials Reviews* **1993**, *38* (4), 157-192.
133. Schmon, A.; Aziz, K.; Pottlacher, G., Density Determination of Liquid Copper and Liquid Nickel by Means of Fast Resistive Pulse Heating and Electromagnetic Levitation. *Metallurgical and Materials Transactions A* **2015**, *46* (6), 2674-2679.
134. Prokoshkina, D.; Esin, V.; Wilde, G.; Divinski, S., Grain boundary width, energy and self-diffusion in nickel: effect of material purity. *Acta Materialia* **2013**, *61* (14), 5188-5197.
135. Lu, Y.; Chen, W., Sub-nanometre sized metal clusters: from synthetic challenges to the unique property discoveries. *Chemical Society Reviews* **2012**, *41* (9), 3594-3623.
136. Jin, R.; Zeng, C.; Zhou, M.; Chen, Y., Atomically precise colloidal metal nanoclusters and nanoparticles: Fundamentals and opportunities. *Chemical reviews* **2016**, *116* (18), 10346-10413.

137. Yang, Y.; Ghildiyal, P.; Zachariah, M. In *Rapid and scalable synthesis of sub-10 nm metal nanoparticles in on-the-fly aerosols*, 256th ACS National Meeting, Boston, MA, American Chemical Society: Boston, MA, 2018.
138. Anumol, E. A.; Kundu, P.; Deshpande, P. A.; Madras, G.; Ravishankar, N., New insights into selective heterogeneous nucleation of metal nanoparticles on oxides by microwave-assisted reduction: rapid synthesis of high-activity supported catalysts. *ACS nano* **2011**, 5 (10), 8049-8061.
139. Wang, X.; Zhuang, J.; Peng, Q.; Li, Y., A general strategy for nanocrystal synthesis. *Nature* **2005**, 437 (7055), 121.
140. Chen, S.; Duan, J.; Ran, J.; Jaroniec, M.; Qiao, S. Z., N-doped graphene film-confined nickel nanoparticles as a highly efficient three-dimensional oxygen evolution electrocatalyst. *Energy & Environmental Science* **2013**, 6 (12), 3693-3699.
141. Luo, J.; Jang, H. D.; Sun, T.; Xiao, L.; He, Z.; Katsoulidis, A. P.; Kanatzidis, M. G.; Gibson, J. M.; Huang, J., Compression and aggregation-resistant particles of crumpled soft sheets. *ACS nano* **2011**, 5 (11), 8943-8949.
142. Ma, X.; Zachariah, M. R.; Zangmeister, C. D., Crumpled nanopaper from graphene oxide. *Nano letters* **2011**, 12 (1), 486-489.
143. Brockner, W.; Ehrhardt, C.; Gjikaj, M., Thermal decomposition of nickel nitrate hexahydrate, Ni (NO₃)₂ · 6H₂O, in comparison to Co (NO₃)₂ · 6H₂O and Ca (NO₃)₂ · 4H₂O. *Thermochimica Acta* **2007**, 456 (1), 64-68.
144. Subrahmanyam, K.; Manna, A. K.; Pati, S. K.; Rao, C., A study of graphene decorated with metal nanoparticles. *Chemical Physics Letters* **2010**, 497 (1-3), 70-75.
145. Chen, Y.; Egan, G. C.; Wan, J.; Zhu, S.; Jacob, R. J.; Zhou, W.; Dai, J.; Wang, Y.; Danner, V. A.; Yao, Y.; Fu, K.; Wang, Y.; Bao, W.; Li, T.; Zachariah, M. R.; Hu, L., Ultra-fast self-assembly and stabilization of reactive nanoparticles in reduced graphene oxide films. *Nature communications* **2016**, 7, 12332.
146. Ghosh, T.; Biswas, C.; Oh, J.; Arabale, G.; Hwang, T.; Luong, N. D.; Jin, M.; Lee, Y. H.; Nam, J.-D., Solution-processed graphite membrane from reassembled graphene oxide. *Chemistry of Materials* **2012**, 24 (3), 594-599.
147. Ferrari, A. C.; Basko, D. M., Raman spectroscopy as a versatile tool for studying the properties of graphene. *Nature nanotechnology* **2013**, 8 (4), 235.
148. Jang, H. D.; Kim, S. K.; Chang, H.; Choi, J.-W.; Luo, J.; Huang, J., One-step synthesis of Pt-nanoparticles-laden graphene crumples by aerosol spray pyrolysis and evaluation of their electrocatalytic activity. *Aerosol Science and Technology* **2013**, 47 (1), 93-98.

149. Li, Y.; Cao, Y.; Jia, D., Enhanced catalytic hydrogenation activity of Ni/reduced graphene oxide nanocomposite prepared by a solid-state method. *Journal of Nanoparticle Research* **2018**, *20* (1), 8.
150. Bai, S.; Shen, X.; Zhu, G.; Li, M.; Xi, H.; Chen, K., In situ Growth of Ni_xCo_{100-x} Nanoparticles on Reduced Graphene Oxide Nanosheets and Their Magnetic and Catalytic Properties. *ACS applied materials & interfaces* **2012**, *4* (5), 2378-2386.
151. Ji, Z.; Wang, Y.; Yang, J.; Shen, X.; Yu, Q.; Kong, L.; Zhou, H., Reduced graphene oxide uniformly decorated with Co nanoparticles: facile synthesis, magnetic and catalytic properties. *RSC Advances* **2016**, *6* (109), 107709-107716.
152. Smits, A. J.; Dussauge, J.-P., *Turbulent shear layers in supersonic flow*. Springer Science & Business Media: 2006.
153. Kästner, C.; Thünemann, A. F., Catalytic reduction of 4-nitrophenol using silver nanoparticles with adjustable activity. *Langmuir* **2016**, *32* (29), 7383-7391.
154. Lara, L. R.; Zottis, A. D.; Elias, W. C.; Faggion, D.; de Campos, C. E. M.; Acuña, J. J. S.; Domingos, J. B., The catalytic evaluation of in situ grown Pd nanoparticles on the surface of Fe₃O₄@ dextran particles in the p-nitrophenol reduction reaction. *RSC Advances* **2015**, *5* (11), 8289-8296.
155. Dunn, B.; Kamath, H.; Tarascon, J.-M., Electrical energy storage for the grid: a battery of choices. *Science* **2011**, *334* (6058), 928-935.
156. Larcher, D.; Tarascon, J.-M., Towards greener and more sustainable batteries for electrical energy storage. *Nature chemistry* **2015**, *7* (1), 19.
157. Haxel, G. B.; Hedrick, J. B.; Orris, G. J.; Stauffer, P. H.; Hendley II, J. W. *Rare earth elements: critical resources for high technology*; 2327-6932; 2002.
158. Liang, Y.; Chen, Z.; Jing, Y.; Rong, Y.; Facchetti, A.; Yao, Y., Heavily n-dopable π -conjugated redox polymers with ultrafast energy storage capability. *Journal of the American Chemical Society* **2015**, *137* (15), 4956-4959.
159. Yabuuchi, N.; Kubota, K.; Dahbi, M.; Komaba, S., Research development on sodium-ion batteries. *Chemical reviews* **2014**, *114* (23), 11636-11682.
160. Mathew, V.; Kim, S.; Kang, J.; Gim, J.; Song, J.; Baboo, J. P.; Park, W.; Ahn, D.; Han, J.; Gu, L., Amorphous iron phosphate: potential host for various charge carrier ions. *NPG Asia Materials* **2014**, *6* (10), e138.
161. Recham, N.; Rouse, G. I.; Sougrati, M. T.; Chotard, J.-N. I.; Frayret, C.; Mariyappan, S.; Melot, B. C.; Jumas, J.-C.; Tarascon, J.-M., Preparation and characterization of a stable FeSO₄F-based framework for alkali ion insertion electrodes. *Chemistry of Materials* **2012**, *24* (22), 4363-4370.

162. Zhang, C.; Xu, Y.; Zhou, M.; Liang, L.; Dong, H.; Wu, M.; Yang, Y.; Lei, Y., Potassium Prussian Blue Nanoparticles: A Low-Cost Cathode Material for Potassium-Ion Batteries. *Advanced Functional Materials* **2017**, *27* (4).
163. Padigi, P.; Thiebes, J.; Swan, M.; Goncher, G.; Evans, D.; Solanki, R., Prussian green: a high rate capacity cathode for potassium ion batteries. *Electrochimica Acta* **2015**, *166*, 32-39.
164. Chen, Y.; Luo, W.; Carter, M.; Zhou, L.; Dai, J.; Fu, K.; Lacey, S.; Li, T.; Wan, J.; Han, X., Organic electrode for non-aqueous potassium-ion batteries. *Nano Energy* **2015**, *18*, 205-211.
165. Zelang, J.; Zhenyu, X.; Clement, B.; Zhifei, L.; Xiulei, J., Hard Carbon Microspheres: Potassium - Ion Anode Versus Sodium - Ion Anode. *Advanced Energy Materials* **2016**, *6* (3), 1501874.
166. Tai, Z.; Zhang, Q.; Liu, Y.; Liu, H.; Dou, S., Activated carbon from the graphite with increased rate capability for the potassium ion battery. *Carbon* **2017**, *123*, 54-61.
167. Jian, Z.; Luo, W.; Ji, X., Carbon electrodes for K-ion batteries. *Journal of the American Chemical Society* **2015**, *137* (36), 11566-11569.
168. Komaba, S.; Hasegawa, T.; Dahbi, M.; Kubota, K., Potassium intercalation into graphite to realize high-voltage/high-power potassium-ion batteries and potassium-ion capacitors. *Electrochemistry Communications* **2015**, *60*, 172-175.
169. Luo, W.; Wan, J.; Ozdemir, B.; Bao, W.; Chen, Y.; Dai, J.; Lin, H.; Xu, Y.; Gu, F.; Barone, V., Potassium ion batteries with graphitic materials. *Nano letters* **2015**, *15* (11), 7671-7677.
170. Liang, Y.; Tian, H.; Repac, J.; Liou, S.-C.; Chen, J.; Han, W.; Wang, C.; Ehrman, S., Colloidal spray pyrolysis: A new fabrication technology for nanostructured energy storage materials. *Energy Storage Materials* **2018**, *13*, 8-18.
171. Sultana, I.; Ramireddy, T.; Rahman, M. M.; Chen, Y.; Glushenkov, A. M., Tin-based composite anodes for potassium-ion batteries. *Chemical Communications* **2016**, *52* (59), 9279-9282.
172. Li, Z.; Ding, J.; Mitlin, D., Tin and tin compounds for sodium ion battery anodes: phase transformations and performance. *Accounts of chemical research* **2015**, *48* (6), 1657-1665.
173. Lee, K. T.; Jung, Y. S.; Oh, S. M., Synthesis of tin-encapsulated spherical hollow carbon for anode material in lithium secondary batteries. *Journal of the American Chemical Society* **2003**, *125* (19), 5652-5653.

174. Kim, H.; Park, G.-S.; Kim, E.; Kim, J.; Doo, S.-G.; Cho, J., Observation of reversible pore change in mesoporous tin phosphate anode material during Li alloying/dealloying. *Journal of The Electrochemical Society* **2006**, *153* (9), A1633-A1636.
175. Yin, J.; Wada, M.; Tanase, S.; Sakai, T., Nanocrystalline Ag-Fe-Sn anode materials for Li-ion batteries. *Journal of The Electrochemical Society* **2004**, *151* (4), A583-A589.
176. Zhang, W.-J., A review of the electrochemical performance of alloy anodes for lithium-ion batteries. *Journal of Power Sources* **2011**, *196* (1), 13-24.
177. Qian, J.; Chen, Y.; Wu, L.; Cao, Y.; Ai, X.; Yang, H., High capacity Na-storage and superior cyclability of nanocomposite Sb/C anode for Na-ion batteries. *Chemical Communications* **2012**, *48* (56), 7070-7072.
178. Sangster, J.; Pelton, A., The Li-Sb (lithium-antimony) system. *Journal of phase equilibria* **1993**, *14* (4), 514-517.
179. McCulloch, W. D.; Ren, X.; Yu, M.; Huang, Z.; Wu, Y., Potassium-ion oxygen battery based on a high capacity antimony anode. *ACS applied materials & interfaces* **2015**, *7* (47), 26158-26166.
180. Aurbach, D., Review of selected electrode–solution interactions which determine the performance of Li and Li ion batteries. *Journal of Power Sources* **2000**, *89* (2), 206-218.
181. Lei, Y.; Qin, L.; Liu, R.; Lau, K. C.; Wu, Y.; Zhai, D.; Li, B.; Kang, F., Exploring stability of nonaqueous electrolytes for potassium-ion batteries. *ACS Applied Energy Materials* **2018**.
182. Wu, X.; Leonard, D. P.; Ji, X., Emerging non-aqueous potassium-ion batteries: challenges and opportunities. *Chemistry of Materials* **2017**, *29* (12), 5031-5042.
183. Hohenberg, P.; Kohn, W., Inhomogeneous electron gas. *Physical review* **1964**, *136* (3B), B864.
184. Kohn, W.; Sham, L. J., Self-consistent equations including exchange and correlation effects. *Physical review* **1965**, *140* (4A), A1133.
185. Kresse, G.; Hafner, J., Ab initio molecular-dynamics simulation of the liquid-metal–amorphous-semiconductor transition in germanium. *Physical Review B* **1994**, *49* (20), 14251.
186. Blöchl, P. E., Projector augmented-wave method. *Physical review B* **1994**, *50* (24), 17953.
187. Perdew, J. P.; Burke, K.; Ernzerhof, M., Generalized gradient approximation made simple. *Physical review letters* **1996**, *77* (18), 3865.

188. Ping Ong, S.; Wang, L.; Kang, B.; Ceder, G., Li-Fe-P-O₂ phase diagram from first principles calculations. *Chemistry of Materials* **2008**, *20* (5), 1798-1807.
189. Momma, K.; Izumi, F., VESTA 3 for three-dimensional visualization of crystal, volumetric and morphology data. *Journal of applied crystallography* **2011**, *44* (6), 1272-1276.
190. Su, F.; Zhao, X.; Wang, Y.; Zeng, J.; Zhou, Z.; Lee, J. Y., Synthesis of graphitic ordered macroporous carbon with a three-dimensional interconnected pore structure for electrochemical applications. *The Journal of Physical Chemistry B* **2005**, *109* (43), 20200-20206.
191. Hou, H.; Jing, M.; Yang, Y.; Zhang, Y.; Song, W.; Yang, X.; Chen, J.; Chen, Q.; Ji, X., Antimony nanoparticles anchored on interconnected carbon nanofibers networks as advanced anode material for sodium-ion batteries. *Journal of Power Sources* **2015**, *284*, 227-235.
192. Jian, Z.; Xing, Z.; Bommier, C.; Li, Z.; Ji, X., Hard carbon microspheres: potassium-ion anode versus sodium-ion anode. *Advanced Energy Materials* **2016**, *6* (3).
193. Darwiche, A.; Marino, C.; Sougrati, M. T.; Fraisse, B.; Stievano, L.; Monconduit, L., Better cycling performances of bulk Sb in Na-ion batteries compared to Li-ion systems: an unexpected electrochemical mechanism. *Journal of the American Chemical Society* **2012**, *134* (51), 20805-20811.
194. Hou, H.; Zou, G.; Ge, P.; Zhao, G.; Wei, W.; Ji, X.; Huang, L., Synergistic effect of cross-linked carbon nanosheet frameworks and Sb on the enhancement of sodium storage performances. *New Journal of Chemistry* **2017**, *41* (22), 13724-13731.
195. Weppner, W.; Huggins, R. A., Determination of the kinetic parameters of mixed-conducting electrodes and application to the system Li₃Sb. *Journal of The Electrochemical Society* **1977**, *124* (10), 1569-1578.
196. Xu, Y.; Zhang, C.; Zhou, M.; Fu, Q.; Zhao, C.; Wu, M.; Lei, Y., Highly nitrogen doped carbon nanofibers with superior rate capability and cyclability for potassium ion batteries. *Nature communications* **2018**, *9*.
197. Ra, E.; Raymundo-Piñero, E.; Lee, Y.; Béguin, F., High power supercapacitors using polyacrylonitrile-based carbon nanofiber paper. *Carbon* **2009**, *47* (13), 2984-2992.
198. Chiu, K.-F.; Lai, P., Recycled crystalline micro-sized silicon particles modified by pyrolytic coatings using poly (ether ether ketone) precursor for stable lithium ion battery anodes. *Materials Science and Engineering: B* **2018**, *228*, 52-59.
199. Cheng, X. B.; Zhang, R.; Zhao, C. Z.; Wei, F.; Zhang, J. G.; Zhang, Q., A review of solid electrolyte interphases on lithium metal anode. *Advanced Science* **2016**, *3* (3).

200. Xu, C.; Sun, B.; Gustafsson, T.; Edström, K.; Brandell, D.; Hahlin, M., Interface layer formation in solid polymer electrolyte lithium batteries: an XPS study. *Journal of Materials Chemistry A* **2014**, *2* (20), 7256-7264.
201. Phase Diagram App, Materials Projects, (<http://www.materialsproject.org>).
202. Share, K.; Cohn, A. P.; Carter, R.; Rogers, B.; Pint, C. L., Role of nitrogen-doped graphene for improved high-capacity potassium ion battery anodes. *ACS nano* **2016**, *10* (10), 9738-9744.
203. Han, C.; Han, K.; Wang, X.; Wang, C.; Li, Q.; Meng, J.; Xu, X.; He, Q.; Luo, W.; Wu, L., Three-dimensional carbon network confined antimony nanoparticle anodes for high-capacity K-ion batteries. *Nanoscale* **2018**, *10* (15), 6820-6826.
204. Zhang, Q.; Mao, J.; Pang, W. K.; Zheng, T.; Sencadas, V.; Chen, Y.; Liu, Y.; Guo, Z., Boosting the Potassium Storage Performance of Alloy-Based Anode Materials via Electrolyte Salt Chemistry. *Advanced Energy Materials* **2018**, 1703288.
205. Ma, G.; Huang, K.; Ma, J.-S.; Ju, Z.; Xing, Z.; Zhuang, Q.-c., Phosphorus and oxygen dual-doped graphene as superior anode material for room-temperature potassium-ion batteries. *Journal of Materials Chemistry A* **2017**, *5* (17), 7854-7861.
206. Zhang, W.; Mao, J.; Li, S.; Chen, Z.; Guo, Z., Phosphorus-based alloy materials for advanced potassium-ion battery anode. *Journal of the American Chemical Society* **2017**, *139* (9), 3316-3319.
207. Sultana, I.; Rahman, M. M.; Mateti, S.; Ahmadabadi, V. G.; Glushenkov, A. M.; Chen, Y., K-ion and Na-ion storage performances of $\text{Co}_3\text{O}_4\text{-Fe}_2\text{O}_3$ nanoparticle-decorated super P carbon black prepared by a ball milling process. *Nanoscale* **2017**, *9* (10), 3646-3654.
208. Han, J.; Xu, M.; Niu, Y.; Li, G.-N.; Wang, M.; Zhang, Y.; Jia, M.; ming Li, C., Exploration of $\text{K}_2\text{Ti}_8\text{O}_{17}$ as an anode material for potassium-ion batteries. *Chemical Communications* **2016**, *52* (75), 11274-11276.
209. Yi, Z.; Lin, N.; Zhang, W.; Wang, W.; Zhu, Y.; Qian, Y., Preparation of Sb nanoparticles in molten salt and their potassium storage performance and mechanism. *Nanoscale* **2018**, *10* (27), 13236-13241.
210. Jian, Z.; Xing, Z.; Bommier, C.; Li, Z.; Ji, X., Hard carbon microspheres: potassium-ion anode versus sodium-ion anode. *Advanced Energy Materials* **2016**, *6* (3), 1501874.
211. Huang, J.; Lin, X.; Tan, H.; Zhang, B., Bismuth Microparticles as Advanced Anodes for Potassium-Ion Battery. *Advanced Energy Materials* **2018**, 1703496.

212. Jian, Z.; Hwang, S.; Li, Z.; Hernandez, A. S.; Wang, X.; Xing, Z.; Su, D.; Ji, X., Hard-Soft Composite Carbon as a Long-Cycling and High-Rate Anode for Potassium-Ion Batteries. *Advanced Functional Materials* **2017**, *27* (26), 1700324.
213. Ren, X.; Zhao, Q.; McCulloch, W. D.; Wu, Y., MoS₂ as a long-life host material for potassium ion intercalation. *Nano Research* **2017**, *10* (4), 1313-1321.
214. Ge, J.; Fan, L.; Wang, J.; Zhang, Q.; Liu, Z.; Zhang, E.; Liu, Q.; Yu, X.; Lu, B., MoSe₂/N-Doped Carbon as Anodes for Potassium-Ion Batteries. *Advanced Energy Materials* **2018**, 1801477.
215. Adams, R. A.; Syu, J.-M.; Zhao, Y.; Lo, C.-T.; Varma, A.; Pol, V. G., Binder-Free N-and O-Rich Carbon Nanofiber Anodes for Long Cycle Life K-Ion Batteries. *ACS applied materials & interfaces* **2017**, *9* (21), 17872-17881.
216. Zhao, J.; Baibuz, E.; Vernieres, J.; Grammatikopoulos, P.; Jansson, V.; Nagel, M.; Steinhauer, S.; Sowwan, M.; Kuronen, A.; Nordlund, K., Formation mechanism of Fe nanocubes by magnetron sputtering inert gas condensation. *ACS nano* **2016**, *10* (4), 4684-4694.
217. Wipf, H., Solubility and diffusion of hydrogen in pure metals and alloys. *Physica Scripta* **2001**, *2001* (T94), 43.
218. Luidold, S.; Antrekowitsch, H., Hydrogen as a reducing agent: State-of-the-art science and technology. *Jom* **2007**, *59* (6), 20-26.
219. Lin, H.-Y.; Chen, Y.-W.; Li, C., The mechanism of reduction of iron oxide by hydrogen. *Thermochimica Acta* **2003**, *400* (1-2), 61-67.
220. Alcock, C.; Itkin, V.; Horrigan, M., Vapour pressure equations for the metallic elements: 298–2500K. *Canadian Metallurgical Quarterly* **1984**, *23* (3), 309-313.
221. Cho, K.; Biswas, P., Sintering rates for pristine and doped titanium dioxide determined using a tandem differential mobility analyzer system. *Aerosol science and technology* **2006**, *40* (5), 309-319.
222. Yang, Y.; Kline, D.; Ghildiyal, P.; Zachariah, M. In *Laser pulse induced growth of unaggregated Sub-5 nm metal nanoparticles in free-standing graphene films*, 256th ACS National Meeting, Boston, MA, American Chemical Society: Boston, MA, 2018.
223. Schweizer, A.; Kerr, G., Thermal decomposition of hexachloroplatinic acid. *Inorganic Chemistry* **1978**, *17* (8), 2326-2327.
224. Peng, Z.; Yang, H., Designer platinum nanoparticles: Control of shape, composition in alloy, nanostructure and electrocatalytic property. *Nano Today* **2009**, *4* (2), 143-164.

225. Tao, A. R.; Habas, S.; Yang, P., Shape control of colloidal metal nanocrystals. *small* **2008**, *4* (3), 310-325.
226. Wei, H.; Huang, K.; Wang, D.; Zhang, R.; Ge, B.; Ma, J.; Wen, B.; Zhang, S.; Li, Q.; Lei, M., Iced photochemical reduction to synthesize atomically dispersed metals by suppressing nanocrystal growth. *Nature communications* **2017**, *8* (1), 1490.
227. Li, Y.; Gao, T.; Yao, Y.; Liu, Z.; Kuang, Y.; Chen, C.; Song, J.; Xu, S.; Hitz, E. M.; Liu, B., In Situ “Chainmail Catalyst” Assembly in Low-Tortuosity, Hierarchical Carbon Frameworks for Efficient and Stable Hydrogen Generation. *Advanced Energy Materials* **2018**, *8* (25), 1801289.
228. Feitosa, M.; Mesquita, O., Wall-drag effect on diffusion of colloidal particles near surfaces: a photon correlation study. *Physical Review A* **1991**, *44* (10), 6677.
229. Davis, A. M.; Kezirian, M. T.; Brenner, H., On the Stokes-Einstein model of surface diffusion along solid surfaces: Slip boundary conditions. *Journal of colloid and interface science* **1994**, *165* (1), 129-140.
230. Munson, R., Surface energies of liquid metal interfaces with carbon. *Carbon* **1967**, *5* (5), 471-474.
231. Eustathopoulos, N., Wetting by liquid metals—application in materials processing: the contribution of the Grenoble group. *Metals* **2015**, *5* (1), 350-370.
232. Shi, Y.; Yang, B.; Xie, X.; Brechtel, J.; Dahmen, K. A.; Liaw, P. K., Corrosion of Al_xCoCrFeNi high-entropy alloys: Al-content and potential scan-rate dependent pitting behavior. *Corrosion Science* **2017**, *119*, 33-45.

Publications and Presentations

Publications:

a. Publications that have appeared in print:

1. **Yong Yang**, Pankaj Ghilgiyal, and Michael R. Zachariah; Thermal Shock Synthesis of Metal Nanoclusters in On-the-fly Graphene Particles. *Langmuir*, **2019**, 35 (9), 3413-3420

DOI: 10.1021/acs.langmuir.8b03532

Highlighted by Nanowerk:

<https://www.nanowerk.com/spotlight/spotid=52053.php>

2. **Yong Yang**, Michelangelo Romano, Guangjie Feng, Xizheng Wang, Tao Wu, Scott Holdren, Michael R Zachariah, *Growth of sub-5 nm Metal Nanoclusters in Polymer Melt Aerosol Droplets*, *Langmuir*, **2018**, 34 (2), pp 585–594

DOI: 10.1021/acs.langmuir.7b02900

3. Jing Zheng‡, **Yong Yang‡** (‡ **co-first authors**), Xiulin Fan, Guangbin Ji, Xiao Ji, Haiyang Wang, Singyuk Hou, Michael Zachariah, and Chunsheng Wang. Extremely Stable Antimony-carbon Composite Anodes for Potassium-ion Batteries, *Energy & Environmental Science*, **2019**, 12, 615-623 (Journal impact factor of the year 2018: 30.067)

DOI: 10.1039/C8EE02836B

Highlighted by National Science Foundation, University of Maryland, ChemistryViews, Nanowerk, et al.:

<https://chbe.umd.edu/news/story/nanostructure-of-carbon-and-metal-could-solve-potassiumbattery-puzzle>

https://nanocenter.umd.edu/news/news_story.php?id=11931

<https://isr.umd.edu/news/story/nanostructure-of-carbon-and-metal-could-solve-potassiumbattery-puzzle>

https://twitter.com/NSF_MPS/status/1106205202129084417

<https://www.chemistryviews.org/details/news/11125012/High-Performance-Anode-Material-for-Potassium-Ion-Batteries.html>

<https://www.nanowerk.com/spotlight/spotid=51930.php>

<https://inventions.news/2019-05-04-antimony-carbon-anode-next-gen-batteries.html>

<https://www.x-mol.com/news/16864>

4. Pankaj Ghildiyal, **Yong Yang**, and Michael R. Zachariah. “Laser-Induced Photothermal Writing of Uniformly Dispersed Metal Nanoclusters in Polymer Thin Films” *Nanoscale*, **2019**, 11, 13354-13365.

DOI: 10.1039/C9NR02839K

5. Yonggang Yao, Zhennan Huang, Pengfei Xie, Tangyuan Li, Steven D Lacey, Miaolun Jiao, Hua Xie, Kun Kelvin Fu, Rohit Jiji Jacob, Dylan Jacob Kline, **Yong Yang**, Michael R Zachariah, Chao Wang, Reza Shahbazian-Yassar, Liangbing Hu; Ultrafast, Controllable Synthesis of Sub-Nano Metallic Clusters through Defect Engineering; *ACS applied materials & interfaces*, **2019**, 11 (33), 29773-29779

DOI: 10.1021/acsami.9b07198

6. Rohit J. Jacob, Kevin J Hill, **Yong Yang**, Michelle L Pantoya, Michael R Zachariah; “Pre-stressing aluminum nanoparticles as a strategy to enhance reactivity of nanothermite composites”; *Combustion and Flame*, **2019**, 205, 33-40
DOI: 10.1016/j.combustflame.2019.03.024
7. Jiaojie Tan, **Yong Yang**, Hind El Hadri, Mingdong Li, Vincent A. Hackley, and Michael R. Zachariah, “*Fast quantification of nanorod geometry by DMA-spICP-MS*” 2019, 144, 2275
DOI: 10.1039/c8an02250j
8. Jing Zheng, Guangbin Ji, Xiulin Fan, Jichen, Qin Li, Haiyang Wang, **Yong Yang**, Kelly C. DeMella, Srini R. Raghavan, Chunsheng Wang; “*High-Fluorinated Electrolytes for Li-S Batteries.*” *Advanced Energy Materials*, **2019**, 9, 1803774
DOI: 10.1002/aenm.201803774
9. Haiyang Wang, Miles Rehwoldt, Xizheng Wang, **Yong Yang**, Michael Zachariah; “*On the Promotion of High Temperature AP Decomposition with Silica Mesoparticles.*” *Combustion and Flame* 200 (**2019**): 296-302.
DOI: 10.1016/j.combustflame.2018.11.021
10. Xizheng Wang; Tao Wu; Haiyang Wang; Jeff DeLisio; **Yang Yang**; Michael Zachariah; *Boron Ignition and Combustion with Doped δ -Bi₂O₃: Bond Energy/Oxygen Vacancy Relationships*; *Combustion and Flame*, **2019**, 197, 127-133

DOI: 10.1016/j.combustflame.2018.07.015

11. Miles C. Rehwoldt, **Yong Yang**, Haiyang Wang, Scott Holdren, and Michael R. Zachariah. "Ignition of Nanoscale Titanium/Potassium Perchlorate Pyrotechnic Powder: Reaction Mechanism Study." *The Journal of Physical Chemistry C* 122, no. 20 (**2018**): 10792-10800.

DOI: 10.1021/acs.jpcc.8b03164

12. Guangjie Feng, Zhuoran Li, Xxiaolong Xu, Zhongke Shen, **Yong Yang**, *Glass-Copper anodic bonding through activated Sn-0.6 Al solder*, *Journal of Materials Processing Technology* **2018**, 254, 108-113

DOI: 10.1016/j.jmatprotec.2017.11.038

13. Haiyang Wang, Jeffery B. DeLisio, Scott Holdren, Tao Wu, **Yong Yang**, Junkai Hu, and Michael R. Zachariah. "Mesoporous Silica Spheres Incorporated Aluminum/Poly (Vinylidene Fluoride) for Enhanced Burning Propellants." *Advanced Engineering Materials* 20, no. 2 (**2018**): 1700547.

DOI: 10.1002/adem.201700547

14. Guanine Feng, Zhuoran Li, Zhi Zhou, **Yong Yang**, Dusan P Sekulic, Michael R Zachariah; *Microstructure and mechanical properties of Cf/Al-TiAl laser-assisted brazed joint*, *Journal of Materials Processing Technology*, **2018**, 255

DOI: 10.1016/j.matdes.2017.04.044

15. Yujia Liang, Huilong Hou, **Yong Yang**, Howard Glicksman, and Sheryl Ehrman. "Conductive One-and Two-Dimensional Structures Fabricated Using Oxidation-Resistant Cu–Sn Particles." *ACS applied materials & interfaces* 9, no. 40 (2017): 34587-34591.

DOI: 10.1021/acsami.7b10076

16. Guangjie Feng, Zhuoran Li, Rohit J Jacob, **Yong Yang**, Yu Wang, Zhi Zhou, Dusan P Sekulic, Michael R Zachariah, Laser-induced exothermic bonding of carbon fiber/Al composites and TiAl alloys, *Materials & Design* 2017, 126, 197-206

DOI: 10.1016/j.matdes.2017.04.044

17. Rohit Jacob, Yichen Zong, **Yong Yang**, Shiquan Li, Michael R. Zachariah, Size-Resolved Burn Rate Measurements of Metal NanoParticles, 54th AIAA Aerospace Sciences Meeting, 0687, 2016

DOI: 10.2514/6.2016-0687

b. Publications that have been submitted and are under review:

1. **Yong Yang**, Boao Song, Xiang Ke, Feiyu Xu, Krassimir Bozhilov, Liangbing Hu, Reza Shahbazian-Yassar, Michael R. Zachariah, Aerosol Synthesis of High Entropy Alloy Nanoparticles. *Under review*, 2019

2. **Yong Yang**, Yonggang Yao, Dylan Kline, Tangyuan Li, Haiyang Wang, Liangbing Hu, Michael R. Zachariah, Laser Shock-Assisted Ultrafast Synthesis of Supported

Metal Nanoclusters with Kinetically Tunable Size and Surface Density. *Under review, 2019*

3. Jinpeng Shen, Haiyang Wang, Dylan J. Kline, **Yong Yang**, Xizheng Wang, Miles Rehwoldt, Tao Wu, Scott Holdren, Xin Liao, Zeshan Wang, Michael R. Zachariah; 3D Printing Reactive and Reinforced 90 wt.% Loading Nanothermite Structure. *Under review, 2019*

c. Publications that will be submitted after the defense:

1. Dylan J. Kline, **Yong Yang**, Wanjun Zhao, Rohit J. Jacob, Liangbing Hu, Michael R. Zachariah. Combustion Dynamics of Nanoaluminum-laden Reduced Graphene Oxide Fabricated by Laser Pulse Heating. *To be submitted, 2019*
2. Feiyu Xu, Prithwish Biswas, Dylan J. Kline, **Yong Yang**, Haiyang Wang and Michael R. Zachariah, *Superior Reactivity of Al/Bi₂WO₆ Metastable Intermolecular Composite. To be submitted, 2019*

Presentations:

a. Presentations that have been delivered:

1. **Yong Yang**, Growth of Sub-5 nm Metal Nanoclusters in a Continuous Flow Reactor; Pizza Seminar, Department of Chemical and Biomolecular Engineering, University of Maryland, August 29, **2018**

2. **Yong Yang**, Pankaj Ghildiyal, Michael R. Zachariah, Rapid and scalable synthesis of sub-10 nm metal nanoparticles in on-the-fly aerosols, ACS 256th National Meeting, Boston, August 19-23, **2018**
3. **Yong Yang**, Dylan J. Kline, Pankaj Ghildiyal, Michael R. Zachariah, Laser pulse induced growth of unaggregated Sub-5 nm metal nanoparticles in free-standing graphene films, ACS 256th National Meeting, Boston, August 19-23, **2018**
4. **Yong Yang**, Michelangelo Romano, Michael Zachariah, Synthesis and stabilization of ultrasmall-metal nanoparticles (Ni, Co, Cu) within a polymer matrix via a one-step aerosol spray pyrolysis. ACS 254th National Meeting, DC, August 20-24, **2017**
5. Rohit Jacob, Yichen Zong, **Yong Yang**, Shiquan Li, Michael R. Zachariah, Size-Resolved Burn Rate Measurements of Metal Nanoparticles, 54th AIAA Aerospace Sciences Meeting, 0687, **2016**